

**GROWTH, CHARACTERIZATION AND GAS SENSING  
PROPERTIES OF ONE DIMENSIONAL OXIDE  
NANOSTRUCTURES ON Ti AND Ti-6Al-4V ALLOY  
SUBSTRATES SYNTHESIZED BY THERMAL OXIDATION**

**MD. ARAFAT MAHMOOD**

**FACULTY OF ENGINEERING  
UNIVERSITY OF MALAYA  
KUALA LUMPUR**

**2017**

**GROWTH, CHARACTERIZATION AND GAS  
SENSING PROPERTIES OF ONE DIMENSIONAL  
OXIDE NANOSTRUCTURES ON Ti AND Ti-6Al-4V  
ALLOY SUBSTRATES SYNTHESIZED BY THERMAL  
OXIDATION**

**MD. ARAFAT MAHMOOD**

**THESIS SUBMITTED IN FULFILMENT OF THE  
REQUIREMENTS FOR THE DEGREE OF DOCTOR OF  
PHILOSOPHY**

**FACULTY OF ENGINEERING  
UNIVERSITY OF MALAYA  
KUALA LUMPUR**

**2017**

**UNIVERSITY OF MALAYA**  
**ORIGINAL LITERARY WORK DECLARATION**

Name of Candidate: Md. Arafat Mahmood ██████████

Matric No: KHA120031

Name of Degree: Doctor of Philosophy

Title of Thesis (“this Work”):

**Growth, Characterization and Gas Sensing Properties of One Dimensional Oxide Nanostructures on Ti and Ti-6Al-4V Alloy Substrates Synthesized by Thermal Oxidation**

Field of Study: Advanced Materials/Nanomaterials (Materials Engineering)

I do solemnly and sincerely declare that:

- (1) I am the sole author/writer of this Work;
- (2) This Work is original;
- (3) Any use of any work in which copyright exists was done by way of fair dealing and for permitted purposes and any excerpt or extract from, or reference to or reproduction of any copyright work has been disclosed expressly and sufficiently and the title of the Work and its authorship have been acknowledged in this Work;
- (4) I do not have any actual knowledge nor do I ought reasonably to know that the making of this work constitutes an infringement of any copyright work;
- (5) I hereby assign all and every rights in the copyright to this Work to the University of Malaya (“UM”), who henceforth shall be owner of the copyright in this Work and that any reproduction or use in any form or by any means whatsoever is prohibited without the written consent of UM having been first had and obtained;
- (6) I am fully aware that if in the course of making this Work I have infringed any copyright whether intentionally or otherwise, I may be subject to legal action or any other action as may be determined by UM.

Candidate’s Signature

Date:

Subscribed and solemnly declared before,

Witness’s Signature

Date:

Name:

Designation:

## ABSTRACT

One dimensional (1-D) nanostructures of titanium dioxide ( $\text{TiO}_2$ ) are of particular interest due to their capabilities of being used as functional materials in various applications such as mesoscopic physics and nanoscale devices. Wide variety of fabrication routes such as hydrothermal, electrospinning, anodization, UV lithography and thermal oxidation have been developed for synthesizing  $\text{TiO}_2$  nanostructures. Among all these routes, thermal oxidation is attractive for mass production due to its simplicity, scalability and low production cost. In this research work, 1-D nanostructures of  $\text{TiO}_2$  were synthesized on pure Ti and Ti-6Al-4V (Ti64) substrates by thermal oxidation. The oxidation parameters were optimized by investigating the effects of alloy microstructure, temperature, oxidation atmosphere, gas flow rate, residual stress and oxidation duration. The resultant nanostructures were investigated using X-ray diffractometer, X-ray photoelectron spectroscopy, Raman spectroscopy, transmission electron microscope, scanning electron microscope etc. For the preparation of gas sensors, Ti and Ti64 particles were deposited on Au interdigitated alumina substrates and thermally oxidized under optimum conditions for the growth of 1-D nanostructures. The as-prepared sensors were exposed to different target gases including  $\text{H}_2$ ,  $\text{H}_2\text{S}$ ,  $\text{CO}$ ,  $\text{CH}_4$ ,  $\text{CH}_3\text{OH}$ ,  $\text{C}_2\text{H}_5\text{OH}$ ,  $\text{C}_2\text{H}_4$ ,  $\text{NO}_2$  and  $\text{O}_2$ . The ratio of the electrical resistance in the background and the target gas environment was used to denote the sensing response of the sensors. Results revealed that during thermal oxidation oxide scales were formed on the Ti and Ti64. The 1-D nanostructures were evolved from the top surface of the oxide scales at  $750\text{ }^\circ\text{C}$  in oxygen deprived conditions ( $<100\text{ ppm O}_2$  in Ar). The presence of residual stress inside Ti and Ti64 significantly improved the coverage of 1-D nanostructures. New surfaces were formed in the form of 1-D nanostructures due to the relaxation of residual stress during

thermal oxidation. The 1-D nanostructures on pure Ti were rutile  $\text{TiO}_2$  and they formed in moist Ar environment.  $\text{TiO}_2$  scale was formed beneath the 1-D nanostructures. On the other hand, 1-D core-shell  $\text{TiO}_2\text{-Al}_2\text{O}_3$  nanostructures were formed during thermal oxidation of Ti64 in the presence of tens of ppm  $\text{O}_2$  in flowing dry Ar. A double layer of oxide scales was formed beneath the 1-D nanostructures. The top oxide scale is a mixture of  $\text{TiO}_2$  and  $\text{Al}_2\text{O}_3$  whereas the inner oxide scale is only  $\text{TiO}_2$ . It is proposed that during thermal oxidation metal ions diffuse in the outward direction and reacts with the oxygen containing species at  $[0\ 0\ 2]$  crystallographic direction of rutile to form 1-D nanostructures. The gas sensing results showed that the optimum operating temperature of the sensor was  $650\ ^\circ\text{C}$  and possessed selective response towards  $\text{H}_2\text{S}$ ,  $\text{CH}_3\text{OH}$  and  $\text{C}_2\text{H}_5\text{OH}$ . However, the highest response of 1109 was seen for 1000 ppm  $\text{C}_2\text{H}_5\text{OH}$  at  $650\ ^\circ\text{C}$ . Due to the catalytic activity of 1-D nanostructures,  $\text{C}_2\text{H}_5\text{OH}$  was decomposed and an amorphous layer of carbon was deposited on the nanostructures. Deposition of amorphous carbon significantly reduced the resistance of the sensor which is the reason for high selective response towards  $\text{C}_2\text{H}_5\text{OH}$ . The sensor showed complete recovery during the exposure in background environment.

## ABSTRAK

Satu dimensi (1-D) nano titanium dioksida ( $\text{TiO}_2$ ) adalah kepentingan tertentu kerana keupayaan mereka digunakan sebagai bahan berfungsi dalam pelbagai aplikasi seperti fizik dan nanoscale peranti mesoscopic. Pelbagai laluan fabrikasi seperti hidroterma, electrospinning, penganodan, litografi UV dan pengoksidaan haba telah dibangunkan untuk mensintesis nanostruktur  $\text{TiO}_2$ . Di antara semua laluan ini, pengoksidaan terma adalah menarik untuk pengeluaran besar-besaran kerana kesederhanaan, berskala dan kos pengeluaran yang rendah. Dalam penyelidikan ini, 1-D nanostruktur daripada  $\text{TiO}_2$  telah disintesis pada Ti tulen dan Ti-6Al-4V gabungan (Ti64) substrat oleh pengoksidaan terma. Parameter pengoksidaan telah dioptimumkan dengan menyiasat kesan mikrostruktur aloi, suhu, suasana pengoksidaan, kadar aliran gas, tegasan baki dan masa pengoksidaan. The nanostruktur paduan telah disiasat menggunakan X-ray diffractometer, sinar-X fotoelektron spektroskop, Raman spektroskop, penghantaran elektron mikroskop, mikroskop elektron pengimbas dan lain-lain Untuk penyediaan sensor gas, zarah Ti dan Ti64 telah didepositkan di Au substrat alumina interdigitated dan terma teroksida di bawah optimum syarat untuk pertumbuhan 1-D nanostruktur. Sensor as-bersedia terkena gas sasaran yang berbeza termasuk  $\text{H}_2$ ,  $\text{H}_2\text{S}$ ,  $\text{CO}$ ,  $\text{CH}_4$ ,  $\text{CH}_3\text{OH}$ ,  $\text{C}_2\text{H}_5\text{OH}$ ,  $\text{C}_2\text{H}_4$ ,  $\text{NO}_2$  dan  $\text{O}_2$ . Nisbah rintangan elektrik dalam persekitaran ambien dan gas sasaran telah digunakan untuk menunjukkan sensitiviti sensor. Hasil kajian menunjukkan bahawa, semasa terma pengoksidaan skala oksida terbentuk pada Ti dan Ti64. 1-D nanostruktur telah berkembang daripada permukaan atas skala oksida pada  $750^\circ\text{C}$  dalam oksigen dilucutkan syarat ( $<100$  ppm  $\text{O}_2$  di Ar). Kehadiran tegasan baki dalam Ti dan Ti64 ketara meningkatkan liputan 1-D nanostruktur. Permukaan baru dibentuk dalam bentuk 1-D nanostruktur disebabkan oleh kelonggaran sisa tekanan selama pengoksidasian panas. 1-D nanostruktur pada murni Ti adalah rutil  $\text{TiO}_2$  dan mereka telah

membentuk dalam persekitaran Ar lembap. Skala oksida  $\text{TiO}_2$  telah ditubuhkan di bawah nanostructure 1-D. Sebaliknya, struktur nano 1-D teras-shell  $\text{TiO}_2\text{-Al}_2\text{O}_3$  telah ditubuhkan semasa pengoksidaan terma  $\text{Ti64}$  di hadapan puluhan ppm  $\text{O}_2$  dalam aliran Ar kering. Satu lapisan berganda skala oksida telah ditubuhkan di bawah 1-D nanostruktur. Skala oksida utama ialah campuran  $\text{TiO}_2$  dan  $\text{Al}_2\text{O}_3$  manakala skala oksida dalaman hanya  $\text{TiO}_2$ . Adalah dicadangkan semasa pengoksidaan terma ion logam meresap ke arah yang zahir dan bertindak balas dengan oksigen yang mengandungi spesies di  $[0\ 0\ 2]$  arah kristalografi daripada rutil untuk membentuk 1-D nanostruktur. Keputusan sensitiviti menunjukkan bahawa suhu operasi optimum sensor adalah  $650\ ^\circ\text{C}$  dan mempunyai respon tertentu terhadap  $\text{H}_2\text{S}$ ,  $\text{CH}_3\text{OH}$  and  $\text{C}_2\text{H}_5\text{OH}$ . Bagaimanapun juga, respon tertinggi dari 1109 terlihat untuk 1000 ppm  $\text{C}_2\text{H}_5\text{OH}$  pada suhu  $650\ ^\circ\text{C}$ . Oleh kerana aktiviti pemangkin 1-D nanostruktur,  $\text{C}_2\text{H}_5\text{OH}$  telah reput dan lapisan amorfus karbon telah didepositkan di nanostruktur. Pemendapan karbon amorfus secara signifikan mengurangi rintangan sensor yang menjadi sebab atas selektif respon yang tinggi terhadap  $\text{C}_2\text{H}_5\text{OH}$ . Sensor menunjukkan pemulihan yang sempurna semasa pendedahan pada lingkungan asal.

## ACKNOWLEDGEMENTS

First and foremost, I would also like to express my deepest appreciation, sincere thanks and gratitude to my honorable supervisors, Prof. Dr. A. S. M. A. Haseeb from Department of Mechanical Engineering, University of Malaya. I would like to express my sincere gratitude to my external advisor Prof. Dr. S. A. Akbar from Department of Materials Science and Engineering, Ohio State University, Columbus, OH, USA. I would like to give special thanks to Dr. Ben Dinan from Ohio State University, USA for providing useful information to build the experimental setup. I am also grateful to Dr. M. Z. Quadir from School of Materials Science and Engineering, University of New South Wales, Sydney, Australia for providing transmission electron microscope facility. I greatly appreciate their contributions, precious time to monitor and guidance during my period of study.

I deeply appreciate the High Impact Research Grant (HIR-MOHE, Project No. UM.C/HIR/MOHE/ENG/26) and University of Malaya Research Grant (UMRG, Project No. RP021-2012D) for providing financial support throughout the period of my study.

Special thanks to Mr. Nazarul Zaman bin Mohd Nazir from Department of Mechanical Engineering, Mr. Zaharudin bin Mohd Salleh from Department of Geology and Ms. Zurina binti Marzuki from Department of Physics in University Malaya for providing assistance at different stages during the characterization of materials.

My dearest thanks go to my group members Dr. Tharsika Thabothanayakam, Dr. Goh Yingxin, Ms. Leong Yee Mei, Ms. Chia Pay Ying, Mr. Sujan Kumer Ghosh and Mr. Sazzad bin Sharif for their help in experimental works and technical discussions. Special

thanks to Ms. Fayeka Mansura and Mr. Md. Shariful Islam for providing generous help and guidance during editing the thesis. I would also like to thank all the members and staffs in the Department of Mechanical Engineering, University of Malaya for their generous helps on different issues. I am very grateful to my university colleagues for providing a friendly and relaxed atmosphere for conducting research.

Special thanks are owed to Mr. C. K. Leong from NovaScientific Resources (M) Sdn. Bhd. and Mr. Wong William from GW OA Sales & Services for supplying research materials in urgent basis.

I gratefully acknowledge to my all friends for their inputs and cooperation during the period of my study. Last but not the least, I would like to thank my parents (Md. Ali and Anowara Khatun) and my sister Riffat Mahmood for their kind support and encouragements. Finally, I would like to give special thanks to my wife Venny Agustrin Ningsih for her care, support and inspirations throughout this process.

## TABLE OF CONTENTS

Abstract .....	iii
Abstrak .....	v
Acknowledgements .....	vii
Table of Contents .....	ix
List of Figures .....	xv
List of Tables.....	xxiii
List of Symbols and Abbreviations.....	xxiv
List of Appendices .....	xxxi
<b>CHAPTER 1: INTRODUCTION .....</b>	<b>1</b>
1.1 Background.....	1
1.2 Research Objectives.....	3
1.3 Scope of Research.....	4
1.4 Organization of the Thesis.....	5
<b>CHAPTER 2: LITERATURE REVIEW.....</b>	<b>6</b>
2.1 Introduction.....	6
2.2 1-D Nanostructures on Ti and Ti Alloys by Thermal Oxidation.....	8
2.2.1 Tube Furnace Oxidation .....	8
2.2.2 Effects of Different Parameters during Oxidation .....	10
2.2.2.1 Effects of Alloying Elements and Microstructures .....	14
2.2.2.2 Effects of Oxidation Environment .....	15
2.2.2.3 Effects of Temperature .....	17
2.2.2.4 Effects of Oxidation Duration .....	18

2.2.3	Characterization of 1-D Nanostructures .....	18
2.2.4	Characterization of Oxide Scale beneath 1-D Nanostructures .....	20
2.2.5	Growth Mechanism of 1-D Nanostructures during Oxidation .....	20
2.2.6	Summary of Thermal Oxidation for 1-D Growth on Ti Particles .....	21
2.3	Gas Sensing using Semiconducting Metal Oxides .....	24
2.3.1	General Mechanism of Gas Sensing .....	24
2.3.2	Gas Sensor Performance Characteristics .....	26
2.3.3	Evaluation of Dimensionality in Nanostructures for Gas Sensing .....	27
2.3.4	Mechanism of Gas Sensing by 1-D Oxide Nanostructures .....	29
2.3.5	Recent Developments and Sensing Mechanism .....	32
2.3.6	Fabrication of Sensors Using 1-D Nanostructures .....	35
2.3.7	Gas Sensing Performance of TiO <sub>2</sub> Based Materials .....	37
2.3.8	Summary and Research Gap in Gas Sensing using TiO <sub>2</sub> .....	43
<b>CHAPTER 3: METHODOLOGY .....</b>		<b>45</b>
3.1	Raw Materials .....	45
3.2	Preparation of Substrates before Oxidation .....	46
3.2.1	Heat Treatment of Particles .....	46
3.2.2	Milling of Particles .....	47
3.2.3	Stress Relaxation of Milled Particles .....	47
3.2.4	Cleaning of Particles and Sheets .....	47
3.2.5	Preparation of Ink for Dispersing the Particles .....	47
3.3	Experimental Setup for Thermal Oxidation and Growth Parameters .....	48
3.3.1	Design of the Experimental Setup .....	48
3.3.2	Thermal Oxidation Process .....	50
3.4	Experimental Setup for Gas Sensing and Sensing Parameters .....	52
3.4.1	Design for Experimental Setup .....	52

3.4.2	Gas Sensing Parameters .....	53
3.4.2.1	Measurement of Response .....	53
3.4.2.2	Selectivity of Sensor.....	54
3.4.2.3	Optimum Operating Temperatures.....	54
3.4.2.4	Effect of Concentration of Target Gases.....	54
3.4.2.5	Response Time and Recovery Time.....	55
3.5	Characterizations of Samples .....	55
3.5.1	Characterizations before Oxidation.....	55
3.5.1.1	Measurement of Particle Size.....	55
3.5.1.2	Determination of Oxidation Temperature .....	55
3.5.1.3	Observation of Phases Microstructures .....	56
3.5.1.4	Determination of Phase Content .....	56
3.5.1.5	Measurement of Residual Stress .....	56
3.5.2	Characterizations after Oxidation.....	58
3.5.2.1	Determination of Phase Content .....	58
3.5.2.2	Determination of Oxidation States.....	58
3.5.2.3	Surface Morphologies and Elemental Analysis .....	59
3.5.2.4	Oxide Scales beneath 1-D Nanostructures .....	59
3.5.2.5	Epitaxy between Substrate Orientation and 1-D Growth.....	60
3.5.2.6	Characterization of 1-D Nanostructures.....	60
3.5.3	Characterizations of Sensors .....	61
3.5.3.1	Physical and Structural Observation of Sensors .....	61
3.5.3.2	Resistance Measurements of Sensors.....	61
3.5.3.3	Compositional Characterization of Sensors .....	61
<b>CHAPTER 4: RESULTS AND DISCUSSION .....</b>		<b>62</b>
4.1	Growth of 1-D Nanostructures on Ti Particles .....	62

4.1.1	Characterization of As-received Ti Particles.....	62
4.1.2	Thermal Oxidation of Ti Particles.....	64
4.1.2.1	Effects of Oxidation Temperature.....	64
4.1.2.2	Effects of Oxidation Environment.....	67
4.1.2.3	Effects of Residual Stress on Oxidation.....	70
4.1.2.4	Effects of Dynamic Oxygen Partial Pressure.....	75
4.1.3	Characterization of Oxidized Ti Particles.....	80
4.1.3.1	Surface Characterization of Oxidized Ti Particles.....	81
4.1.3.2	Morphological Oddities of 1-D Nanostructures.....	84
4.1.4	Mechanism of 1-D Growth on Ti Particles.....	86
4.1.5	Summary of Thermal Oxidation of Ti Particles.....	90
4.2	Growth of 1-D Nanostructures on Ti-6Al-4V (Ti64).....	91
4.2.1	Characterization of the As-received Ti64 Particles and Sheets.....	91
4.2.1.1	Elemental Analysis of Ti64 Particles and Sheets.....	91
4.2.1.2	Crystal and Phase of Ti64 Particles and Sheets.....	93
4.2.2	Thermal Oxidation of Ti64.....	94
4.2.2.1	Effects of Oxidation Temperatures.....	94
4.2.2.2	Effects of Alloy Microstructures.....	96
4.2.2.3	Effects of Oxidation Environment.....	100
4.2.2.4	Effects of Dynamic Oxygen Partial Pressure.....	102
4.2.2.5	Effects of Residual Stress on Oxidation.....	106
4.2.2.6	Effects of Oxidation Duration.....	120
4.2.3	Characterization of Oxidized Ti64 Substrates.....	125
4.2.3.1	Surface Characterization of Oxidized Ti64.....	125
4.2.3.2	Characterization of 1-D Nanostructures on Ti64.....	128
4.2.3.3	Cross-sectional Characterization of Oxidized Ti64.....	135

4.2.3.4	Structure of Oxidized Ti64 Particles .....	138
4.2.3.5	Epitaxy between 1-D Nanostructures and Ti64 Sheets .....	139
4.2.3.6	Initial Morphology of 1-D Nanostructures.....	146
4.2.4	Mechanism of 1-D Growth on Ti64 Substrates.....	147
4.2.5	Summary of Thermal Oxidation of Ti64 Particles .....	151
4.2.6	Comparison of 1-D Growth on Ti and Ti64 Substrates .....	153
4.3	Gas Sensing .....	156
4.3.1	Gas Sensing Nanostructures .....	156
4.3.2	Optimization of Sensor Fabrication .....	158
4.3.2.1	Sensors with Different wt% of Particle Loading .....	158
4.3.2.2	Determination of Resistance of As-prepared Sensors.....	158
4.3.2.3	Relation between Sensor Resistance and Particle Loading.....	159
4.3.3	Gas Sensing Performance.....	164
4.3.3.1	Effects of Composition, Morphology and Selectivity.....	164
4.3.3.2	Performance towards H <sub>2</sub> S, CH <sub>3</sub> OH and C <sub>2</sub> H <sub>5</sub> OH.....	167
4.3.4	Characterization of Nanostructures before Recovery.....	171
4.3.4.1	Appearance of Sensors .....	172
4.3.4.2	Morphological Observations and Characterization.....	172
4.3.5	Characterization of Nanostructures after Recovery .....	177
4.3.6	Stability and Reproducibility of Sensors.....	178
4.3.7	Mechanism of Gas Sensing .....	179
4.3.7.1	Role of Al <sub>2</sub> O <sub>3</sub> on Sensing Structure .....	179
4.3.7.2	Semiconducting Behavior of Rutile TiO <sub>2</sub> .....	180
4.3.7.3	Proposed Mechanism of Gas Sensing .....	182
4.3.7.4	Performance Determining Factors for Sensing .....	187
4.3.7.5	Comparison of Gas Sensing .....	188

4.3.8	Summary of Gas Sensing .....	193
4.4	Summary of Thesis .....	193
<b>CHAPTER 5: CONCLUSIONS AND RECOMMENDATIONS .....</b>		<b>195</b>
5.1	Conclusions .....	195
5.1.1	Growth of Nanostructures on Ti Particles .....	195
5.1.2	Growth of Nanostructures on Ti64 Substrates .....	195
5.1.3	Gas Sensing .....	197
5.2	Recommendations.....	198
	References .....	200
	List of Publications and Papers Presented .....	216
	Appendices.....	217

## LIST OF FIGURES

Figure 2.1: Synthesis processes of 1-D nanostructures.....	6
Figure 2.2: Schematic experimental setup for the synthesis of 1-D nanostructures on Ti and its alloy substrate by thermal oxidation process. This figure is not in scale. ....	9
Figure 2.3: Ti-6.85Al-1.6V substrate after thermal oxidation at 700 °C for 8 h in presence of trace amount of oxygen in Ar at a flow rate of 500 sccm. The 1-D nanostructures are seen to grow preferentially on $\beta$ phase during thermal oxidation (Huyong Lee et al., 2010). .....	14
Figure 2.4: TiO <sub>2</sub> nanostructures grown on Ti foil by thermal oxidation at 850 °C in presence of different oxygen sources (a) pure oxygen (99%) (Xinsheng Peng & Chen, 2004), (b) 1 sccm flow of O <sub>2</sub> in 200 sccm flow of Ar (Xinsheng Peng & Chen, 2004), (c) water vapor in Ar (Xinsheng Peng et al., 2005) and (d) acetone in Ar (Xinsheng Peng et al., 2005). ....	15
Figure 2.5: SEM images of 1-D nanostructures on Ti wire oxidized in ethanol vapor at different temperatures of (a) 700 °C, (b) 750 °C, (c) 800 °C and (d) 850 °C (Daothong et al., 2007). ....	17
Figure 2.6: (a-b) High resolution TEM image of the 1-D core-shell TiO <sub>2</sub> -C nanostructure grown on Ti substrate using acetone as oxidation medium and corresponding low magnification view with SADE pattern (Huo et al., 2008), (c) TEM image of the 1-D core-shell TiO <sub>2</sub> -Al <sub>2</sub> O <sub>3</sub> nanostructure grown on Ti64 substrate (B. J. Dinan et al., 2013). .....	19
Figure 2.7: Mechanism of reducing gas sensing using <i>n</i> -type metal oxides: (a) before adsorption of oxygen, (b) adsorption of oxygen from ambient and creation of electron depleted layer and (c) electron donation by reducing species where <i>R</i> represents reducing gas (Adapted from the Ref. (C. Wang et al., 2010)). ....	25
Figure 2.8: Change in resistance of <i>p</i> -type TeO <sub>2</sub> during the exposure of (a) oxidizing NO <sub>2</sub> and (b) reducing H <sub>2</sub> S (Z. Liu et al., 2007). ....	26
Figure 2.9: (a) Thick film of SnO <sub>2</sub> screen printed on Al <sub>2</sub> O <sub>3</sub> substrate (Montméat et al., 2004), (b) Al doped ZnO films deposited onto SiO <sub>2</sub> /Si substrates (390 nm) (Chang et al., 2002) and (c) In <sub>2</sub> O <sub>3</sub> nanofibers grown by electrospinning (W. Zheng et al., 2009). ....	28
Figure 2.10: (a) Vertically aligned 1-D ZnO nanostructures produced by hydrothermal process (Z. Yang et al., 2008), (b) ZnO nanorods with a flowerlike morphology grown by	

hydrothermal process (Feng et al., 2005) and (c) hierarchical dendrites of ZnO produced by vapor phase transport route (N. Zhang et al., 2008).....	30
Figure 2.11: (a) Contacts of 1-D nanostructures with flower-like morphology, (b) magnified view of a contact and (c) energy band diagram in presence of reducing gas (Adapted from Ref. (Feng et al., 2005)).....	32
Figure 2.12: (a) TiO <sub>2</sub> nanotubes prepared by anodization process (Paulose et al., 2005) and (b) Au nanoparticles loaded In <sub>2</sub> O <sub>3</sub> nanowire (Singh et al., 2011).....	33
Figure 2.13: Schematic band bending at heterojunctions with no adsorbed surface species (a-b) <i>n-n</i> junction (adopted from Ref. (Miller et al., 2014; Zeng, Liu, & Wang, 2010)), (c-d) <i>p-p</i> junction (adopted from Ref. (Y. Wang et al., 2015)) and (e-f) <i>n-p</i> junction (adopted from Ref. (Miller et al., 2014)). .....	35
Figure 2.14: Schematics of sensor fabrication (a) single nanostructure arrangement, (b) aligned nanostructure arrangements and (c) randomly distributed arrangement. ....	36
Figure 3.1: Stereoscopic top view of the Au interdigitated alumina substrate and its dimensions. ....	45
Figure 3.2: Heat treatment cycle for the “normalized” and “annealed” Ti and Ti64 particles. ....	46
Figure 3.3: The schematic of the experimental setup for the thermal oxidation process. ....	48
Figure 3.4: Temperature profile of the horizontal tube furnace for thermal oxidation process.....	50
Figure 3.5: The schematic of the experimental setup for the gas sensing experimentation. ....	52
Figure 4.1: (a) FESEM image of the as-received Ti particles, (b) EDX spectrum from the spot analysis of as-received Ti particles.....	63
Figure 4.2: XRD peaks of the as-received Ti particles. ....	63
Figure 4.3: TGA analysis of as-received Ti particles in ambient environment and commercial N <sub>2</sub> flown at 200 sccm. ....	65
Figure 4.4: FESEM images of thermally oxidized Ti particles in the presence of 5 ppm O <sub>2</sub> in flowing Ar (150 sccm) at different temperatures (a) 650 °C, (b) 700 °C, (c) 750 °C, (d) 800 °C, (e) 850 °C and (f) 900 °C. ....	66

Figure 4.5: Magnified views thermally oxidized Ti particles in presence of 5 ppm O <sub>2</sub> in flowing Ar (150 sccm) at 750 °C at different locations shown in Figure 4.4(c): (a) location A, (b) location B, (c) location C and (d) location D. ....	67
Figure 4.6: FESEM images of Ti particles after oxidation for 4 h at 750 °C in atmosphere containing 5 ppm of O <sub>2</sub> in Ar at a flow rate of 150 sccm in (a) dry oxidation and (b) humid oxidation conditions. ....	68
Figure 4.7: (a) FESEM image of the milled Ti particles (Ti-20h), (b) EDX spectrum of Ti-20h particles and (c) XRD peaks of the Ti-20h particles. ....	71
Figure 4.8: (a) XRD peaks of (2 1 3) plane in Ti-0h particles, (b) XRD peaks of (2 1 3) plane in Ti-20h particles, (c) $d\text{-sin}^2\psi$ plot for the Ti-0h and Ti-20h particles and (d) estimated compressive residual stress inside the particles. ....	73
Figure 4.9: FESEM images of Ti-20h particles after oxidation at 750 °C containing 5 ppm of O <sub>2</sub> in humid Ar at a flow rate of 150 sccm. ....	74
Figure 4.10: FESEM images of the Ti-20h particles after humid oxidation at 750 °C for 4 h in (a) 20 sccm flow with 5 ppm O <sub>2</sub> , (b) 20 sccm flow with 105 ppm O <sub>2</sub> , (c) 50 sccm flow with 5 ppm O <sub>2</sub> , (d) 50 sccm flow with 55 ppm O <sub>2</sub> , (e) 50 sccm flow with 105 ppm O <sub>2</sub> , (f) 150 sccm flow with 5 ppm O <sub>2</sub> , (g) 150 sccm flow with 105 ppm O <sub>2</sub> , (h) 300 sccm flow with 5 ppm O <sub>2</sub> and (i) 300 sccm flow with 105 ppm O <sub>2</sub> . ....	77
Figure 4.11: Theoretical representation of dynamic oxygen partial pressure inside the tube for different flow rates and oxygen concentrations. The experimental conditions conducted on Ti-20h particles are shown by purple color. ....	79
Figure 4.12: EDX spectrum on Ti-20h particles oxidized at 750 °C containing 5 ppm of O <sub>2</sub> in humid Ar at a flow rate of 150 sccm. ....	81
Figure 4.13: XRD peaks of Ti-20h particles oxidized for 4 h at 750 °C in presence of 5 ppm of O <sub>2</sub> in humid Ar flown at a rate of 150 sccm. ....	82
Figure 4.14: (a) XPS spectra of Ti sheet oxidized at 750 °C for 4 h in presence of 5 ppm O <sub>2</sub> in humid Ar at flow rate of 500 sccm, (b) narrow scan of Ti2p spectra and (c) narrow scan of O1s spectra. ....	83
Figure 4.15: The growth of different types of nanostructures during oxidation of Ti particles (a) stacked morphology, (b) ribbon morphology, (c) plateau morphology and (d) lamp post shaped morphology. ....	85
Figure 4.16: Schematics of 1-D growth on Ti substrate during humid oxidation. ....	88
Figure 4.17: (a) FESEM image of the as-received Ti64 particles, (b-d) elemental mapping of the particles for the elements of Ti (green), Al (red) and V (blue) respectively and (e) EDX spectrum of the Ti64 particles. ....	92

Figure 4.18: FESEM image of Ti64 sheet after polishing and etching.....	92
Figure 4.19: XRD pattern of as-received (a) Ti64 particles and (b) Ti64 sheet. ....	93
Figure 4.20: TGA analysis of as-received Ti64 particles in ambient environment and commercial N <sub>2</sub> flown at 200 sccm. ....	95
Figure 4.21: Thermal oxidation of Ti64 particles with 40 ppm of O <sub>2</sub> in flowing Ar (500 sccm) for 8 h at different temperatures (a) 650 °C, (b) 700 °C, (c) 750 °C, (d) 800 °C, (e) 850 °C and (f) 900 °C. ....	96
Figure 4.22: XRD peaks of Ti64 particles in (a) as-received, (b) normalized and (c) annealed conditions. ....	97
Figure 4.23: Microstructures of polished and etched Ti64 particles in (a-b) as-received, (c-d) normalized and (e-f) annealed conditions. ....	98
Figure 4.24: FESEM images of the Ti64 particles oxidized at 750 °C for 4 h in presence of 15 ppm of O <sub>2</sub> in flowing Ar (500 sccm): (a) as-received, (b) normalized and (c) annealed particles. ....	99
Figure 4.25: FESEM images of the as-received Ti64 particles oxidized for 4 h at 750 °C in presence of 15 ppm of O <sub>2</sub> in flowing Ar (500 sccm). ....	101
Figure 4.26: FESEM images of the Ti64 particles oxidized at 750 °C for 4 h in (a) 20 sccm flow with 5 ppm O <sub>2</sub> , (b) 20 sccm flow with 105 ppm O <sub>2</sub> , (c) 50 sccm flow with 5 ppm O <sub>2</sub> , (d) 50 sccm flow with 105 ppm O <sub>2</sub> , (e) 500 sccm flow with 15 ppm O <sub>2</sub> , (f) 500 sccm flow with 40 ppm O <sub>2</sub> , (g) 500 sccm flow with 55 ppm O <sub>2</sub> , (h) 500 sccm flow with 80 ppm O <sub>2</sub> and (i) 500 sccm flow with 105 ppm O <sub>2</sub> . ....	103
Figure 4.27: Theoretical representation of dynamic oxygen partial pressure inside the tube for different flow rates and oxygen concentrations. The experimental conditions conducted on Ti64 particles are shown by purple color. ....	104
Figure 4.28: FESEM images of Ti64 particles milled for (a) 2 h, (b) 5 h, (c) 10 h, (c) 15 h, (e) 20h, (f) 25 h and (g) 30h. ....	107
Figure 4.29: (a) Distribution of particle size at different hours of milling and (b) effects of milling on the average size of Ti64 particles. ....	108
Figure 4.30: EDX spectrum of Ti64 particles milled for 20 h (Ti64-20h particles). ....	109
Figure 4.31: XRD peaks of Ti64 particles milled for 20 h in planetary ball mill (Ti64-20h particles). ....	110

Figure 4.32: (a) XRD peak of (1 0 3) plan in Ti64-0h particles, (b) XRD peak of (1 0 3) plan in Ti64-20h particles, (c) $d\text{-sin}^2\psi$ plot for the Ti64-0h and Ti64-20h particles and (d) estimated residual stress inside the particles.....	111
Figure 4.33: FESEM micrographs of Ti64 particles after thermal oxidation for 8 hours at 750 °C with 40 ppm O <sub>2</sub> in flowing Ar (a) Ti64-0h, (b) Ti64-2h, (c) Ti64-5h, (d) Ti64-10h, (e) Ti64-15h, (f) Ti64-20h, (g) Ti64-25h and (h) Ti64-30h.....	113
Figure 4.34: FESEM images of Ti64 oxidized in presence of 15 ppm of O <sub>2</sub> in flowing Ar for 4 h (a) Ti64-0h particles oxidized at 750 °C, (b) Ti64-20h particles oxidized at 750 °C, (c) Ti64-0h particles oxidized at 800 °C and (d) Ti64-20h particles oxidized at 800 °C. ....	114
Figure 4.35: (a) FESEM image of the Ti64-20h particles after heat treatment at 1000 °C for 3 h in presence of flowing Ar+5%H <sub>2</sub> environment and (b) EDX spectrum of the heat treated Ti64-20h particles. ....	115
Figure 4.36: (a) XRD peak of (2 1 3) plan in stress relaxed Ti64-20h particles, (b) $d\text{-sin}^2\psi$ plot for the stress relaxed Ti64-20h particles.....	116
Figure 4.37: FESEM image of the heat treated Ti64-20h particles oxidized at 750 °C in presence of 15 ppm of O <sub>2</sub> in flowing Ar for 4 h. ....	117
Figure 4.38: (a) Ti64 sheet (25mm x 3 mm x 1 mm), and FESEM micrograph on the Ti64 sheet after thermal oxidation at 750 °C for 8 hours with 40 ppm oxygen in flowing Ar at (b) position 1, (c) position 2, (d) position 3, (e) position 4, (f) position 5, (g) position 6. ....	118
Figure 4.39: FESEM images of thermally oxidized Ti64-0h particles under optimum conditions of 750 °C in presence of 15 ppm of O <sub>2</sub> in flowing Ar (500 sccm) for variant duration of time (a) 1 min, (b) 5 min, (c) 15 min, (d) 30 min, (e) 1 h, (f) 2 h, (g) 4 h, (h) 8 h, (i) 16 h and (j) 24 h. ....	121
Figure 4.40: Line scanning of Ti64-0h particles oxidized for 1 min at 750 °C in presence of 15 ppm of O <sub>2</sub> in flowing Ar (500 sccm). ....	122
Figure 4.41: FESEM images of thermally oxidized Ti64-20h particles under optimum conditions of 750 °C in presence of 15 ppm of O <sub>2</sub> in flowing Ar (500 sccm) for different time periods: (a) 1 min, (b) 5 min, (c) 15 min, (d) 30 min, (e) 1 h, (f) 2 h, (g) 4 h, (h) 8 h, (i) 16 h and (j) 24 h. ....	124
Figure 4.42: XRD pattern of the Ti64 particles oxidized at 750 °C in presence of 15 ppm oxygen in Ar flowing at 500 sccm (a) oxidized as-received Ti64 (Ti64-0h) and (b) oxidized 20 h milled Ti64 (Ti64-20h).....	126

Figure 4.43: (a) XPS spectra of Ti64 sheet oxidized at 750 °C for 4 h in presence of 15 ppm O <sub>2</sub> in Ar at flow rate of 500 sccm, (b) narrow scan of Ti2p spectra and (c) narrow scan of Al2p spectra. ....	127
Figure 4.44: (a) FESEM image of oxidized Ti64-20h particles after thermal oxidation at 750 °C in presence of 20 ppm of O <sub>2</sub> in flowing Ar (500 sccm) for 8 h, (b) EDX spectrum taken at position ‘X’ and (c) EDX spectrum taken at position ‘Y’ shown in figure (a). ....	128
Figure 4.45: FESEM image of 1-D nanostructures grown on Ti64-20h particles followed by ultrasonication and collection on a Cu grid.....	129
Figure 4.46: (a) TEM image of a single fine 1-D nanostructure, (b) HRTEM image focused at location X and (c) HRTEM image focused at location Y.....	129
Figure 4.47: (a) STEM images of a fine 1-D nanostructure and (b) EDX line scanning spectroscopy of fine 1-D nanostructure.....	130
Figure 4.48: (a) TEM image of a single thick 1-D nanostructure, (b) HRTEM image focused at location X and (c) HRTEM image focused at location Y.....	131
Figure 4.49: (a) STEM images of a thick 1-D nanostructure and (b) EDX line scanning spectroscopy of thick 1-D nanostructure.....	131
Figure 4.50: (a) TEM image of a bundled nanostructure, (b) HRTEM image focused at location A, (c) location B, (d) location C and (e) location E.....	132
Figure 4.51: (a) STEM image of a bundled nanostructure and (b) EDX line scanning spectroscopy of the bundled nanostructure.....	133
Figure 4.52: (a) Bright field TEM image, (b) dark field TEM image and (c) SAD pattern of the 1-D nanostructure grown on Ti64 particles at 750 °C for 4 h in the presence of 15 ppm O <sub>2</sub> in flowing Ar (500 sccm).....	134
Figure 4.53: (a) Cross-sectional SEM view of the Ti64-0h particles after thermal oxidation, and corresponding elemental maps of (b) Ti, (c) Al, (d) O and (e) V. ....	135
Figure 4.54: (a) Cross-sectional SEM view of the Ti64-20h particles after thermal oxidation, and corresponding elemental maps of (b) Ti, (c) Al, (d) O and (e) V. ....	136
Figure 4.55: Schematic cross-sectional view after thermal oxidation of spherical Ti64 particles (a) particles having larger diameter (>20 μm) and (b) particles having smaller diameter (<20 μm). The schematics are not proportioned with actual scale. ....	139
Figure 4.56: (a) IPF triangle of α-Ti (hexagonal) crystal, (b-d) Schematic orientations of hexagonal crystals in α-Ti grains for the corner regions in IPF triangle.....	140

Figure 4.57: (a) SEM image of the polished Ti64 sheets containing hexagonal crystals in $\alpha$ -Ti grains and (b) orientation mapping image. ....	141
Figure 4.58: <i>Kikuchi pattern</i> of (a-b) “R” grain and corresponding crystal orientation, (c-d) “G” grain and corresponding crystal orientation and (e-f) “B” grain and corresponding crystal orientation. The (0 0 0 1), (2 $\bar{1}$ $\bar{1}$ 0) and (1 0 $\bar{1}$ 0) planes are shown on the oriented crystal by the dotted lines in Figure (b), (d) and (f), respectively.....	142
Figure 4.59: FESEM image of Ti64 sheet oxidized for 1 min identifying similar grains donated by “R”, “G” and “B” shown in the orientation map. ....	143
Figure 4.60: Thermally oxidized Ti64 sheet for 1 min with 15 ppm O <sub>2</sub> in flowing Ar (500 sccm) at 750 °C showing (a) “R” grain where (0 0 0 1) plane is parallel to the oxidation surface, (b) “G” grain where (2 $\bar{1}$ $\bar{1}$ 0) plane is parallel to the oxidation surface and (c) “B” grain where (1 0 $\bar{1}$ 0) plane is parallel to the oxidation surface. ....	144
Figure 4.61: The $\langle 2 \bar{2} 0 1 \rangle$ directions of hexagonal $\alpha$ -Ti crystal observed from the top view projections of (a) (2 $\bar{1}$ $\bar{1}$ 0) crystallographic plane and (b) (1 0 $\bar{1}$ 0) crystallographic plane. ....	145
Figure 4.62: Thermally oxidized Ti64 sheet under non-optimum conditions of 40 ppm O <sub>2</sub> in flowing Ar (500 sccm) at 750 °C for 8 h. ....	146
Figure 4.63: Growth mechanism of 1-D nanostructures on Ti64 substrate during thermal oxidation.....	150
Figure 4.64: 1-D nanostructures for gas sensing (a) S-1 sensor contains TiO <sub>2</sub> nanostructures on Ti-20h particles grown at 750 °C, (b) S-2 sensor contains fine core-shell TiO <sub>2</sub> -Al <sub>2</sub> O <sub>3</sub> nanostructures on Ti64-20h particles grown at 750 °C and (c) S-3 sensor contains thick core-shell TiO <sub>2</sub> -Al <sub>2</sub> O <sub>3</sub> nanostructures on Ti64-20h particles grown at 800 °C. ....	157
Figure 4.65: Resistance of the S-2 sensors containing varying amount of particle loading at room temperature, 450 °C and 650 °C.....	159
Figure 4.66: Top view of the as-prepared S-2 sensors at different magnifications prepared from ink containing different wt% of particles (a-b) 1 wt% of Ti64 particles in the ink, (c-d) 5 wt% of Ti64 particles in the ink and (e-f) 20 wt% of Ti64 particles in the ink. ....	160
Figure 4.67: (a) The particles of S-2 sensor containing 10 wt% of loading is detached as flakes, (b) stereoscopic view of the top side and flip side facing particles, (c) FESEM image of the top side facing particles and (d) FESEM image of the flip side facing particles. ....	161
Figure 4.68: Schematics of the sensors prepared from ink containing different wt% of particles (a) loading of <2 wt%, (b) loading of 2-5 wt% and (c) loading of >5 wt%... ..	163

Figure 4.69: Resistance response towards 1000 ppm of H <sub>2</sub> , H <sub>2</sub> S, CO, CH <sub>4</sub> , CH <sub>3</sub> OH, C <sub>2</sub> H <sub>5</sub> OH, C <sub>2</sub> H <sub>4</sub> , NO <sub>2</sub> and O <sub>2</sub> at 650 °C of (a) S-1 sensor, (b) S-2 sensor, (c) S-3 sensor and (d) comparison of the sensing response among the S-1, S-2 and S-2 sensors. ....	165
Figure 4.70: Effects of operating temperatures on S-2 sensor during the exposure of 1000 ppm of (a) H <sub>2</sub> S, (b) CH <sub>3</sub> OH, (c) C <sub>2</sub> H <sub>5</sub> OH and (d) relation between sensor response and operating temperatures for 1000 ppm H <sub>2</sub> S, CH <sub>3</sub> OH and C <sub>2</sub> H <sub>5</sub> OH. ....	168
Figure 4.71: Effects of target gas concentration on the performance of S-2 sensor at 650 °C for exposure to H <sub>2</sub> S, CH <sub>3</sub> OH and C <sub>2</sub> H <sub>5</sub> OH (a) resistance as a function of gas concentration and (b) effects of target gas concentrations on response. ....	169
Figure 4.72: (a) Response and (b) recovery times of S-2 sensor during the exposure of different concentrations of target gases (H <sub>2</sub> S, CH <sub>3</sub> OH and C <sub>2</sub> H <sub>5</sub> OH) at optimum operating temperature of 650 °C. ....	171
Figure 4.73: FESEM image of the sensors containing 1-D nanostructures grown on Ti64-20h particles at 750 °C for 4 h with 15 ppm O <sub>2</sub> flow in flowing Ar (a) as-prepared sensor, (b-d) sensor exposed to 1000 ppm H <sub>2</sub> S, CH <sub>3</sub> OH and C <sub>2</sub> H <sub>5</sub> OH respectively in N <sub>2</sub> at 650 °C for 30 min. ....	173
Figure 4.74: TEM image of 1-D core-shell TiO <sub>2</sub> -Al <sub>2</sub> O <sub>3</sub> nanostructures after exposing to 1000 ppm C <sub>2</sub> H <sub>5</sub> OH for 30 min at 650 °C and (b) EDX spectroscopy area analysis of 1-D nanostructure. ....	175
Figure 4.75: Raman spectroscopy analysis of (a) as-prepared S-2 sensor and (b-d) after exposing to 1000 ppm of H <sub>2</sub> S, CH <sub>3</sub> OH and C <sub>2</sub> H <sub>5</sub> OH, respectively at 650 °C for 30 min. ....	176
Figure 4.76: FESEM images of 1-D nanostructures in S-2 sensors after recovery from the exposure of (a) H <sub>2</sub> S, (b) CH <sub>3</sub> OH and (c) C <sub>2</sub> H <sub>5</sub> OH. ....	177
Figure 4.77: Raman spectroscopy analysis of S-2 sensor after recovery in N <sub>2</sub> for 20 min at 650 °C from (a) CH <sub>3</sub> OH and (b) C <sub>2</sub> H <sub>5</sub> OH. ....	178
Figure 4.78: Proposed electron tunneling assisted surface depletion model for sensing reducing gas using 1-D core-shell TiO <sub>2</sub> -Al <sub>2</sub> O <sub>3</sub> nanostructure: (a) before adsorption of oxygen; (b) during adsorption of oxygen and (c) in reducing environment where <i>R</i> represents reducing gas. ....	184
Figure 4.79: Schematics of CH <sub>3</sub> OH and C <sub>2</sub> H <sub>5</sub> OH sensing using 1-D core-shell TiO <sub>2</sub> -Al <sub>2</sub> O <sub>3</sub> nanostructures: (a) sensor in ambient environment and (b) sensors in CH <sub>3</sub> OH and C <sub>2</sub> H <sub>5</sub> OH gas containing environment. ....	187

## LIST OF TABLES

Table 2.1: Summary of the 1-D nanostructure grown by thermal oxidation process on Ti and Ti-alloy substrates. ....	11
Table 2.2: The research findings and gaps for 1-D growth on Ti and its alloy substrates by thermal oxidation. ....	22
Table 2.3: Summary of electrical response of the <i>n</i> -type and <i>p</i> -type semiconducting metal oxides in reducing and oxidizing gases.....	26
Table 2.4: Comparison of the sensor response using different forms of TiO <sub>2</sub> .....	39
Table 2.5: Findings on gas sensing and research gaps using 1-D TiO <sub>2</sub> based materials.	44
Table 3.1: Experimental conditions of thermal oxidation of Ti and Ti64 substrates.....	51
Table 3.2: Experimental details for measuring of the residual stress of as-received, milled and relaxed Ti and Ti64 particles.....	58
Table 4.1: Elemental analysis of different phases in Ti64 sheet by EDX spectrum.....	93
Table 4.2: Atomic percentage of different elements in the oxide scales of Ti64-0h and Ti64-20h particles. ....	137
Table 4.3: Comparison of 1-D nanostructures grown on Ti and Ti64 substrates. ....	154
Table 4.4: The structural morphology, density of 1-D nanostructures and surface area of the sensors.....	157
Table 4.5: Elemental composition of top side and flip side particles in S-2 sensors prepared from ink containing 10 wt% of particle loading. ....	162
Table 4.6: Change in color of the sensors during exposure to different gases.....	172
Table 4.7: Elemental composition of the sensors in as-prepared conditions and after exposing to different target gases.....	174
Table 4.8: Response of the as-prepared and stored S-2 sensors towards 1000 ppm of H <sub>2</sub> S, CH <sub>3</sub> OH and C <sub>2</sub> H <sub>5</sub> OH gases in N <sub>2</sub> background at 650 °C. ....	179
Table 4.9: Response towards different gases obtained in the present work.....	191

## LIST OF SYMBOLS AND ABBREVIATIONS

### List of Symbols

$\Delta V_b$	: Change in barrier potential of metal oxide
$\mu_b$	: Electron mobility in the neutral grain body
$\mu_d$	: Electron mobility in the depleted layer
$2\theta$	: Bragg angle in XRD analysis
$d$	: Lattice spacing
$e$	: Charge of electron
$e^-$	: An electron
$E$	: Young modulus
$E_C$	: Energy level of conduction band
$E_F$	: Fermi level
$E_{gap}$	: Difference between conduction band and valence band
$E_V$	: Energy level of valence band
$F$	: Gas flow rate
$F_{RT}$	: Flow rate of the mixed gas in sccm
$h^+$	: Hole conductivity
$I_a$	: Current flow in the sensor in N <sub>2</sub> environment
$I_g$	: Current flow in the sensor in target gas environment
$\Delta I$	: $ I_a - I_g $ or $ I_o - I_g $
$k_B$	: Boltzmann's constant
$L$	: Length of the 1-D nanostructure
$m$	: Slope of the $d - \sin^2\psi$ curve
$n_b$	: Free electron density

$n_d$	: Free-electron density in the depleted layer
$P$	: Dynamic pressure
$P_{H_2O}$	: Dynamic water vapor partial pressure
$P_{O_2}$	: Dynamic oxygen partial pressure
$r$	: Radius of the oxidation tube ( $2.2 \times 10^{-2}$ m)
$R_a$	: Resistance of sensor in air or in ambient
$R_o$	: Resistance of sensor in background ( $N_2$ or air) environment
$\Delta R$	: $ R_a - R_g $ or $ R_a - R_g $
$R_C$	: Resistance for contacts with 1-D nanostructures
$R_g$	: Resistance of sensor in target gas
$r_m$	: Radius of 1-D nanostructures
$R_N$	: Resistance of individual 1-D nanostructures
$r_o$	: Width of depletion layer
$S$	: Response of the sensor
$T$	: Absolute temperature
$T_{oxi}$	: Oxidation temperature in Kelvin scale (1023 K)
$T_{rec}$	: Recovery time of the sensor
$T_{res}$	: Response time of the sensor
$T_{RT}$	: Room temperature (298 K)
$T_{RT}$	: Room temperature in Kelvin scale (298 K)
$\rho_{RT}$	: Density of Ar ( $1.784 \text{ kg/m}^3$ )
$\nu$	: Poison ratio
$\chi$	: Concentration of oxygen in ppm in Ar environment
$\psi$	: Tilt angle of the sample in XRD analysis

## List of Abbreviations

1-D	: One dimensional
2-D	: Two dimensional
3-D	: Three dimensional
DAQ	: Data acquisition
DC	: Direct current
DGDE	: Diethylene glycol dibutyl ether
DSC	: Differential scanning calorimetry
EBS	: Electron backscattered diffraction
EDX	: Energy dispersive X-ray
FESEM	: Field emission scanning electron microscope
FIB	: Focused ion beam
HRTEM	: High resolution transmission electron microscope
IPF	: Inverse pole figure
MFC	: Mass flow controllers
MO	: Metal oxide
OVL	: Overloaded
ppb	: Parts per billion
ppm	: Parts per million
RF	: Radio frequency
rpm	: Rotation per minute
RT	: Room temperature
SAD	: Selected area diffraction
scm	: Standard cubic centimeters per minute
SEM	: Scanning electron microscope
STEM	: Scanning transmission electron microscope

TEM	: Transmission electron microscope
TGA	: Thermogravimetric analysis
UV	: Ultraviolet
VLS	: Vapor-liquid-solid
VS	: Vapor-solid
XPS	: X-ray photoelectron spectroscopy
XRD	: X-ray diffraction

### List of Chemical Formulas

Ag	: Silver
AgVO <sub>3</sub>	: Silver vanadium oxide
Al	: Aluminum
Al <sub>2</sub> O <sub>3</sub>	: Aluminum oxide
Ar	: Argon
Au	: Gold
Bi <sub>2</sub> O <sub>3</sub>	: Bismuth (III) oxide
C	: Carbon
C <sub>2</sub> H <sub>4</sub>	: Ethylene
C <sub>2</sub> H <sub>5</sub> O <sup>-</sup>	: Ethoxide
C <sub>2</sub> H <sub>5</sub> OH	: Ethanol
C <sub>32</sub> H <sub>64</sub> O <sub>4</sub> Sn	: Dibutyltin dilaurate
CdO	: Cadmium oxide
CH <sub>3</sub> CH <sub>2</sub> COOCH <sub>3</sub>	: Ethyl acetate
CH <sub>3</sub> CHO	: Acetaldehyde
CH <sub>3</sub> COCH <sub>3</sub>	: Acetone

$\text{CH}_3\text{O}^-$	: Methoxides
$\text{CH}_3\text{-O-CH}_3$	: Dimethyl ether
$\text{CH}_3\text{OH}$	: Methanol
$\text{CH}_4$	: Methane
$\text{Cl}_2$	: Chlorine
$\text{CO}$	: Carbon monoxide
$\text{CO}_2$	: Carbon dioxide
$\text{Co}_2\text{O}_3$	: Cobalt (III) oxide
$\text{Cr}$	: Chromium
$\text{Cr}_2\text{O}_3$	: Chromium (III) oxide
$\text{Cu}$	: Copper
$\text{Cu}_2\text{O}$	: Copper(I) oxide
$\text{CuO}$	: Copper (II) oxide
$\text{Eu}_2\text{O}_3$	: Europium (III) oxide
$\text{Fe}$	: Iron
$\text{Fe}_2\text{O}_3$	: Iron (III) oxide
$\text{Ga}_2\text{O}_3$	: Gallium (III) oxide
$\text{H}_2$	: Hydrogen
$\text{H}_2\text{O}$	: Water
$\text{H}_2\text{S}$	: Hydrogen sulfide
$\text{HCHO}$	: Formaldehyde
$\text{HCOOH}$	: Formic acid
$\text{HF}$	: Hydrofluoric acid
$\text{HNO}_3$	: Nitric acid
$\text{In}_2\text{O}_3$	: Indium (III) oxide
$\text{La}_2\text{O}_3$	: Lanthanum oxide

Mo	: Molybdenum
MoO <sub>3</sub>	: Molybdenum trioxide
N <sub>2</sub>	: Nitrogen
Nb	: Niobium
Nb <sub>2</sub> O <sub>5</sub>	: Niobium pentoxide
NiO	: Nickel oxide
NO <sub>2</sub>	: Nitrogen dioxide
NO <sub>x</sub>	: Generic term for the mono-nitrogen oxides NO and NO <sub>2</sub>
O	: Atomic oxygen
O <sup>-</sup> , O <sub>2</sub> <sup>-</sup> or O <sup>2-</sup>	: Oxygen ions
O <sub>2</sub>	: Oxygen
OH <sup>-</sup>	: Hydroxyl group
OH <sub>o</sub> <sup>-</sup>	: Hydroxide ion
Pd	: Palladium
Pt	: Platinum
Si	: Silicon
SiO <sub>2</sub>	: Silicon dioxide
SnO <sub>2</sub>	: Tin dioxide
SO <sub>2</sub>	: Sulfur dioxide
TeO <sub>2</sub>	: Tellurium dioxide
Ti	: Titanium
Ti-0h	: As-received titanium particles
Ti-20h	: Titanium particles milled for 20 h
Ti <sub>2</sub> O <sub>3</sub>	: Titanium (III) oxide
Ti <sub>3</sub> O <sub>5</sub>	: Titanium pentoxide
Ti64	: Ti-6Al-4V

Ti64-0h	: As-received Ti64 particles
Ti64-2h	: Ti64 particles milled for 2 h
Ti64-5h	: Ti64 particles milled for 5 h
Ti64-10h	: Ti64 particles milled for 10 h
Ti64-15h	: Ti64 particles milled for 15 h
Ti64-20h	: Ti64 particles milled for 20 h
Ti64-25h	: Ti64 particles milled for 25 h
Ti64-30h	: Ti64 particles milled for 30 h
TiO	: Titanium (II) oxide
TiO <sub>2</sub>	: Titanium dioxide
V	: Vanadium
W	: Tungsten
WO <sub>3</sub>	: Tungsten trioxide
WO <sub>x</sub>	: Tungsten oxide
Zn	: Zinc
ZnO	: Zinc oxide
Zr	: Zirconium
ZrO <sub>2</sub>	: Zirconium dioxide
$\alpha$ -Ti	: Hexagonal phase of titanium
$\beta$ -Ti	: Body centered cubic phase of titanium
$\beta$ -Ti(5-5-5)	: Ti-5Al-5V-5Mo-3.5Cr-0.5Fe

## LIST OF APPENDICES

Appendix A: Schematics of Quartz Tube	217
Appendix B: Calculations on Dynamic Oxygen Partial Pressure	218
Appendix C: Ellingham Diagram for Oxidation of Ti, Al and V	221
Appendix D: Angles of Crystallographic Directions of Hexagonal Ti	222

University of Malaya

## CHAPTER 1: INTRODUCTION

### 1.1 Background

Metal oxides are one of the most important groups of materials which can exhibit metallic, semiconducting or insulating characteristics. For this reason, metal oxides are being used as functional materials in engineering applications such as in electronics, optoelectronics, and electro-mechanical devices (Xia et al., 2003). Ease of fabrication, compatibility and low cost of metal oxides are additional benefits in various applications (Comini, Faglia, Sberveglieri, Pan, & Wang, 2002).

So far, a wide variety of metal oxides such as  $\text{Al}_2\text{O}_3$ ,  $\text{Bi}_2\text{O}_3$ ,  $\text{CdO}$ ,  $\text{Co}_2\text{O}_3$ ,  $\text{Cr}_2\text{O}_3$ ,  $\text{CuO}$ ,  $\text{Eu}_2\text{O}_3$ ,  $\text{Fe}_2\text{O}_3$ ,  $\text{Ga}_2\text{O}_3$ ,  $\text{In}_2\text{O}_3$ ,  $\text{MoO}_3$ ,  $\text{Nb}_2\text{O}_5$ ,  $\text{NiO}$ ,  $\text{SiO}_2$ ,  $\text{SnO}_2$ ,  $\text{TiO}_2$ ,  $\text{WO}_3$ ,  $\text{ZnO}$ ,  $\text{ZrO}_2$  have been developed by various routes. Out of these,  $\text{TiO}_2$  gained great attention for applications such as, gas sensors, solar cells, optical coating, corrosion protective coating, white pigments, electrical devices, ceramics, catalyst, and bone implants (Diebold, 2003). Superior chemical stability, high temperature stability, corrosion protective properties, improved hardness, and higher band gap of  $\text{TiO}_2$  is particularly suitable for these engineering applications.

Decreasing the size of  $\text{TiO}_2$  to nanometer level is expected to lead interesting phenomena due to having enhanced surface area (Y. J. Hwang, Boukai, & Yang, 2008), quantum confinement (H. Peng & Li, 2008), altered mechanical, optical, electrical and photoconductive properties (Chueh et al., 2007), which are greatly different from their bulk counterparts. These opportunities have prompted research on the fabrication of nanostructured  $\text{TiO}_2$  materials. So far, spherical nanoparticles (Patra, Das, & Bhaumik, 2011), one dimensional (1-D) (Xinsheng Peng & Chen, 2004; Xinsheng Peng, Wang,

Thomas, & Chen, 2005), two dimensional (2-D) (Leng, Chen, & Xue, 2014) and three dimensional (3-D) (X. Yang et al., 2015) nanostructures of TiO<sub>2</sub> have been developed by various routes. Out of these, 1-D TiO<sub>2</sub> is being used in various applications such as gas sensors (Paulose, Varghese, Mor, Grimes, & Ong, 2005; Rout, Kulkarni, & Rao, 2007; O. K. Varghese, Gong, Paulose, Ong, & Grimes, 2003), solar cells (B. Liu & Aydil, 2009; B. Tan & Wu, 2006), catalyst (Yunarti et al., 2014) and bone implants (A. Tan et al., 2014). Different forms of 1-D TiO<sub>2</sub> such as nanowires, nanorods, nanotubes, nanobelts, and nanofibers have been synthesized for different applications by various processes.

Out of different synthesis routes of 1-D TiO<sub>2</sub>, the process thermal oxidation appears to be most simple, inexpensive and highly scalable. This process requires only heating of the Ti substrates under appropriate oxidizing environment (Xinsheng Peng & Chen, 2004; Xinsheng Peng et al., 2005). The 1-D nanostructures evolve in outward direction from the Ti substrates during oxidation which can be readily used for different applications. In various studies, the effects of oxidation medium and temperature on 1-D growth during oxidation of Ti substrates are reported (Cai et al., 2012; Daothong, Songmee, Thongtem, & Singjai, 2007; Hansen, Lu, & Chen, 2008; Y. Liu et al., 2008). However, the effects of a vast number of other parameters such as oxygen concentration, oxygen partial pressure, and oxidation duration are not studied yet. In addition, the effect of substrate conditions including alloy microstructure and residual stress are not investigated yet. The characterization of as-grown 1-D nanostructures on Ti and its alloy substrates are not completed and the growth mechanism of 1-D nanostructure requires further study.

So far, the 1-D TiO<sub>2</sub> nanostructures grown on Ti and its alloy substrates are not extensively studied for engineering applications. Limited studies for bone implant showed superior properties by incorporating 1-D TiO<sub>2</sub> grown by thermal oxidation (B. Dinan, Gallego-Perez, Lee, Hansford, & Akbar, 2013; A. Tan et al., 2014). The usage of

1-D TiO<sub>2</sub> grown by thermal oxidation has not yet been studied in other applications such as gas sensors, solar cells, and catalysts. Thermally oxidized 1-D TiO<sub>2</sub> nanostructures open the door for in-situ sensor fabrication with the potential of offering superior sensing properties which has not been studied so far. In addition, this process also opens the possibility to use the binary 1-D TiO<sub>2</sub>-MO (where, MO is the metal oxide) nanostructures for gas sensing application by oxidizing Ti alloy substrates instead of pure Ti.

In this research work, the pure Ti and Ti-6Al-4V (Ti64) substrates (particles and sheets) are thermally oxidized in tube furnace. The effects of different oxidation parameter such as temperature, oxidation medium, oxygen concentration, dynamic oxygen partial pressure, and oxidation duration are investigated. In addition, the effects of substrate states such as alloy microstructures, residual stress and substrate orientations are studied. The as-grown 1-D nanostructures and the oxide scale beneath the 1-D nanostructures are characterized by different techniques. The 1-D nanostructures are utilized for gas sensing and the oxidation process is optimized for in-situ sensor fabrication. The sensors are tested towards different oxidizing and reducing gases and the oxide nanostructures are characterized at the different stage of gas sensing. A sensing mechanism is proposed based on the findings from this research.

## **1.2 Research Objectives**

The objectives of this research are listed as below:

1. To investigate the effects of different parameters on the growth of 1-D nanostructures during thermal oxidation of Ti and Ti64 substrates.
2. To characterize the oxidized Ti and Ti64 substrates by different analytical techniques.

3. To develop a simple, in-situ, single step route for producing gas sensors containing 1-D nanostructures on Ti and Ti64 particles grown by thermal oxidation.
4. To evaluate the performance of the sensors towards oxidizing and reducing gas environments.

### **1.3 Scope of Research**

The overall aim of this research is to investigate the effects different parameters on the growth of 1-D nanostructures during thermal oxidation of Ti and Ti64 substrates and to utilize the as-grown 1-D nanostructures for gas sensing applications. For this reason, the Ti and Ti64 substrates are oxidized in different conditions inside a tube furnace. The effects of temperature, alloy microstructure, oxidation environment, dynamic oxygen partial pressure, residual stress, and oxidation duration have been investigated during oxidation of Ti and Ti64 substrates.

The as-grown 1-D nanostructures are characterized by using several analytical techniques including transmission electron microscopy (TEM), field emission scanning electron microscopy (FESEM), energy dispersive X-ray (EDX) spectroscopy, electron backscattered diffraction (EBSD), X-ray diffraction (XRD), X-ray photoelectron spectroscopy (XPS), and Raman spectroscopy. Based on the findings, mechanisms are proposed for the 1-D growth on Ti and Ti64 substrates during thermal oxidation.

The 1-D nanostructures grown on Ti and Ti64 particles are tested for gas sensing applications. An in-situ sensor fabrication method has been presented in this work. The effect of particle loading on sensor fabrication is reported. The performance of 1-D nanostructures for detecting reducing ( $H_2$ ,  $H_2S$ ,  $CO$ ,  $CH_4$ ,  $CH_3OH$ ,  $C_2H_5OH$ ,  $C_2H_4$ ) and oxidizing ( $NO_2$  and  $O_2$ ) gases have been tested. The response, selectivity, optimum

operating temperature, effects of gas concentration, response time, and recovery time of the sensors are presented in this work. Finally, the mechanism of gas sensing is investigated and presented.

#### **1.4 Organization of the Thesis**

This thesis consists of five chapters. Chapter 1 provides a brief introduction of this research work. This chapter gives the research background, the current issues in this field, research objectives and the scope of this research. Chapter 2 provides a comprehensive overview of the existing literature on various topics related to this research. These topics include the growth of 1-D TiO<sub>2</sub> nanostructures by thermal oxidation, highlights the research gaps for the oxidation of Ti substrates, recent developments in gas sensing, and research gaps in gas sensing using TiO<sub>2</sub> based materials. Chapter 3 contains the experimental procedure used in this work. This chapter describes the equipment for 1-D growth and gas sensing, growth procedure of 1-D nanostructures, characterization techniques, and gas sensing procedure. Chapter 4 in this thesis reports the results obtained from the experimental work. This chapter is divided into three broad sections. In the first section, results on the growth of 1-D nanostructures on Ti substrates are presented. In the second section, the growth of 1-D nanostructures on Ti64 substrates is presented. Finally, in the third section results on gas sensing are presented. Chapter 5 provides a brief summary of this research work and recommendation for future work.

## CHAPTER 2: LITERATURE REVIEW

### 2.1 Introduction

One dimensional (1-D) metal oxide nanostructures are particularly interesting due to their versatile usage in various engineering applications. For this reason, different innovative synthesis processes have been developed for synthesizing metal oxide nanostructures. The synthesis of 1-D metal oxides is divided into five processes: (1) wet processing, (2) solid-state processing, (3) molten-state processing, (4) vapor phase processing, and (5) hybrid processing. Each of the process is sub-divided into different methods for the production of 1-D metal oxide nanostructures as shown in Figure 2.1.

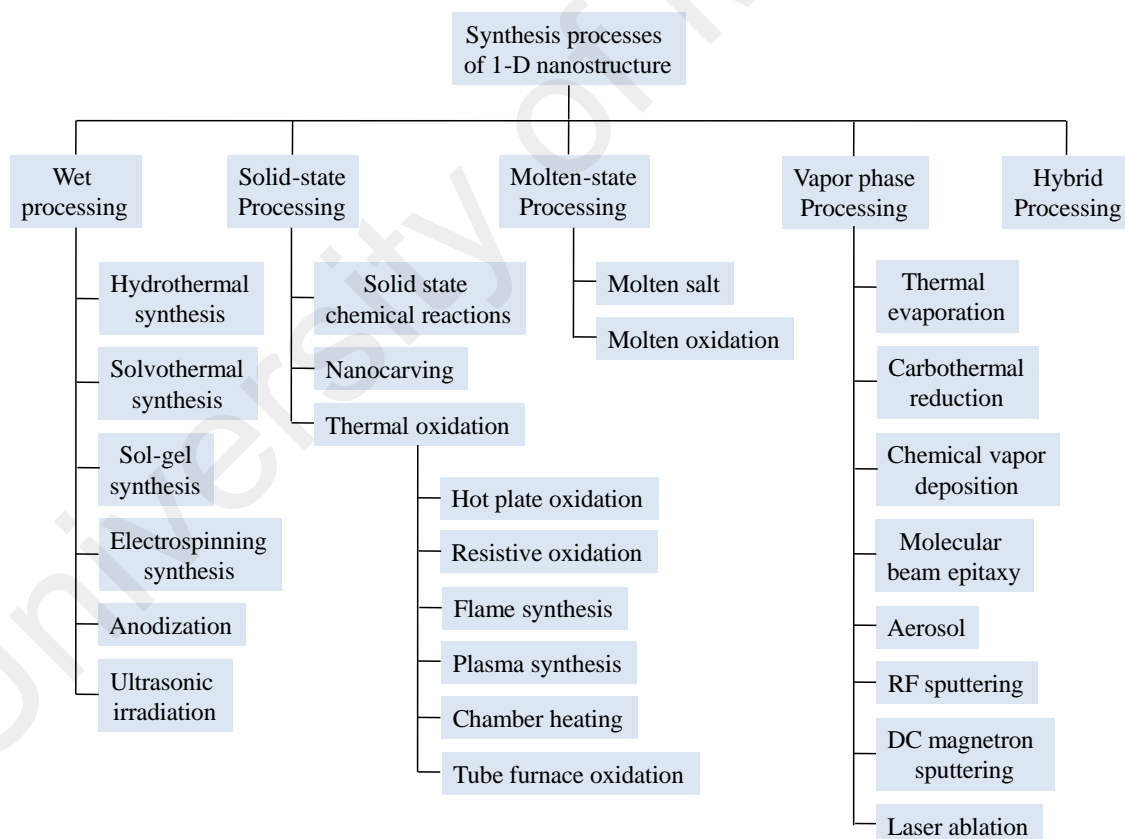


**Figure 2.1: Synthesis processes of 1-D nanostructures.**

So far, one dimensional (1-D) metal oxides of  $\text{AgVO}_3$ ,  $\text{Al}_2\text{O}_3$ ,  $\text{Bi}_2\text{O}_3$ ,  $\text{CdO}$ ,  $\text{Co}_2\text{O}_3$ ,  $\text{Cr}_2\text{O}_3$ ,  $\text{CuO}$ ,  $\text{Eu}_2\text{O}_3$ ,  $\text{Fe}_2\text{O}_3$ ,  $\text{Ga}_2\text{O}_3$ ,  $\text{In}_2\text{O}_3$ ,  $\text{MoO}_3$ ,  $\text{Nb}_2\text{O}_5$ ,  $\text{NiO}$ ,  $\text{SiO}_2$ ,  $\text{SnO}_2$ ,  $\text{TiO}_2$ ,  $\text{WO}_3$ ,

ZnO and ZrO<sub>2</sub> have been synthesized with various size, shape, structure, and morphology. Out of that 1-D TiO<sub>2</sub> gained attentions to the researchers worldwide due to having applications in gas sensors (Paulose et al., 2005; Rout et al., 2007; O. K. Varghese et al., 2003), solar cells (B. Liu & Aydil, 2009; B. Tan & Wu, 2006), catalyst (Yunarti et al., 2014), and bone implants (A. Tan et al., 2014). However, not all of the processes mentioned in Figure 2.1 are suitable for the production of 1-D TiO<sub>2</sub> nanostructures. Based on reported literatures, 1-D TiO<sub>2</sub> can be synthesized by hydrothermal (Rout et al., 2007), solvothermal (Xie & Shang, 2007), sol-gel (Galatsis et al., 2002), electrospinning (B. Wang et al., 2010), anodization (Paulose et al., 2005; O. K. Varghese et al., 2003), solid-state chemical reactions (Yang Wang, Cao, Li, Jia, & Xie, 2014), nanocarving (Yoo, Akbar, & Sandhage, 2004a, 2004b), thermal oxidation (Huo et al., 2008), thermal evaporation (J.-M. Wu, Shih, & Wu, 2005; J.-M. Wu, Wu, & Shih, 2005), carbothermal reduction (J. Yu, Chen, & Glushenkov, 2009), chemical vapor deposition (Baik et al., 2008; J. Shi & Wang, 2011), RF sputtering (W.-Y. Wu, Chang, & Ting, 2010), DC magnetron sputtering (Meng, Chen, Li, & Dos Santos, 2014) and laser ablation (Sun, Fuge, & Ashfold, 2004) methods. All of these methods produce 1-D TiO<sub>2</sub> nanostructures with various size, shape, morphology, uniformity and crystallinity with some merits and demerits in the process. However, thermal oxidation seems to be a viable, cheap and highly scalable method which is capable of producing 1-D TiO<sub>2</sub> nanostructures on Ti substrates. For this reason, in recent years, a great deal of research efforts has been employed to optimize and investigate the growth of 1-D TiO<sub>2</sub> by thermal oxidation. In the following sections the details of thermal oxidation process, reported findings and research gaps for the production of 1-D TiO<sub>2</sub> nanostructures are discussed. In the succeeding sections, the use of 1-D TiO<sub>2</sub> in gas sensing applications is summarized by providing appropriate background and theories. The research gaps are also identified in the gas sensing applications by using TiO<sub>2</sub> nanostructures.

## **2.2 1-D Nanostructures on Ti and Ti Alloys by Thermal Oxidation**

The growth of 1-D TiO<sub>2</sub> nanostructures by thermal oxidation is a very simple method which requires only heating Ti substrates in oxidizing medium. So far, few variations of thermal oxidation method have been proposed for the growth of 1-D nanostructures on different metal substrates including hot plate oxidation (T. Yu et al., 2006), resistive oxidation (Nasibulin et al., 2009), flame synthesis (Wooldridge et al., 2002), plasma synthesis (Cvelbar, Chen, Sunkara, & Mozetič, 2008), chamber heating (G. Chen, Stolojan, Cox, Giusca, & Silva, 2006) and tube furnace oxidation (Ren et al., 2007; B. Varghese, Haur, & Lim, 2008). Since, the growth of 1-D nanostructures on Ti and its alloy substrates require minute amount of oxygen, the oxidation in ambient environment or containing higher amount of oxygen is not suitable. For this reason, the hot plate oxidation, resistive oxidation, flame synthesis, plasma synthesis and chamber heating are not capable of producing 1-D nanostructures on Ti and its alloy substrates. However, in tube furnace oxidation the oxidation environment can be controlled precisely and for this reason tube furnace oxidation is popular for the growth of 1-D nanostructures on Ti and its alloy substrates. In the following sections, the details of tube furnace oxidation and resultant 1-D nanostructures are discussed in details.

### **2.2.1 Tube Furnace Oxidation**

The oxidation environment requires precise control for the growth of 1-D nanostructure on Ti and its alloy substrates. For this reason, tube furnace oxidation is used to oxidize Ti substrates. It should be noted that tube furnace oxidation is also used for 1-D growth on other metal substrates including niobium (Nb) (B. Varghese et al., 2008), zinc (Zn) (Ren et al., 2007), tungsten (W) (Jin et al., 2004) and iron (Fe) (Srivastava, Tiwari, Srivastava, & Nandedkar, 2007).

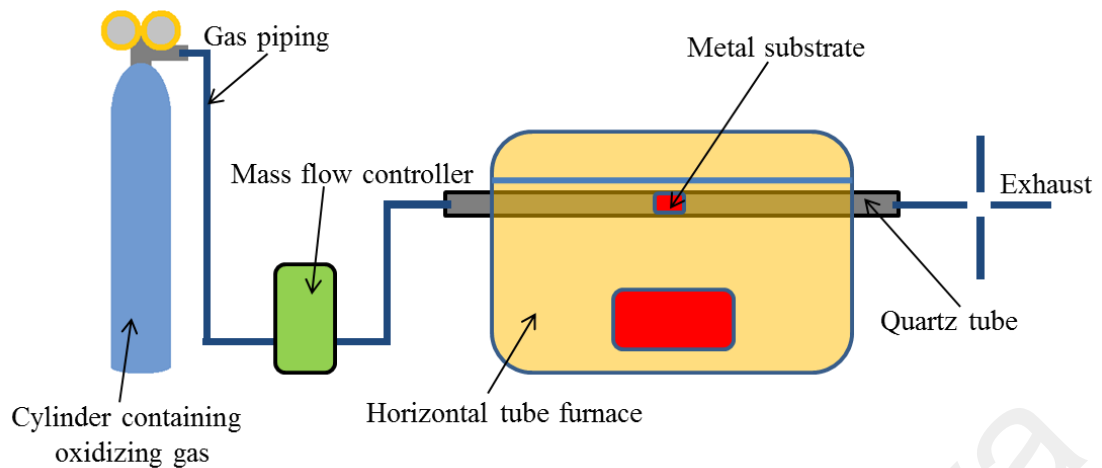


**Figure 2.2: Schematic experimental setup for the synthesis of 1-D nanostructures on Ti and its alloy substrate by thermal oxidation process. This figure is not in scale.**

The general setup of a tube furnace oxidation is shown in Figure 2.2. In this setup a quartz tube is placed inside a horizontal tube furnace. The metal substrates (Ti, its alloy or any other metal) are placed inside the quartz tube. One end of the quartz tube is connected to a mass flow controller (MFC) for the precise control of the gas flow for oxidation. The MFC is connected with the cylinder containing oxidizing gas. Typically, the cylinder contains Ar gas with trace amount of oxidizing gases such as oxygen ( $O_2$ ) (Xinsheng Peng & Chen, 2004), water ( $H_2O$ ) (Xinsheng Peng et al., 2005), acetone ( $CH_3COCH_3$ ) (Huo et al., 2009), ethanol ( $C_2H_5OH$ ) (Xinsheng Peng et al., 2005), acetaldehyde ( $CH_3CHO$ ) (Xinsheng Peng et al., 2005) and dibutyltin dilaurate ( $C_{32}H_{64}O_4Sn$ ) (X Peng & Chen, 2005). In some variations of tube furnace oxidation, two gas cylinders are connected with MFCs where one cylinder contains pure Ar and other cylinder contains trace amount of oxidizing gas in Ar. The gases from two cylinders are mixed at different ratios using MFCs for further dilution of the oxidizing environment. During oxidation, the furnace is heated to the oxidation temperatures and the substrate is allowed to react with the oxygen containing species for a certain period of time. The gases are continuously flown and allowed to exhaust from the other end of the quartz tube.

Finally, after oxidation for a certain period of time the furnace is cooled down to the room temperature and substrate containing 1-D nanostructure is collected.

### **2.2.2 Effects of Different Parameters during Oxidation**

The synthesis process of 1-D nanostructures on Ti and its alloy substrate is sensitive towards different parameters such as alloying elements, microstructures, oxidation environment, temperature and oxidation duration. Under different oxidation conditions nanostructures with different morphologies are formed which is tabulated in Table 2.1. The effects of different parameters during thermal oxidation of Ti and its alloy are discussed in the following sections.

University of Malaysia

**Table 2.1: Summary of the 1-D nanostructure grown by thermal oxidation process on Ti and Ti-alloy substrates.**

Nanostructure	Substrate, dimensions and source	Oxidation environment	Other conditions	Growth temperature (°C)	Growth time	Dimension of the 1-D nanostructures	Crystal structure	Growth direction	Reference
TiO <sub>2</sub> nanowires	Ti foil (Aldrich, 99.7%), dimension: 10 mm x 10 mm x 1 mm	Acetone vapor in Ar	Flow rate: 50 sccm Post annealing in air at 650°C for 30 min is required to remove carbon from the shell.	800 °C	1 h	Diameter: 20-50 nm	Rutile	-	(Huo et al., 2009)
TiO <sub>2</sub> nanofibers	Ti sheet (Grade 1), dimension: 30 mm x 15 mm x 0.8 mm	Mixture of Ar and O <sub>2</sub>	Flow rate: 200 sccm (Ar) and 1 sccm (O <sub>2</sub> )	850°C	1.5 h	<u>Chain-like structure:</u> Diameter: 200 nm Length: several micrometers <u>Ribbon-like structure:</u> Width: 200-1500 nm Thickness: 60 nm Length: several micrometers	Rutile	[0 0 1]	(Xinsheng Peng & Chen, 2004)
TiO <sub>2</sub> nanorods	Ti sheet (Grade 1), dimension: 30 mm x 15 mm x 0.8 mm	Acetone vapor in Ar	Flow rate: 200 sccm	850°C	1.5 h	<u>Tetragonal structure:</u> Width: ~1.5 μm Thickness: 100 nm Length: 1-2 μm <u>Columnar structure:</u> Diameter: 230 nm Length: 2-3 μm	Rutile	[0 0 1]	(Xinsheng Peng & Chen, 2004; Xinsheng Peng et al., 2005)

**Table 2.1, Continued.**

Nanostructure	Substrate, dimensions and source	Oxidation environment	Other conditions	Growth temperature (°C)	Growth time	Dimension of the 1-D nanostructures	Crystal structure	Growth direction	Reference
TiO <sub>2</sub> micro-crystalline fibers	Ti sheet (Grade 1), dimension: 30 mm x 15 mm x 0.8 mm	Water vapor in Ar	Flow rate: 200 sccm	850°C	1.5 h	Diameter: ~1 μm Length: 5 μm	Rutile	-	(Xinsheng Peng et al., 2005)
TiO <sub>2</sub> plate-like nanostructures	Ti sheet (Grade 1), dimension: 30 mm x 15 mm x 0.8 mm	Ethanol vapor in Ar	Flow rate: 200 sccm	850°C	1.5 h	Width: 500 nm Thickness: 150 nm Length: 1 μm	Rutile	-	(Xinsheng Peng et al., 2005)
TiO <sub>2</sub> nanorods	Ti sheet (Grade 1), dimension: 30 mm x 15 mm x 0.8 mm	Acetaldehyde vapor in Ar	Flow rate: 200 sccm	850°C	1.5 h	Width: 500 nm Thickness: 150 nm Length: 1 μm	Rutile	-	(Xinsheng Peng et al., 2005)
TiO <sub>2</sub> nanowire	Ti particles (H.C. Starck GmbH, Germany)	Ethanol	Pressure: 10 Torr	650-800°C	30-180 min	Diameter: 60-150 nm Length: ~2 μm	Rutile	-	(Kaewsai et al., 2010)
TiO <sub>2</sub> nanowire	Ti wire (Advent Research Materials Ltd., 99.8%), diameter: 0.25 mm	Ethanol	Pressure: 10 Torr	650-850°C	30-180 min	Diameter: 23-73 nm	Rutile	[0 0 1]	(Daothong et al., 2007)
TiO <sub>2</sub> nanorods	Ti sheet (Grade 1), dimension: 30 mm × 15 mm × 0.8 mm	Dibutyltin dilaurate in Ar	-	600-900°C	4 h	Width: 150 nm Length: several hundred nanometer Height: 1.5 μm	Rutile	[0 0 1]	(X Peng & Chen, 2005)
TiO <sub>2</sub> nanowire	α-Ti bar (grade 2)	Tens of ppm O <sub>2</sub> in Ar	Flow rate: 200 sccm	600°C	8 h	Length: 50-400 nm	-	-	(Huyong Lee, Dregia, Akbar, & Alhoshan, 2010)
TiO <sub>2</sub> nanowire	Ti64 bar (Ti-6Al-4V, Onlinemetals, Seattle, WA, grade 5)	Tens of ppm O <sub>2</sub> in Ar	Flow rate: 200-1000 sccm	700°C	8 h	-	-	-	(Huyong Lee et al., 2010)
TiO <sub>2</sub> nanowire	β-Ti (5-5-5) bar (Ti-5Al-5V-5Mo-3.5Cr-0.5Fe)	Tens of ppm O <sub>2</sub> in Ar	Flow rate: 200-1000 sccm	700°C	8 h	-	-	-	(Huyong Lee et al., 2010)

**Table 2.1, Continued.**

Nanostructure	Substrate, dimensions and source	Oxidation environment	Other conditions	Growth temperature (°C)	Growth time	Dimension of the 1-D nanostructures	Crystal structure	Growth direction	Reference
Core-shell TiO <sub>2</sub> -Al <sub>2</sub> O <sub>3</sub>	Ti64 coupon (Ti-6Al-4V, Onlinemetals, Seattle, WA, grade 5), dimension: 1 cm x 1 cm	5-500 ppm O <sub>2</sub> in Ar	Flow rate: 500 sccm	700°C	8 h	Diameter: ~50-100 nm Length: 300 nm - 2 µm	Rutile	[0 0 1]	(B. J. Dinan, Dregia, & Akbar, 2013)
Core-shell TiO <sub>2</sub> -C	Ti foil (99.6%), dimension: 10 mm x 10 mm x 1 mm	Acetone vapor in Ar	Flow rate: 150 sccm	850°C	1.5 h	Diameter: 15-20 nm (TiO <sub>2</sub> )	Rutile	[1 0 1]	(Huo et al., 2008)

### 2.2.2.1 Effects of Alloying Elements and Microstructures

A significant amount of work has been done for the growth of 1-D nanostructures on  $\alpha$ -Ti substrates by thermal oxidation process. It is seen that the growth window for 1-D nanostructures is too narrow on  $\alpha$ -Ti substrates and requires very precise control over oxidation temperature and oxidizer concentration. Higher concentration of oxygen resulted in oxide scale instead of 1-D nanostructures on  $\alpha$ -Ti substrates. The resultant 1-D nanostructures are not properly aligned and thickness is not uniform. It is reported that the  $\beta$  phase stabilizers such as vanadium (V), molybdenum (Mo), and chromium (Cr) in the Ti matrix widens the growth window for 1-D growth with higher coverage (Huyong Lee et al., 2010).

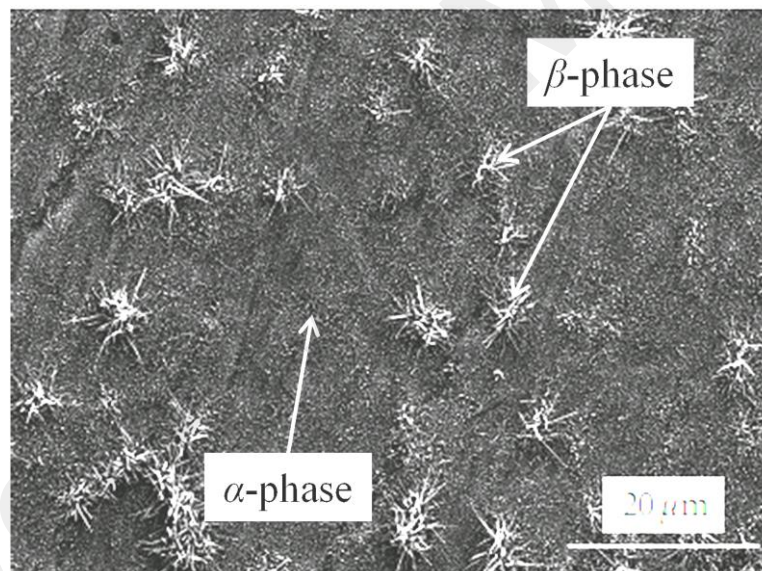


**Figure 2.3: Ti-6.85Al-1.6V substrate after thermal oxidation at 700 °C for 8 h in presence of trace amount of oxygen in Ar at a flow rate of 500 sccm. The 1-D nanostructures are seen to grow preferentially on  $\beta$  phase during thermal oxidation (Huyong Lee et al., 2010).**

Reported results on the oxidation of  $\beta$  phases containing Ti alloys such as Ti-6Al-4V (Ti64) and Ti-5Al-5V-5Mo-3.5Cr-0.5Fe (also known as  $\beta$ -Ti(5-5-5)) shows higher coverage of 1-D nanostructures compared with  $\alpha$ -Ti substrates (Huyong Lee et al., 2010). To demonstrate this, the  $\alpha$  and  $\beta$  phase containing Ti-6.85Al-1.6V substrate was thermally oxidized with trace amount of oxygen in Ar at 700 °C for 8 h at a flow rate of 500 sccm

(Huyong Lee et al., 2010). It was seen that the length and coverage of 1-D nanostructures are higher on the  $\beta$  phase as shown in Figure 2.3. The  $\alpha$  phase of Ti also showed 1-D growth but the length and coverage was lower than  $\beta$  phase. Thus, the presence of  $\beta$  phase stabilizers (V, Mo, and Cr) in Ti matrix is suitable for higher coverage of 1-D nanostructures during thermal oxidation.

#### 2.2.2.2 Effects of Oxidation Environment

The oxidation of Ti for the growth of 1-D nanostructures is very sensitive towards oxidation environment. It is seen that the oxidation requires minute amount of oxygen for 1-D growth and excess  $O_2$  results in the formation of oxide scale. This is unlike from the oxidation of Cu and Fe substrate where 1-D nanostructures are grown during oxidation in pure  $O_2$  or ambient environment (Cai et al., 2012; Hansen et al., 2008; Y. Liu et al., 2008).

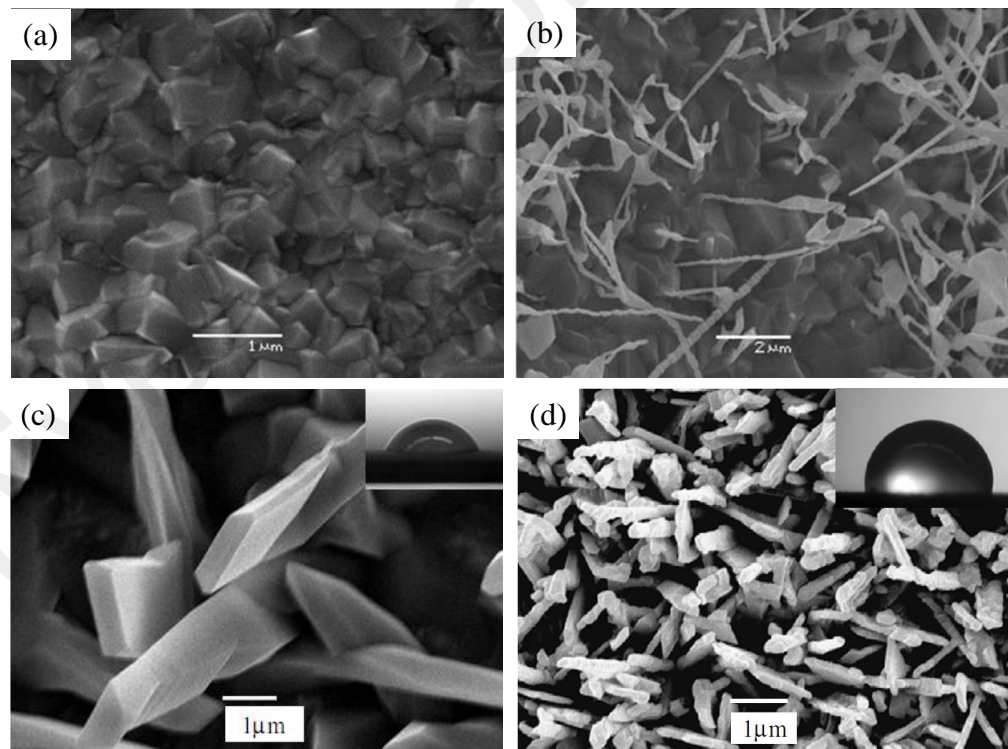


**Figure 2.4:  $TiO_2$  nanostructures grown on Ti foil by thermal oxidation at  $850\text{ }^\circ\text{C}$  in presence of different oxygen sources (a) pure oxygen (99%) (Xinsheng Peng & Chen, 2004), (b) 1 sccm flow of  $O_2$  in 200 sccm flow of Ar (Xinsheng Peng & Chen, 2004), (c) water vapor in Ar (Xinsheng Peng et al., 2005) and (d) acetone in Ar (Xinsheng Peng et al., 2005).**

The oxidation of Ti in pure O<sub>2</sub> (99%) resulted in polycrystalline TiO<sub>2</sub> films instead of 1-D nanostructures as seen in Figure 2.4(a) (Xinsheng Peng & Chen, 2004; Xinsheng Peng et al., 2005). Similar results were obtained for the higher concentration of formic acid (HCOOH) as an oxidizer (Xinsheng Peng et al., 2005). Decreasing the O<sub>2</sub> content in a mixture of Ar (1 sccm flow of O<sub>2</sub> in 200 sccm flow of Ar) showed uneven 1-D nanostructures as shown in Figure 2.4(b) (Xinsheng Peng & Chen, 2004). Further decrease of oxidizer content by using water (H<sub>2</sub>O), acetone (CH<sub>3</sub>COCH<sub>3</sub>), ethanol (C<sub>2</sub>H<sub>5</sub>OH), acetaldehyde (CH<sub>3</sub>CHO) and dibutyltin dilaurate (C<sub>32</sub>H<sub>64</sub>O<sub>4</sub>Sn) vapor in Ar resulted in higher coverage of 1-D nanostructures. Micro-crystalline fiber was seen in presence of water (H<sub>2</sub>O) vapor in Ar during oxidation as shown in Figure 2.4(c) (Xinsheng Peng et al., 2005). Oxidation using acetone (CH<sub>3</sub>COCH<sub>3</sub>) vapor in Ar resulted in dense and well-aligned 1-D TiO<sub>2</sub> (Figure 2.4(d)) (Xinsheng Peng & Chen, 2004; Xinsheng Peng et al., 2005). Similarly, presence of ethanol (C<sub>2</sub>H<sub>5</sub>OH), acetaldehyde (CH<sub>3</sub>CHO), dibutyltin dilaurate (C<sub>32</sub>H<sub>64</sub>O<sub>4</sub>Sn) vapor in Ar results in dense and aligned 1-D TiO<sub>2</sub> nanostructures during thermal oxidation (X Peng & Chen, 2005; Xinsheng Peng et al., 2005).

It was reported that in Ti64 and  $\beta$ -Ti(5-5-5) alloys, the range of oxygen concentration for the growth of 1-D nanostructures is wider (B. J. Dinan et al., 2013). For example, during oxidation of Ti64, 1-D nanostructure are grown until the oxygen concentration of 500 ppm in Ar (B. J. Dinan et al., 2013). However, for the oxygen concentration more than 500 ppm in Ar greatly reduces the 1-D coverage. Though the growth window of 1-D nanostructures is wider for Ti64 and  $\beta$ -Ti (5-5-5) substrates, pure oxygen resulted in oxide scales in all samples instead of 1-D nanostructures.

### 2.2.2.3 Effects of Temperature

Many literature reported that the optimum temperature for 1-D growth during oxidation of Ti is in the range of 700-850 °C (Huo et al., 2009; Kaewsai et al., 2010; Xinsheng Peng & Chen, 2004; Xinsheng Peng et al., 2005). It is confirmed that thicker structures yielded at temperatures above the optimum (Daothong et al., 2007). Figure 2.5 shows the variation in diameters of 1-D nanostructures during oxidation of Ti wire in ethanol vapor at different temperatures (700-850 °C) (Daothong et al., 2007). It was reported that the diameter of the 1-D nanostructures were 23 nm during oxidation at 750 °C which increased to 73 nm at the oxidation temperature of 850 °C.

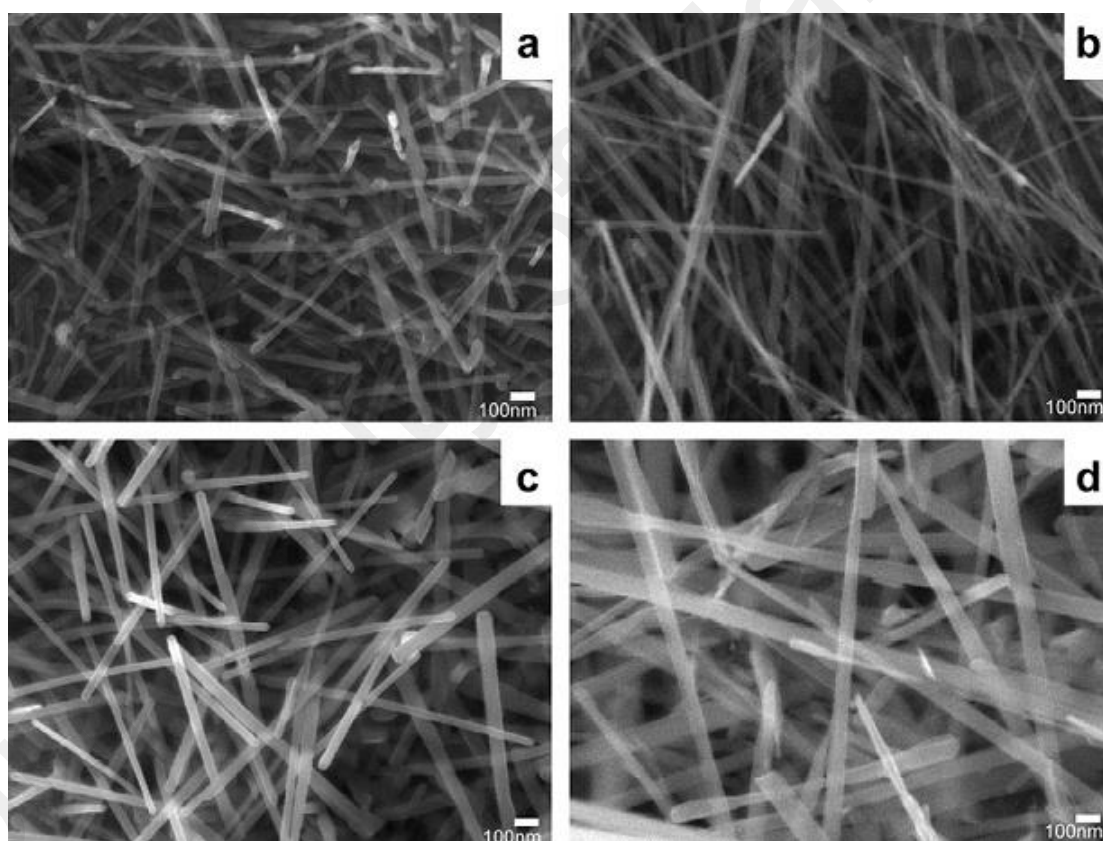


**Figure 2.5: SEM images of 1-D nanostructures on Ti wire oxidized in ethanol vapor at different temperatures of (a) 700 °C, (b) 750 °C, (c) 800 °C and (d) 850 °C (Daothong et al., 2007).**

Similarly, the optimum oxidation temperature for 1-D growth on Ti64 and  $\beta$ -Ti (5-5-5) substrates was reported to be 700-800 °C (Huyong Lee et al., 2010). Increasing the temperatures to 900 °C resulted in faceted nanostructures. It was proposed that at low

temperatures the oxidation is driven by anisotropy with preferential growth on certain crystal faces. This anisotropy decreases at higher temperature promoting growth on other surfaces leading to faceted crystals (Huyong Lee et al., 2010). However, the correlation between the diameter of 1-D nanostructures and temperature is not reported in the literature.

#### **2.2.2.4 Effects of Oxidation Duration**

The effects of oxidation time for 1-D growth on Ti and its alloy substrates are not studied extensively. Some of the literatures only reported that the length of the 1-D nanostructures are increased with increasing oxidation time (Daothong et al., 2007; Xinsheng Peng & Chen, 2004; Xinsheng Peng et al., 2005). For example, during oxidation of Ti substrate with acetone vapor in Ar, short and oriented dots emerged for 12 min of oxidation (Xinsheng Peng et al., 2005). Increasing the oxidation time to 30 min, dense array of 1-D nanostructure with shorter length was formed. Increment of the oxidation time to 90 min resulted in long array of 1-D nanostructures (Xinsheng Peng & Chen, 2004). However, in the literature the maximum oxidation time was 8 h and good amount of 1-D nanostructures were seen for this oxidation time (B. J. Dinan et al., 2013; Huyong Lee et al., 2010). Extension of oxidation duration beyond 8 h was not investigated for Ti and its alloy substrates. It should be noted that during oxidation of Cu, the coverage of 1-D nanostructures decreased for prolonged oxidation after reaching optimum at 5 h of oxidation (F. Wu, Myung, & Banerjee, 2014). Similar phenomenon is anticipated for the thermal oxidation of Ti and its alloy substrates.

#### **2.2.3 Characterization of 1-D Nanostructures**

In different studies the diameter and length of the 1-D nanostructures were reported to be 15-200 nm and 1-5  $\mu\text{m}$ , respectively as tabulated in Table 2.1. Depending

on the alloy conditions and oxidation environment, different types of 1-D nanostructures were reported. For example, oxidation with low concentration of oxygen or water vapor resulted in 1-D TiO<sub>2</sub> only (Xinsheng Peng & Chen, 2004; Xinsheng Peng et al., 2005). Oxidation with acetone vapor resulted in quasi-aligned 1-D nanostructure consisting of core-shell TiO<sub>2</sub>-C as shown in Figure 2.6(a) (Huo et al., 2009; Huo et al., 2008). It was proposed that during oxidation, acetone decomposes to ·CH<sub>3</sub> and CO (Montoro, Corio, & Rosolen, 2007). The CO preferentially adsorbed on the surface of Ti substrate and reacts to form TiO<sub>2</sub> and amorphous C (Daothong et al., 2007). The amorphous C at the shell can be removed by annealing the 1-D nanostructures in air at 650 °C for 30 min (Huo et al., 2009).

Oxidation of Ti64 substrate for the growth of 1-D nanostructures yielded core-shell TiO<sub>2</sub>-Al<sub>2</sub>O<sub>3</sub> nanostructures shown in Figure 2.6(b) (B. J. Dinan et al., 2013). It should be noted that the Ti64 substrates contain 6 wt% of Al with 4 wt% of V. During oxidation, both Ti and Al are oxidized forming 1-D core-shell TiO<sub>2</sub>-Al<sub>2</sub>O<sub>3</sub> nanostructure.

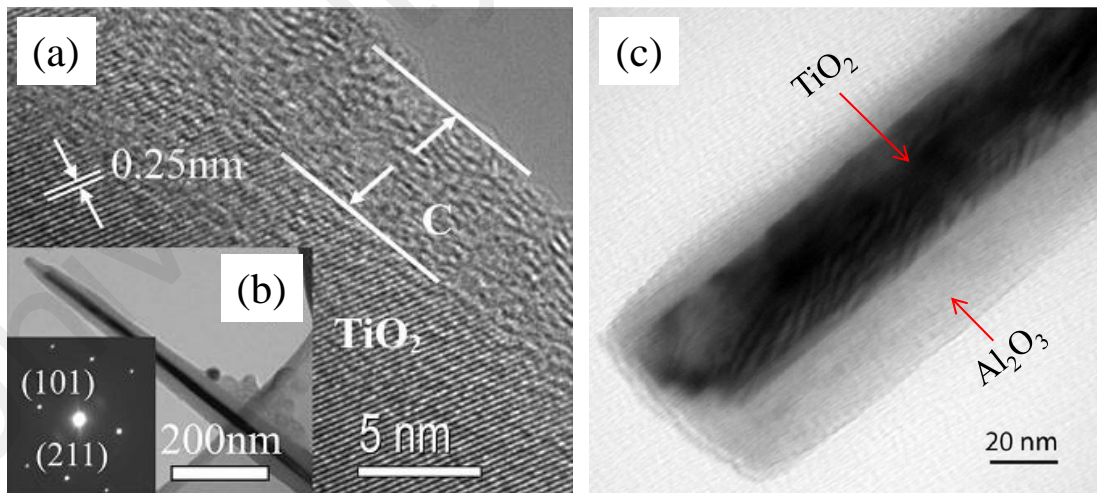


**Figure 2.6: (a-b) High resolution TEM image of the 1-D core-shell TiO<sub>2</sub>-C nanostructure grown on Ti substrate using acetone as oxidation medium and corresponding low magnification view with SADE pattern (Huo et al., 2008), (c) TEM image of the 1-D core-shell TiO<sub>2</sub>-Al<sub>2</sub>O<sub>3</sub> nanostructure grown on Ti64 substrate (B. J. Dinan et al., 2013).**

Regardless of the substrates, during oxidation rutile phase of TiO<sub>2</sub> was obtained. In most cases, the growth direction of TiO<sub>2</sub> is reported to be [0 0 1] on  $\alpha$ -Ti (Table 2.1) (Daothong et al., 2007; Xinsheng Peng & Chen, 2004; Xinsheng Peng et al., 2005). However, exceptions were found in growth direction of TiO<sub>2</sub> and reported as [1 0 1] as well (Huo et al., 2008). On the other hand, the growth directions of TiO<sub>2</sub> in 1-D TiO<sub>2</sub>-Al<sub>2</sub>O<sub>3</sub> on Ti64 substrate was reported to be [ 0 0 1] though further confirmations are required (B. J. Dinan et al., 2013). The growth direction of Al<sub>2</sub>O<sub>3</sub> in 1-D TiO<sub>2</sub>-Al<sub>2</sub>O<sub>3</sub> nanostructures was not reported. None of the study characterized the 1-D nanostructures during oxidation of  $\beta$ -Ti(5-5-5) and Ti-6.85Al-1.6V substrates.

#### **2.2.4 Characterization of Oxide Scale beneath 1-D Nanostructures**

During thermal oxidation of Ti and its alloy substrate oxide scale is formed beneath the 1-D nanostructures. The 1-D nanostructures are evolved from the oxide scale. So far, no study revealed the state of oxide scale beneath 1-D nanostructures on Ti substrate, but it is presumed to be TiO<sub>2</sub> (X. Chen & Mao, 2007; Xinsheng Peng et al., 2005). Other states of oxides were not reported in the literature during oxidation of  $\alpha$ -Ti for the growth of 1-D nanostructures. On the other hand, no study revealed the oxide scale beneath the 1-D nanostructures on Ti64,  $\beta$ -Ti (5-5-5) and Ti-6.85Al-1.6V substrates.

#### **2.2.5 Growth Mechanism of 1-D Nanostructures during Oxidation**

The growth mechanism of 1-D nanostructures during oxidation of Ti64,  $\beta$ -Ti (5-5-5) and Ti-6.85Al-1.6V substrates are not investigated yet. A diffusion based growth model was proposed by Peng *et al.* for the oxidation of  $\alpha$ -Ti substrates (Xinsheng Peng et al., 2005). It was hypothesized that during oxidation, active oxygen species and Ti atoms diffuse through grain boundaries. Then the active oxygen species and Ti atoms react on a specific crystal plane forming 1-D TiO<sub>2</sub> nanostructures (Xinsheng Peng et al., 2005).

However, it was reported in several studies that Ti ions diffuses through interstitial sites during oxidation of Ti (Stringer, 1960; Taniguchi, Hongawara, & Shibata, 2001), which is completely ignored in the model proposed by Peng *et al.* (Xinsheng Peng et al., 2005). Moreover, formation of different oxidation states of Ti and the role of oxidizers are not considered in this model. For this reason, a better understanding of the growth mechanism of 1-D nanostructures on Ti and its alloy substrates is required.

### 2.2.6 Summary of Thermal Oxidation for 1-D Growth on Ti Particles

Thermal oxidation is a very simple and inexpensive process to produce 1-D nanostructures on Ti and its alloy substrates. Pure Ti and a number of Ti alloys such as Ti64,  $\beta$ -Ti (5-5-5) and Ti-6.85Al-1.6V were studied for 1-D growth by thermal oxidation. It was shown that for 1-D growth, the substrate needs to be heated at 700-850 °C in an environment containing trace amount of O<sub>2</sub>. The  $\beta$  phase containing Ti alloys showed higher coverage of 1-D nanostructures compared with pure Ti. Characterization of the 1-D nanostructures showed rutile phase of TiO<sub>2</sub> on Ti substrate and core-shell rutile-corundum TiO<sub>2</sub>-Al<sub>2</sub>O<sub>3</sub> on Ti64 substrates. In Table 2.2, the research findings and gaps are highlighted for the growth of 1-D nanostructures on Ti and its alloy substrates during thermal oxidation. It reveals from Table 2.2 that the effects of oxidation environment has not been studied for Ti alloy substrates. In addition, the effects of oxygen partial pressure, alloy microstructures, residual stress and oxidation duration have not been studied during thermal oxidation for 1-D growth on Ti and Ti alloy substrates. The characterization of 1-D nanostructures and oxide scale beneath 1-D nanostructures on Ti and Ti alloy substrates have not been completely reported. The mechanism proposed to explain the 1-D growth on Ti substrates require modifications.

**Table 2.2: The research findings and gaps for 1-D growth on Ti and its alloy substrates by thermal oxidation.**

Criteria	Parameters	Reported findings	Research gap
Process parameters for oxidation	Oxidation temperatures	Studied for both Ti and Ti64 alloys substrates.	-
	Oxidation environment	The Ti substrates are oxidized in different environment containing water, acetone, ethanol, acetaldehyde or dibutyltin dilaurate. Other Ti alloys are oxidized in Ar with trace amount of O <sub>2</sub> .	There is no study investigating the effects of different oxidizers on Ti alloy substrates.
	Relation between 1-D growth and O <sub>2</sub> partial pressure	-	Studies are required.
	Effects of alloy microstructure	-	Studies are required.
	Effects of residual stress	-	No study on the effect of residual stress for 1-D growth on Ti and its alloy substrates.
	Effects of oxidation duration	Studies are only conducted for Ti substrates. However, the studies are not comprehensive.	No comprehensive study for Ti64 and other Ti alloy substrates.

**Table 2.2, Continued.**

Criteria	Parameters	Reported findings	Research gap
Characterizations	Size and shape of the 1-D nanostructures	Studies only found for 1-D nanostructures on Ti substrates.	No study is conducted for the 1-D nanostructures on Ti64 substrate. Correlation between the oxidation condition and 1-D shape is to be reported.
	Characterization of the 1-D nanostructures	The 1-D nanostructures on Ti substrates are characterized. It is reported that the TiO <sub>2</sub> possessed of rutile phase. The growth direction of the 1-D nanostructure is also reported. However, the 1-D growth on Ti64 is partially characterized. It is reported that 1-D core-shell rutile-corundum TiO <sub>2</sub> -Al <sub>2</sub> O <sub>3</sub> nanostructure exists on Ti64.	1-D nanostructures having different shapes on Ti64 are to be characterized. The growth directions of TiO <sub>2</sub> and Al <sub>2</sub> O <sub>3</sub> are to be reported.
	Characterization of oxide scale beneath the 1-D nanostructures	It is presumed that the oxide scale beneath the 1-D nanostructures in Ti substrate is TiO <sub>2</sub> .	No comprehensive study for Ti and Ti alloy substrates.
	Epitaxial relation between the 1-D growth and substrate	-	No reported studies.
	Initial growth morphology of 1-D nanostructures	-	No study confirmed the initial growth morphology of 1-D nanostructures on Ti and its alloy.
Growth mechanism	-	Mechanism is suggested only for 1-D growth on Ti substrate.	Modifications are required for the 1-D growth mechanism on Ti substrates. No studies reported the 1-D growth mechanism on Ti alloy substrates.

## 2.3 Gas Sensing using Semiconducting Metal Oxides

Over the last few years, research on gas sensing using metal oxide nanostructures has intensified due to their high surface-to-volume ratio, charge confinement ability and improved crystallinity. So far, a wide variety of metal oxides such as  $\text{AgVO}_3$ ,  $\text{CdO}$ ,  $\text{Co}_3\text{O}_4$ ,  $\text{CuO}$ ,  $\text{Fe}_2\text{O}_3$ ,  $\text{In}_2\text{O}_3$ ,  $\text{MoO}_3$ ,  $\text{NiO}$ ,  $\text{TeO}_2$ ,  $\text{TiO}_2$ ,  $\text{SnO}_2$ ,  $\text{WO}_x$ , and  $\text{ZnO}$  have been investigated for gas sensing applications with varying degree of success. For this reason, a number of processes have been developed for the productions of metal oxide nanostructures. The yield, cost and quality of the materials varied from process to process. In the following the recent developments in gas sensing materials are discussed.

### 2.3.1 General Mechanism of Gas Sensing

The fundamental mechanism of gas sensing using semiconducting metal oxides is proposed based on the change in resistivity during the exposure of target gases (Kong & Li, 2005; Yamazoe, 1991). To explain this, the intrinsic property of  $n$ -type semiconducting metal oxide and corresponding valance band, Fermi level and conduction band is shown in Figure 2.7(a). During the exposure in ambient, oxygen are adsorbed on the surface of  $n$ -type metal oxide in the form of  $\text{O}^-$ ,  $\text{O}_2^-$  or  $\text{O}^{2-}$  ions by capturing electron from the conduction band ( $E_c$ ) as shown in Figure 2.7(b). For this reason, an electron depleted layer is created on the surface of  $n$ -type semiconducting metal oxide (Figure 2.7(b)). The thickness of electron depleted layer varies from semiconductor to semiconductor and for  $\text{TiO}_2$  it is approximately 10-25 nm (P. Hu et al., 2010), and for  $\text{ZnO}$  it is several nanometers (Y. Chen, Nie, Xue, Wang, & Wang, 2006). When  $n$ -type metal oxides encounter reducing gases ( $R$ ), electrons are donated to the metal oxide (Chengxiang Wang, Yin, Zhang, Xiang, & Gao, 2010). As a result, the thickness of the electron depleted layer is decreased, vanished or may be over-flown with electrons depending on the nature of  $n$ -type metal oxides and reducing gases (Figure 2.7(c)). For

this reason, the resistance of the  $n$ -type metal oxide is reduced and this type of electrical modification is utilized for gas sensing.

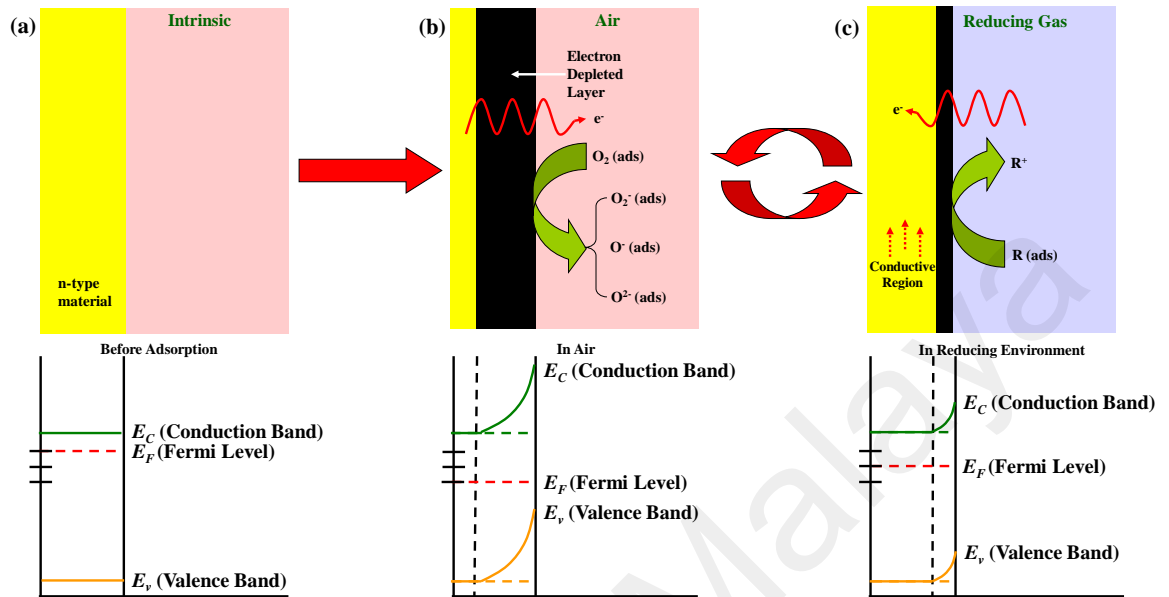


**Figure 2.7: Mechanism of reducing gas sensing using  $n$ -type metal oxides: (a) before adsorption of oxygen, (b) adsorption of oxygen from ambient and creation of electron depleted layer and (c) electron donation by reducing species where  $R$  represents reducing gas (Adapted from the Ref. (C. Wang et al., 2010)).**

In  $p$ -type metal oxides the resistance is increased in presence of reducing gases due to hole conductivity of the materials (Gou, Wang, Yang, Park, & Wexler, 2008). An opposite phenomenon is seen during the exposure of oxidizing gases on  $n$ -type and  $p$ -type semiconducting metal oxides. In Table 2.3, the change in electrical properties of  $n$ -type and  $p$ -type semiconducting metal oxides during the exposure of reducing and oxidizing gases are summarized. For example, the change in resistance of  $p$ -type  $TeO_2$  is shown in Figure 2.8 during the exposure of oxidizing  $NO_2$  and reducing  $H_2S$  gases (Z. Liu et al., 2007). It is seen that the resistance of  $p$ -type  $TeO_2$  is the decreased in oxidizing  $NO_2$  (Figure 2.8(a)) and increased in reducing  $H_2S$  (Figure 2.8(b)).

**Table 2.3: Summary of electrical response of the *n*-type and *p*-type semiconducting metal oxides in reducing and oxidizing gases.**

Target gases	<i>n</i> -type material (AgVO <sub>3</sub> , CdO, In <sub>2</sub> O <sub>3</sub> , MoO <sub>3</sub> , SnO <sub>2</sub> , TiO <sub>2</sub> , WO <sub>x</sub> , ZnO)	<i>p</i> -type material (Co <sub>3</sub> O <sub>4</sub> , CuO, NiO, TeO <sub>2</sub> )
<b>Oxidizing gas</b> (O <sub>2</sub> , NO <sub>2</sub> , Cl <sub>2</sub> etc)	Resistivity is increased	Resistivity is decreased
<b>Reducing Gas</b> (H <sub>2</sub> , H <sub>2</sub> S, CO, CH <sub>4</sub> , HCHO, CH <sub>3</sub> OH, C <sub>2</sub> H <sub>5</sub> OH, C <sub>2</sub> H <sub>4</sub> etc)	Resistivity is decreased	Resistivity is increased

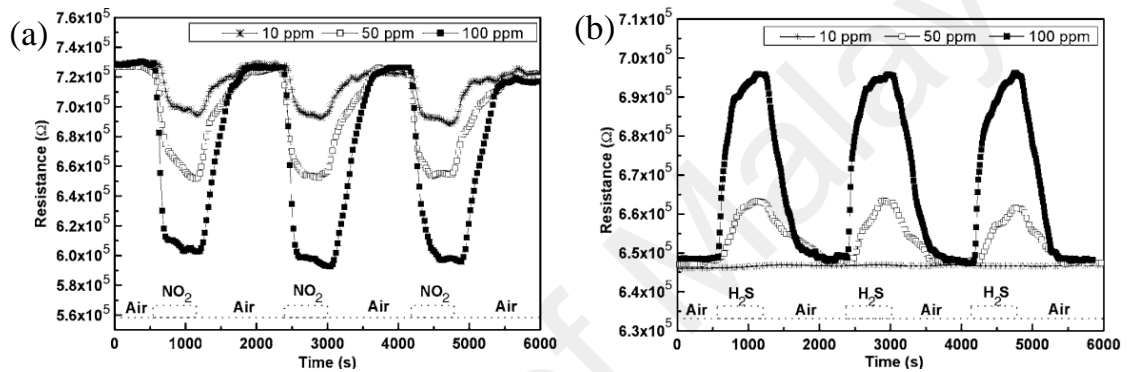


**Figure 2.8: Change in resistance of *p*-type TeO<sub>2</sub> during the exposure of (a) oxidizing NO<sub>2</sub> and (b) reducing H<sub>2</sub>S (Z. Liu et al., 2007).**

### 2.3.2 Gas Sensor Performance Characteristics

The response of a sensor is measured from the change in resistance of metal oxides during the exposure of target gases. Based on the electrical response, different approaches are used to determine the sensitivity of a gas sensor. So far, four forms of sensitivity ( $S$ ) have been reported in the literature:  $S=R_g/R_a$ ,  $S=R_a/R_g$ ,  $S=\Delta R/R_g$  and  $S=\Delta R/R_a$ ; where  $R_a$  is the resistance of the sensor in the ambient,  $R_g$  is the resistance in the target gas, and  $\Delta R=|R_a-R_g|$  (LQ Mai, Hu, Hu, Chen, & Gu, 2006; Liqiang Mai et al., 2010; Z. Yang, Li, Wan, Liu, & Wang, 2008).

Response time and recovery time are other important parameters for determining the performance of a sensor towards a specific gas. The response time and recovery time are defined as the time to reach 90% of the total change in resistance during exposure and

removal of target gas, respectively. In addition, selectivity towards specific gas, optimum operating temperature and lower limit of detection are also used as performance determining factor.

### 2.3.3 Evaluation of Dimensionality in Nanostructures for Gas Sensing

Metal oxides nanostructures are being used in different forms in gas sensors including thick film, thin film, nanoparticles and 1-D nanostructures (Min, Tuller, Palzer, Wöllenstein, & Böttner, 2003). Previously, thick film of metal oxides (thickness of 10-80  $\mu\text{m}$ ) were used in gas sensors due to ease of fabrication (Montméat, Lalauze, Viricelle, Tournier, & Pijolat, 2004; Rao & Rao, 1999). One such thick film sensor is shown in Figure 2.9(a), where  $\text{SnO}_2$  layer was printed on  $\text{Al}_2\text{O}_3$  substrates (Montméat et al., 2004). According to the gas sensing mechanism, the adsorption and desorption of the gas molecules occur at the surface (within the depth of  $<100$  nm) of the metal oxides. So, in the thick film sensors, the bulk is unaffected by the adsorption and desorption of gas molecules. As a result, the change in resistance is insignificant in thick film sensors resulting in poor sensitivity and for this reason they have limited use in real applications (Bruno, Pijolat, & Lalauze, 1994; Klöber, Ludwig, & Schneider, 1991; Korotcenkov, Brinzari, Schwank, DiBattista, & Vasiliev, 2001; Mochida, Kikuchi, Kondo, Ueno, & Matsuura, 1995; Montméat et al., 2004).

To improve the performance of the sensors, the research direction was shifted from thick film to thin film, where the thickness of metal oxides was several hundreds of nanometers. One such example of thin film sensor is shown in Figure 2.9(b), where Al doped ZnO film was deposited on  $\text{SiO}_2/\text{Si}$  substrate (Chang, Kuo, Leu, & Hon, 2002). It is reported that the performance of thin film sensor is better than thick film sensors (Chang et al., 2002; Korotcenkov & Cho, 2009). However, still in this case the adsorption and desorption of the gas molecules occurs at the surface (within the depth of  $<100$  nm) and

rest of the material is unaffected. For this reason, the research direction shifted towards developing materials with dimensions less than 100 nm. It was expected that nanomaterials having size less than 100 nm will have better performance compared with the thin film sensors.

Recent developments in nanomaterials showed remarkable improvements in gas sensing due to having comparable size with the electron depleted layer in metal oxides (Cao, Hu, Pan, Huang, & Jia, 2008; W.-S. Kim, Kim, & Hong, 2010; J. Zhang et al., 2009). Spherical nanoparticles of SnO<sub>2</sub> (J. Zhang et al., 2009), MoO<sub>3</sub> (W.-S. Kim et al., 2010) showed better performances compared with thin film sensors. But, the performance of spherical nanoparticles can be further improved by altering the shape to 1-D nanostructures. Since the gas adsorption and desorption occur only at the surface, higher surface area is desired in the metal oxides for gas sensing applications. Spherical shaped nanoparticles have lowest surface-to-volume ratio for a given volume compared to 1-D nanostructures. For this reason, recently the research direction has shifted towards 1-D metal oxide nanostructures for gas sensing applications. Different studies showed that 1-D nanostructures exhibit higher sensitivity compared to spherical shaped nanoparticles (Cao et al., 2008; Sysoev et al., 2009).

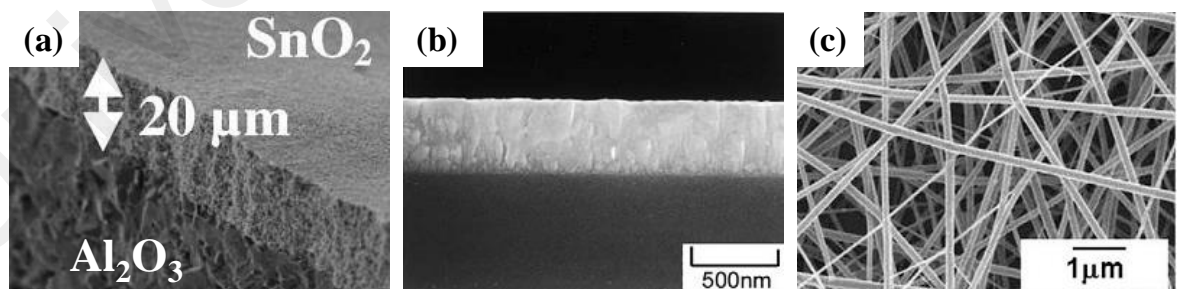


**Figure 2.9:** (a) Thick film of SnO<sub>2</sub> screen printed on Al<sub>2</sub>O<sub>3</sub> substrate (Montméat et al., 2004), (b) Al doped ZnO films deposited onto SiO<sub>2</sub>/Si substrates (390 nm) (Chang et al., 2002) and (c) In<sub>2</sub>O<sub>3</sub> nanofibers grown by electrospinning (W. Zheng et al., 2009).

So far, 1-D nanostructures of  $\text{AgVO}_3$ ,  $\text{CdO}$ ,  $\text{CuO}$ ,  $\text{Fe}_2\text{O}_3$ ,  $\text{In}_2\text{O}_3$ ,  $\text{MoO}_3$ ,  $\text{TeO}_2$ ,  $\text{TiO}_2$ ,  $\text{SnO}_2$ ,  $\text{WO}_x$  and  $\text{ZnO}$  have been synthesized for gas sensing applications with different morphologies including nanorods (Caihong Wang, Chu, & Wu, 2006; Z. Yang et al., 2008), nanotubes (A. Hu et al., 2011), nanowires (Huang et al., 2001), nanofibers (Qi, Zhang, Liu, & Zheng, 2009), nanobelts (Sadek, Choopun, Wlodarski, Ippolito, & Kalantar-zadeh, 2007), nanoribbons (Kong & Li, 2005), nanowhiskers (Ying, Wan, Song, & Feng, 2004), nanoneedles (Qurashi, El-Maghraby, Yamazaki, & Kikuta, 2010), nanopushpins (Qurashi, Yamazaki, El-Maghraby, & Kikuta, 2009), fiber-mats (Baratto, Sberveglieri, Onischuk, Caruso, & Di Stasio, 2004), urchins (Hao et al., 2011) and lamellar structure (Imawan, Solzbacher, Steffes, & Obermeier, 2000). A great variety of processing routes including hydrothermal (Lupan, Chai, & Chow, 2008), ultrasonic irradiation (Oh et al., 2009), electrospinning (Qi et al., 2009), anodization (A. Hu et al., 2011), sol-gel (X. Lu & Yin, 2011), molten-salt (D. Wang, Chu, & Gong, 2006), carbothermal reduction (Huang et al., 2001), solid-state chemical reaction (Cao et al., 2008), thermal evaporation (Wan, Lin, Yu, & Wang, 2004), vapor-phase transport (N. Zhang, Yu, Li, Zhu, & Wan, 2008), aerosol (Baratto et al., 2004), RF sputtering (Sadek et al., 2007), molecular beam epitaxy (H.-T. Wang et al., 2005), chemical vapor deposition (S. S. Kim et al., 2010), nanocarving (Carney, Yoo, & Akbar, 2005), UV lithography and dry plasma etching (Francioso, Taurino, Forleo, & Siciliano, 2008) have been developed for synthesizing 1-D nanostructures. One such randomly oriented 1-D  $\text{In}_2\text{O}_3$  nanofibers produced by electrospinning is shown in Figure 2.9(c) (W. Zheng et al., 2009).

#### **2.3.4 Mechanism of Gas Sensing by 1-D Oxide Nanostructures**

The basic mechanism of gas sensing using metal oxides is explained in section 2.3.1. This mechanism is also applicable for gas sensing using 1-D nanostructures. Due to

having higher surface area compared with the bulk materials, higher amount of gas adsorptions and desorption occur at the surface of 1-D nanostructure resulting in better performance. In addition with higher surface area, some features of 1-D nanostructures provide some extra benefits towards gas sensing.

In gas sensors, 1-D nanostructures are distributed randomly as shown in Figure 2.9(c) or aligned to certain periods as seen for vertically aligned (Z. Yang et al., 2008), flower-like (Feng, Wan, & Wang, 2005) and hierarchical dendrites (N. Zhang et al., 2008) structures shown in Figure 2.10(a-c). In all these nanostructures, the total resistance in the ambient is the combination of the resistance of individual 1-D nanostructures ( $R_N$ ) and the resistance for contacts ( $R_C$ ) with other 1-D nanostructures.

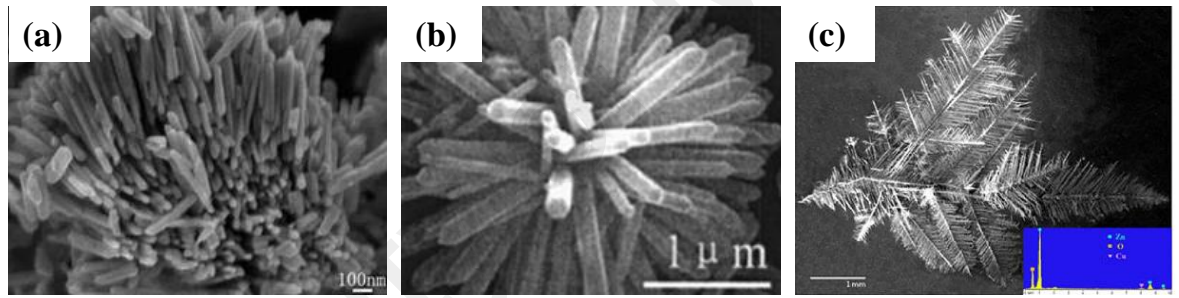


**Figure 2.10: (a) Vertically aligned 1-D ZnO nanostructures produced by hydrothermal process (Z. Yang et al., 2008), (b) ZnO nanorods with a flowerlike morphology grown by hydrothermal process (Feng et al., 2005) and (c) hierarchical dendrites of ZnO produced by vapor phase transport route (N. Zhang et al., 2008).**

The resistance of individual 1-D nanostructures is deduced from the model of neck grain boundary as follows (Ma, Wang, Liao, & Kong, 2002):

$$R_N = \frac{L}{\pi e [\mu_b n_b r_o^2 + n_d \mu_d (r_m^2 - r_o^2)]} \quad (2.1)$$

In this equation,  $e$  is the charge of electron,  $\mu_b$  is the electron mobility in the neutral grain body,  $\mu_d$  is the electron mobility in the depleted layer,  $n_b$  is the free electron density,  $n_d$  is the free-electron density in the depleted layer,  $r_o$  is the width of depletion layer,  $r_m$  is the radius, and  $L$  is the length of the 1-D nanostructure. It is seen from equation (2.1),

when the depletion width ( $r_o$ ) is almost similar to the radius of the 1-D nanostructure (Jin et al.), the surface depletion width becomes the dominant factor in determining the resistance by the following equation:

$$R_N = \frac{L}{\pi e \mu_b n_b r_o^2} \quad (2.2)$$

On the other hand, the contact resistance of 1-D nanostructure is presented by the following equation:

$$R_C = R_a \exp \left\{ -\frac{e \Delta V_b}{k_B T} \right\} \quad (2.3)$$

Here,  $R_a$  is the resistance in ambient,  $\Delta V_b$  is the change in barrier potential,  $e$  is the charge of an electron,  $k_B$  is Boltzmann's constant and  $T$  is the absolute temperature.

So, the total resistance of the 1-D nanostructure is the combination of individual resistance of 1-D nanostructures and contact resistances. The density and mobility of the electrons in 1-D nanostructures is controlled by the surface depletion layer. The transportation of electrons between the 1-D nanostructures are controlled by the contact energy barrier. So, the total resistance in a system composed of 1-D nanostructures possessing of depletion layer and contact barrier can be represented as:

$$R = R_N + R_C$$

$$\Rightarrow R = \frac{L}{\pi e [\mu_b n_b r_o^2 + n_d \mu_d (r_m^2 - r_o^2)]} + R_a \exp \left\{ -\frac{e \Delta V_b}{k_B T} \right\} \quad (2.4)$$

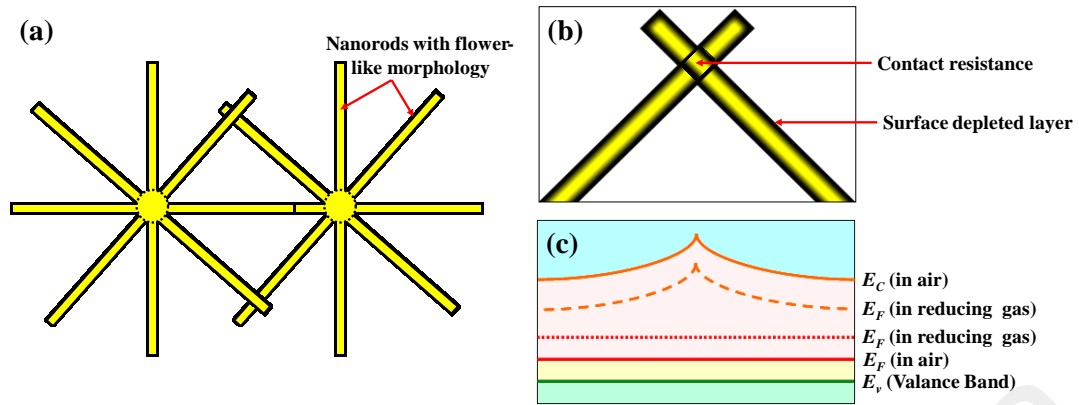


**Figure 2.11: (a) Contacts of 1-D nanostructures with flower-like morphology, (b) magnified view of a contact and (c) energy band diagram in presence of reducing gas (Adapted from Ref. (Feng et al., 2005)).**

According to this model, a simple schematic is presented in Figure 2.11(a) to explain the high sensitivity of  $n$ -type 1-D nanostructures having flower-like morphology. The surface depletion layer and a contact barrier of the 1-D nanostructures are shown in Figure 2.11(b). The total resistance of the nanostructure in ambient is deduced from equation 2.4. However, in reducing environment, electrons are donated to the conduction band and  $R_C$  is decreased and  $\Delta V_b$  is increased according to equation (2.3). However, increase of the potential barrier ( $\Delta V_b$ ) shifts the Fermi level towards the conduction band as shown in Figure 2.11(c). As a result, the interconnected 1-D nanostructures provide direct paths for efficient electron transport with low-energy barrier of the contacts. As a result, the change in resistance is seen higher in 1-D nanostructures. This type of electrical enhancement in 1-D nanostructures provides higher sensitivity towards different gases.

### 2.3.5 Recent Developments and Sensing Mechanism

The performance of 1-D nanostructures for gas sensing can be further improved by incorporating several modifications. For example, creating rougher surface in 1-D nanostructure showed better gas sensing performance compared to smoother surface due to providing more surfaces for gas adsorption and desorption (C. Wang et al., 2006). Another way to improve the surface area is to create hollow and porous 1-D

nanostructures, which has been reported for TiO<sub>2</sub> (Paulose et al., 2005), SnO<sub>2</sub> (Hyodo, Sasahara, Shimizu, & Egashira, 2005; Y. Tan, Li, Wang, Tang, & Ouyang, 2008), ZnO (Tian et al., 2008),  $\alpha$ -Fe<sub>2</sub>O<sub>3</sub> (Hao et al., 2011) and CdO (Guo, Li, & Liu, 2008) nanostructure. One such 1-D TiO<sub>2</sub> nanotubes prepared by anodization process is shown in Figure 2.12(a). Coating of 1-D nanostructures to improve the catalytic activity towards target gases also improves the sensing performance as reported for ZnO nanorods coated with Pd (H.-T. Wang et al., 2005). Similarly, addition of different nanoparticles such as Pt, Pd, Au, Ag, La<sub>2</sub>O<sub>3</sub> and CuO on 1-D nanostructures also improve the gas sensing performance by lowering the oxidation energy, increasing catalytic surface area and changing the chemical nature (Han et al., 2007; P. Hu et al., 2010; Kong & Li, 2005; S. Shi et al., 2009; Singh, Gupta, & Lee, 2011; W. Zheng et al., 2009). An example of Au nanoparticles loaded In<sub>2</sub>O<sub>3</sub> nanowire is shown in Figure 2.12(b). Doping of novel metals such as Pt and Pd in the 1-D metal oxides also improve the gas sensing performance by increasing the resistance at the grain boundaries and adsorbing higher amount of oxygen (Cabot et al., 2000; Dong et al., 2011; Kang & Kim, 1994).

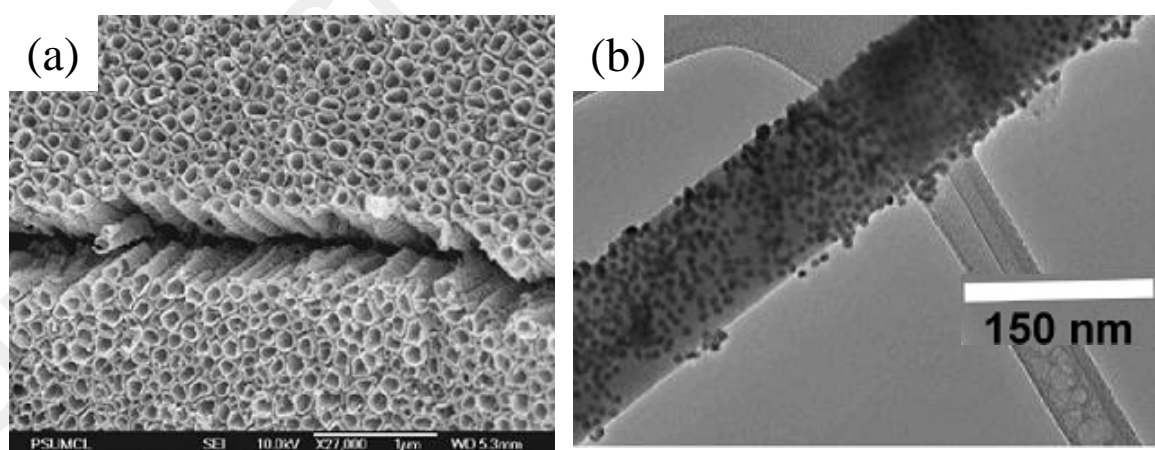


**Figure 2.12: (a) TiO<sub>2</sub> nanotubes prepared by anodization process (Paulose et al., 2005) and (b) Au nanoparticles loaded In<sub>2</sub>O<sub>3</sub> nanowire (Singh et al., 2011).**

It was reported that the usage of binary oxides has remarkable effect on gas sensing through different mechanisms including enhanced charge transfer (S. Sen et al., 2010), higher adsorption of gas molecules (Park et al., 2010), thicker electron depleted layer (I-

S. Hwang et al., 2010) and modification of band energies (Miller, Akbar, & Morris, 2014). So far, three types of mixed oxides are being used in gas sensing application including *n-n*, *p-p* and *n-p* combinations. The gas sensing performances of *n-n* SnO<sub>2</sub>-W<sub>18</sub>O<sub>49</sub> (S. Sen et al., 2010), *p-p* CuO-NiO (Y. Wang et al., 2015) and *n-p* ZnO-Co<sub>3</sub>O<sub>4</sub> (Na, Woo, Kim, & Lee, 2011) have been reported in the literature. The schematic of band bending at the *n-n*, *p-p* and *n-p* heterojunctions with no adsorbed surface species is shown in Figure 2.13.

It is proposed that the presence of *n-n* junction transfers electrons to the lower energy conduction band to form an “electron accumulation” layer (Figure 2.13(a-b)). The electron accumulation layer is depleted by subsequent oxygen adsorptions. As a result, the resistance of the 1-D nanostructure is increased and better performance is seen towards electron donating reducing gases (Miller et al., 2014; Zeng et al., 2010).

For the case of *p-p* junction, electrons are transferred to lower energy Fermi levels as proposed by Wang *et al.* (Y. Wang et al., 2015). A “hole depletion” and “hole accumulation” layer is formed at the *p-p* interface as shown in Figure 2.13(c-d). Adsorption of oxygen at the surface transfers hole to the valance band of *p*-type oxide. Some of these holes are also transferred to the hole depleted layer. As a result, the resistance of the *p-p* interface is decreased. Presence of reducing gas donates electrons, which reduces the hole concentration at the valance band and *p-p* interface by recombination process. For this reason, the resistance of *p-p* interface is increased in presence of reducing gases. Similarly, *n-p* junction increases the resistance of the 1-D nanostructures by electron-hole recombination process and depletion layer is created at the interface (Figure 2.13(e-f)). Presence of reducing gas reduces the resistance of the *n-p* interface by donating electrons (Miller et al., 2014).

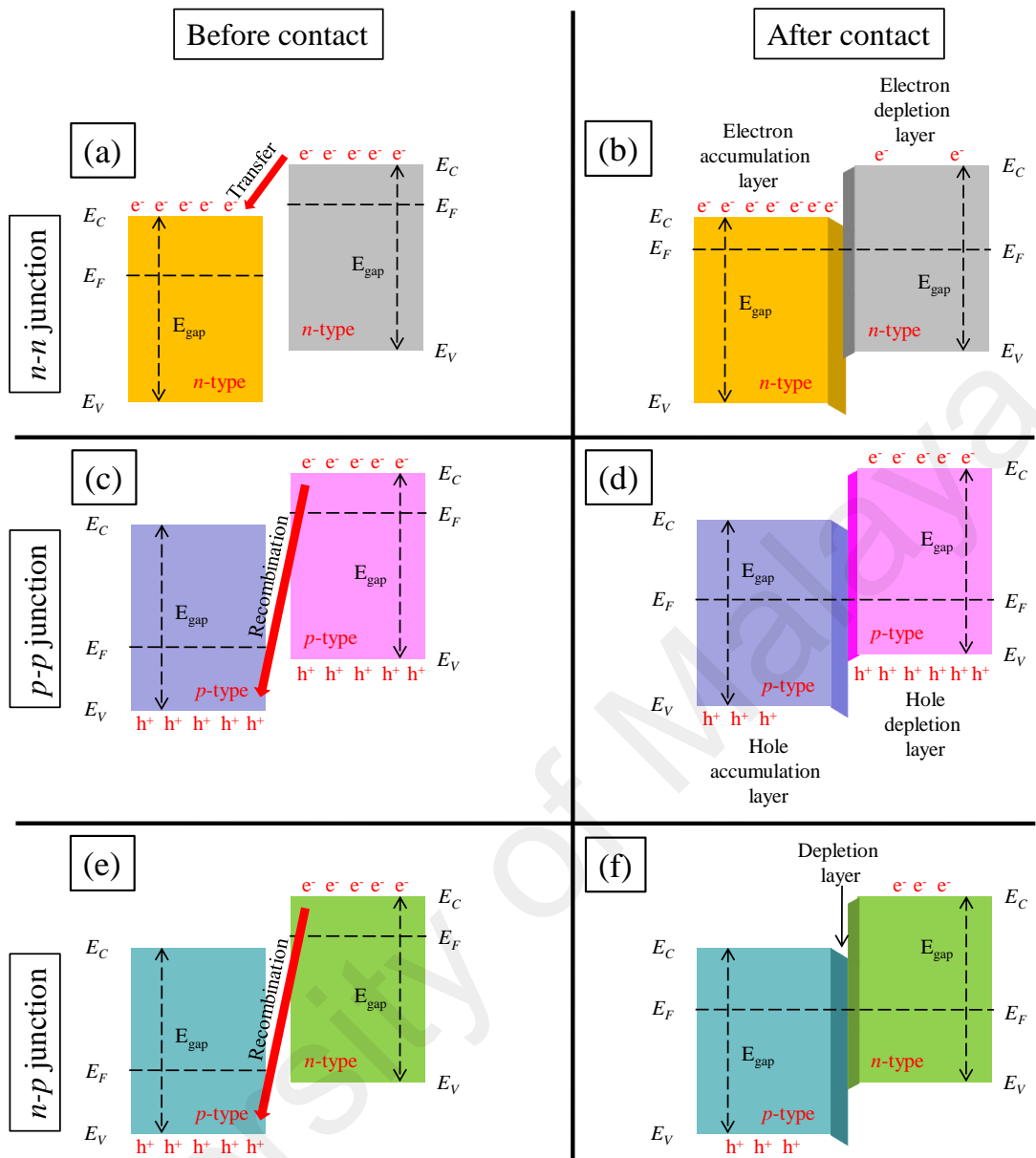


**Figure 2.13: Schematic band bending at heterojunctions with no adsorbed surface species (a-b) *n-n* junction (adopted from Ref. (Miller et al., 2014; Zeng, Liu, & Wang, 2010)), (c-d) *p-p* junction (adopted from Ref. (Y. Wang et al., 2015)) and (e-f) *n-p* junction (adopted from Ref. (Miller et al., 2014)).**

### 2.3.6 Fabrication of Sensors Using 1-D Nanostructures

The various forms of 1-D nanostructures are arranged in three different ways for the fabrication of a sensor: (a) single nanostructure arrangement, (b) aligned nanostructure arrangements and (c) randomly distributed arrangement. The schematic of these arrangements is shown in Figure 2.14.

In single nanostructure arrangement, one individual 1-D nanostructure is positioned on substrate and connected with electrodes by *in-situ* lift-out technique using focused ion beam (FIB) as shown in Figure 2.14(a) (Chai, Lupan, Chow, & Heinrich, 2009; Lupan, Chai, & Chow, 2007; Lupan et al., 2008; Lupan et al., 2010). However, this technique is complex and high precision is required; hence not popular for making sensors.

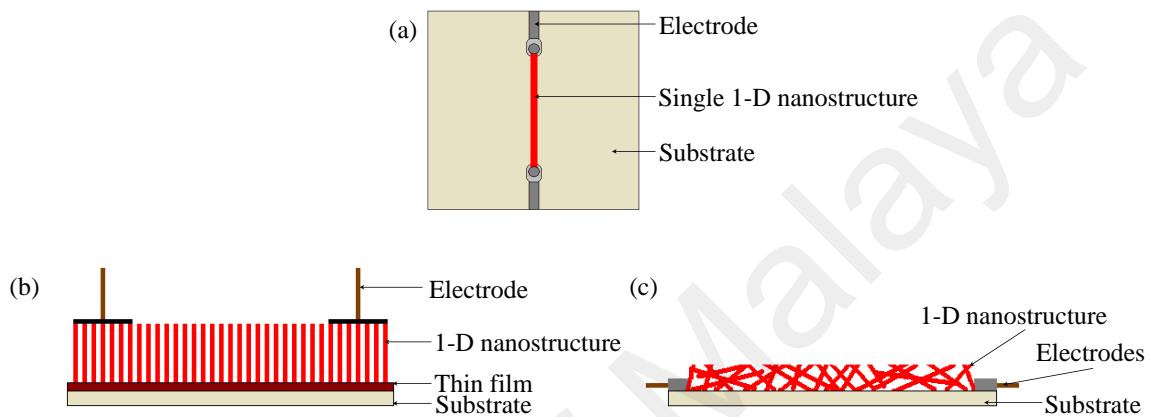


**Figure 2.14: Schematics of sensor fabrication (a) single nanostructure arrangement, (b) aligned nanostructure arrangements and (c) randomly distributed arrangement.**

In the aligned nanostructures arrangements, the 1-D nanostructures are grown on the substrate and electrical connections are made among the 1-D nanostructures as shown in Figure 2.14(b) (Liao et al., 2007; O. K. Varghese et al., 2003). For example, Varghese *et al.* (O. K. Varghese et al., 2003) developed TiO<sub>2</sub> nanotubes by anodization of Ti foil. During anodization a thin film of TiO<sub>2</sub> was also formed on the substrate. Two spring-loaded Pt pads were connected with the nanotubes as shown in Figure 2.14(b). This type of electrical connection is complex, requires multi-stepped process and fragile.

Randomly distributed 1-D nanostructure arrangement is most popular arrangement for the preparation of sensors. Three types of variations are seen for this type of arrangement: (i) nanostructures distributed on flat substrates (Y.-J. Choi et al., 2008; Hsueh, Hsu, Chang, & Chen, 2007; Qing Wan et al., 2004), (ii) nanostructures distributed on the circumference of a tube (Hao et al., 2011; Qi et al., 2009; B. Wang et al., 2010; C. Wang

et al., 2006) and (iii) nanostructures pressed in a form of tablet (Zhou, Li, Ma, & Xue, 2011). The electrical connections are made with the 1-D nanostructures at two opposite ends of the substrates or tablets. One such randomly distributed flat substrate arrangement is shown in Figure 2.14(c). In many instances interdigitated substrates (electrodes are printed on the flat or tube shaped substrates) are used for sensor fabrication which is much convenient process for sensor fabrication (Y.-J. Choi et al., 2008; Hsueh et al., 2007; Qing Wan et al., 2004). Moreover, the 1-D nanostructures can be directly grown on the interdigitated substrate which is a much simpler and time saving process for the preparation of sensors (Y.-J. Choi et al., 2008; Hsueh et al., 2007).

### **2.3.7 Gas Sensing Performance of TiO<sub>2</sub> Based Materials**

Semiconducting metal oxides are being used as gas sensing materials due to their numerous benefits such as high sensitivity, easy fabrication and low cost (Comini et al., 2002). Many of these metal oxides exhibit optimum sensitivity at low temperatures (Al-Hardan, Abdullah, Aziz, & Ahmad, 2010; Baratto et al., 2004; Fields, Zheng, Cheng, & Xiong, 2006; S. Shi et al., 2009), whereas TiO<sub>2</sub> is capable of operating at temperatures as high as 550-600 °C (Dutta, Frank, Hunter, & George, 2005; Savage, Akbar, & Dutta, 2001). Moreover, TiO<sub>2</sub> is stable at high temperatures, whereas low temperature gas sensing materials may undergo morphological and phase changes. Additionally, catalytic activity of TiO<sub>2</sub> towards different gases offers higher electron exchange which is beneficial for gas sensing (Idriss & Seebauer, 2000; Nadeem, Waterhouse, & Idriss, 2012; Y. Wang et al., 2015; Yanxin et al., 1999). Non-toxicity, easy fabrication, chemical stability and low cost are additional benefits of TiO<sub>2</sub> in high temperature gas sensing applications.

A great variety of TiO<sub>2</sub> nanomaterials have been used for detecting different gases. These include nanowires (Rout et al., 2007; Yoo et al., 2004b), nanotubes (Han et al.,

2007; H. F. Lu et al., 2008; Paulose et al., 2005; O. K. Varghese et al., 2003), nanofibers (Carney et al., 2005; Landau, Rothschild, & Zussman, 2008; B. Wang et al., 2010), nanobelts (Galatsis et al., 2002), spherical colloids (Cheng, Xu, Gao, Zhao, & Huo, 2011) and nanoparticles (Rella et al., 2007; Seo et al., 2009) as tabulated in Table 2.4. It is seen in the literature that mostly anatase form of TiO<sub>2</sub> has been used for sensing different gases. Anatase form of TiO<sub>2</sub> might transform to rutile during gas sensing at high temperatures, which might affect the reproducibility of sensing results. Stabilizing the phase content at a temperature higher than the sensing temperatures was ignored in most of the studies.

In Table 2.4, the response of different forms of TiO<sub>2</sub> towards different gases is presented. It is seen that the sensing results are highly scattered and direct comparison is not possible due to variations in processing, dimensions and sensor preparation techniques. Moreover, in different studies different equations were used to report the response of the sensors which made it more difficult for comparison. For this reason, the reported response values are converted to  $R_o/R_g$  for reducing gases and  $R_g/R_o$  for oxidizing gases (where,  $R_o$  and  $R_g$  are the resistances of the sensors in N<sub>2</sub>/air/ambient and in target gas, respectively) and tabulated in Table 2.4. It is seen that the response of TiO<sub>2</sub> based sensors are very high towards C<sub>2</sub>H<sub>5</sub>OH compared with other gases and responses as high as  $2.5 \times 10^5$  was reported (Arafat, Haseeb, & Akbar, 2014). TiO<sub>2</sub> nanostructures prepared by anodization process normally possess higher response compared with others (Kwon et al., 2012; O. K. Varghese et al., 2003). Defect states of anodized samples might be attributed to higher response by enhancing the catalytic activity towards specific gas. It is also seen in Table 2.4 that commercial TiO<sub>2</sub> nanoparticles and cold pressed samples possess good response due to having higher initial resistance which dropped in presence of target gases.

**Table 2.4: Comparison of the sensor response using different forms of TiO<sub>2</sub>.**

Gas Tested	Morphology	Crystal Structure	Dimension	Fabrication route	Response			Response Time	Recovery Time	References
					Sensitivity	Concentration	Temperature (°C)			
H <sub>2</sub>	TiO <sub>2</sub> nanowire	Rutile	Diameter: 20-80 nm Length: 100-800 nm	Hydrothermal	8	1000 ppm	RT	-	-	(Rout et al., 2007)
	TiO <sub>2</sub> nanotube array	Anatase, rutile	Diameter: 46-76 nm Length: 400 nm	Anodization	~1,000	1000 ppm	400	3 min	-	(O. K. Varghese et al., 2003)
	TiO <sub>2</sub> nanotube array	-	Diameter: 30-110 nm Length: 380 nm-6 μm	Anodization	~10 <sup>9</sup>	1000 ppm	-	-	-	(Paulose et al., 2005)
	TiO <sub>2</sub> nanofiber	Rutile	Diameter: 15-50 nm Length: 1-5 μm	Nanocarving	3.7	4%	400C	~10 min	-	(Yoo et al., 2004b)
	TiO <sub>2</sub> -SnO <sub>2</sub> nanofiber	Rutile	Diameter: 5-10 nm Length: 0.2-1 μm	Nanocarving	1.25	2%	400	1-2 min	5-7 min	(Carney et al., 2005)
	TiO <sub>2</sub> -Al <sub>2</sub> O <sub>3</sub> thick film	Anatase	-	Cold pressing and heating followed by printing on substrate	~1000	10%	600	-	-	(Birkefeld, Azad, & Akbar, 1992)
H <sub>2</sub> S	TiO <sub>2</sub> film	Anatase	Thickness: 2-3 μm	Solution precipitation	3.16	1000 ppm	325	-	-	(Chaudhari, Bambole, Bodade, & Padole, 2006)
	TiO <sub>2</sub> -Al <sub>2</sub> O <sub>3</sub> film	Anatase	Thickness: 2-3 μm	Solution precipitation	7.9	1000 ppm	325	-	-	(Chaudhari et al., 2006)

**Table 2.4, Continued.**

Gas Tested	Morphology	Crystal Structure	Dimension	Fabrication route	Response			Response Time	Recovery Time	References
					Sensitivity	Concentration	Temperature (°C)			
CO	TiO <sub>2</sub> nanoparticles doped with Al	Anatase	Diameter: 100 nm	Solution precipitation	1.54	500 ppm	600	-	-	(Y. J. Choi, Seeley, Bandyopadhyay, Bose, & Akbar, 2007)
	TiO <sub>2</sub> nanofibers doped with Cu	Anatase, rutile, brookite	Diameter: 80 nm	Electrospinning	21	100 ppm	300	4 s	8 s	(B. Wang et al., 2010)
	TiO <sub>2</sub> -Al <sub>2</sub> O <sub>3</sub> film	Anatase-rutile mixture	Particle size: 18.2-21.8 nm	Sol-gel	12.6	400 ppm	400	47 s	56s	(Mohammadi, 2014)
	TiO <sub>2</sub> -Al <sub>2</sub> O <sub>3</sub> film	Anatase	-	Cold pressing and heating followed by printing on substrate	~100	2300 ppm	800	-	-	(Birkefeld et al., 1992)
CH <sub>3</sub> OH	TiO <sub>2</sub> film	Anatase	Particle size: 3-30 nm	Sol-gel	18 [In the literature the response was reported as 1700% by using $(\Delta I/I_0) \times 100\%$ formula where $I$ is current]	100 ppm	500	0.5 min	< 1 min	(Garzella, Comini, Tempesti, Frigeri, & Sberveglieri, 2000)

**Table 2.4, Continued.**

Gas Tested	Morphology	Crystal Structure	Dimension	Fabrication route	Response			Response Time	Recovery Time	References
					Sensitivity	Concentration	Temperature (°C)			
C <sub>2</sub> H <sub>5</sub> OH	TiO <sub>2</sub> nanoparticles	Anatase and rutile mixture	-	Hydrothermal	65	47 ppm	450	-	-	(Seo et al., 2009)
	TiO <sub>2</sub> nanobelt	Anatase	Thickness: 50 nm Width: 100-150 nm	Anodization	46.153	500 ppm	200	1-2 s	1-2 s	(P. Hu et al., 2010)
	TiO <sub>2</sub> nanotube array	Anatase	Diameter: 70-120 nm	Anodization	13801 [In the literature the response was reported as 1380000% by using $(\Delta R/R_g) \times 100\%$ formula]	1000 ppm	250	90 s	14 s	(Kwon et al., 2012)
	TiO <sub>2</sub> nanoparticles	Anatase, rutile	Diameter: 60.1 ± 30.7 nm	Drop casting of commercial nanoparticles	2.5 × 10 <sup>5</sup>	1000 ppm	600	-	-	(Arafat et al., 2014)
	TiO <sub>2</sub> nanowire array	Anatase	Width: 90-180 nm Length: 1400 μm	UV lithography, dry plasma etching	50	2%	550	-	-	(Francioso et al., 2008)
	TiO <sub>2</sub> nanoparticles doped with Nb	Anatase and rutile mixture	Diameter: 11 nm	Flame synthesis	41.4	1000 ppm	350	9 s	-	(Phanichphant, Liewhiran, Wetchakun, Wisitsoraat, & Tuantranont, 2011)

**Table 2.4, Continued.**

Gas Tested	Morphology	Crystal Structure	Dimension	Fabrication route	Response			Response Time	Recovery Time	References
					Sensitivity	Concentration	Temperature (°C)			
NO <sub>2</sub> /NO <sub>x</sub>	TiO <sub>2</sub> nanotubes loaded with Al <sub>2</sub> O <sub>3</sub>	Anatase	Diameter: 200 nm	Sol-gel	1.8804 [In the literature the response was reported as 88.04% by using $(\Delta R/R_g) \times 100\%$ formula]	97 ppm	-	8 s	-	(Lü et al., 2013)
	TiO <sub>2</sub> nanofibers	Anatase	Diameter: 120-850 nm	Electrospinning	74.3	250 ppb	300	48 s	4.4 min	(Landau et al., 2008)
O <sub>2</sub>	Nanotube array	Amorphous	Diameter: 150 nm	Anodization	~101	-	100	-	-	(H. F. Lu et al., 2008)

### 2.3.8 Summary and Research Gap in Gas Sensing using TiO<sub>2</sub>

A great variety of semiconducting metal oxides including AgVO<sub>3</sub>, CdO, Co<sub>3</sub>O<sub>4</sub>, CuO, Fe<sub>2</sub>O<sub>3</sub>, In<sub>2</sub>O<sub>3</sub>, MoO<sub>3</sub>, NiO, TeO<sub>2</sub>, TiO<sub>2</sub>, SnO<sub>2</sub>, WO<sub>x</sub>, and ZnO have been tested for gas sensing applications with varying degree of success. These metal oxides are used in different forms in gas sensing devices such as thick film, thin film, nanomaterials and 1-D nanostructures. Results reveal that 1-D metal oxides have better sensing performance compared with other forms of metal oxides due to having higher surface-to-volume ratio. It is also shown that the performance of 1-D nanostructures is further improved by adopting different techniques such as usage of binary oxides.

So far, different forms of 1-D TiO<sub>2</sub> nanostructures such as nanowires, nanotubes, nanofibers, and nanobelts have been used for gas sensing. The TiO<sub>2</sub> based materials has additional benefits over other types of metal oxides such as non-toxicity, easy fabrication, low cost, chemical stability and capable of working at high temperatures. In Table 2.5, the findings on gas sensing using 1-D TiO<sub>2</sub> based materials and research gaps are summarized. So far, no in-situ sensor fabrication method has been developed by thermal oxidation process for gas sensing applications. The effects of 1-D core-shell TiO<sub>2</sub>-MO (where MO is metal oxides other than TiO<sub>2</sub>) are not studied towards gas sensing. In most of the studies the catalytic effect of TiO<sub>2</sub> towards different gases is ignored during the explanation of sensing mechanism.

**Table 2.5: Findings on gas sensing and research gaps using 1-D TiO<sub>2</sub> based materials.**

Criteria	Parameters	Reported findings	Research gap
Processing of 1-D TiO <sub>2</sub> materials	-	1-D TiO <sub>2</sub> nanostructures grown by hydrothermal, sol-gel, anodization, electrospinning and nanocarving were used for gas sensing	1-D nanostructures grown by thermal oxidation has never been utilized for gas sensing
	Crystal structure	Anatase form of TiO <sub>2</sub> is used in most of the literatures. Rutile phase of TiO <sub>2</sub> is also used in some of the studies	Rutile phase of TiO <sub>2</sub> is not tested towards many gases
Morphology of 1-D nanostructures	Usage of binary oxides	The <i>n-n</i> type of 1-D TiO <sub>2</sub> -SnO <sub>2</sub> , TiO <sub>2</sub> -ZnO is reported in the literature for gas sensing	The <i>n-p</i> semiconductor combination of mixed TiO <sub>2</sub> structures is not investigated. Also, 1-D insulating Al <sub>2</sub> O <sub>3</sub> on TiO <sub>2</sub> has never been used for gas sensing
	In-situ fabrication	1-D TiO <sub>2</sub> nanostructures are produced separately and then electrodes are connected with the nanostructures	No in-situ fabrication process is reported using 1-D TiO <sub>2</sub> nanostructures
Fabrication of the sensor	Effects of particle content in the sensor	-	No study
	Selectivity	Limited reported literature on selectivity	Study required considering a vast number of target gases
Sensing performance	-	Surface depletion model is widely used	The catalytic activity of TiO <sub>2</sub> is ignored in the reported studies. The alteration and deposition of other materials on TiO <sub>2</sub> during gas sensing is ignored
Sensing Mechanism	-	-	-

## CHAPTER 3: METHODOLOGY

### 3.1 Raw Materials

Ti and Ti-6Al-4V (Ti64) particles were purchased from Powder Alloy Corporation, USA. Ti64 sheet was bought from GoodFellow Cambridge Limited, England. The  $\text{Al}_2\text{O}_3$  nanoparticles were purchased from Sigma-Aldrich (product ID: 544833-50G). Au interdigitated alumina substrates having dimensions of 5 mm x 5 mm were ordered from Case Western Reserve University, USA. The stereoscopic top view of the Au interdigitated alumina substrate is shown in Figure 3.1.

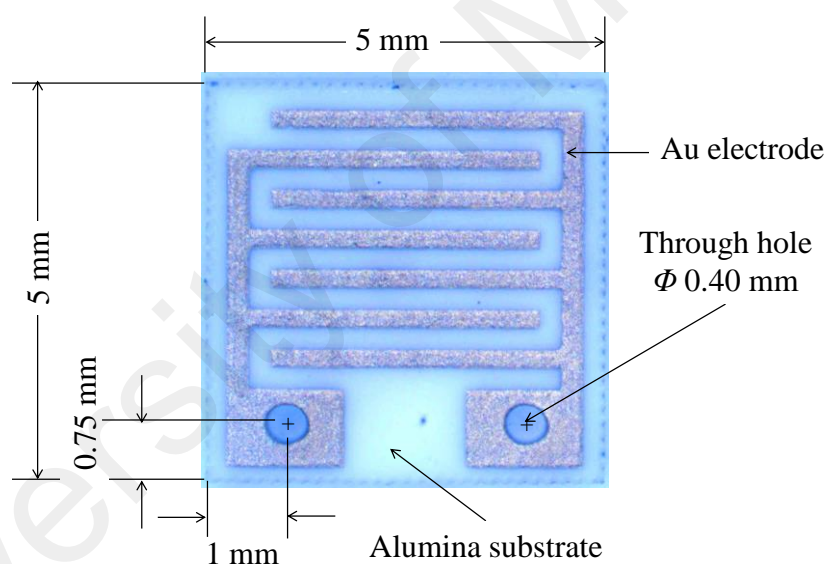


**Figure 3.1: Stereoscopic top view of the Au interdigitated alumina substrate and its dimensions.**

Au wire having diameter of 0.2 mm was purchased from Alfa Aesar, USA. The purity of the Au wire was 99.9%. Au paste was bought from Heraeus, USA. Chemicals and reagent used throughout the research was analytical grade and no further purification was conducted. Diethylene glycol dibutyl ether (DGDE),  $\alpha$ -terpineol, and ethyl cellulose were purchased from Sigma-Aldrich having product ID of 205621-100ML, 432628-50ML, and

200646-250G, respectively. Gas cylinders containing pure and mixed gases were purchased from Linde Malaysia Sdn Bhd.

### 3.2 Preparation of Substrates before Oxidation

#### 3.2.1 Heat Treatment of Particles

To investigate the effect of phase microstructures of the substrates on one dimensional (1-D) growth, Ti64 particles were heat treated in a horizontal tube furnace (Lindberg Blue M: TF55035COMA1). For this, approximately 5 gm of the particles were taken in a quartz boat and placed inside the quartz tube of the furnace. Before ramping up the furnace, the quartz tube was purged with (Ar + 5% H<sub>2</sub>) gas for 10 minutes. Then the furnace was heated to 1000 °C at a rate of 30 °C/min and soaked for 1 h in the flowing (Ar + 5% H<sub>2</sub>) environment. The flow rate of (Ar + 5% H<sub>2</sub>) was maintained at 20 sccm by using mass flow controller (MFC). After that the furnace was cooled in (Ar + 5% H<sub>2</sub>) environments at different rates. For one set of particles, the quartz tube were cooled in air (the particles remained inside the quartz tube in (Ar + 5% H<sub>2</sub>) environment) and referred to as “normalized” particles. For another set of particles, the quartz tube was cooled very slowly (cooling rate was 1 °C/min) inside the furnace in (Ar + 5% H<sub>2</sub>) environment and referred to as “annealed” particles. The heat treatment cycle of the particles is shown in Figure 3.2.

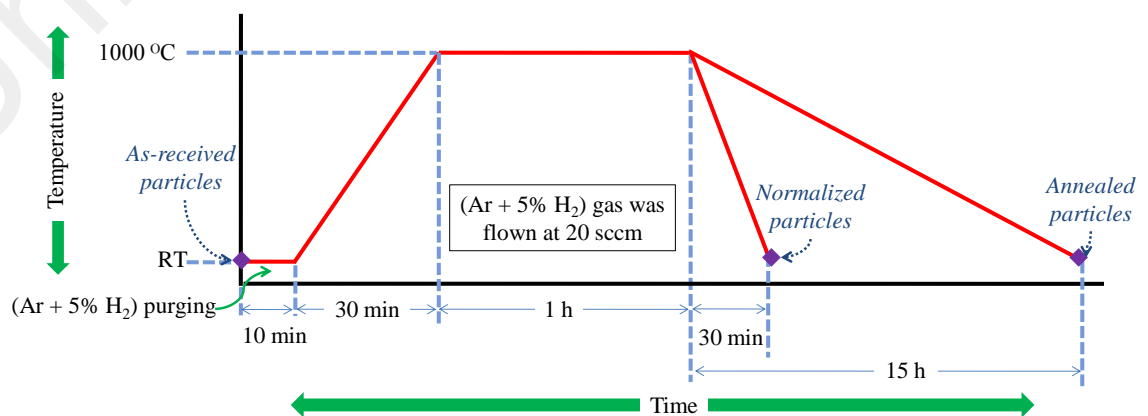


**Figure 3.2: Heat treatment cycle for the “normalized” and “annealed” Ti and Ti64 particles.**

### **3.2.2 Milling of Particles**

To investigate the effect of residual stress in the particles on 1-D growth, the as-received Ti and Ti64 particles were milled in a planetary ball mill (Retsch: PM 400 - MA type). The particles were milled up to 30 h at 250 rpm in ambient environment. Twenty four ZrO<sub>2</sub> balls having diameter of 1 cm and weight of 3 gm were used in the milling process. The weight ratio between the ball and particles was 10:1.

### **3.2.3 Stress Relaxation of Milled Particles**

The residual stress inside the milled particles was relaxed by annealing at 1000 °C for 3 h in an atmosphere of (Ar + 5% H<sub>2</sub>). Approximately 5 gm of milled particles were taken in a quartz boat and placed inside the quartz tube of horizontal tube furnace. Before ramping, the quartz tube was purged with (Ar + 5% H<sub>2</sub>) gas for 10 minutes. Then the furnace was heated to 1000 °C at a rate of 30 °C/min and (Ar + 5% H<sub>2</sub>) was flown to the quartz tube at a rate of 20 sccm. The particles were heated for 3 h and the quartz tube was cooled at a rate of 1 °C/min inside the furnace in (Ar + 5% H<sub>2</sub>) atmosphere.

### **3.2.4 Cleaning of Particles and Sheets**

During heat treatments and milling process the Ti and Ti64 particles might be contaminated with oxides. The Ti64 sheets might have native oxides at the surface. To avoid any contamination by oxides the particles and sheets were cleaned in 30 vol.% HCl for 30 min before thermal oxidation. After that, the particles were cleaned in distilled water for several times.

### **3.2.5 Preparation of Ink for Dispersing the Particles**

An ink was formulated to disperse the particles on the substrate for the subsequent growth of one dimensional (1-D) nanostructures by thermal oxidation process. For this,

$\alpha$ -terpineol (Sigma-Aldrich) and diethylene glycol dibutyl ether (DGDE: Sigma-Aldrich) were mixed at a ratio of 1:1 at room temperature. After that 8 wt% of ethyl cellulose (Sigma-Aldrich) was added to the solution. To dissolve ethyl cellulose, the solution was heated at 200 °C for 2 hours. Then the ink was loaded with the particles up to 20 wt%. The composite ink was ultrasonicated for 1 hour to disperse the particles. Then the composite ink was stored in dry cabinet for the use in future.

### 3.3 Experimental Setup for Thermal Oxidation and Growth Parameters

#### 3.3.1 Design of the Experimental Setup

The schematic of the experimental setup for thermal oxidation is shown Figure 3.3. The oxidation of the particles and sheets was carried out inside the quartz tube placed inside the horizontal tube furnace (Lindberg Blue M: TF55035COMA1). The quartz tube had a flexible socket with an adjustable clamp through which samples can be placed inside the tube. The length and other dimensions of the quartz tube are given in Appendix A.

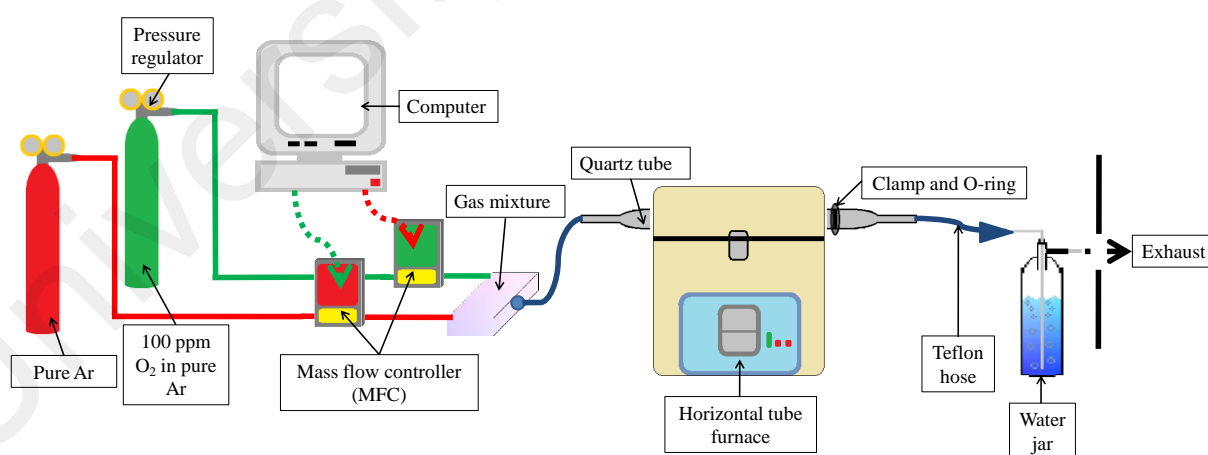


**Figure 3.3: The schematic of the experimental setup for the thermal oxidation process.**

The quartz tube was connected to the computer controlled MFCs (Sierra: C100L-CM-NR-2-0V1-SV1-PV2-V1) through a gas mixture. Two gas cylinders were connected with the MFCs through the pressure regulators where one cylinder contained pure Ar

(99.99999%) and another cylinder contained 105 ppm O<sub>2</sub> in Ar. The concentration of O<sub>2</sub> was diluted in the gas mixture by adjusting the flow from two MFCs. After that the diluted gas was flown into the quartz tube inside the horizontal tube furnace. At the downstream, the gases were passed through a water jar and finally exhausted outside.

The total flow rate ( $F$ ) of the mixed gases was varied from 20 sccm to 500 sccm. The concentration of O<sub>2</sub> inside the quartz tube was varied from 5 ppm to 105 ppm. To obtain this, the flows from the two cylinders are adjusted. The flow rate for the MFC which was connected with the cylinder containing 105 ppm O<sub>2</sub> in Ar can be calculated for any concentration of target gas in the quartz tube as follows:

$$F_1 = \frac{F}{C_1} \times \chi \quad (3.1)$$

Here,  $F_1$  is the required flow rate in sccm for the MFC which was connected with the cylinder containing 105 ppm O<sub>2</sub> in Ar,  $F$  is the total flow rate in sccm,  $C_1$  is the concentration of O<sub>2</sub> in the cylinder in ppm and  $\chi$  is the targeted O<sub>2</sub> concentration inside the quartz tube in ppm.

The flow rate for the MFC connected with cylinder containing pure Ar can be calculated as follows:

$$F_2 = F - F_1 \quad (3.2)$$

As an example, for targeted 40 ppm O<sub>2</sub> in Ar inside the quartz tube in a total flow of 500 sccm, the flow rate  $F_1$  and  $F_2$  can be deduced:

$$F_1 = \frac{500}{105} \times 40 \text{ sccm} = 190.5 \text{ sccm}, \quad \text{and } F_2 = (500 - 190.5) \text{ sccm} = 309.5 \text{ sccm}.$$

### 3.3.2 Thermal Oxidation Process

Thermal oxidation of the particles and sheets were carried out under different conditions to investigate different aspects of 1-D growth. The experimentations to investigate the effect of different growth parameters are tabulated in Table 3.1. Effects of the alloying elements, oxidation temperature, alloy microstructures, oxidation environment, residual stress, and oxidation duration were investigated to optimize the 1-D growth. For this, about 3  $\mu\text{L}$  of the composite ink loaded with 20 wt% particles (as described in section 3.2.5) was taken by a micropipette and dropped on to alumina substrate. Then the substrate along with the particles in composite ink was placed inside the quartz tube of the horizontal tube furnace. The furnace was heated to the desired temperatures according to the profile shown in Figure 3.4. Pure Ar gas (99.99999%) was purged for 10 min into the quartz tube before ramping up the furnace. In all cases, the furnace was heated at the rate of 30  $^{\circ}\text{C}/\text{min}$  and kept at the oxidation temperature for 1 min to 24 h. Then the quartz tube of the furnace was cooled in air. The gas flow inside the quartz tube was kept constant throughout the cooling process.

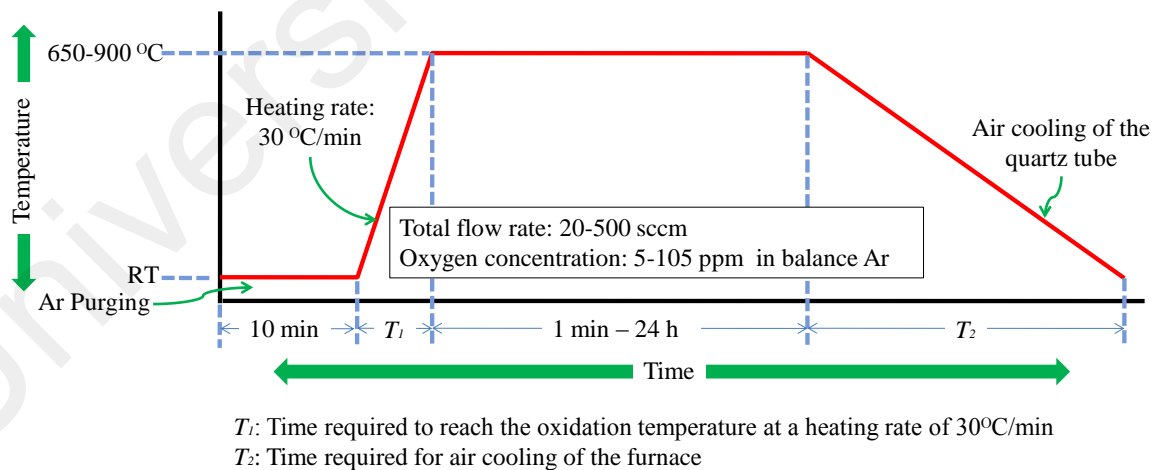


**Figure 3.4: Temperature profile of the horizontal tube furnace for thermal oxidation process.**

**Table 3.1: Experimental conditions of thermal oxidation of Ti and Ti64 substrates.**

Investigation	Particles	Oxidation temperature	Total flow rate of the gas	O <sub>2</sub> concentration	Oxidation time
Effect of temperatures	As-received Ti and Ti64 particles	650-900 °C	500 sccm dry flow	5 ppm for Ti and 40 ppm for Ti64 particles	4 h for Ti and 8 h for Ti64 particles
Effect of alloy microstructure	As-received Ti64 particles were heat treated at 1000 °C for 1 h followed by cooling at different rates	750 °C	500 sccm dry flow	15 ppm	4 h
Effects of oxidation environment	As-received Ti and Ti64 particles	750 °C	150 sccm for Ti and 500 sccm for Ti64 in dry and humid environment	5 ppm for Ti and 15 ppm for Ti64	4 h
Effect of oxygen concentration	Ti particles milled for 20 h and as-received Ti64 particles	750 °C	20-300 sccm humid flow for Ti particles. 20-500 sccm dry flow for Ti64 particles	5-105 ppm	4 h
Effect of Milling/Stress	Milled Ti and Ti64 particles, heat treated Ti64 particles and Ti64 sheet	750 °C	150 sccm for Ti particles. 500 sccm for Ti64 particles and sheet	5 ppm O <sub>2</sub> in humid Ar for Ti particles. 15-40 sccm O <sub>2</sub> in dry Ar for Ti64 particles and sheet	4 h for Ti particles. 4-8 h for Ti64 particles and sheet
Effect of oxidation time	As-received and milled Ti64 particles	750 °C	500 sccm dry flow	15 ppm	1 min - 24 h

### 3.4 Experimental Setup for Gas Sensing and Sensing Parameters

#### 3.4.1 Design for Experimental Setup

A similar setup described in section 3.3.1 was used for gas sensing experimentations. However, some small modifications were performed in the experimental setup for gas sensing. The schematic experimental setup for gas sensing is shown in Figure 3.5. In this case, the oxide nanostructures on Au interdigitated substrate (sensor) were placed inside the quartz tube. The sensor was connected to a data acquisition system (DAQ: Agilent 34972A) using Au wire (Alfa Aesar, 0.2 mm). Au paste (Heraeus) was applied to the sensor-wire junction and cured at 650 °C for 1 h in Ar environment (500 sccm).

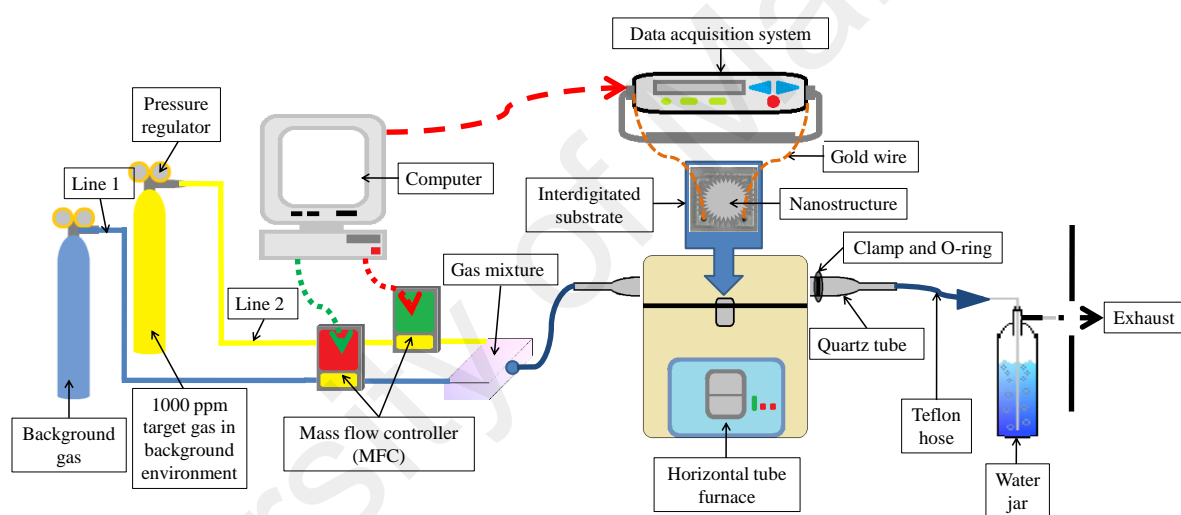


**Figure 3.5: The schematic of the experimental setup for the gas sensing experimentation.**

For the gas sensing experiments, two gas cylinders were utilized. One of the cylinders contained the background gas ( $N_2$  or air) and another cylinder contained 1000 ppm of target gas in background environment. The cylinders were connected to the computer controlled MFCs (Sierra: C100L-CM-NR-2-0V1-SV1-PV2-V1) through pressure regulators. The flow from the different cylinders was controlled by MFCs to dilute the concentration of the target gas in similar principle mentioned in section 3.3.1. Gas flow from the MFCs were mixed inside the gas mixture and sent to the quartz tube placed

inside the horizontal tube furnace. The gases encountered with the sensor inside the quartz tube. Finally, the gas was exhausted outside from the quartz tube through a water jar.

Before starting sensing experiments, the quartz tube was purged with the background gas for 10 min. The furnace was heated to the sensing temperature at a heating rate of 30 °C/min in background environment. After reaching the sensing temperature, the sensor was kept in the background environment for 10 min and the resistance ( $R_o$ ) of the sensor was monitored by DAQ system. Then the sensor encountered different concentration of target gases in background environment for 30 min and the resistance ( $R_g$ ) of the sensor was monitored. Finally, the background environment was introduced to the quartz tube to recover the initial resistance of the sensor.

In the gas sensing experiments, the target gases included reducing hydrogen ( $H_2$ ), hydrogen sulfide ( $H_2S$ ), carbon monoxide (CO), methane ( $CH_4$ ), methanol ( $CH_3OH$ ), ethanol ( $C_2H_5OH$ ), and ethylene ( $C_2H_4$ ) and oxidizing gases of nitrogen dioxide ( $NO_2$ ) and oxygen ( $O_2$ ). In all cases,  $N_2$  was used as background gas except for  $NO_2$ , where air was used as background gas due to stability issues.

### **3.4.2 Gas Sensing Parameters**

During sensing different parameters were investigated such as response, selectivity, operating temperature, effects of target gas concentration, response and recovery time. The details of these experiments are discussed in the following sections.

#### **3.4.2.1 Measurement of Response**

The response of the sensor towards reducing gases is defined as the ratio of the resistance when exposed to background and target gas environments. On the other hand, the response towards oxidizing gases is defined as the ratio of the resistance when

exposed to target gas and background environment. The response of the sensor is calculated by the following equations:

$$\text{For reducing environments; } S = R_o/R_g \quad (3.3)$$

$$\text{For oxidizing environments; } S = R_g/R_o \quad (3.4)$$

Where,  $R_o$  and  $R_g$  are the resistances of the sensor in background gas and in presence of target gas, respectively, and  $S$  is the response of the sensor.

#### **3.4.2.2 Selectivity of Sensor**

The sensor responses were measured towards 1000 ppm of different target gases at 650 °C. The selectivity of the sensor was identified from the response values which showed significantly higher value compared with the responses towards other gases.

#### **3.4.2.3 Optimum Operating Temperatures**

The response of the sensors was measured towards different target gases at the operating temperatures ranging from 100 to 650 °C. The operating temperature at which highest response was achieved is designated as optimum operating temperature of the sensor.

#### **3.4.2.4 Effect of Concentration of Target Gases**

The response of the sensors was evaluated towards different concentrations of target gases at the optimum operating temperatures. For this, the concentrations of target gases were varied from 20 ppm to 1000 ppm in background environment. To achieve this, the flow from different cylinders was adjusted by equation 3.1 and 3.2.

### **3.4.2.5 Response Time and Recovery Time**

The response time ( $T_{res}$ ) and recovery time ( $T_{rec}$ ) of the sensor are defined as the time to reach 90% of the total resistance change in case of gas exposure and removal of the target gases, respectively. From the response curves the  $T_{res}$  and  $T_{rec}$  for different gases were measured at the optimum operating temperature.

## **3.5 Characterizations of Samples**

During thermal oxidation and gas sensing the samples were characterized at different stages of the experiments. In the following sections the characterization procedure of the samples are discussed.

### **3.5.1 Characterizations before Oxidation**

#### **3.5.1.1 Measurement of Particle Size**

The size of the Ti and Ti64 particles before and after milling was measured from the field emission scanning electron microscope (FESEM: Zeiss Ultra-60) images. For this, small amount of particles were taken on double stick conductive carbon tape attached with the FESEM sample holder. The particles were observed at various locations at low magnifications by using SE2 detector. Due to the irregular shape of the particles, the length of the particles was measured at two perpendicular directions and averaged. At least, the size of 300 particles was measured and the average is reported to present the particle size for a particular condition.

#### **3.5.1.2 Determination of Oxidation Temperature**

To determine the oxidation temperatures of Ti and Ti64 particles, thermogravimetric analysis (TGA: Mettler DSC 820, Switzerland) were carried. For this, small amount of particles (<20 mg) were placed on a 70  $\mu$ L platinum crucible inside the differential

scanning calorimetry (DSC) furnace. Then the furnace was heated to 1000 °C at a heating rate of 10 °C/min in ambient and N<sub>2</sub> environment (flow rate of N<sub>2</sub> was 200 sccm).

### **3.5.1.3 Observation of Phases Microstructures**

For the observation of different phases inside the as-received and heat treated particles, the particles were mounted in epoxy and polished using standard metallographic techniques until 0.02 μm finishes. The polished particles were etched for 15 s by using Kroll's reagent having 6 vol.% HNO<sub>3</sub> and 2 vol.% HF in distilled water. Then the particles were observed under optical microscope (Meiji Techno, Model: MT7530, Japan) and field emission scanning electron microscope (FESEM: FEI Quanta FEG 450) equipped with energy dispersive X-ray spectroscopy (EDX: Oxford instruments).

### **3.5.1.4 Determination of Phase Content**

The phase content of the as-received, heat-treated, and milled Ti and Ti64 particles and sheets were determined using X-ray diffractometer (XRD: PANalytical Empyrean). For this, CuK<sub>α</sub> radiation having wavelength of 0.1540598 nm was used at 40 KV and 40 mA. The samples were scanned in Bragg angle ( $2\theta$ ) of 30° to 90°.

### **3.5.1.5 Measurement of Residual Stress**

The residual stress in Ti and Ti64 particles was determined by using X-ray diffractometer (XRD: PANalytical Empyrean) using CuK<sub>α</sub> radiation (0.1540598 nm) at 40 KV and 40 mA. The as-received, milled and relaxed particles were used to determine the residual stress. XRD-sin<sup>2</sup>ψ technique was employed at different tilt angles (ψ) ranging from 0-40° for measuring the residual stress (Cullity & Stock, 2001; Fitzpatrick et al., 2005; Hauk, 1982). The incident X-ray beam was introduced through a window having a width of 0.5 inch, 0.125° divergence slit and 0.0625° anti-scattering slit, to hit the sample

surface at a fixed incident angle of  $\Omega$ . A computer controlled Omega-goniometer was used for the  $\psi$  tilt of the samples. As a criterion for determining the residual stress, the selection of diffraction peak should have the following characteristics (Luo & Jones, 2010; X. Zheng, Li, & Zhou, 2004):

01. The diffraction peak should be higher in Bragg angle ( $2\theta$ ), typically more than  $130^\circ$ .
02. The selected diffraction peak should not overlap with other peaks.
03. The diffraction peak should be single, well-shaped with high intensity.

It was recommended by Prev y *et al.* (Prev y, 1986) to scan the (2 1 3) crystallographic plane of Ti and Ti64 substrate for determining the residual stress. The (2 1 3) crystallographic plane appears at  $2\theta$  angle of  $139.5^\circ$  and  $141.7^\circ$  using  $\text{CuK}\alpha$  radiation for Ti and Ti64 substrates, respectively. For this reason, Ti particles were scanned from  $2\theta$  angle of  $136^\circ$  to  $142^\circ$  at different tilt angles ( $\psi$ ). On the other hand, the as-received and milled Ti64 particles were not scanned at  $2\theta$  angle of  $141.7^\circ$  due to absent of any significant, well-shaped and single peak. The as-received and milled Ti64 particles were scanned in  $2\theta$  region from  $70\text{-}73^\circ$  for the (1 0 3) crystallographic plane. Again, the relaxed Ti64 particles were scanned in the  $2\theta$  region from  $140\text{-}146^\circ$  for the (2 1 3) crystallographic plane at different tilt angles ( $\psi$ ). The residual stress inside the particles is calculated by the following formula (Cullity & Stock, 2001; Fitzpatrick et al., 2005; Hauk, 1982):

$$\sigma = \frac{E}{1+\nu} \cdot m \quad (3.5)$$

Where,  $\sigma$  is the residual stress,  $E$  is Young modulus,  $\nu$  is Poison ratio and  $m$  is the slope of the  $d\text{-}\sin^2\psi$  curve. The average value of the elastic constant  $[E/(1+\nu)]$  for (2 1 3) crystallographic plane is reported to be 90.3 and 84.1 GPa for commercial Ti and Ti64 substrates, respectively (Prev y, 1986). However, the value of the elastic constant  $[E/(1+$

$\nu$ ] for the (1 0 3) crystallographic plane is not reported, so assumptions are applied for as-received and milled Ti64 particles. The average value of Young's modulus ( $E$ ) and Poisson ratio ( $\nu$ ) for Ti64 alloy is used in the present case which is 115 GPa and 0.31, respectively. The experimental details of measurement of residual stress is summarized in Table 3.2.

**Table 3.2: Experimental details for measuring of the residual stress of as-received, milled and relaxed Ti and Ti64 particles.**

Particles	Scanned crystallographic plane	Scanned $2\theta$ angle	Tilt angles ( $\psi$ )	Elastic constant $[E/(1+\nu)]$ (GPa)
As-received and milled Ti particles	(2 1 3)	136-142°		90.3
As-received and milled Ti64 particles	(1 0 3)	70-73°	0-40°	87.8
Relaxed Ti64 particles after milling	(2 1 3)	140-146°		84.1

### 3.5.2 Characterizations after Oxidation

#### 3.5.2.1 Determination of Phase Content

The phase content of the oxidized Ti and Ti64 particles were determined using X-ray diffractometer (XRD: PANalytical Empyrean).  $\text{CuK}\alpha$  radiation having wavelength of 0.1540598 nm was used for this purpose at 40 KV and 40 mA. The Ti particles were scanned in Bragg angle ( $2\theta$ ) of 30° to 80° whereas Ti64 particles were scanned in Bragg angle ( $2\theta$ ) of 25° to 85°.

#### 3.5.2.2 Determination of Oxidation States

The oxidation states of oxidized Ti and Ti64 were determined by X-ray photoelectron spectroscopy (XPS: ULVAC-PHI Quantera II). For this, Ti and Ti64 sheets were cut having dimensions of 15 mm x 15 mm x 1 mm and polished using standard

metallographic techniques until 0.02  $\mu\text{m}$  finishes followed by cleaning. Then the sheets were oxidized under optimum conditions for the growth of 1-D nanostructures. The oxidized sheets were characterized under XPS to identify the oxidation states of Ti and Ti64. To obtain this, monochromatic  $\text{AlK}_\alpha$  radiation (1486.6 eV) was used with the instrument base pressure of  $3 \times 10^{-7}$  Pa operated at 25.6 W. The diameter of the beam was 100  $\mu\text{m}$ . The electron flood gun and mono-atomic Ar ion gun was used as charge neutralizer. The wide scan analysis was performed using pass energy of 280 eV with 1 eV per step. The narrow scan (chemical states analysis) was performed using pass energy of 112 eV with 0.1 eV per step. The Multipak Spectrum: ESCA software was used for the analysis the XPS data.

### **3.5.2.3 Surface Morphologies and Elemental Analysis**

The surface morphology of the oxidized particles and sheets were observed under FESEM (Zeiss Ultra-60 and FEI Quanta FEG 450) equipped with energy dispersive X-ray (EDX: EDAX-Genesis Utilities and Oxford instruments) spectroscopy at various stages of experiments. The SE, SE2 and InLens detectors were utilized for the best visualization of the surface morphology. The EDX spectroscopy spot analysis and line scanning were carried out to determine the compositions of the samples.

### **3.5.2.4 Oxide Scales beneath 1-D Nanostructures**

After thermal oxidation of Ti64 particles, some selected samples were mounted in epoxy and polished using standard metallographic techniques until 0.02  $\mu\text{m}$  finishes. The cross sectional view of the oxidized samples was observed under conventional scanning electron microscope (SEM: Hitachi S3400N). The elemental composition of the oxide scales were determined by energy dispersive X-ray (EDX: Horiba EMAX) spectroscopy spot analysis and elemental mapping.

### 3.5.2.5 Epitaxy between Substrate Orientation and 1-D Growth

The Ti64 sheets were annealed at 1000 °C in (Ar + 5% H<sub>2</sub>) environment by the heat treatment profile shown in Figure 3.2 to obtain coarse grains. Then the sheet was polished by standard metallographic techniques until 0.02 μm finishes and etched for 15 s using Kroll's reagent (6 vol.% HNO<sub>3</sub> + 2 vol.% HF + balance distilled water). The electron backscattered diffraction (EBSD: EDAX - Hikari XP EBSD Camera) equipped with TEAM Pegasus-integrated EDS and EBSD software was utilized for orientation mapping on selected area to identify the grain orientations of Ti64 sheet. The OIM analysis software was used for cleanup and some post processing of the EBSD mapping. After mapping, the sheet was oxidized under optimum conditions for 1 min and observed under FESEM at the similar location to identify the epitaxy between the substrates and 1-D nanostructures.

### 3.5.2.6 Characterization of 1-D Nanostructures

The 1-D nanostructures on oxidized particles were characterized by transmission electron microscope (TEM: FEI Tecnai F-20) at various stages of the experiments. For this, a small amount of oxidized particles were taken in a small bottle followed by the addition of 2.5 ml ethanol. Then the suspension was ultrasonicated for 2 min to scale off the 1-D nanostructures from the particles. Then a tiny amount of the suspension was dropped on a carbon coated Cu grid by using a micro pipette followed by drying at 100 °C for 10 min. Then the Cu grid was placed on the sample holder for imaging and high resolution transmission electron microscope (HRTEM) observation. Scanning transmission electron microscope (STEM) equipped with energy dispersive X-ray (EDX) spectroscopy was utilized for line scanning of the 1-D nanostructures. The selected area diffraction (SAD) was performed to confirm the phase structure and growth direction of the 1-D nanostructures.

### **3.5.3 Characterizations of Sensors**

#### **3.5.3.1 Physical and Structural Observation of Sensors**

The as-prepared sensors were observed at low magnifications under stereoscope (Olympus SZX10) to observe the distribution of oxidized particles on the substrates and connectivity with the electrodes. Images of the sensors were taken using DSLR camera (Nikon D3100) at different stages during gas sensing experiments. The oxide nanostructures were observed under FESEM (FEI Quanta FEG 450) before and after recovery and compared with the as-prepared sensors. Some selected oxide nanostructures were also observed under TEM (FEI Tecnai F-20). EDX analysis was performed on the oxide nanostructures at different stages.

#### **3.5.3.2 Resistance Measurements of Sensors**

To optimize the sensor fabrication process, the resistance of the sensors was measured by the data acquisition (DAQ: Agilent 34972A) system at room temperature, at 450 °C and 650 °C in N<sub>2</sub> environment. For this, the sensors were placed inside the quartz tube of horizontal tube furnace and connected with the DAQ system. The furnace was heated to the desired temperatures while N<sub>2</sub> was flown at a rate of 500 sccm. The resistance of the sensors in background and target gas environments was also measured by the DAQ system as described in section 3.4.2.1.

#### **3.5.3.3 Compositional Characterization of Sensors**

The sensors were characterized by Raman spectroscope (Renishaw inVia Raman microscope) before and after recovery from the target gases. The results are compared with the as-prepared sensors. For this, the samples were scanned at room temperatures from 100 to 2000 cm<sup>-1</sup> wavelengths having spectral resolution of 1.3 cm<sup>-1</sup>. Green laser source having wavelength of 532 nm was used to excite the samples.

## CHAPTER 4: RESULTS AND DISCUSSION

This chapter contains three major parts: (1) growth of one dimensional (1-D) nanostructures on Ti particles, (2) growth of 1-D nanostructures on Ti-6Al-4V (Ti64) particles and sheets and (3) gas sensing using 1-D nanostructures. In the first section, the process of thermal oxidation for the growth of 1-D nanostructures on Ti substrates is optimized and the as-grown nanostructures are characterized. In the second section, the thermal oxidation process for the growth of 1-D nanostructures on Ti64 particles and sheets are optimized followed by characterizations. Finally, in the third section, the 1-D nanostructures grown on Ti and Ti64 particles are utilized for gas sensing applications.

### 4.1 Growth of 1-D Nanostructures on Ti Particles

The first approach of this investigation is to optimize the growth of 1-D nanostructures on Ti particles. The as-grown oxide nanostructures are characterized by different techniques. Based on the findings a model is proposed for the growth of 1-D nanostructures on Ti substrates during thermal oxidation.

#### 4.1.1 Characterization of As-received Ti Particles

Figure 4.1(a-b) shows the FESEM image and EDX spectrum of the as-received Ti particles. It is seen from the FESEM image that the as-received Ti particles has irregular shape. The average size of the as-received Ti particles was calculated from the FESEM images. About 300 particles were used to calculate the average size of the particles. The average size of the as-received Ti particles is found to be 135  $\mu\text{m}$ . In the EDX spectroscopy spot analysis Ti peaks are observed with a small peak of C (Figure 4.1(b)).

Conductive carbon tape was used to stick the particles with the FESEM sample holder and C peak is obtained from there.

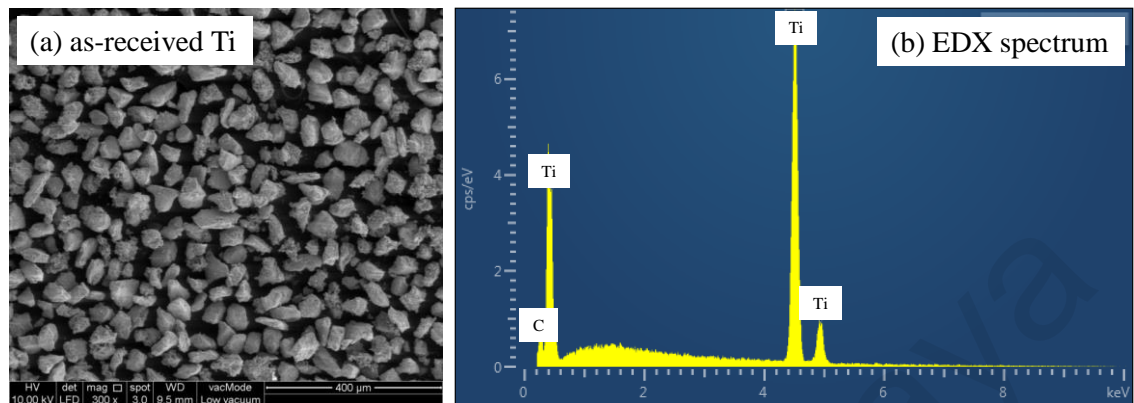


**Figure 4.1: (a) FESEM image of the as-received Ti particles, (b) EDX spectrum from the spot analysis of as-received Ti particles.**

Figure 4.2 shows the XRD peaks of the as-received Ti particles. Peaks from  $\alpha$ -Ti phase (hexagonal) are revealed in the XRD analysis. No peak is attributed to  $\beta$ -Ti (body centered cubic) as seen in the XRD pattern shown in Figure 4.2. In addition, no peak belonging to the oxides of Ti or any contamination is observed.

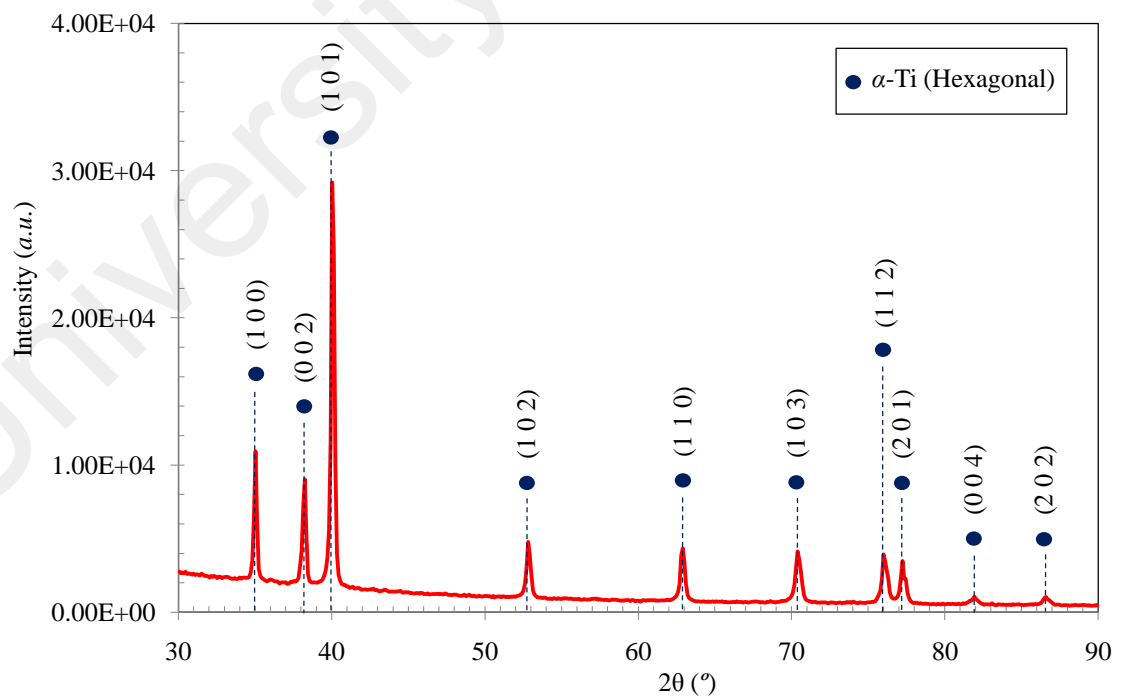


**Figure 4.2: XRD peaks of the as-received Ti particles.**

So, from the above observations it is concluded that the as-received Ti particles has irregular shape with an average size of 135  $\mu\text{m}$ . The as-received particles consist of only  $\alpha$ -Ti phase (hexagonal).

#### **4.1.2 Thermal Oxidation of Ti Particles**

To optimize the growth of 1-D nanostructures on Ti particles, the effects of various parameters such as oxidation temperatures, oxidation environments, residual stress, and oxygen partial pressure during oxidation were investigated. In the following sections the effects of these parameters during oxidation of Ti particles is presented.

##### **4.1.2.1 Effects of Oxidation Temperature**

###### **(a) *Determination of oxidation temperature***

Thermo-gravimetric analysis (TGA) was carried on as-received Ti particles to identify the oxidation temperature. It is seen from Figure 4.3 that Ti particles do not undergo oxidation until the temperature reaches 650  $^{\circ}\text{C}$  in ambient and  $\text{N}_2$  environments. Below this temperature, a slight decrease in mass is observed for ambient oxidation which might be due to the decomposition of any volatile compound present and removal of  $\text{H}_2\text{O}$ . Above the temperatures of 650  $^{\circ}\text{C}$ , Ti particles show a parabolic increase of mass in ambient and  $\text{N}_2$ . Similar, phenomenon of parabolic increase of mass was also observed during air oxidation of commercial Ti sheets (Song, Han, Jeong, Lee, & Park, 2014). So, from the above observations, it is concluded that the oxidation of Ti particles starts at 650  $^{\circ}\text{C}$ . Further oxidation experiments for the growth of 1-D nanostructures were therefore conducted at temperatures of 650  $^{\circ}\text{C}$  and above.

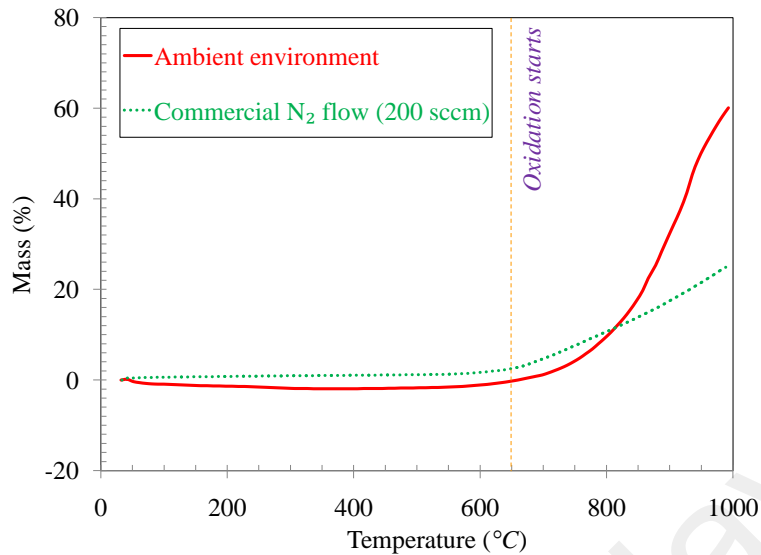


**Figure 4.3: TGA analysis of as-received Ti particles in ambient environment and commercial N<sub>2</sub> flow at 200 sccm.**

In the literature, information on the optimum temperature for 1-D growth during oxidation of Ti substrates is ambiguous. Different studies reported that the optimum oxidation temperature for 1-D growth on Ti substrates is between 700 to 850 °C (Huo et al., 2009; Kaewsai et al., 2010; Xinsheng Peng & Chen, 2004; Xinsheng Peng et al., 2005). The difference in oxidation temperatures might be attributed from the variations of impurities in commercial substrates and difference in experimental procedures.

**(b) Oxidation of Ti particles at different temperatures**

Oxidation of as-received Ti particles was carried out at different temperatures ranging from 650-900 °C. From different studies it is observed that the oxidation of Ti requires minute amount of oxygen for 1-D growth (Xinsheng Peng & Chen, 2004; Xinsheng Peng et al., 2005). For this reason, the oxidation environment contains 5 ppm of O<sub>2</sub> in flowing Ar at a rate of 150 sccm. The FESEM images of the Ti particles oxidized at different temperatures are shown in Figure 4.4.

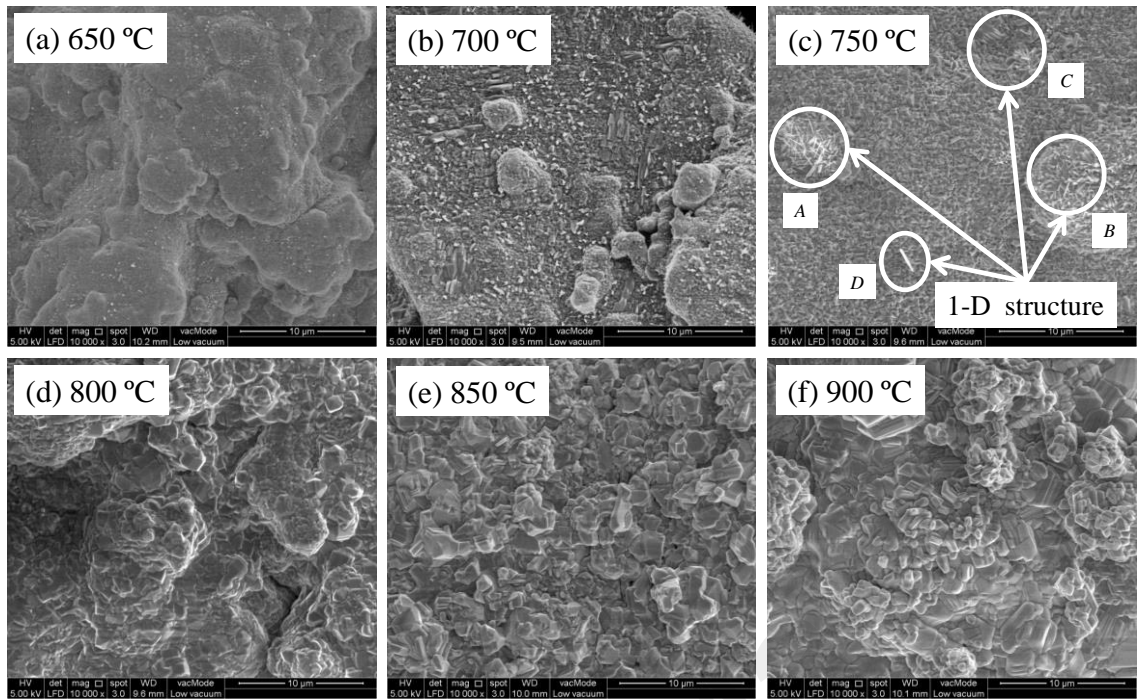


**Figure 4.4: FESEM images of thermally oxidized Ti particles in the presence of 5 ppm O<sub>2</sub> in flowing Ar (150 sccm) at different temperatures (a) 650 °C, (b) 700 °C, (c) 750 °C, (d) 800 °C, (e) 850 °C and (f) 900 °C.**

No 1-D nanostructure is observed at low oxidation temperatures of 650-700 °C as seen in Figure 4.4(a-b). At 750 °C, some 1-D nanostructures are observed which are encircled by white circles (Figure 4.4(c)). However, these 1-D structures are discretely located and their coverage is very low. Magnified images at different locations having 1-D appearance in Figure 4.4(c) are shown Figure 4.5. It appears from Figure 4.5 that the 1-D nanostructures are short having a length of about 500 nm with no entanglement (Figure 4.5(a-d)). Further increase of temperature to 800-900 °C results in oxide scale instead of 1-D nanostructure as seen Figure 4.4(d-f). So, it is concluded that the optimum oxidation temperatures for the growth of 1-D nanostructures on Ti particles under the present experimental condition is 750 °C. Further optimizations of 1-D growth on Ti particles are carried out at 750 °C.

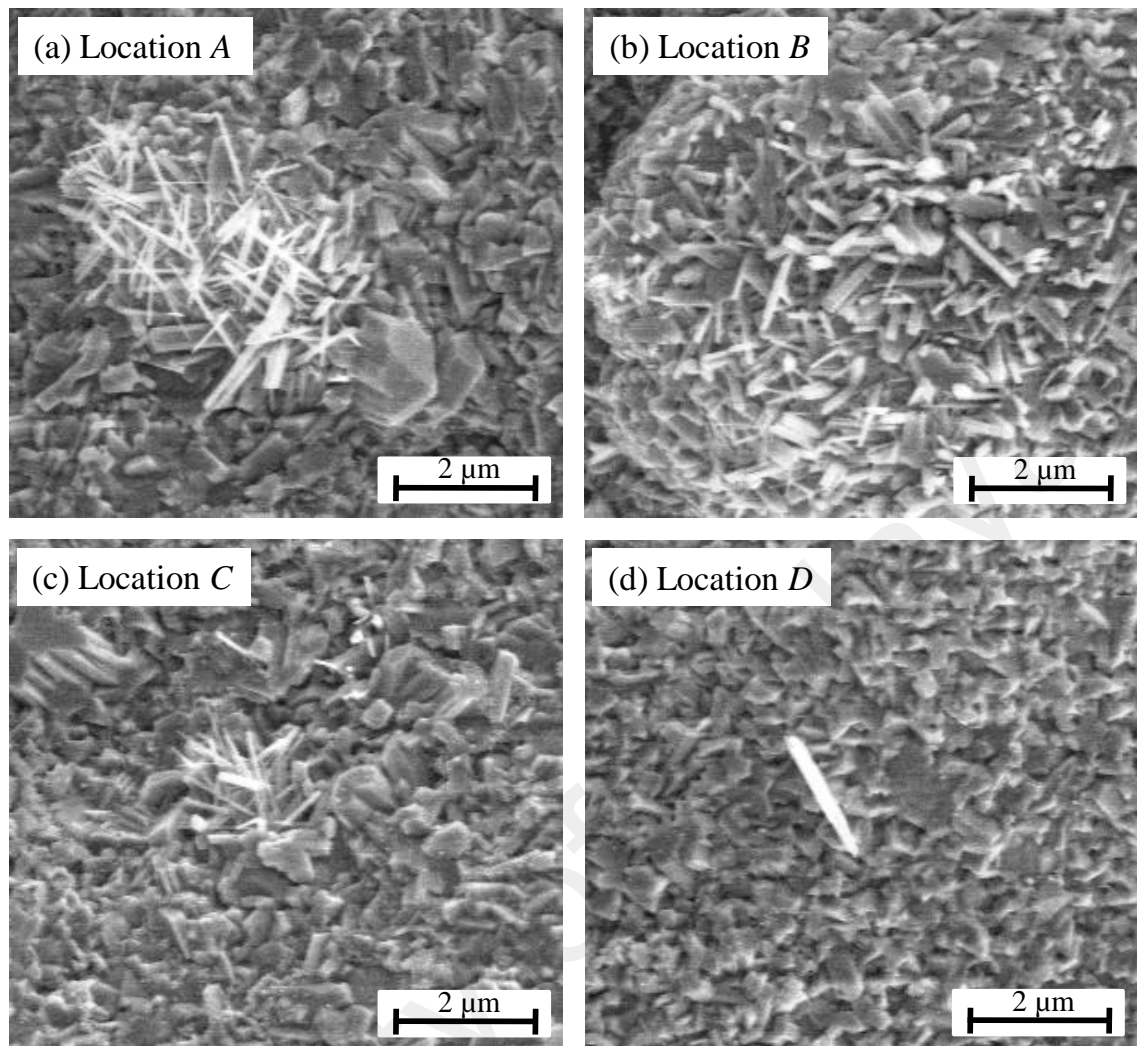


**Figure 4.5: Magnified views thermally oxidized Ti particles in presence of 5 ppm O<sub>2</sub> in flowing Ar (150 sccm) at 750 °C at different locations shown in Figure 4.4(c): (a) location A, (b) location B, (c) location C and (d) location D.**

#### 4.1.2.2 Effects of Oxidation Environment

The feasibility of 1-D growth on Ti particles during oxidation was investigated in dry and humid oxygen. For dry oxidation, the experimental setup shown in Figure 3.3 was used. For humid oxidation, similar experimental setup was used but a water jar filled with 300 ml of distilled water was placed in between gas mixture and quartz tube. The oxidation was carried out at 150 sccm flow rate and the results from dry and humid oxidation are compared.

The FESEM images of Ti particles oxidized for 4 h at 750 °C in dry and humid environment containing 5 ppm of O<sub>2</sub> in Ar at a flow rate of 150 sccm are shown in Figure

4.6. The growth of 1-D nanostructures is not evident during dry oxidation; it is only seen in discrete locations (Figure 4.6(a)). However, humid oxidation results in the growth of entangled 1-D nanostructures as seen in Figure 4.6(b). The length of the nanostructures is about 10  $\mu\text{m}$ . The coverage density of the entangled nanostructures is found to be about  $1.27 \times 10^{10}$  1-D  $\text{m}^{-2}$  during humid oxidation.

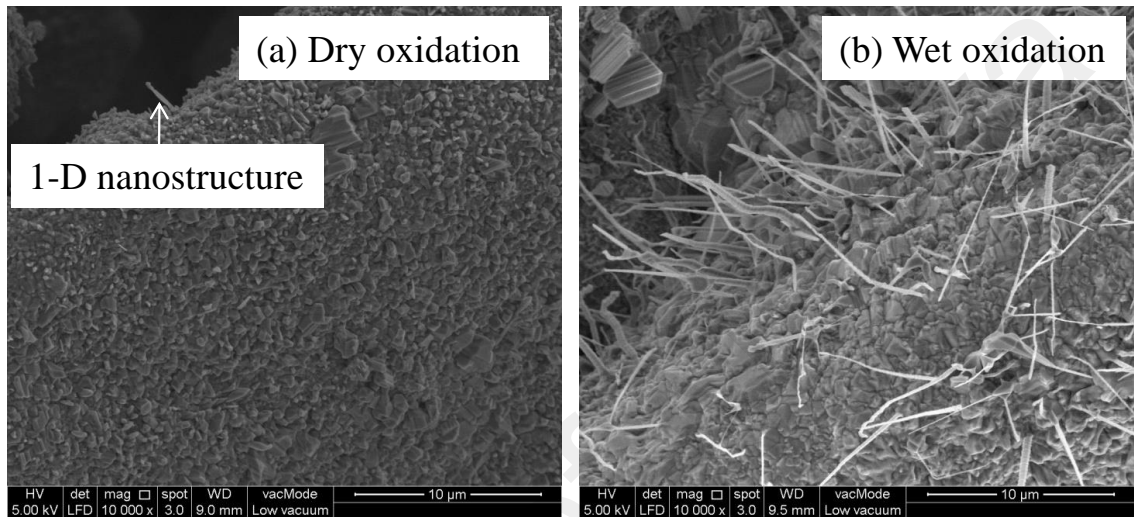


**Figure 4.6: FESEM images of Ti particles after oxidation for 4 h at 750 °C in atmosphere containing 5 ppm of O<sub>2</sub> in Ar at a flow rate of 150 sccm in (a) dry oxidation and (b) humid oxidation conditions.**

It is reported in the literatures that high concentration of O<sub>2</sub> forms oxide scale instead of 1-D nanostructures during the oxidation of Ti substrates (Xinsheng Peng & Chen, 2004; Xinsheng Peng et al., 2005). Peng *et al.* (Xinsheng Peng & Chen, 2004; Xinsheng Peng et al., 2005) showed that presence of 99% O<sub>2</sub> during oxidation of Ti substrate produced polycrystalline films of TiO<sub>2</sub>. Similar results were obtained when formic acid (HCOOH) was used as the oxidation medium (Xinsheng Peng et al., 2005). Decrease of the O<sub>2</sub> content in a mixture of Ar (1 sccm flow of O<sub>2</sub> in 200 sccm flow of Ar) resulted in 1-D nanostructures with low coverage (Xinsheng Peng & Chen, 2004). Further decrease of the oxygen content by using oxygen containing species such as acetone (CH<sub>3</sub>COCH<sub>3</sub>), ethanol (C<sub>2</sub>H<sub>5</sub>OH), acetaldehyde (CH<sub>3</sub>CHO) and dibutyltin dilaurate (C<sub>32</sub>H<sub>64</sub>O<sub>4</sub>Sn) vapor in Ar resulted in higher coverage of 1-D nanostructures (Xinsheng Peng & Chen, 2004;

X Peng & Chen, 2005; Xinsheng Peng et al., 2005). Similar phenomenon is also observed in the present case where it is found that the presence of H<sub>2</sub>O in low oxygen environment significantly improves the length and coverage of 1-D nanostructures compared with the dry oxidation. The coverage of 1-D nanostructure is insignificant in dry oxidation. So, it is assumed that the oxidation kinetics is different in dry and humid environments. Pérez *et al.* (Pérez, 2007) investigated the oxidation behavior of Ti in presence of dry and humid air. It was found that multilayered oxide scale is developed at the initial stage of oxidation in presence of humid air. Based on the findings of Galerie *et al.* (Galerie, Wouters, & Petit, 1997), the water molecules dissociate to hydroxide ion (OH<sup>-</sup>) during humid oxidation of Ti. The titanium ions diffuse to outer surface through diffusion via interstitial sites (Stringer, 1960; Taniguchi et al., 2001) and react with surface adsorbed water molecule to form outer oxide layer (Göbel, Sunderkötter, Mircea, Jenett, & Stroosnijder, 2000). The oxygen ions also diffuse inward via vacancy sites to form inner oxide layer (Stringer, 1960; Taniguchi et al., 2001). As a result, multiple oxide layers are formed during humid oxidation of Ti substrates and promotes the densification of the innermost oxide layer (Pérez, 2007).

Formation of multilayer oxide scale is also seen during oxidation of Cu (Hansen et al., 2008; Yuan, Wang, Mema, & Zhou, 2011) and Fe (Cai et al., 2012) substrates for 1-D growth. It was reported by Kumar *et al.* (Kumar, Srivastava, Tiwari, & Nandedkar, 2004) that during oxidation of Cu substrates, CuO and Cu<sub>2</sub>O layer are formed beneath the 1-D nanostructures. It was assumed that stress is induced between the CuO and Cu<sub>2</sub>O layers due to the difference in crystallographic structures, molar volumes and densities. During oxidation of the substrate the surface induced stress is released by forming new surfaces such as 1-D CuO nanostructures.

In the present case, similar scenario is anticipated for the humid oxidation of Ti substrates. Due to the formation of multilayered oxide scales during humid oxidation, stress is induced among the oxide layers. As a result of stress accumulation, new surfaces are created in the form of entangled 1-D nanostructures to minimize the induced stress. In contrast with dry oxidation, only one oxide layer is formed due to inward diffusion of oxygen ion via vacancy sites (Stringer, 1960; Taniguchi et al., 2001). As a result, the induced stress is not high enough to create new 1-D surfaces during dry oxidation.

#### **4.1.2.3 Effects of Residual Stress on Oxidation**

During humid oxidation of Ti, multi layered oxides are formed (Galerie et al., 1997; G. Lu, Bernasek, & Schwartz, 2000; Pérez, 2007) and for this reason stress is induced among the oxide layers. It is proposed that induced stress play significant role for the 1-D growth. Similarly, it is anticipated that residual stress imposed by mechanical process might have significant effect on the 1-D growth on Ti particles. It was seen by the other researchers that residual stress imposed on Cu substrates by bending (Mema, Yuan, Du, Wang, & Zhou, 2011) and sand blasting (Yuan & Zhou, 2012) enhance the 1-D growth.

To investigate the effect of residual stress on 1-D growth, the Ti particles were milled in a planetary ball mill for 20 h. After milling the particles were characterized by FESEM, EDX and XRD. The residual stress inside the Ti particles was measured by XRD- $\sin^2\psi$  technique. Then the milled Ti particles were thermally oxidized under the optimum conditions of 750 °C containing 5 ppm O<sub>2</sub> in humid Ar at a flow rate of 150 sccm. Hereafter, the as-received and milled Ti particles will be denoted as Ti-0h and Ti-20h, respectively.

(a) *Characterization of milled particles*

The FESEM image of the milled Ti particles is shown in Figure 4.7(a). It is seen that after milling the particles have an irregular shape and the distribution of particle size varies widely ranging from 3 to 20  $\mu\text{m}$ . Comparing the FESEM image of the as-received Ti particles shown in Figure 4.1(a), it is seen that the average size of the particles is reduced from 135  $\mu\text{m}$  to 10  $\mu\text{m}$ . The EDX analysis of Ti-20h particles shows the presence of Ti with a small peak of C (Figure 4.7(b)). The peak of C is obtained from the carbon tape which was used to stick the particles on FESEM sample holder.

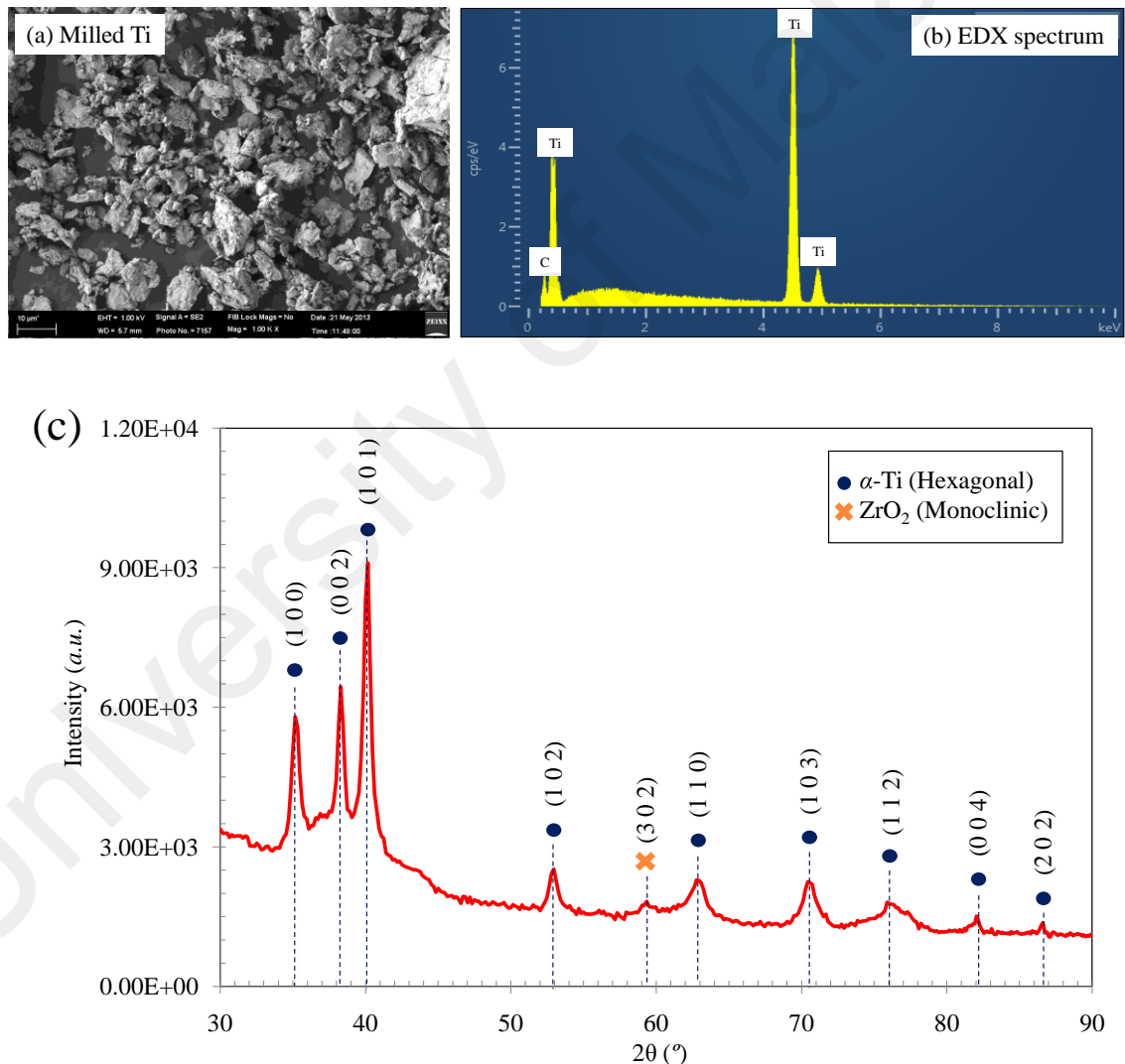


**Figure 4.7:** (a) FESEM image of the milled Ti particles (Ti-20h), (b) EDX spectrum of Ti-20h particles and (c) XRD peaks of the Ti-20h particles.

The XRD analysis of the Ti-20h particles is shown in Figure 4.7(c). The presence of  $\alpha$ -Ti phase (hexagonal) is revealed in the XRD analysis of Ti-20h particles. No peak of the oxides of titanium is observed in XRD. However, a small peak of monoclinic ZrO<sub>2</sub> appears at  $2\theta$  angle of 59.6°. It should be noted that the Ti particles were milled using ZrO<sub>2</sub> balls and the peak appears due to the erosion of the ZrO<sub>2</sub> balls during milling.

(b) ***Residual stress in as-received and milled Ti particles***

During the milling of the as-received Ti, residual stress is incorporated in the particles. The residual stress inside the Ti-0h and Ti-20h particles was evaluated by XRD- $\sin^2\psi$  technique. For this reason, Ti-0h and Ti-20h particles were scanned from  $2\theta$  angle of 136° to 142° at different tilt angles ( $\psi$ ) ranging from 0° to 40° as shown in Figure 4.8(a-b). The peak shift is more evident for Ti-20h particles at different  $\psi$  angles. The lattice spacing ( $d$ ) is plotted against  $\sin^2\psi$  in Figure 4.8(c) for both Ti-0h and Ti-20h particles. The slopes of the  $d$ - $\sin^2\psi$  plot are found to be +0.0011 and +0.003 for Ti-0h and Ti-20h particles, respectively. Substituting these values in equation (3.5), the residual stress obtained for Ti-0h and Ti-20h particles are +99.3 MPa (compressive) and +270.9 MPa (compressive) as shown in Figure 4.8(d).

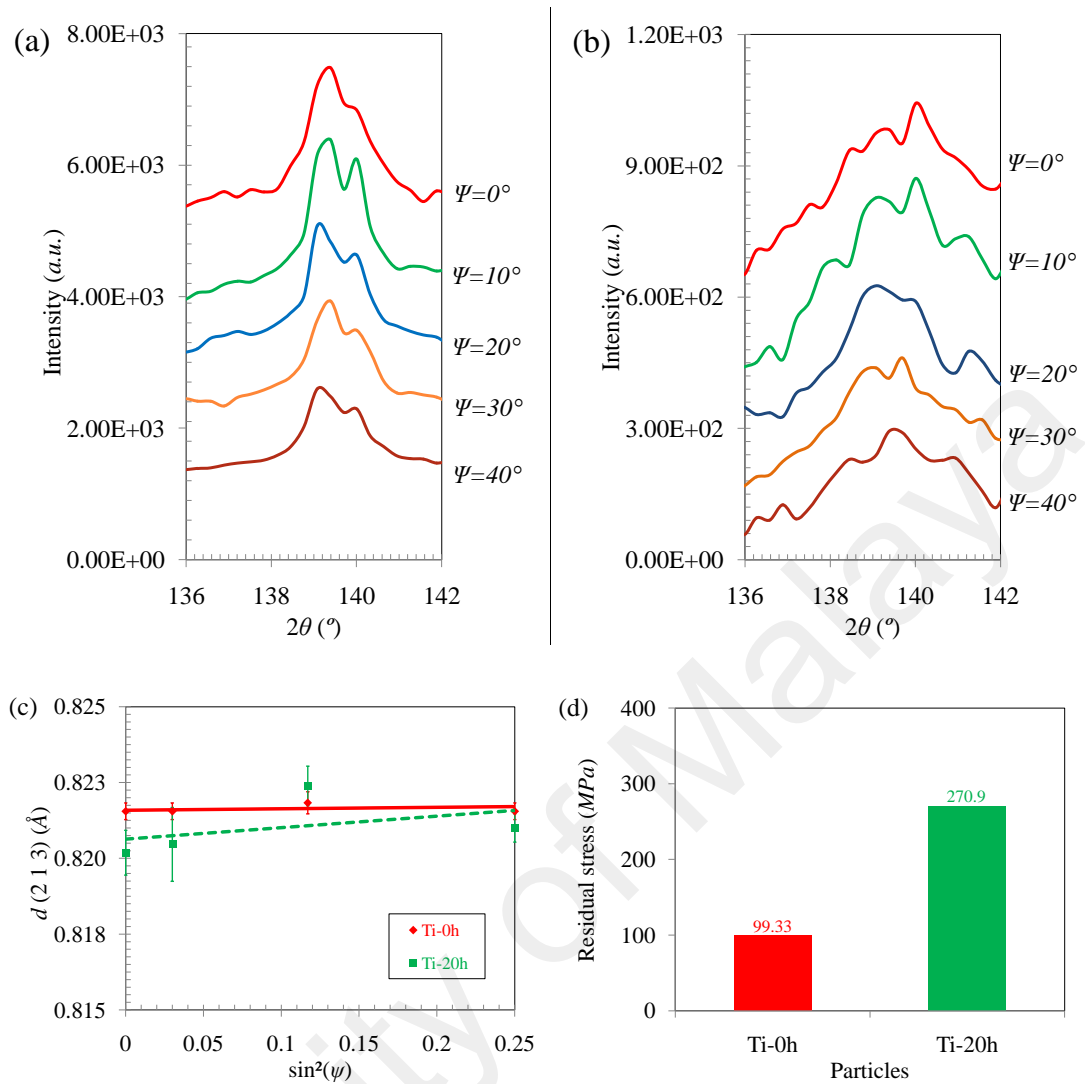


**Figure 4.8: (a) XRD peaks of (2 1 3) plane in Ti-0h particles, (b) XRD peaks of (2 1 3) plane in Ti-20h particles, (c)  $d$ - $\sin^2\psi$  plot for the Ti-0h and Ti-20h particles and (d) estimated compressive residual stress inside the particles.**

According to literature, there are some sources of error in the XRD- $\sin^2\psi$  technique for determining the residual stress which includes the errors in the measurement of diffraction peak, nonlinear relation between lattice spacing ( $d$ ) and  $\sin^2\psi$  due to the grain interactions, anisotropic elastic property of crystalline materials and instrumental conditions (Luo & Jones, 2010; X. Zheng et al., 2004). Nonetheless, the estimated values show the accumulation of compressive stress in the milled samples. The XRD analysis shown in Figure 4.7(c) also indicates the accumulation of stress in the Ti-20h sample through peak broadening.

(c) *Thermal oxidation of milled Ti particles*

To elucidate the effect of residual stress, the milled particles (Ti-20h) were thermally oxidized in a similar condition of as-received particles (Ti-0h) shown in Figure 4.6(b). Figure 4.9 shows the FESEM images of Ti-20h particles oxidized in the presence of 5 ppm of O<sub>2</sub> in humid Ar environment at a flow rate of 150 sccm. The oxidation temperature was 750 °C. The 1-D nanostructures with higher coverage are seen on the surface of Ti-20h particles. Comparing the FESEM images of thermally oxidized Ti-0h particles treated in similar conditions shown in Figure 4.6(b), it is clear that milling significantly enhanced the coverage of 1-D nanostructures during oxidation. The average density of 1-D nanostructures on Ti-20h particles is  $2.7 \times 10^{11} \text{ m}^{-2}$ , whereas it is found to be  $1.27 \times 10^{10} \text{ m}^{-2}$  on Ti-0h particles during humid oxidation under similar conditions. There is about 21 times increase in the coverage of 1-D nanostructures during oxidation of milled particles compared with as-received Ti particles.

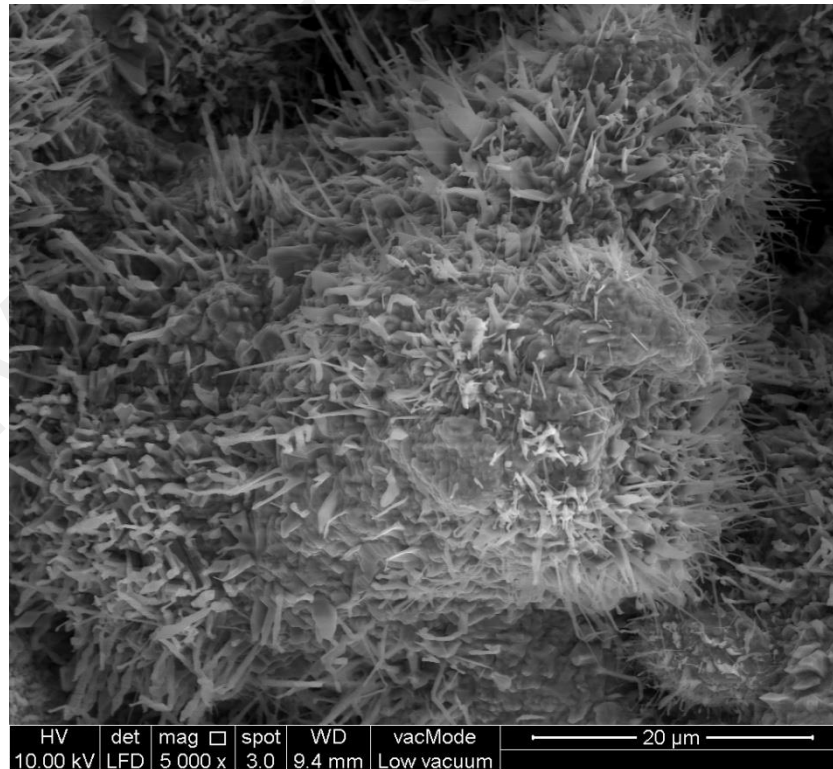


**Figure 4.9: FESEM images of Ti-20h particles after oxidation at 750 °C containing 5 ppm of O<sub>2</sub> in humid Ar at a flow rate of 150 sccm.**

It is concluded from the above observations that incorporation of compressive residual stress by milling significantly enhances the coverage of 1-D nanostructures on Ti substrates during humid oxidation. Similar phenomenon of enhanced 1-D nanostructures was also seen on Cu where residual stress was imposed on the substrate by bending (Mema et al., 2011) and sand blasting (Yuan & Zhou, 2012). It is believed that the imposed residual stress is released during humid oxidation of Ti substrate by creating new surfaces in the form of 1-D nanostructures.

#### **4.1.2.4 Effects of Dynamic Oxygen Partial Pressure**

It is seen that both oxygen and H<sub>2</sub>O content plays a significant role for the growth of 1-D nanostructures on Ti particles. To understand this relationship, oxidation experiments were conducted with various combinations of oxygen concentrations in humid Ar flown at different flow rates in the tube furnace. A theoretical model is developed to calculate the dynamic oxygen partial pressure inside the quartz tube of horizontal tube furnace for the experimental conditions and correlated with the results with the growth of 1-D nanostructures in the following sections.

##### **(a) *Oxidation with various concentrations of oxygen and flow rates***

The Ti-20h particles were oxidized with various concentration of humid oxygen flown at different rates. The oxygen concentrations were varied from 5 to 105 ppm and the flow rates were varied from 20 to 300 sccm. Figure 4.10 shows the FESEM images of Ti-20h particles after thermal oxidation for 4 h under different combinations of flow rate and concentration of humid oxygen. It is seen in Figure 4.10(a) that for 20 sccm humid flow with 5 ppm O<sub>2</sub>, no 1-D nanostructure is seen. However, increasing the oxygen concentration to 105 ppm in 20 sccm humid flow shows some sort of 1-D nanostructures as seen in Figure 4.10(b). Again, for 50 sccm humid flow with 5 ppm O<sub>2</sub>, no 1-D

nanostructures are seen (Figure 4.10(c)). But increasing the oxygen concentrations to 55 and 105 ppm O<sub>2</sub> in 50 sccm humid flow shows a good coverage of 1-D nanostructures as seen in Figure 4.10(d-e). Similarly, for 150 sccm humid flow with 5 ppm O<sub>2</sub> shows high coverage of 1-D nanostructures as seen in Figure 4.10(f). Again, for 105 ppm O<sub>2</sub> with 150 sccm humid flow no 1-D nanostructures but oxide scale are seen (Figure 4.10(g)). For 300 sccm humid flow with 5 ppm O<sub>2</sub> shows 1-D nanostructures (Figure 4.10(h)) but for 105 ppm O<sub>2</sub> the particles are depleted of 1-D nanostructures and oxide scales are seen (Figure 4.10(i)).

From the above observation it is seen that during humid oxidation 1-D nanostructures are seen on Ti particles under different combinations of flow rate and oxygen concentrations. It is suggested that oxygen together with H<sub>2</sub>O partial pressure plays a vital role for the growth of 1-D nanostructures on Ti particles. In the next sections a theoretical model is developed to calculate the dynamic oxygen partial pressure and correlated with the obtained results.

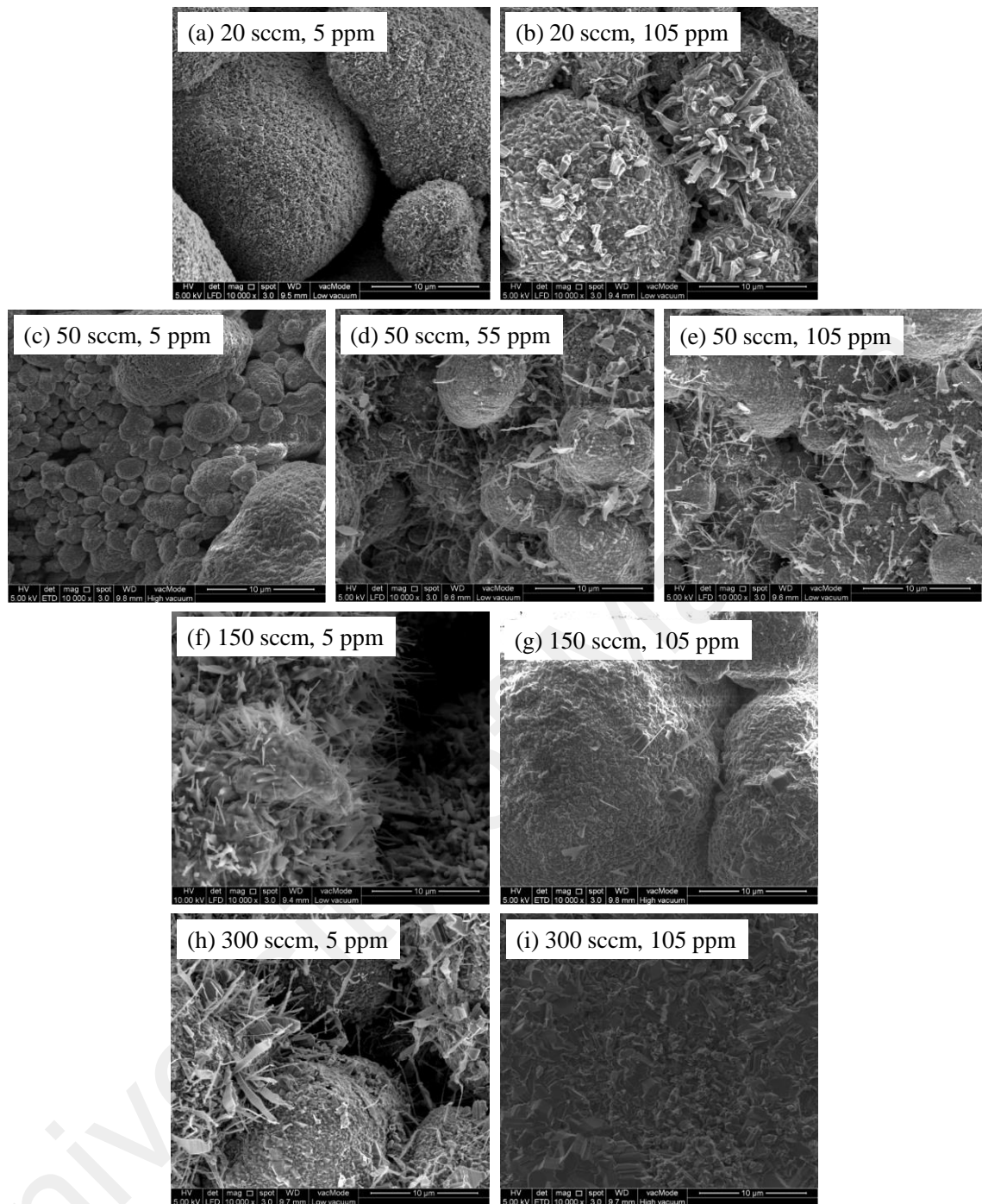


**Figure 4.10: FESEM images of the Ti-20h particles after humid oxidation at 750 °C for 4 h in (a) 20 sccm flow with 5 ppm O<sub>2</sub>, (b) 20 sccm flow with 105 ppm O<sub>2</sub>, (c) 50 sccm flow with 5 ppm O<sub>2</sub>, (d) 50 sccm flow with 55 ppm O<sub>2</sub>, (e) 50 sccm flow with 105 ppm O<sub>2</sub>, (f) 150 sccm flow with 5 ppm O<sub>2</sub>, (g) 150 sccm flow with 105 ppm O<sub>2</sub>, (h) 300 sccm flow with 5 ppm O<sub>2</sub> and (i) 300 sccm flow with 105 ppm O<sub>2</sub>.**

**(b) Theoretical calculations of dynamic pressure of oxygen**

During oxidation in the quartz tube the Ti particles encounters oxygen with different kinetic energies due to having different combination of oxygen concentration and flow

rate. The kinetic energy of the gas in per unit volume is determined by the dynamic pressure. Since mixed gas was used in the present experimental conditions, the dynamic partial pressure of oxygen determines the oxidation condition of Ti particles for the growth of 1-D nanostructures. Theoretical calculations derived in Appendix B show that during oxidation the dynamic oxygen partial pressure inside the tube can be calculated as follows:

$$P_{O_2} = 1.41 \times 10^{-23} \times \frac{\chi \times F_{RT}^2 \times \rho_{RT}}{r^4} \times \frac{T_{oxi}}{T_{RT}} \quad (4.1)$$

Here,  $\chi$  is the concentration of oxygen in ppm in Ar environment,  $F_{RT}$  is flow rate of the mixed gas in sccm,  $\rho_{RT}$  is the density of Ar ( $1.784 \text{ kg/m}^3$ ),  $r$  is the radius of the tube ( $2.2 \times 10^{-2} \text{ m}$ ),  $T_{oxi}$  is the oxidation temperature ( $1023 \text{ K}$ ) and  $T_{RT}$  is the room temperature ( $298 \text{ K}$ ). Substituting these values in equation (4.1),  $P_{O_2}$  can be expressed as:

$$P_{O_2} = 3.7 \times 10^{-16} \times \chi \times F_{RT}^2 \quad (4.2)$$

From equation (4.2) it is seen that for a given set of parameters the dynamic oxygen partial pressure inside the tube depends linearly on oxygen concentration and squarely on flow rates. In Figure 4.11, the theoretical dynamic oxygen partial pressure inside the tube for various combination of flow rate and oxygen concentration is shown. The experimental conditions presented in Figure 4.10 are shown on Figure 4.11 by purple dots.

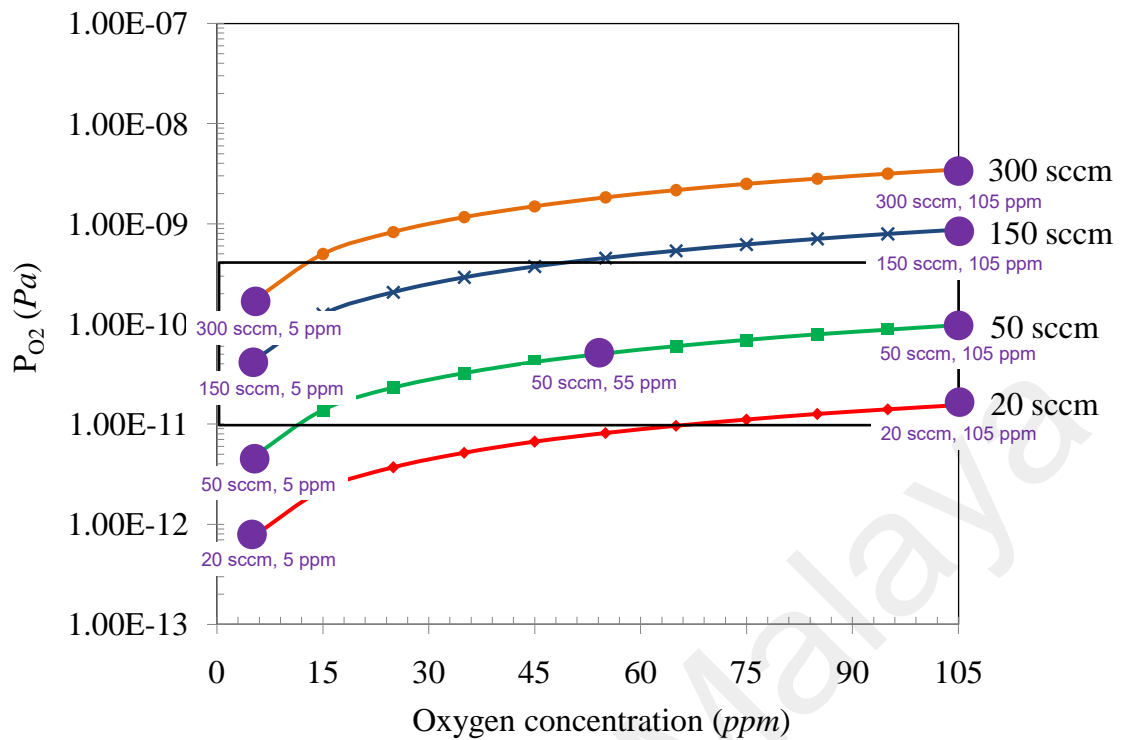


**Figure 4.11: Theoretical representation of dynamic oxygen partial pressure inside the tube for different flow rates and oxygen concentrations. The experimental conditions conducted on Ti-20h particles are shown by purple color.**

According to the Ellingham diagram shown in Appendix C, the  $P_{O_2}$  required for the oxidation of Ti at 750 °C is  $\sim 1 \times 10^{-11}$  Pa (Ellingham, 1944). Oxidation of Ti does not occur at 750 °C if the  $P_{O_2}$  is below  $\sim 1 \times 10^{-11}$  Pa. It is seen from Figure 4.11 that the dynamic oxygen partial pressure is below  $1 \times 10^{-11}$  Pa for the combinations of 20 sccm flow with 5 ppm  $O_2$  and 50 sccm flow with 5 ppm  $O_2$ . So, it is expected that no oxidation will occur at these experimental conditions. It is agreed with the obtained results shown in Figure 4.10(a) and (c) where no 1-D nanostructures are seen for these combinations of experimental conditions. But some sort of oxidation is seen at these experimental conditions which could be due to minute leakage in the tube during the oxidation process.

The 1-D nanostructures are seen for the experimental conditions where the dynamic oxygen partial pressure is in between  $1 \times 10^{-11}$  -  $3 \times 10^{-10}$  Pa. It is seen from Figure 4.11 that the dynamic oxygen partial pressure is in between  $1 \times 10^{-11}$  -  $3 \times 10^{-10}$  Pa for the experimental combinations of 20 sccm flow with 105 ppm  $O_2$ , 50 sccm flow with 55 ppm

O<sub>2</sub>, 50 sccm flow with 105 ppm O<sub>2</sub>, 150 sccm flow with 5 ppm O<sub>2</sub>, and 300 sccm flow with 5 ppm O<sub>2</sub>. For this reason, 1-D nanostructures are seen for these experimental combinations as seen in Figure 4.10(b), (d), (e), (f) and (h). However, when the dynamic oxygen partial pressure is more than  $3 \times 10^{-10}$  Pa, oxide scale is seen instead of 1-D nanostructure. For the experimental combinations of 150 sccm flow with 105 ppm O<sub>2</sub> and 300 sccm flow with 105 ppm O<sub>2</sub>, the dynamic oxygen partial pressure are calculated to be more than  $3 \times 10^{-10}$  Pa. For this reason, oxide scales are seen in these experimental conditions as shown in Figure 4.10(g) and (i).

From the above observations it is clear that minimum  $1 \times 10^{-11}$  Pa dynamic oxygen partial pressure is required for the 1-D growth on Ti substrates. However, increasing the dynamic oxygen partial pressure to  $3 \times 10^{-10}$  Pa depleted the 1-D nanostructures. It is proposed that for limited supply of oxygen (dynamic oxygen partial pressure:  $1 \times 10^{-11}$  -  $3 \times 10^{-10}$  Pa), the growth of TiO<sub>2</sub> nuclei occur in certain direction resulting in 1-D nanostructure (Huyong Lee et al., 2010). At high concentration of oxygen, the growth of TiO<sub>2</sub> nuclei occur in all directions and as a result oxide scale is seen. Beside dynamic oxygen partial pressure, the  $P_{H_2O}$  also plays a significant role for the growth of 1-D nanostructures. However, the role of  $P_{H_2O}$  for 1-D growth on Ti substrate is not clear and further investigations are required on this aspect.

#### **4.1.3 Characterization of Oxidized Ti Particles**

The as-grown 1-D nanostructures on Ti particles are 5-10  $\mu\text{m}$  long with a diameter of 50-200 nm. The oxidized Ti particles were characterized by field emission scanning electron microscope (FESEM) equipped with energy dispersive X-ray (EDX) spectroscope, X-ray diffraction (XRD) and X-ray photoelectron spectroscope (XPS). In the following sections the details of the characterization of oxidized Ti particles is presented.

#### 4.1.3.1 Surface Characterization of Oxidized Ti Particles

##### (a) *Energy dispersive X-ray (EDX) spectroscopy*

The top surface of Ti-20h particles oxidized at 750 °C for 4 h with 5 ppm of O<sub>2</sub> in humid Ar at a flow rate of 150 sccm is shown in Figure 4.9 and the corresponding EDX spectrum is shown in Figure 4.12. The presence of Ti and O peaks are seen in the EDX spectrum with small amount of C peak. The C peak is obtained from the carbon tape used for sticking the sample on FESEM sample holder. Spot analysis at different locations of the oxidized particles shows 35.5 at% of Ti and 64.5 at% of oxygen which is very close to the atomic ratio of Ti and O in TiO<sub>2</sub>.

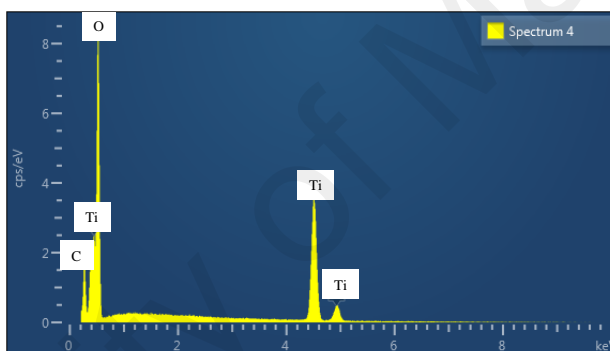


**Figure 4.12: EDX spectrum on Ti-20h particles oxidized at 750 °C containing 5 ppm of O<sub>2</sub> in humid Ar at a flow rate of 150 sccm.**

##### (b) *X-ray diffraction (XRD) analysis*

Figure 4.13 shows the XRD peaks of Ti-20h particles oxidized for 4 h at 750 °C in the presence of 5 ppm of O<sub>2</sub> in humid Ar flown at a rate of 150 sccm. The presence of tetragonal TiO<sub>2</sub> (rutile) is evident in the XRD peaks. However, some peaks of lower valence oxides such as face centered cubic TiO, rhombohedral Ti<sub>2</sub>O<sub>3</sub> and monoclinic Ti<sub>3</sub>O<sub>5</sub> are also seen in the XRD peaks. Presence of lower valence oxides of titanium (TiO, Ti<sub>2</sub>O<sub>3</sub> and Ti<sub>3</sub>O<sub>5</sub>) is also reported in the literature during humid oxidation of Ti in oxygen (Galerie et al., 1997; G. Lu et al., 2000; Pérez, 2007). It should be noted that in the present case, oxidation of Ti is carried out in the presence of 5 ppm oxygen in humid Ar at a flow rate of 150 sccm. Even in this oxygen deprived condition, the formation of lower valence

oxides of Ti is evident. It was reported that during humid oxidation of Ti, multiple oxide layers are formed and TiO<sub>2</sub> forms at the gas-oxide interface whereas lower valence oxides form at the oxide-metal interface (Galerie et al., 1997; G. Lu et al., 2000; Pérez, 2007). In the present case, similar scenario is anticipated. In the XRD analysis, some peaks of  $\alpha$ -Ti is also seen which is obtained from the un-oxidized core of the Ti particles.

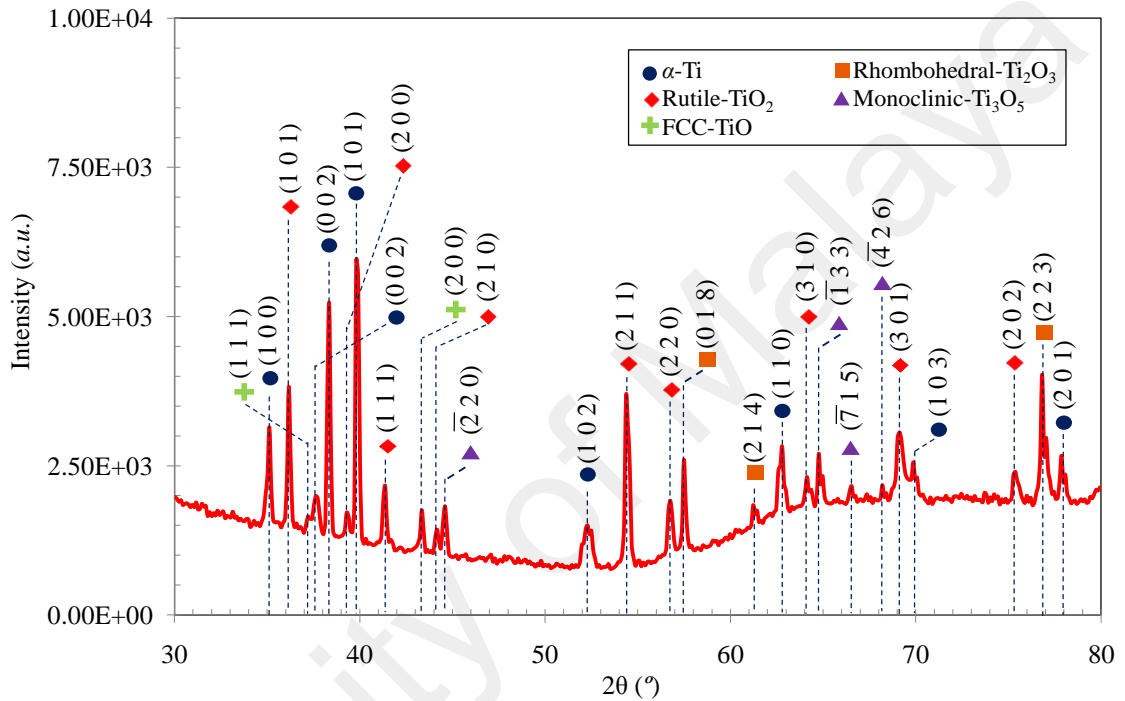


**Figure 4.13: XRD peaks of Ti-20h particles oxidized for 4 h at 750 °C in presence of 5 ppm of O<sub>2</sub> in humid Ar flow at a rate of 150 sccm.**

(c) *X-ray photoelectron spectroscopy (XPS)*

Figure 4.14 shows the XPS spectra of Ti sheet oxidized for 4 h at 750 °C in presence of 5 ppm O<sub>2</sub> in humid Ar at flow rate of 500 sccm. The occurrence of Ti2p peaks (Ti2p<sub>3/2</sub> and Ti2p<sub>1/2</sub>) is seen at the binding energies of 456.8 and 462.01 eV. The Ti2p profile is deconvoluted into three Ti2p components (dotted lines) with binding energies of 454.2, 456.8 and 461.5 which represents the oxidation states of Ti<sup>2+</sup>, Ti<sup>3+</sup> and Ti<sup>4+</sup> oxides, respectively (Figure 4.14(b)). In the literature deviation is observed from the obtained values of the deconvoluted Ti2p peaks which occurred at 455.34, 457.13 and 458.66 eV for Ti<sup>2+</sup>, Ti<sup>3+</sup> and Ti<sup>4+</sup> oxides, respectively (Biesinger, Lau, Gerson, & Smart, 2010).

However, in the present case the shape of the deconvoluted peaks is same with the reported literature. So, it is confirmed from the XPS spectra that TiO, Ti<sub>2</sub>O<sub>3</sub> and TiO<sub>2</sub> is formed during humid oxidation of Ti substrates. No peaks belonging to Ti<sub>3</sub>O<sub>5</sub> is observed in the XPS spectra though Ti<sub>3</sub>O<sub>5</sub> is observed in XRD peaks as shown in Figure 4.13.

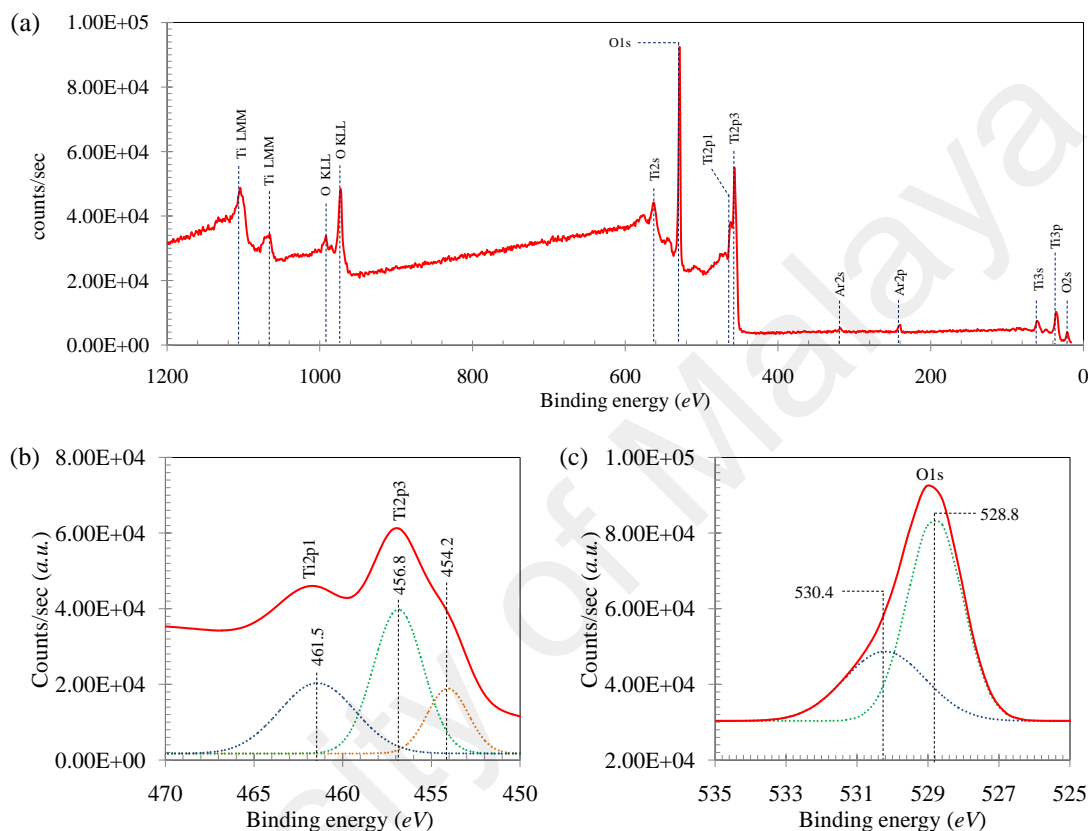


**Figure 4.14: (a) XPS spectra of Ti sheet oxidized at 750 °C for 4 h in presence of 5 ppm O<sub>2</sub> in humid Ar at flow rate of 500 sccm, (b) narrow scan of Ti2p spectra and (c) narrow scan of O1s spectra.**

The occurrence of O1s peak is observed at the binding energy of 529.05 eV as shown in Figure 4.14. The O1s profile is deconvoluted into two components (dotted lines) of binding energies of 530.4 and 528.8 eV as shown in Figure 4.14(c). The major O1s peak at 528.6 eV is associated with TiO<sub>2</sub> or Ti<sub>2</sub>O<sub>3</sub> (G. Lu et al., 2000). In the literature the O1s binding energy for TiO<sub>2</sub> is reported to be 529.9eV (Carley, Roberts, & Roberts, 1990). The minor O1s peak at 530.4 eV is assigned to hydroxide (T. Yu et al.) species on the Ti surface. In the literature, this minor peak is reported at 531.86 eV for OH species on

surface (Erdem et al., 2001). So, it is likely that during humid oxidation of Ti, hydroxide ion is adsorbed on the surface of Ti.

#### 4.1.3.2 Morphological Oddities of 1-D Nanostructures

Most of the 1-D nanostructures grown on Ti particles are not straight as discussed in the previous sections. In many instances, the 1-D nanostructures bend to certain angle while growing resulting in a structure that is not straight. In high magnification FESEM images four types of nanostructures namely (a) stacked, (b) ribbon, (c) plateau and (d) lamp post shaped morphologies were seen. Some of these nanostructures were discussed and reported by Dinan *et al.* (B. Dinan, 2012). In the following sections the details of these nanostructures are presented.

##### (a) *Stacked morphology*

The stacked shaped nanostructures are composed of nanocrystals grown over one another as shown in Figure 4.15(a). This structure is most widely seen during oxidation of Ti substrates. The length of the stacked nanostructures is typically 5 to 10  $\mu\text{m}$ . The nanostructures have non-uniform width varying from 100-500 nm. Generally, the width of the nanostructure is wider at the root compared with the top. The entanglement behavior is most commonly seen in stacked nanostructure. Beside this, formation of nodes is seen on these nanostructures as shown by red circle in Figure 4.15(a) where two 1-D nanostructures are originated from the node. It is assumed that defects sites are involved for the bending of 1-D nanostructures. Further studies are required to obtain a better understanding of the root causes of bending and formation of nodes.

(b) *Ribbon morphology*

The ribbon is the second most widely observed morphology during oxidation of Ti substrate for 1-D growth. The ribbons have flat shape at the root but tapered morphology at the top as shown in Figure 4.15(b). The ribbons are 2 to 4  $\mu\text{m}$  long with width and thickness of 300-400 nm and 60-80 nm, respectively. Some stacked type morphology and entanglement is also evident in ribbon type nanostructures.

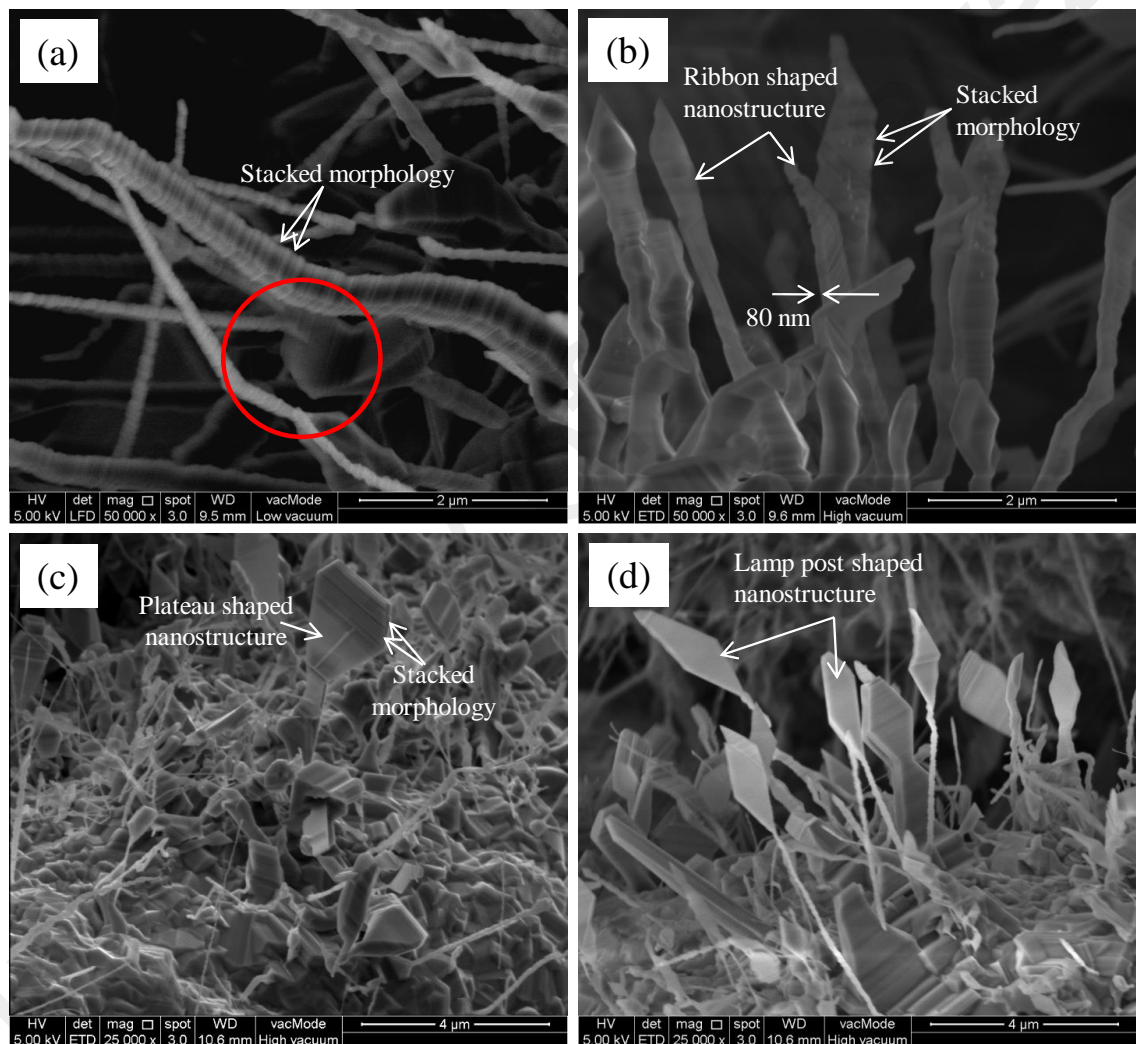


**Figure 4.15: The growth of different types of nanostructures during oxidation of Ti particles (a) stacked morphology, (b) ribbon morphology, (c) plateau morphology and (d) lamp post shaped morphology.**

(c) *Plateau morphology*

Plateau shaped morphology is observed time to times in discrete locations during 1-D growth on Ti substrates. One plateau shaped nanostructure is shown in Figure 4.15(c).

Plateau morphology appears in different size and shapes and has non-uniform width. Typically, plateau nanostructures are 2 to 4  $\mu\text{m}$  long with a thickness of 60-80 nm. The width of the nanostructure can be as high as 2  $\mu\text{m}$  at some points. Stacked morphology and entanglement is also evident on plateau nanostructures.

(d) *Lamp post shaped morphology*

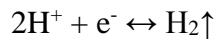
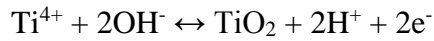
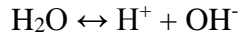
Lamp post shaped 1-D nanostructures are also seen during oxidation of Ti substrates for 1-D growth as shown in Figure 4.15(d). However, the frequency of appearance of lamp post shaped structures is quite low. Lamp post shaped nanostructures are combinations of two morphologies: one stacked 1-D nanostructure at the root and a rhombus shaped nanostructures at the top. Typically these nanostructures are 6 to 8  $\mu\text{m}$  long. The diagonals of the rhombus in lateral and longitudinal directions are 0.8-1  $\mu\text{m}$  and 1.6-2  $\mu\text{m}$ , respectively. Evidence of stacked morphology and entanglement are also observed in lamp post shaped nanostructures.

From the above observations it is seen that a wide variety of 1-D nanostructures are evolved during the oxidation of Ti samples in humid conditions for 1-D growth. These include stacked, ribbon, plateau and lamp post shaped morphology. These types of nanostructures are randomly distributed in samples oxidized in same conditions. However, some of the features such as stacked and bending are common in all nanostructures. Further analysis is necessary to determine what conditions favor the growth of one morphology over another.

#### **4.1.4 Mechanism of 1-D Growth on Ti Particles**

The oxidation behavior of Ti in presence of water vapor in air was studied by several groups of researchers (Galerie et al., 1997; Pérez, 2007; Stringer, 1960; Taniguchi et al., 2001). It was reported that during humid oxidation, water molecules dissociate to

hydroxide ions ( $\text{OH}_6^-$ ) and adsorb on the Ti substrates (Galerie et al., 1997; Stringer, 1960; Taniguchi et al., 2001). The  $\text{Ti}^{4+}$  ions diffuse interstitially to the surface and reacts with the surface adsorbed water molecules to form  $\text{TiO}_2$  (Galerie et al., 1997). Hydrogen evolves as a byproduct of the reactions as follows (Galerie et al., 1997):



On the other hand, the oxygen ions diffuse inward via grain boundaries and reacts with Ti ions (Stringer, 1960; Taniguchi et al., 2001). It was reported that lower valence oxides of Ti ( $\text{Ti}_3\text{O}_5$ ,  $\text{Ti}_2\text{O}_3$ ,  $\text{TiO}$ ) are layered beneath the  $\text{TiO}_2$  scale (Pérez, 2007; Stringer, 1960). No study reports the mechanism of humid oxidation of Ti in oxygen deprived conditions for the growth of 1-D nanostructures.

In the present case,  $\text{TiO}_2$  layer forms at the outermost oxide scale as seen from the EDX spectroscopy analysis (Figure 4.12). Existence of lower valences of Ti is observed from XRD (Figure 4.13) and XPS (Figure 4.14) investigations during humid oxidation. Based on these findings and comparing with the relevant literature survey, one model is proposed for the growth of 1-D nanostructures on Ti substrates during humid oxidation in oxygen deprived conditions.

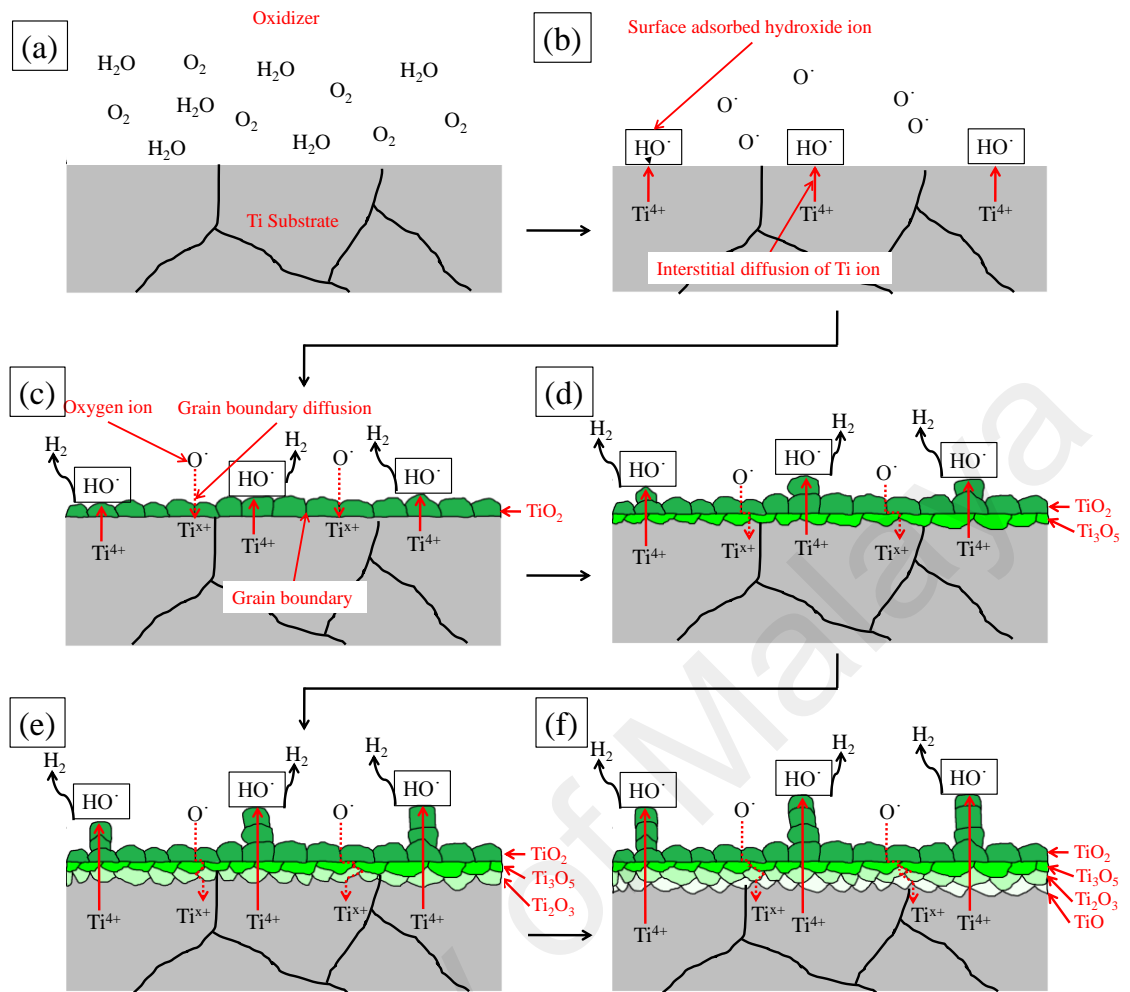


**Figure 4.16: Schematics of 1-D growth on Ti substrate during humid oxidation.**

In Figure 4.16(a), a substrate containing  $\alpha$ -Ti grains is shown. During humid oxidation,  $\text{OH}_o^\cdot$  ions adsorb on the surface of  $\alpha$ -Ti grains as shown in Figure 4.16(b) (Galerie et al., 1997; Stringer, 1960; Taniguchi et al., 2001). The  $\text{Ti}^{4+}$  ions diffuse interstitially to the surface and reacts with  $\text{OH}_o^\cdot$  ion to form  $\text{TiO}_2$  layer composed of multiple grains on one single  $\alpha$ -Ti grain (Figure 4.16(c)) (Galerie et al., 1997). Hydrogen evolves as a byproduct of the reactions (Galerie et al., 1997).

In the next step, oxygen ions diffuse inward via grain boundaries and reacts with Ti ions (Stringer, 1960; Taniguchi et al., 2001). Lower valence oxide of Ti such as  $\text{Ti}_3\text{O}_5$  is formed at this stage of oxidation as shown in Figure 4.16(d).

It was reported that during oxidation of Cu multilayered oxides are formed and stress is induced among the oxide layers (Kumar et al., 2004). This induced stress is compensated by forming new surfaces in the form of 1-D nanostructures. Similar, scenario is proposed for the present case of humid oxidation of Ti in oxygen deprived conditions where multi-layered oxides are seen in XRD (Figure 4.13) and XPS (Figure 4.13) analysis. The presence of multilayer oxides induces stress in the substrate due to the difference in molar volume and crystal structures (Kumar et al., 2004). This induced stress is released by forming  $\text{TiO}_2$  nuclei of 1-D nanostructure on existing  $\text{TiO}_2$  grains. For this,  $\text{Ti}^{4+}$  ions diffuse to the outer surface of  $\text{TiO}_2$  layer via interstitial sites (Stringer, 1960; Taniguchi et al., 2001) and reacts with surface adsorbed water molecule as shown in Figure 4.16(d). It is thermodynamically more viable to form nuclei of 1-D nanostructures on existing  $\text{TiO}_2$  grains as it does not require to overcome the energy barrier for nucleation (Yuan et al., 2011).

Due to continuous diffusion of  $\text{Ti}^{4+}$  via interstitial sites, the 1-D nanostructures become longer in outward directions as seen in Figure 4.16(e-f). On the other hand, diffusion of oxygen via grain boundaries resulted in the formation of  $\text{Ti}_2\text{O}_3$  and  $\text{TiO}$  at the oxide-metal interface at the later stages of oxidation (Figure 4.16(e-f)).

It is proposed that in the presence of limited supply of oxygen, the growth of as-grown  $\text{TiO}_2$  nuclei occurs in certain direction resulting in 1-D  $\text{TiO}_2$  nanostructures (Huyong Lee et al., 2010). At high concentration of oxygen, the growth of nuclei occurs in all directions and as a result oxide scales form seen instead of 1-D nanostructures. Beside this, residual stress imposed by milling enhances the density of 1-D nanostructures significantly. It is proposed that the residual stress is released during oxidation process by forming new surfaces such as 1-D nanostructures (Kumar et al., 2004).

#### 4.1.5 Summary of Thermal Oxidation of Ti Particles

Thermal oxidation is a simple and inexpensive method for synthesizing 1-D TiO<sub>2</sub> nanostructures on Ti substrates. This process requires heating the Ti substrates in oxygen containing humid environment. It is seen that temperature together with oxidation environment has significant effect on the growth of 1-D nanostructures. The optimum growth temperature of 1-D nanostructures on Ti substrate is found to be 750 °C. The coverage of 1-D nanostructures is insignificant in dry oxygen environment. Humid environment containing minute amount of oxygen is required for 1-D growth. Theoretical calculations show that the minimum dynamic oxygen partial pressure required for 1-D growth is 10<sup>-11</sup> Pa. Oxide scale is seen instead of 1-D nanostructures when the dynamic oxygen partial pressure is more than 3x10<sup>-10</sup> Pa. It is proposed that in the presence of limited supply of oxygen, the growth of as-grown TiO<sub>2</sub> nuclei occur in certain direction resulting in 1-D TiO<sub>2</sub> nanostructures.

Besides temperature and oxidation environment, residual stress plays significant role to enhance the 1-D coverage. It is proposed that the residual stress is released during oxidation by creating new surfaces of 1-D nanostructures. As a result, the coverage of 1-D nanostructure is improved by imposing residual stress on Ti particles by milling.

The characterization revealed that the length and diameter of the 1-D nanostructures are 5-10 μm and 50-200 nm, respectively. The as-grown nanostructures possesses rutile (tetragonal) phase of TiO<sub>2</sub>. During oxidation multilayered oxide scale is formed beneath the 1-D nanostructures where TiO<sub>2</sub> is formed at the gas-oxide interface and lower valance of oxides (Ti<sub>3</sub>O<sub>5</sub>, Ti<sub>2</sub>O<sub>3</sub>, TiO) is formed at the oxide-metal interface. The 1-D nanostructures are evolved from the TiO<sub>2</sub> oxide scale in outward directions. Based on these findings a diffusion based model is proposed to explain the mechanism of 1-D growth on Ti substrates.

## 4.2 Growth of 1-D Nanostructures on Ti-6Al-4V (Ti64)

The feasibility of 1-D growth on Ti-6Al-4V (Ti64) particles and sheets during thermal oxidation is investigated in the following sections. In the first section, the as-received Ti64 particles and sheets were characterized by different techniques. After that the thermal oxidation process was optimized by varying different parameters for the growth of 1-D nanostructures on Ti64. After optimizing the 1-D growth, the as-grown nanostructures were characterized in details by various state-of-the-art techniques. Finally, a mechanism is proposed for the growth of 1-D nanostructures during thermal oxidation of Ti64 particles and sheets.

### 4.2.1 Characterization of the As-received Ti64 Particles and Sheets

Both Ti64 particles and sheets were used to investigate the growth of 1-D nanostructures. The as-received Ti64 particles and sheets were characterized using FESEM equipped with EDX spectroscope and XRD which is discussed in the following sections.

#### 4.2.1.1 Elemental Analysis of Ti64 Particles and Sheets

##### (a) *Ti64 particles*

The FESEM image of the as-received Ti64 particles is shown in Figure 4.17(a). The particles has an irregular shape with an average size of 226.4  $\mu\text{m}$ . Elemental mapping of the particles (Figure 4.17(b-d)) shows the presence of Ti, Al and V distributed all over the surface. The EDX spectrum of the particles is shown in Figure 4.17(e) which also shows the presence of Ti, Al and V. It is seen from the EDX results that the Ti64 particles contain  $91.05 \pm 1.1$  wt% Ti,  $6.61 \pm 1.1$  wt% Al and  $2.34 \pm 0.29$  wt% V.

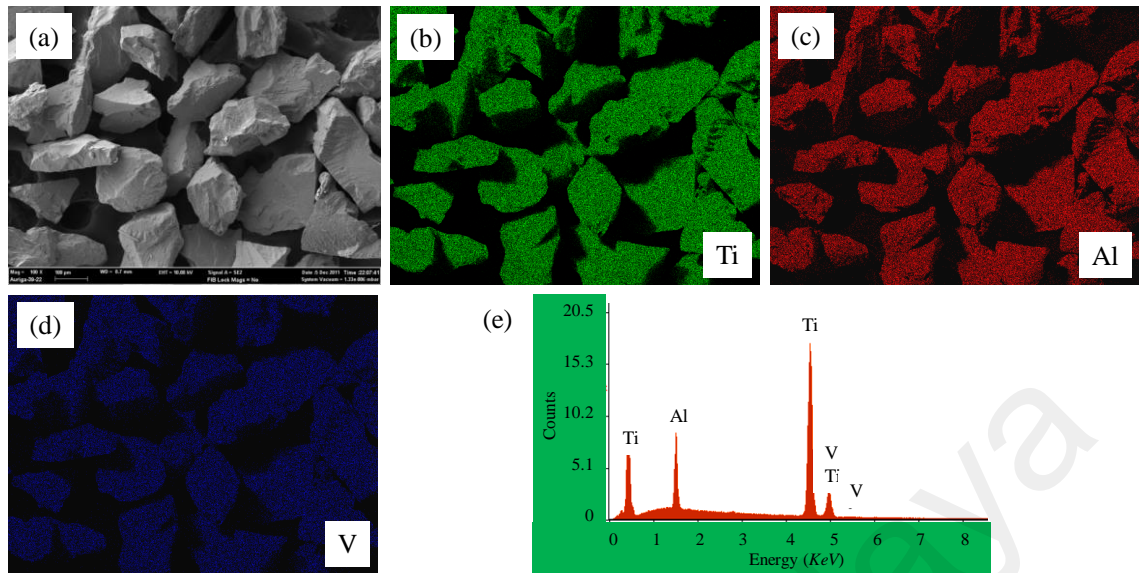


**Figure 4.17: (a) FESEM image of the as-received Ti64 particles, (b-d) elemental mapping of the particles for the elements of Ti (green), Al (red) and V (blue) respectively and (e) EDX spectrum of the Ti64 particles.**

(b) *Ti64 sheet*

The Ti64 sheet having a size of 15 mm x 15 mm x 1 mm was polished and etched followed by observation under FESEM. Two distinct phases are observed under FESEM (Figure 4.18). One phase having white contrast is dispersed in a matrix with a dark contrast. It was reported earlier that the matrix having dark contrast is  $\alpha$  phase and the dispersed white regions are  $\beta$  phase of Ti (Xiao Li, Sugui, Xianyu, & Liqing, 2013).

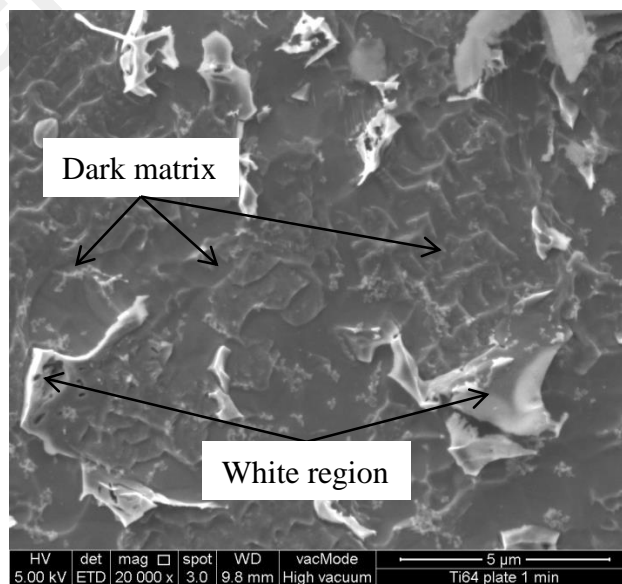


**Figure 4.18: FESEM image of Ti64 sheet after polishing and etching.**

The EDX spot analysis on the dark ( $\alpha$ -Ti) and white ( $\beta$ -Ti) regions is tabulated in Table 4.1. It is seen that the Al content is  $6.3\pm 0.07$  wt% and  $3.32\pm 0.82$  wt% and V content is  $2.15\pm 0.09$  wt% and  $18.42\pm 8.01$  in dark ( $\alpha$ -Ti) and white ( $\beta$ -Ti) regions, respectively. Al is known to be  $\alpha$ -phase stabilizer whereas V is the  $\beta$ -phase stabilizer in Ti alloys (Huyong Lee et al., 2010).

**Table 4.1: Elemental analysis of different phases in Ti64 sheet by EDX spectrum.**

Element	Dark ( $\alpha$ -Ti) region (wt%)	White ( $\beta$ -Ti) region (wt%)
Ti	$90.59\pm 1.51$	$75.15\pm 9.76$
Al	$6.3\pm 0.07$	$3.32\pm 0.82$
V	$2.15\pm 0.09$	$18.42\pm 8.01$
O	$0.95\pm 1.65$	$3.14\pm 4.07$

#### 4.2.1.2 Crystal and Phase of Ti64 Particles and Sheets

The crystal and phase structures of the Ti64 particles and sheet were confirmed by XRD analysis (Figure 4.19). It is seen that both Ti64 particles and sheet contain a mixture of  $\alpha$  (hexagonal) and  $\beta$  (body centered cubic) phase of Ti. No peak is attributed to the oxides of Ti, Al and V.

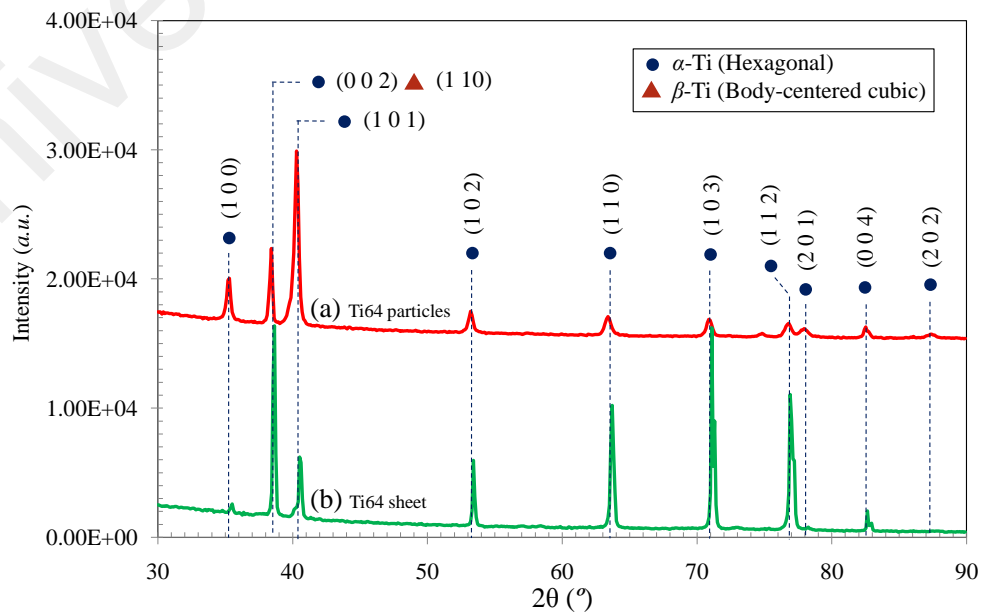


**Figure 4.19: XRD pattern of as-received (a) Ti64 particles and (b) Ti64 sheet.**

From the above observation it is concluded that the as-received Ti64 particles have irregular shape with an average particle size of 226.4  $\mu\text{m}$ . The composition of Al and V varies in the substrates within the acceptable range. Both the particles and sheets are composed of  $\alpha$  and  $\beta$  phase of Ti.

#### **4.2.2 Thermal Oxidation of Ti64**

The Ti64 particles and sheets were thermally oxidized under different conditions to optimize the growth process. For this reason, different parameters such as oxidation temperatures, alloy microstructures, oxidation environments, oxygen partial pressure, residual stress, oxidation duration have been investigated. In the following sections, the effects of the different parameter for 1-D growth on Ti64 substrates are presented.

##### **4.2.2.1 Effects of Oxidation Temperatures**

###### **(a) *Determination of oxidation temperature***

The oxidation temperatures of Ti64 particles were determined by TGA analysis as shown in Figure 4.20. It is seen that the oxidation of Ti64 particles started at 650 °C in commercial N<sub>2</sub> (flown at 200 sccm) and at 700 °C in ambient. The difference in initiating oxidation temperature is due to the difference in flow rates of commercial N<sub>2</sub> and ambient. Further oxidation experiments on Ti64 particles are conducted at temperatures of 650 °C and above.

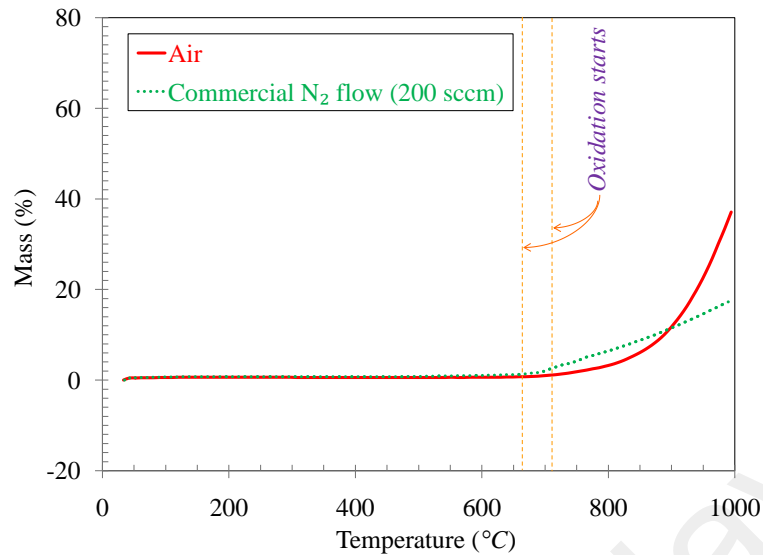


**Figure 4.20: TGA analysis of as-received Ti64 particles in ambient environment and commercial N<sub>2</sub> flow at 200 sccm.**

**(b) Oxidation of Ti64 particles at different temperatures**

The oxidation for 1-D growth on Ti64 particles was conducted at the temperatures of 650-900 °C for 8 h in presence of 40 ppm of O<sub>2</sub> in flowing Ar (500 sccm). The FESEM images of the oxidized particles at different temperatures are shown in Figure 4.21. The evidence of oxide scale is seen during oxidation at 650 °C as shown Figure 4.21(a). However, no 1-D nanostructure is seen on the surface during oxidation at 650 °C. Increasing the oxidation temperature to 700 °C shows 1-D nanostructures at certain locations (Figure 4.21(b)). Further increasing of the oxidation temperature to 750 °C shows homogeneously distributed 1-D nanostructures on the oxidized surface (Figure 4.21(c)). Increasing the oxidation temperatures to 800 and 850 °C reduces the density of 1-D nanostructures (Figure 4.21(d-e)). Moreover, thick 1-D nanostructures are seen as the temperature is increased from 750 to 850 °C (Figure 4.21(c-e)). Oxidation at 900 °C resulted in oxide scales instead of 1-D nanostructures (Figure 4.21(f)).

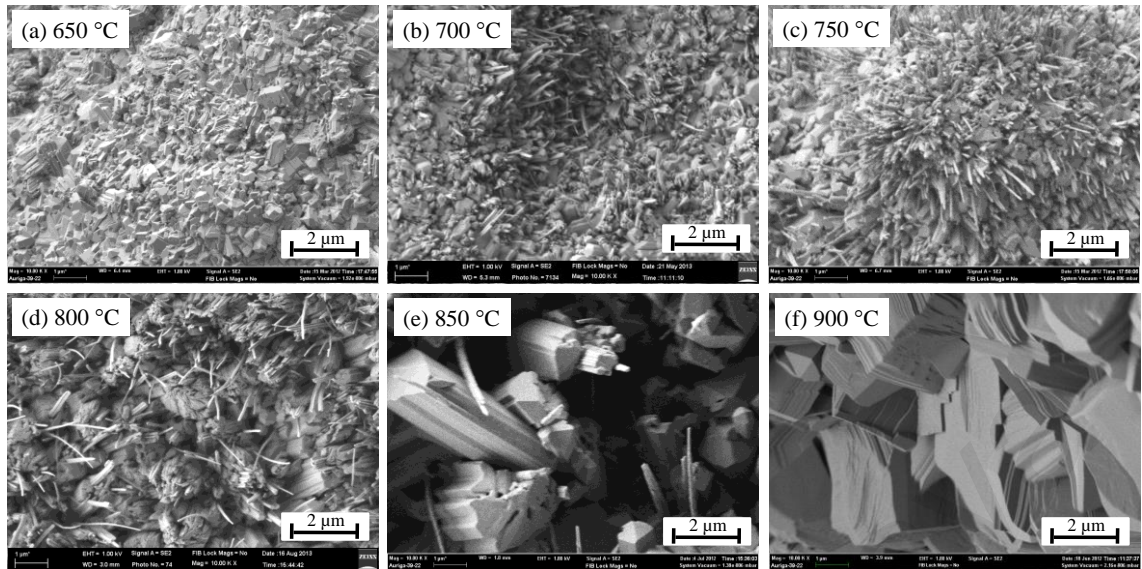


**Figure 4.21: Thermal oxidation of Ti64 particles with 40 ppm of O<sub>2</sub> in flowing Ar (500 sccm) for 8 h at different temperatures (a) 650 °C, (b) 700 °C, (c) 750 °C, (d) 800 °C, (e) 850 °C and (f) 900 °C.**

It can be seen from Figure 4.21 that homogeneously distributed fine 1-D nanostructures are grown at 750 °C during oxidation of Ti64 particles. For this reason, 750 °C is considered the optimum temperature and further experiments were conducted at this temperature.

#### 4.2.2.2 Effects of Alloy Microstructures

The microstructures of as-received Ti64 particles were altered by annealing the samples under different conditions. The alloy microstructures are characterized by optical microscope, FESEM and XRD. Different alloy microstructures of Ti64 are oxidized under similar conditions and the coverage of 1-D nanostructures are compared as discussed in the following sections.

##### (a) *Characterization of different phases in the microstructure*

To alter the alloy microstructures, the as-received Ti64 particles were heat treated in (Ar + 5% H<sub>2</sub>) environment at 1000 °C for 1 h and cooled at different conditions as depicted in Figure 3.2. One set of particles were normalized and another set of particles

were annealed. The as-received, normalized and annealed particles were characterized by XRD as shown in Figure 4.22. It is seen that all particles contains a mixture of  $\alpha$ - and  $\beta$ -Ti. No peak shift is observed and no peak of oxides of Ti is seen in XRD spectra. To find out the morphology of different phases, the particles were polished and etched followed by observation under optical microscope and FESEM.

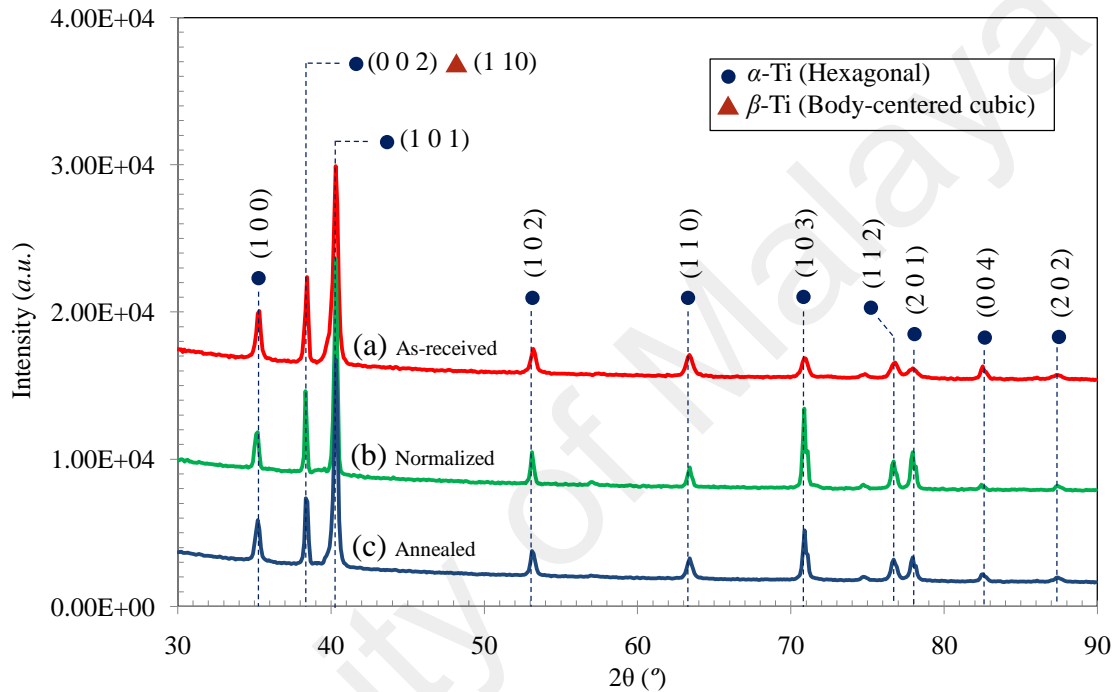


**Figure 4.22: XRD peaks of Ti64 particles in (a) as-received, (b) normalized and (c) annealed conditions.**

Figure 4.23 shows the optical and FESEM images of the polished as-received, normalized and annealed Ti64 particles. In Figure 4.23(a-b), the microstructure of as-received Ti64 particles is shown. It is seen that the particles contain lamellar structure. The dark regions in Figure 4.23(b) are confirmed as  $\alpha$ -Ti phase and the white lines are  $\beta$ -Ti phase (Xiao Li et al., 2013; I. Sen, Tamirisakandala, Miracle, & Ramamurty, 2007). In Figure 4.23(c-d), the optical and FESEM images of normalized particles are shown. It is observed that the normalized particles possessed Widmanstätten structure. The dark regions in the Widmanstätten structure shown in Figure 4.23(d) is  $\alpha$ -Ti whereas the white lines are  $\beta$ -Ti. The microstructure of the annealed particles is shown in Figure 4.23(e-f).

It is seen that the particles contain coarse grains of  $\alpha$ -Ti (dark regions) and  $\beta$ -Ti is precipitates at the grain boundaries (white regions).

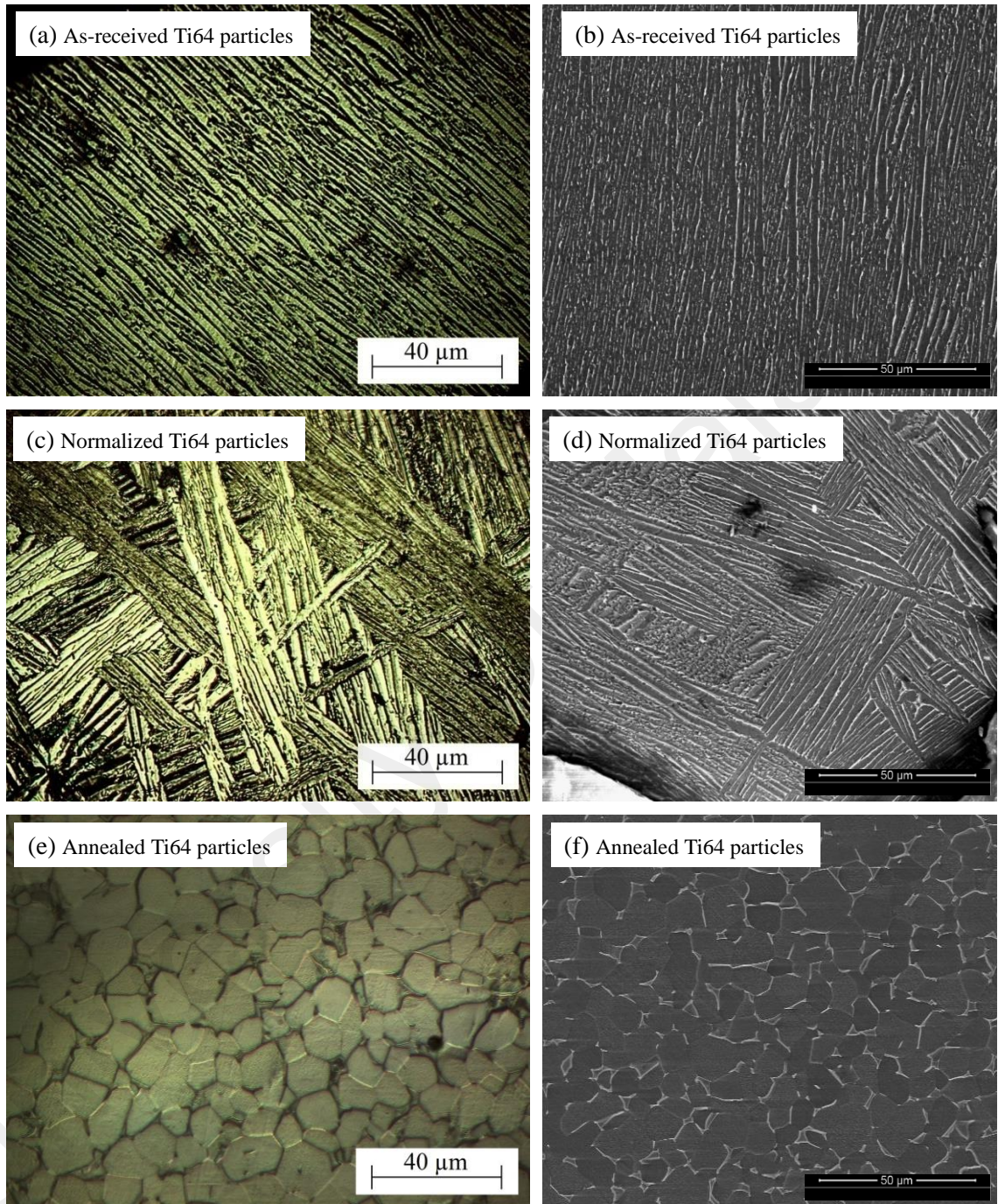


**Figure 4.23: Microstructures of polished and etched Ti64 particles in (a-b) as-received, (c-d) normalized and (e-f) annealed conditions.**

From the above observations it is concluded that the as-received and heat treated Ti64 particles contain  $\alpha$ - and  $\beta$ -phase of Ti but their distributions are different. The as-received

Ti64 particles contain lamellar structure whereas the normalized and annealed particles contain Widmanstätten and coarse grains of  $\alpha/\beta$  structure, respectively.

(b) *Thermal oxidation of Ti64 having different microstructures*

The as-received, normalized and annealed Ti64 particles were thermally oxidized at 750 °C for 4 h in presence of 15 ppm of O<sub>2</sub> in flowing Ar (500 sccm) and the FESEM images of the oxidized surface is shown in Figure 4.24. It is seen that the coverage of 1-D nanostructures on normalized particles is slightly higher compared with as-received particles (Figure 4.24(a-b)). On the other hand, no 1-D nanostructure is observed on the annealed Ti64 particles (Figure 4.24(c)).

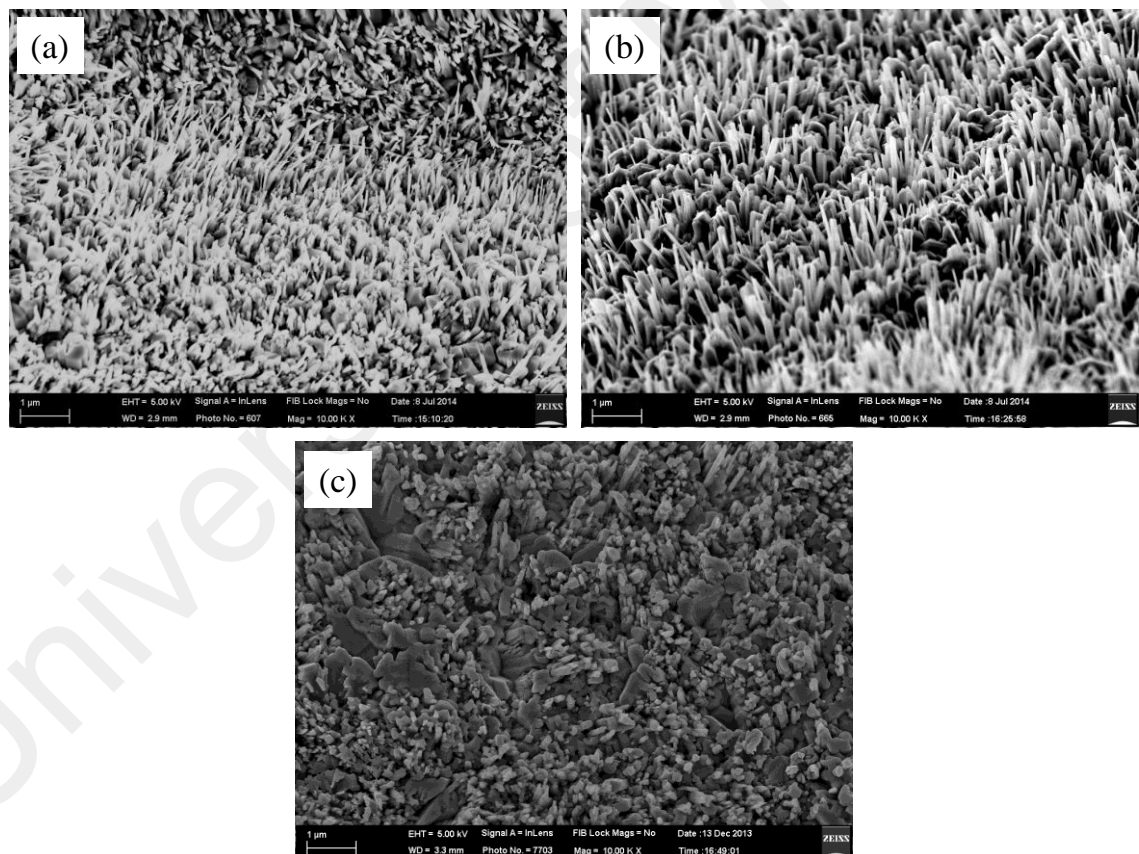


**Figure 4.24: FESEM images of the Ti64 particles oxidized at 750 °C for 4 h in presence of 15 ppm of O<sub>2</sub> in flowing Ar (500 sccm): (a) as-received, (b) normalized and (c) annealed particles.**

It is concluded from the above observation that lamellar and Widmanstätten structure is beneficial for the growth of 1-D nanostructures on Ti64 particles. It is proposed that

lamellar and Widmanstätten structures possessed residual stress due to their fine microstructures. It has been shown that residual stress enhances the 1-D growth during oxidation of Cu substrates (Mema et al., 2011; Yuan & Zhou, 2012). Similar scenario is anticipated in the present case where the residual stress is released during oxidation by forming new surfaces in the form of 1-D nanostructures (Kumar et al., 2004). However, annealed Ti64 particles possess no residual stress and for this reason no 1-D nanostructures are observed on annealed Ti64 particles during oxidation. The effect of stress on 1-D growth during oxidation of Ti64 particles is discussed in details in section 4.2.2.5.

#### 4.2.2.3 Effects of Oxidation Environment

It was observed that humid oxidation is beneficial for 1-D growth on Ti particles (Figure 4.6). No study reported the effect of humid oxidation on 1-D growth on Ti64 substrates. For this reason, the feasibility of 1-D growth on Ti64 particles during humid oxidation was investigated and compared in dry oxidation. For dry oxidation, the experimental set up shown in Figure 3.3 was used whereas for humid oxidation a water jar filled with 300 ml distilled water was placed and connected in between the gas mixture and quartz tube.

Figure 4.25 shows the FESEM image of the Ti64 particles oxidized for 4 h at 750 °C with 15 ppm of O<sub>2</sub> in humid Ar flown at a rate of 500 sccm. The humidity inside the quartz tube for 500 sccm flow of Ar is 93% as measured by Dinan *et al.* (B. Dinan, 2012). It is seen from Figure 4.25 that humid oxidation of as-received Ti64 particles yielded some short 1-D nanostructures with needle-like morphology. Some thick 1-D nanostructures are also seen. Comparing with dry oxidation of as-received particles under similar conditions (Figure 4.24(a)), sustainable amount of 1-D nanostructures are observed during dry oxidation compared with humid oxidation. This is in contrast with

the oxidation of pure Ti particles where opposite scenario is observed, i.e., 1-D nanostructures form during humid oxidation as shown in Figure 4.6. So, it is concluded that humid oxidation is not beneficial for 1-D growth on Ti64 substrates.

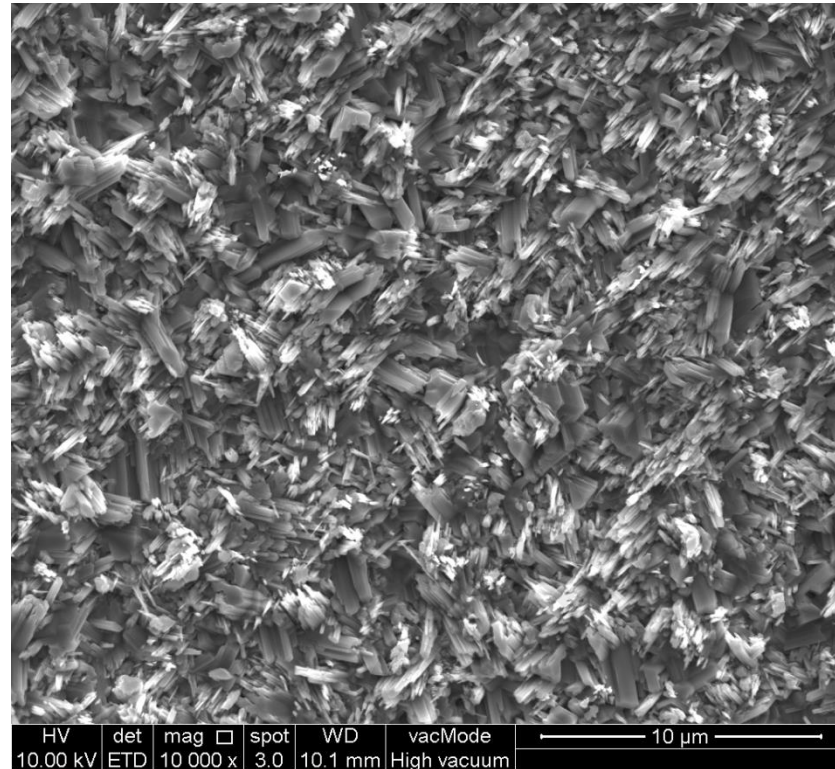


**Figure 4.25: FESEM images of the as-received Ti64 particles oxidized for 4 h at 750 °C in presence of 15 ppm of O<sub>2</sub> in flowing Ar (500 sccm).**

From the above observations it is seen that short and needle-like 1-D nanostructure is evolved during humid oxidation of Ti64 particles. Relevant literature survey shows that the oxidation rate of Ti-Al alloy is higher in humid condition compared with dry oxidation (Kremer & Auer, 1997). It was reported that a continuous and thick oxide scale composed of multi layers is formed during humid oxidation of Ti-Al alloy (Kremer & Auer, 1997). The outermost oxide scale is composed of TiO<sub>2</sub> and innermost oxide scale is a mixture of TiO<sub>2</sub> and Al<sub>2</sub>O<sub>3</sub>. Between the outermost and innermost oxide scales alumina precipitates as separate and large particles. Similar phenomena are anticipated for the humid oxidation of Ti64 particles in the present case. Due to possessing of thick and multi-layered oxide scales and containing alumina particles in between the oxide scales, the growth of 1-D

nanostructures is hindered. As a result, apparently no 1-D nanostructures are observed during humid oxidation of Ti64.

#### **4.2.2.4 Effects of Dynamic Oxygen Partial Pressure**

The Ti64 particles were thermally oxidized under different flow rates with various concentration of oxygen. The surface morphology of the particles after 4 h of oxidation at 750 °C is shown in Figure 4.26. For 20 sccm flow no 1-D nanostructure is seen for 5 ppm oxygen concentration as shown in Figure 4.26(a). But, 20 sccm flow combined with 105 ppm oxygen yields 1-D nanostructures (Figure 4.26(b)). With increasing the flow rate to 50 sccm, no 1-D nanostructure is seen for 5 ppm oxygen as seen in Figure 4.26(c). Increasing the oxygen concentration to 105 ppm shows high coverage of 1-D nanostructures (Figure 4.26(d)). For 500 sccm flow rate, the 1-D nanostructures are seen for 15 ppm of oxygen in Ar (Figure 4.26(e)). Increasing the oxygen concentration to 40 ppm in the flow, the coverage of 1-D nanostructures remained more or less the same (Figure 4.26(f)). But for 55 ppm of oxygen, almost no 1-D nanostructure grew (Figure 4.26(g)). For higher concentration of 80 and 105 ppm oxygen, oxide scale is seen instead of 1-D nanostructures (Figure 4.26(h-i)).

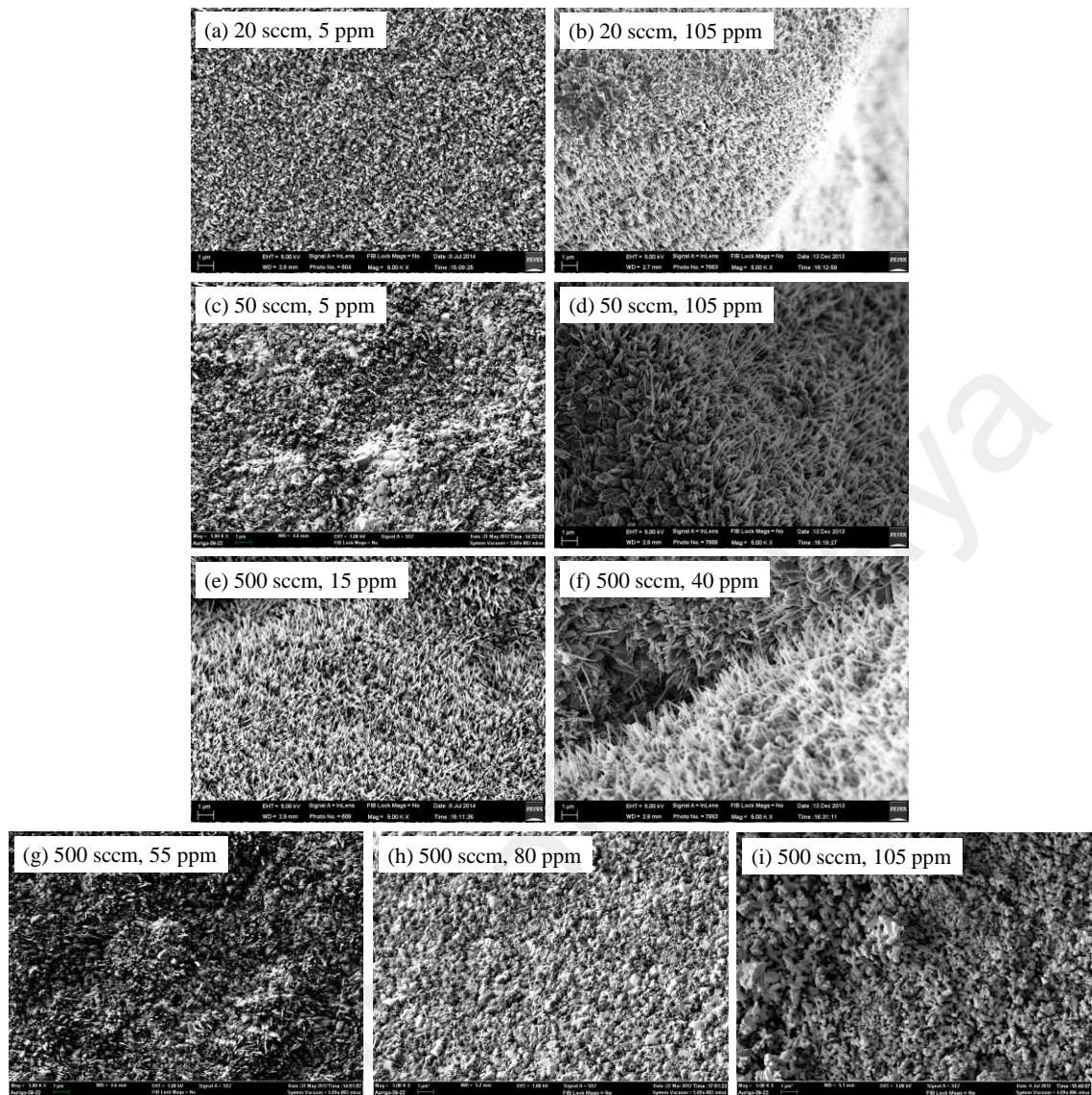


**Figure 4.26: FESEM images of the Ti64 particles oxidized at 750 °C for 4 h in (a) 20 sccm flow with 5 ppm O<sub>2</sub>, (b) 20 sccm flow with 105 ppm O<sub>2</sub>, (c) 50 sccm flow with 5 ppm O<sub>2</sub>, (d) 50 sccm flow with 105 ppm O<sub>2</sub>, (e) 500 sccm flow with 15 ppm O<sub>2</sub>, (f) 500 sccm flow with 40 ppm O<sub>2</sub>, (g) 500 sccm flow with 55 ppm O<sub>2</sub>, (h) 500 sccm flow with 80 ppm O<sub>2</sub> and (i) 500 sccm flow with 105 ppm O<sub>2</sub>.**

It is seen from the above observation that for some combinations of flow rate and oxygen concentration, 1-D nanostructures form on Ti64 particles. For other combinations, no 1-D nanostructure is seen. It is believed that oxygen partial pressure plays the vital role for the growth of 1-D nanostructures. According to the reconstructed Ellingham diagram shown in Appendix C (Ellingham, 1944), the partial pressure of oxygen for the oxidation of Ti at 750 °C is  $\sim 10^{-11}$  Pa. The partial pressure of oxygen for the oxidation of Al and V in Ti64 is not available in the literature. According to the

Ellingham diagram (Ellingham, 1944), the partial pressure of oxygen for the oxidation of pure Al and V at 750 °C is  $\sim 10^{-15}$  and  $\sim 10^{-10}$  Pa, respectively (Appendix C). So, it is likely that during oxidation of Ti64, Al requires lower oxygen partial pressure compared with Ti. For this reason, to oxidize the Ti in Ti64 alloy, the partial pressure of oxygen should be equal or more than  $\sim 10^{-11}$  Pa.

Theoretical calculation on dynamic oxygen partial pressure inside the tube is calculated according to equation 4.1 and 4.2 (derivation is shown in Appendix B). It is seen from equation 4.2 that the dynamic oxygen partial pressure depends linearly on the concentration of oxygen and squarely on the flow rate. The theoretical dynamic oxygen partial pressure for 20 sccm, 50 sccm and 500 sccm flow with 5 to 105 ppm O<sub>2</sub> is plotted in Figure 4.27. The experimental conditions for the oxidation of Ti64 particles presented in Figure 4.26 are shown by purple dots in Figure 4.27.

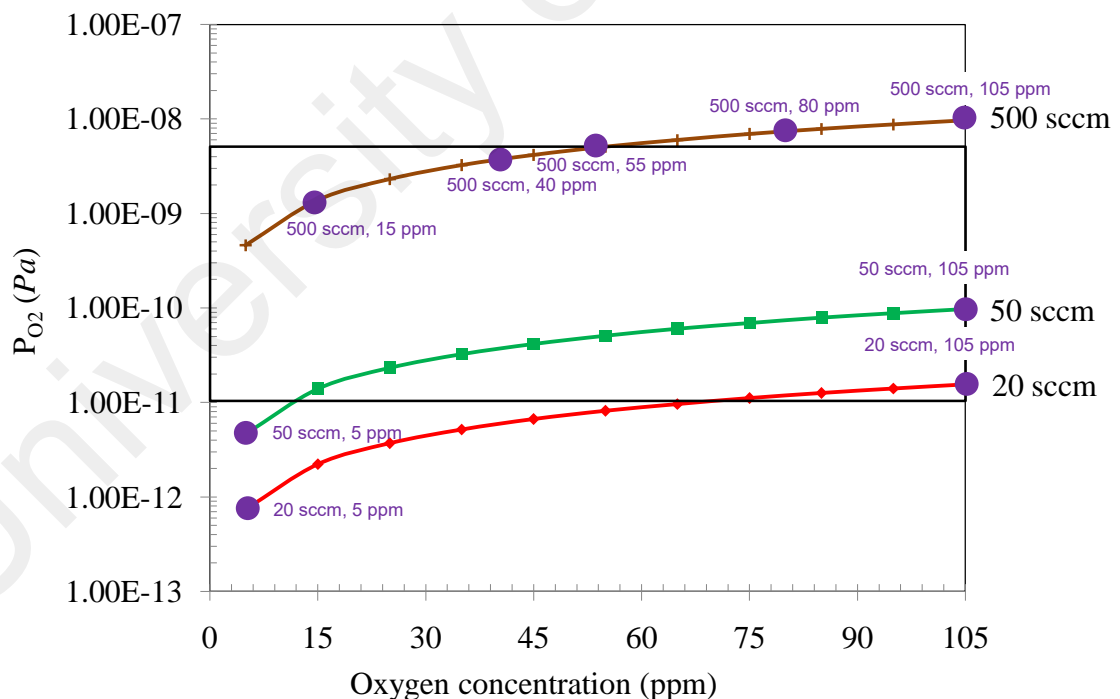


**Figure 4.27: Theoretical representation of dynamic oxygen partial pressure inside the tube for different flow rates and oxygen concentrations. The experimental conditions conducted on Ti64 particles are shown by purple color.**

In Figure 4.26(a) and (c), no 1-D nanostructure formed for 20 and 50 sccm flow containing 5 ppm of oxygen. It is seen in Figure 4.27 that the dynamic oxygen partial pressure for these conditions is below  $10^{-11}$  Pa. According to Ellingham diagram the minimum oxygen partial pressure required to oxidize Ti substrate at 750 °C is  $\sim 10^{-11}$  Pa (Ellingham, 1944). For this reason, no 1-D nanostructure is seen at these points. Though some oxide scales are seen at these conditions, it should be considered that Al oxidized at much lower oxygen partial pressure of  $10^{-15}$  Pa and the oxide scales might be attributed for the oxidation of Al.

The 1-D nanostructures are seen for 20 sccm flow with 105 ppm O<sub>2</sub>, 50 sccm flow with 105 ppm O<sub>2</sub>, 500 sccm flow with 15, 40 and 55 ppm of O<sub>2</sub> as seen in Figure 4.26. It is seen that the dynamic oxygen partial pressure at these point are above  $10^{-11}$  Pa (Figure 4.27). So, it is likely that the oxidation of Ti occurred at these experimental conditions and formed 1-D nanostructures. However, when the dynamic oxygen partial pressure approaches  $3 \times 10^{-9}$  Pa, the coverage of the 1-D nanostructures are greatly reduced.

During oxidation with 500 sccm flow containing 80 and 105 ppm O<sub>2</sub>, oxide scales are seen instead of 1-D nanostructures as seen in Figure 4.26(h-i). It should be noted that at this points the dynamic oxygen partial pressure is more than  $3 \times 10^{-9}$  Pa (Figure 4.27). The 1-D nanostructures are completely depleted at these points due to high dynamic oxygen partial pressure.

So, from the above observation it can be suggested that the minimum dynamic oxygen partial pressure requires for the oxidation of Ti in Ti64 substrates is  $\sim 10^{-11}$  Pa. For the growth of 1-D nanostructures, the dynamic oxygen partial pressure should be within the range of  $10^{-11}$ - $3 \times 10^{-9}$  Pa. Only within this range the coverage of 1-D nanostructures is seen. It is proposed that with limited supply of oxygen, the growth of as-grown nuclei occurs on certain directions resulting in 1-D nanostructure (Huyong Lee et al., 2010).

However, oxide scales are seen instead of 1-D nanostructures when the dynamic oxygen partial pressure is more than  $3 \times 10^{-9}$  Pa. It is assumed that at higher oxygen partial pressure, the growth of as-grown nuclei occurs in all directions resulting in oxide scale (Huyong Lee et al., 2010).

#### **4.2.2.5 Effects of Residual Stress on Oxidation**

It was observed by researchers that residual stress has significant role to enhance the 1-D coverage on Cu substrates (Mema et al., 2011; Yuan & Zhou, 2012). Similar, phenomenon is also observed for Ti particles where it is seen that imposing residual stress by milling of Ti particles increases the 1-D coverage (section 4.1.2.3). To evaluate the effect of residual stress on Ti64 particles for 1-D growth, the particles were milled for up to 30 h in a planetary ball milling machine. The milled particles were characterized under FESEM and EDX spectroscope. The residual stress inside the particles was measured by the XRD- $\sin^2\psi$  technique (Cullity & Stock, 2001; Fitzpatrick et al., 2005; Hauk, 1982). The particles were thermally oxidized and the coverage of 1-D nanostructures on as-received and milled particles is compared under FESEM. In another set of experiments, the residual stress inside the milled particles was released by annealing and the particles were oxidized under similar conditions to compare the 1-D coverage with stressed particles. Finally, to reconfirm the effect of residual stress, a Ti64 sheet was hammered at one end. Then the sheet was thermally oxidized and the coverage of 1-D nanostructures is compared with un-hammered end. In the following sections, the effect of residual stress on 1-D growth on Ti64 substrates is presented.

##### **(a) *Characterization of the milled particles***

To elucidate the effect of stress on 1-D growth, the Ti64 particles were milled for up to 30 h prior to thermal oxidation. The FESEM image of the milled particles is shown in

Figure 4.28(a-g). The FESEM image of the as-received Ti64 particles is shown in Figure 4.17(a). It is seen that the size of the particles was reduced progressively until 20 h of milling and after that the size of particles remains more or less constant. From now on the milling time will be used to designate the Ti64 particles. For example, as-received Ti64 particles will be represented as “Ti64-0h”, while particles subjected to 2, 5, 10, 15, 20, 25 and 30 hours of milling will be represented as Ti64-2h, Ti64-5h, Ti64-10h, Ti64-15h, Ti64-20h, Ti64-25h and Ti64-30h, respectively.

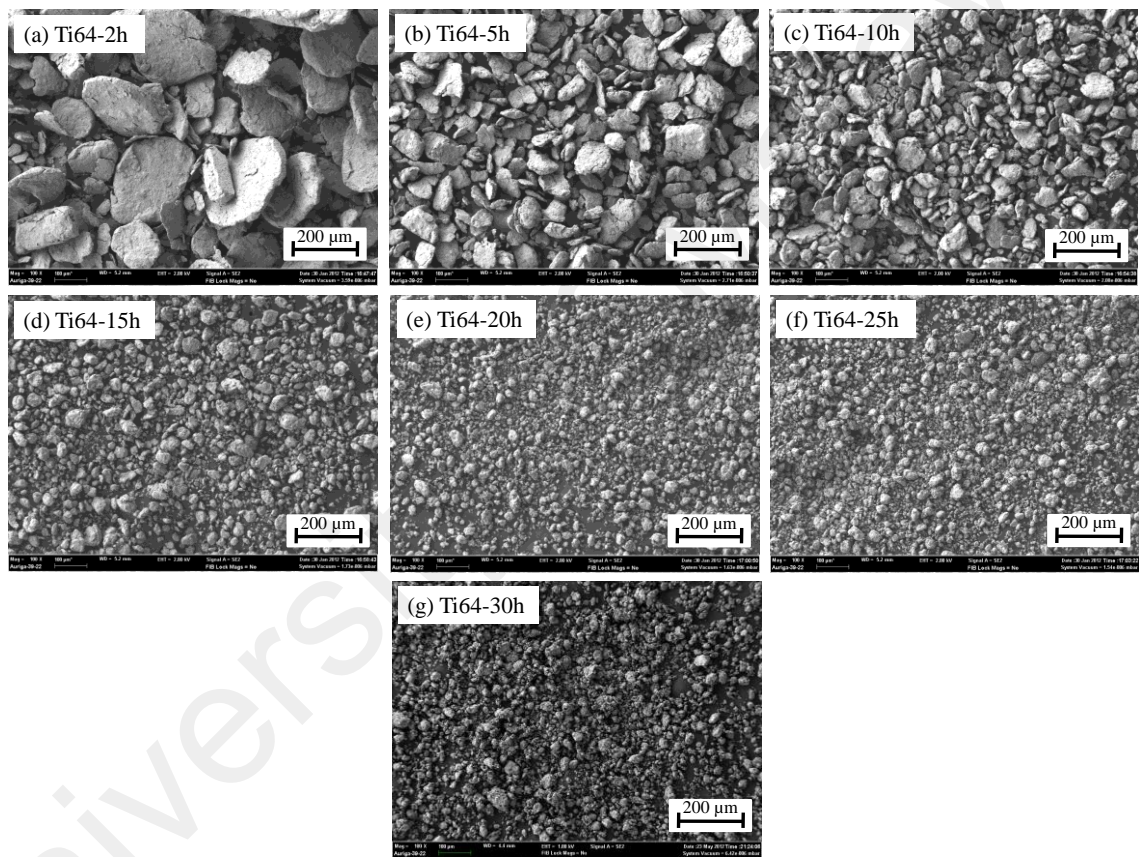


**Figure 4.28: FESEM images of Ti64 particles milled for (a) 2 h, (b) 5 h, (c) 10 h, (d) 15 h, (e) 20 h, (f) 25 h and (g) 30h.**

The size distribution and average size of the milled Ti64 particles were measured from FESEM images and the results are shown in Figure 4.29. It is seen that with the increase in milling time the peak of the particle size is shifted towards smaller size and the distribution became narrower as shown in Figure 4.29(a). Figure 4.29(b) shows the effect of milling time on the average size of Ti64 particles. The average size of the Ti64-0h

particles is 226.4  $\mu\text{m}$  which reduced to 15.5 and 14.4  $\mu\text{m}$  after 20 and 30 hours of milling, respectively. At the beginning of milling, the rate of size reduction is higher compared with the later stage (Figure 4.29(b)).

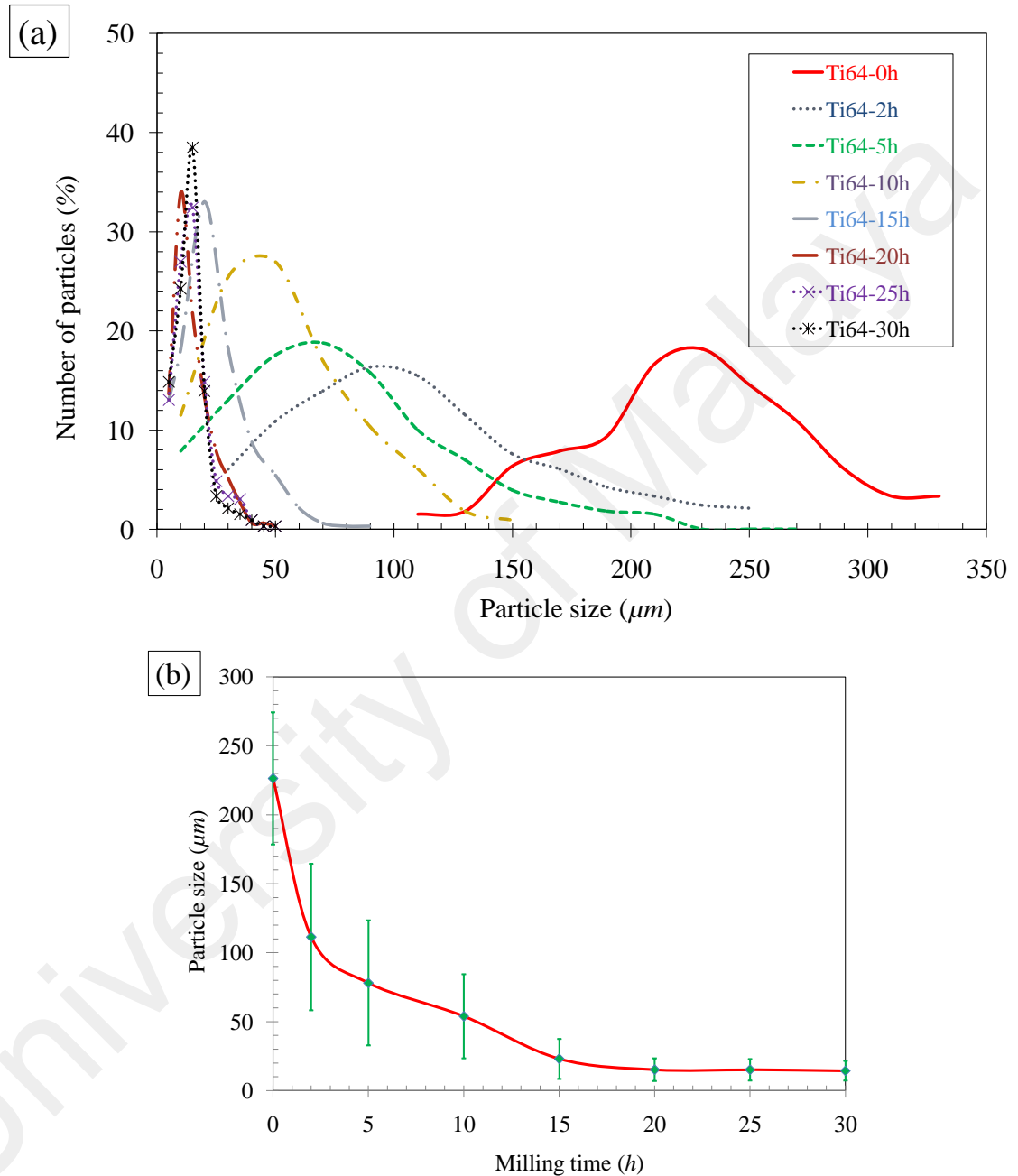


**Figure 4.29: (a) Distribution of particle size at different hours of milling and (b) effects of milling on the average size of Ti64 particles.**

The EDX spectrum of Ti64-20h particles is shown in Figure 4.30. Peaks from Ti, Al and V are evident in the EDX spectrum. However, small peaks of zirconium (Zr) and oxygen (O) are also seen which are attributed to the erosion of milling balls of  $\text{ZrO}_2$ . At

different spots of Ti64-20h particles the average amount of Zr was found to be  $4.1 \pm 1.6$  wt% by EDX analysis. Similar phenomenon of  $ZrO_2$  contaminations during long hours of milling is also reported in the literature (Kurajica et al., 2011). The peak of carbon (C) is attributed from carbon tape which was used to stick the Ti64 particles on FESEM sample holder.

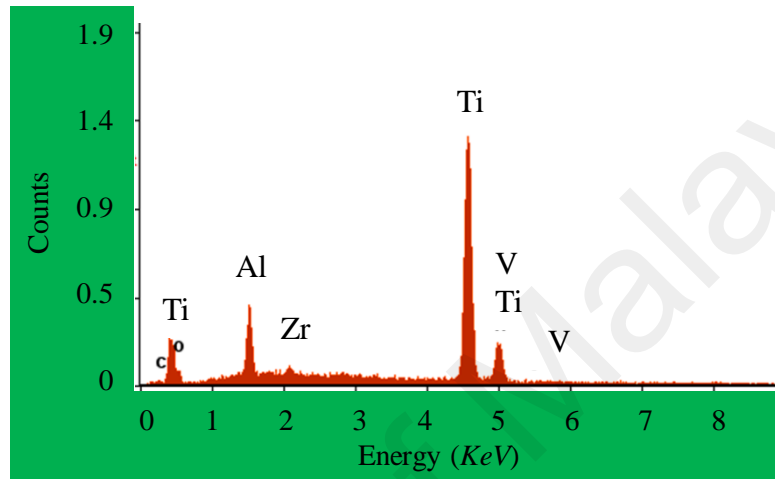


**Figure 4.30: EDX spectrum of Ti64 particles milled for 20 h (Ti64-20h particles).**

To study the changes in phases and crystal structures during milling, the Ti64-20h particles were scanned by XRD in  $2\theta$  region from  $30-90^\circ$  as shown in Figure 4.31. Both  $\alpha$  (hexagonal closed packed) and  $\beta$  (body centered cubic) phases of Ti is present in the milled particles which is similar to the XRD peaks of as-received Ti64 particles shown in Figure 4.19(a). However, a small peak of  $ZrO_2$  is also seen in the milled particles at  $2\theta$  angle of  $50.3^\circ$ . Comparing to the XRD peaks of as-received particles (Figure 4.19(a)), it is seen that the diffraction peaks become wider in milled particles. Broadening of peaks is a possible evidence of an accumulation of stress in the Ti64-20h sample, but can also be related to the size reduction of the particles.

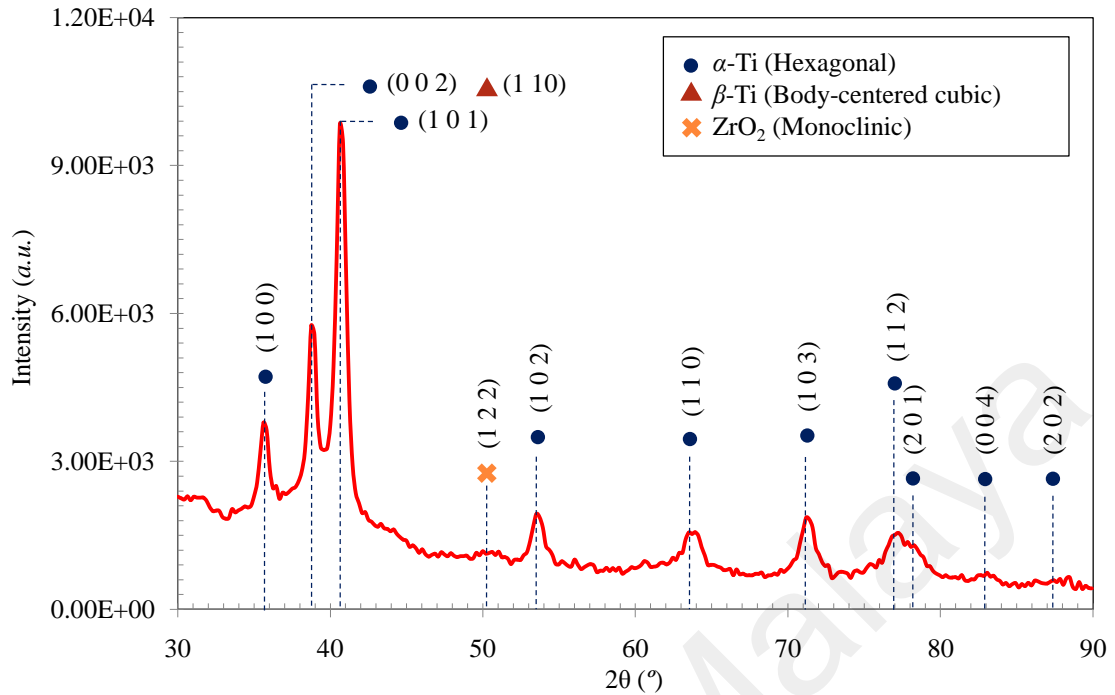


**Figure 4.31: XRD peaks of Ti64 particles milled for 20 h in planetary ball mill (Ti64-20h particles).**

**(b) Measurement of residual stress in as-received and milled Ti64 particles**

The residual stress inside Ti64 particles was measured by the XRD- $\sin^2\psi$  technique (Cullity & Stock, 2001; Fitzpatrick et al., 2005; Hauk, 1982). However, the diffraction angle was not chosen for (2 1 3) crystallographic plane at  $2\theta$  angle of  $141.7^\circ$  as recommended by Prev y *et al.* (Prev y, 1986) due to having insignificant intensity. The peak from the (1 0 3) crystal planes of  $\alpha$ -Ti that occurred at approximately  $71^\circ$  possessed all the properties required to determine the residual stress. This peak was selected to investigate further for residual stress measurement.

The Ti64-0h and Ti64-20h particles were scanned in  $2\theta$  region from  $70$ - $73^\circ$  at different tilt angles ( $\psi$ ) as shown in Figure 4.32(a-b). The tilt angles were varied from  $0$ - $40^\circ$ . For Ti64-0h sample, a peak shift was not evident at different  $\psi$  angles but it was obvious for the Ti64-20h sample. The lattice spacing ( $d$ ) was plotted against  $\sin^2\psi$  as shown in Figure 4.32(c). The residual stress of the particles was calculated by Equation 3.5 (Cullity & Stock, 2001; Fitzpatrick et al., 2005; Hauk, 1982). The value of the elastic constant  $[E/(1+$

$\psi$ ] for (1 0 3) crystallographic plane was assumed to be 87.8 GPa (Table 3.2). The slope of the  $d$ - $\sin^2\psi$  curve ( $m$ ) is calculated from Figure 4.32(c) and found to be -0.008 and 0.022 for Ti64-0h and Ti64-20h particles, respectively. Substituting these values into equation 3.5, the residual stresses obtained for Ti64-0h and Ti64-20h particles are -702.24 MPa (tensile) and +1931.2 MPa (compressive), respectively as presented in Figure 4.32(d).

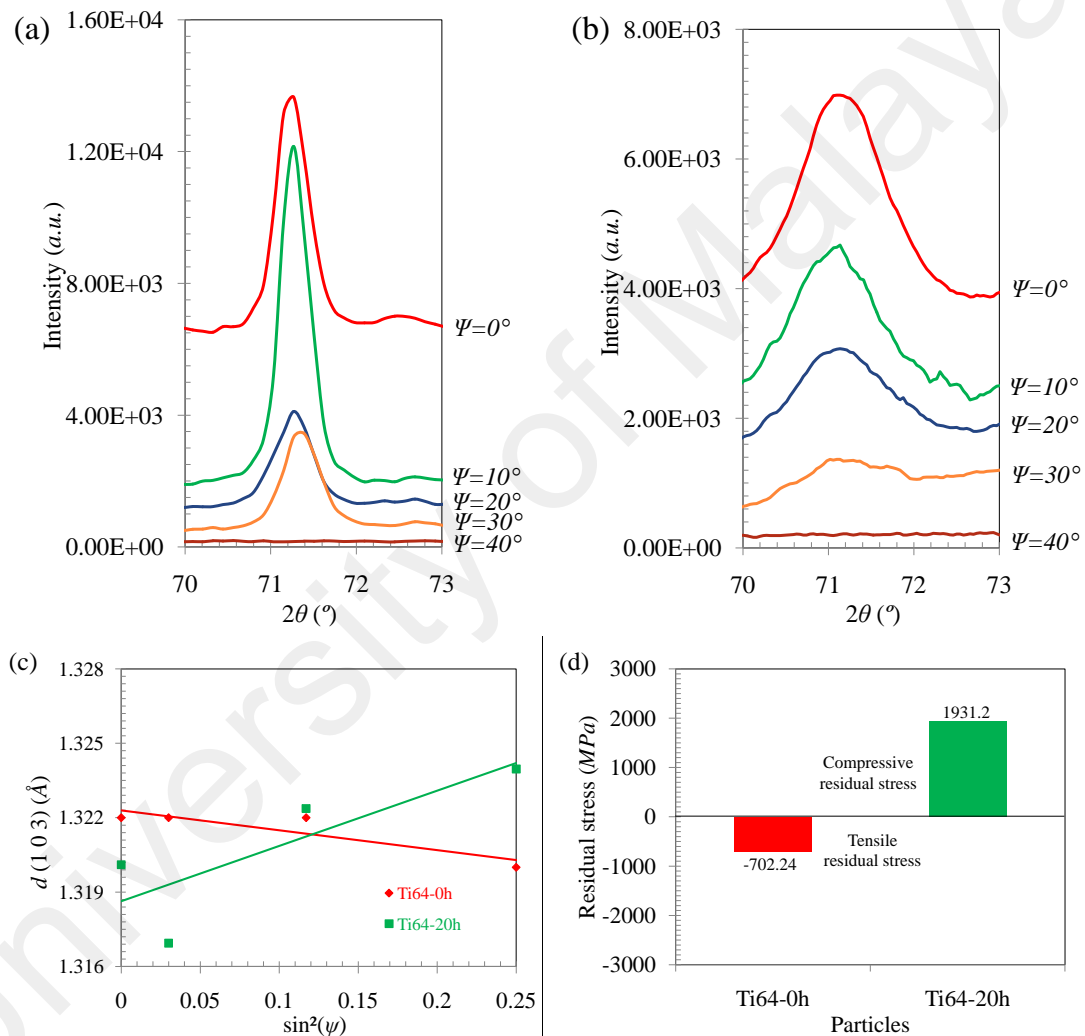


**Figure 4.32: (a) XRD peak of (1 0 3) plan in Ti64-0h particles, (b) XRD peak of (1 0 3) plan in Ti64-20h particles, (c)  $d$ - $\sin^2\psi$  plot for the Ti64-0h and Ti64-20h particles and (d) estimated residual stress inside the particles.**

According to literature, residual stress determined by the XRD- $\sin^2\psi$  method can contain uncertainty caused by errors in the diffraction peak measurement, nonlinear relation between lattice spacing ( $d$ ) and  $\sin^2\psi$  due to the grain interactions, anisotropic

elastic property of crystalline materials and instrumental setup (Luo & Jones, 2010; Prev y, 1996). Nonetheless, the estimated values show an accurate trend for the accumulation of stress in the milled samples.

(c) ***Thermal oxidation of as-received and milled Ti64 particles***

The as-received and milled Ti64 particles were thermally oxidized at 750  C for 8 h in presence of 40 ppm of O<sub>2</sub> in flowing Ar (under non-optimum conditions). 1-D nanostructures are seen in all particles with varying coverage as shown in Figure 4.33. The lowest coverage of 1-D nanostructures is observed on the Ti64-0h sample (Figure 4.33(a)). The coverage of 1-D nanostructures is increased with increasing the milling time until 20h (Figure 4.33(b-f)). For milling hours more than 20 h, the coverage of 1-D nanostructures remains more or less constant (Figure 4.33(g-h)). Thus, accumulation of residual stress by milling of the particles prior to oxidation is considered advantageous for 1-D growth.

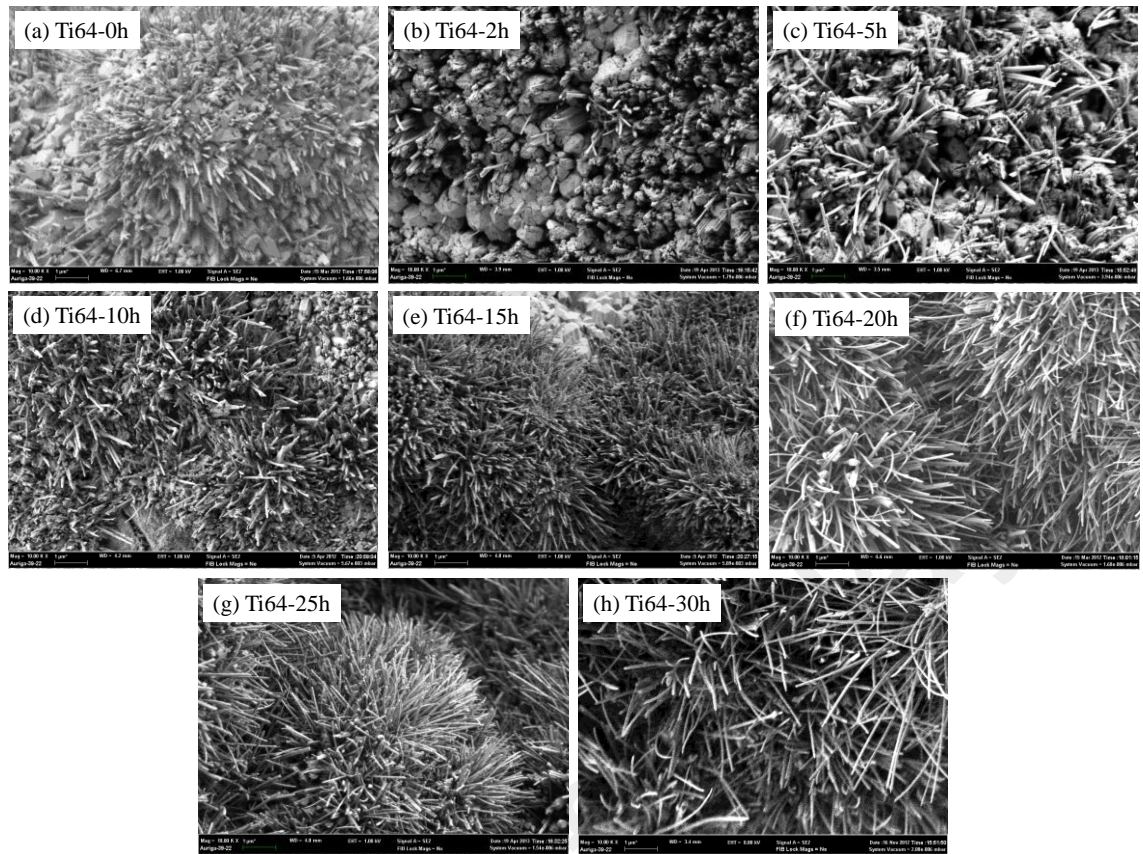


**Figure 4.33: FESEM micrographs of Ti64 particles after thermal oxidation for 8 hours at 750 °C with 40 ppm O<sub>2</sub> in flowing Ar (a) Ti64-0h, (b) Ti64-2h, (c) Ti64-5h, (d) Ti64-10h, (e) Ti64-15h, (f) Ti64-20h, (g) Ti64-25h and (h) Ti64-30h.**

To further elucidate the effect of stress, as-received and milled Ti64 particles were thermally oxidized under optimum conditions of 15 ppm of O<sub>2</sub> in flowing Ar for 4h. The oxidation temperatures were 750 °C and 800 °C. The FESEM images of the oxidized particles are shown in Figure 4.34. Similar observation as shown in Figure 4.33 is also observed for the oxidation under optimum conditions. It is seen that during oxidation at 750 °C, the 1-D nanostructures are short and have low coverage on Ti64-0h particles (Figure 4.34(a)). In many instances, the 1-D nanostructures are seen to be bundled as shown by the red circles in Figure 4.34(a). The coverage of 1-D nanostructures is seen to be increased on Ti64-20h particles during oxidation at 750 °C (Figure 4.34(b)). The 1-D nanostructures on Ti64-20h particles are finer, longer with higher coverage (Figure 4.34(b)). During oxidation at 800 °C, thick and short 1-D nanostructures are seen on Ti64-0h particles with very few thin 1-D nanostructures (Figure 4.34(c)). However, on Ti64-

20h particles, the diameter of thick 1-D nanostructures are slightly reduced and the number of thin 1-D nanostructures is increased during oxidation at 800 °C (Figure 4.34(d)).

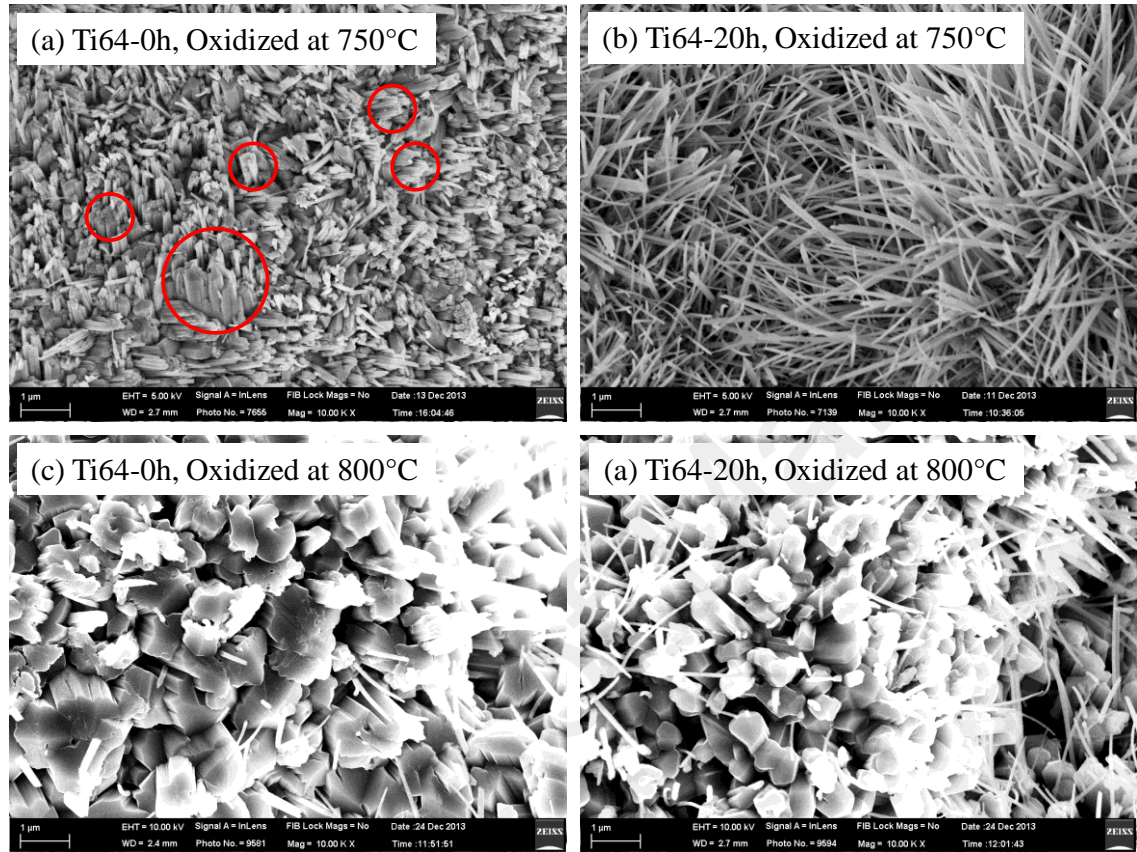


**Figure 4.34: FESEM images of Ti64 oxidized in presence of 15 ppm of O<sub>2</sub> in flowing Ar for 4 h (a) Ti64-0h particles oxidized at 750 °C, (b) Ti64-20h particles oxidized at 750 °C, (c) Ti64-0h particles oxidized at 800 °C and (d) Ti64-20h particles oxidized at 800 °C.**

It was proposed that at the initial stage of oxidation the diameter of the metal oxide nuclei depends on the surface stress of the substrate (Choopun, Wongrat, & Hongstith, 2010). High surface stress resulted in smaller diameter of the as-grown nuclei (Choopun et al., 2010). In the present case, the residual stress is high in the milled particles as shown in Figure 4.32. For this reason, the diameter of the 1-D nanostructures is smaller on Ti64-20h particles during oxidation at 750° and 800° C as seen in Figure 4.34. The 1-D nanostructures appear to be bundled on as-received particles due to having larger diameter of 1-D nanostructures.

It was reported that at the initial stage the number of metal oxide nuclei depends on the oxidation temperatures (Choopun et al., 2010). Higher number of nuclei forms during high temperature oxidation. The nuclei are coalesced at high temperatures due to their close proximity for reducing the surface energy. As a result, nuclei having larger diameter are formed. For this reason, 1-D nanostructures possessing of thick dimensions are seen at high temperature oxidation as shown in Figure 4.34(c-d).

**(d) Oxidation of relaxed Ti64 particles**

To investigate the effect of stress relaxation, Ti64-20h particles were annealed at 1000 °C for 3 h prior to thermal oxidation in presence of (Ar + 5% H<sub>2</sub>) environment flowing at a rate of 20 sccm. After that the particles were cleaned by 30 vol% of HCl to remove any oxides formed during the annealing process. Then the particles were observed under FESEM and characterized by EDX spot analysis as shown in Figure 4.35. It reveals that the size of the Ti64-20h particles remains more or less constant during the annealing process with an average size of 20 μm (Figure 4.35(a)). The EDX spot analysis shows the presence of Ti, Al and V with the presence of Zr, O. It should be noted that ZrO<sub>2</sub> balls were used during milling of Ti64 particles. The peaks of Zr and O are attributed for the presence of ZrO<sub>2</sub> particles in the milled powders. The peak of C is obtained from the carbon tape used to hold the particles on FESEM sample holder.

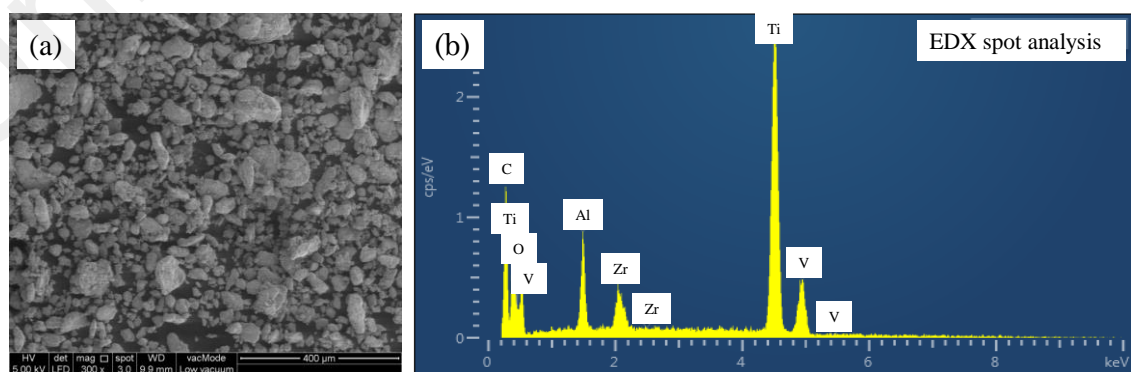


**Figure 4.35: (a) FESEM image of the Ti64-20h particles after heat treatment at 1000 °C for 3 h in presence of flowing Ar+5%H<sub>2</sub> environment and (b) EDX spectrum of the heat treated Ti64-20h particles.**

The residual stress of the heat treated Ti64-20h particles was measured by XRD- $\sin^2\psi$  technique (Cullity & Stock, 2001; Fitzpatrick et al., 2005; Hauk, 1982). In this case peak from the (2 1 3) crystal planes of  $\alpha$ -Ti was scanned in the  $2\theta$  region from 140-146° at different tilt angles ( $\psi$ ) ranging 0-40° as shown in Figure 4.36(a). The slope of the  $d$ - $\sin^2\psi$  curve ( $m$ ) is calculated from Figure 4.36(b) and found to be -0.002. Substituting the values of elastic constant [ $E/(1+\nu)$ ] for (2 1 3) crystallographic plane in Ti64 (84.1 GPa) and  $m=-0.002$  in equation 3.5, it is found that the residual stress in the annealed Ti64-20h particles is -168.2 MPa (tensile). It should be noted that the residual stress in the Ti64-20h particles before heat treatment was +1931.2 MPa (compressive).

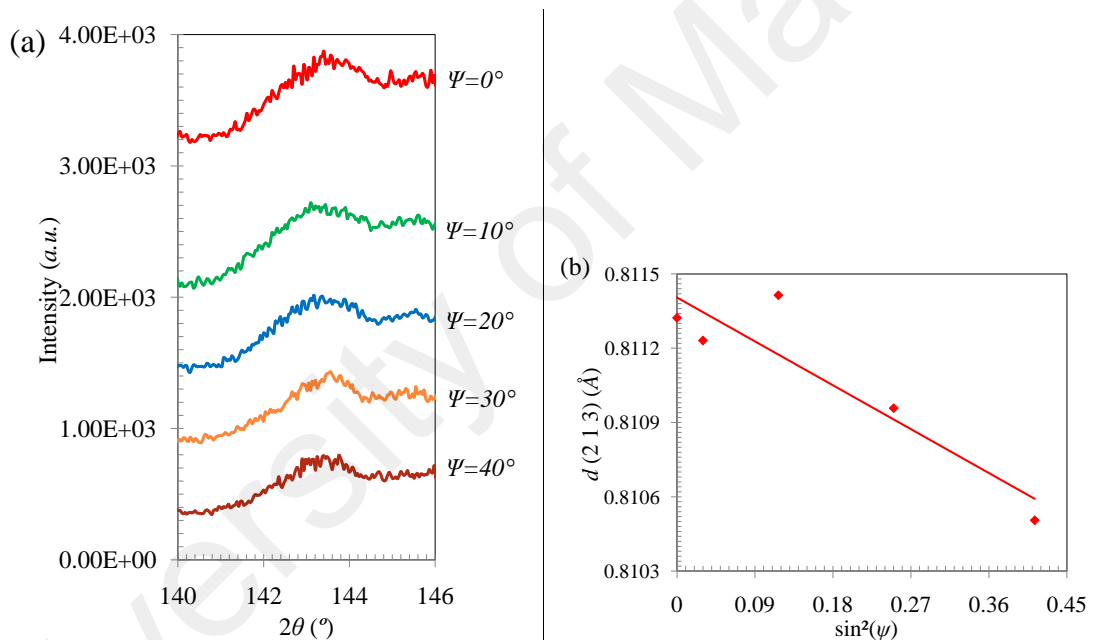


**Figure 4.36: (a) XRD peak of (2 1 3) plan in stress relaxed Ti64-20h particles, (b)  $d$ - $\sin^2\psi$  plot for the stress relaxed Ti64-20h particles.**

The heat treated Ti64-20h particles were thermally oxidized under optimum conditions of 750 °C in presence of 15 ppm of  $O_2$  in flowing Ar for 4 h and the FESEM image is shown in Figure 4.37. It is seen that the coverage of 1-D nanostructures is greatly reduced in the heat treated Ti64-20h particles due to the reduction of compressive residual stress. So, it is concluded that residual stress imposed by milling is beneficial for 1-D growth on Ti64 substrates during thermal oxidation.

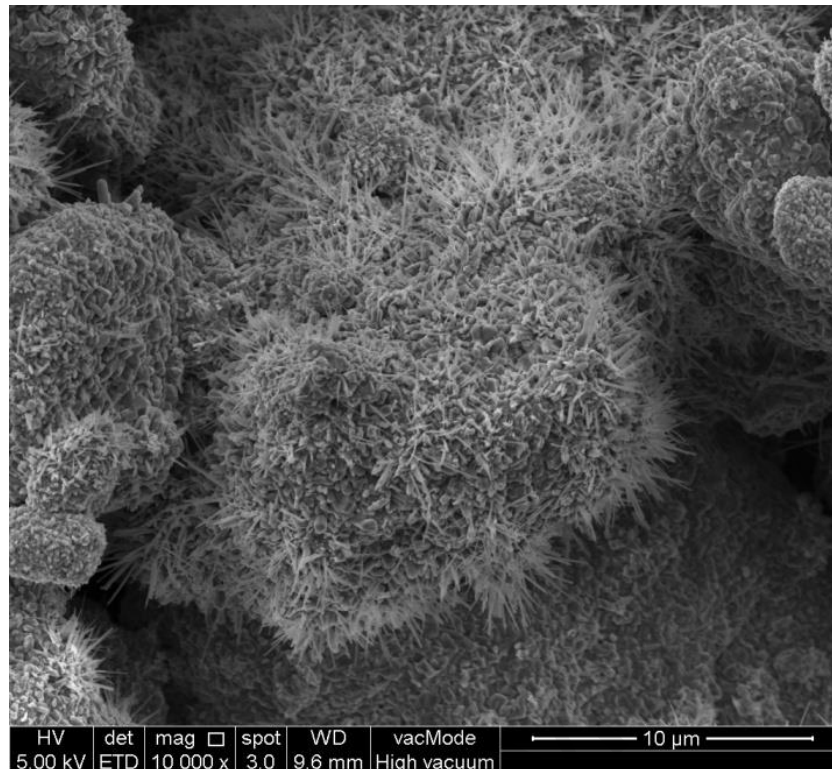


**Figure 4.37: FESEM image of the heat treated Ti64-20h particles oxidized at 750 °C in presence of 15 ppm of O<sub>2</sub> in flowing Ar for 4 h.**

**(e) *Thermal oxidation of hammered Ti64 sheet***

To reconfirm the observed effects of stress on 1-D growth, a Ti64 sheet having a dimension of 25 mm X 3 mm X 1 mm was hammered at one end until the compressive strain value of 0.6 of the original sample thickness was achieved as shown in Figure 4.38(a). The other end was un-hammered resulting in zero strain. The non-uniform deformation resulted in a stress gradient along the length of the sheet as can be seen in Figure 4.38(a). Oxidation was carried out at 750 °C for 8 hours with 40 ppm oxygen flow (under non-optimum conditions). After oxidation, the Ti64 sheet was characterized by FESEM at different positions as shown in Figure 4.38(b-g). As can be seen from Figure 4.38(b), no 1-D nanostructure is observed at the un-hammered end (position 1). The surface was occupied by faceted grains. At position 2, the formation of some 1-D nanostructures is seen (Figure 4.38(c)). Coverage of 1-D nanostructures is further increased at position 3 where the strain reached a value of 0.3 (Figure 4.38(d)). It is also

observed that at this position the 1-D nanostructures are bundled in many instances. The 1-D nanostructures become longer at position 4 where the strain reached a value of 0.4 as shown in Figure 4.38(e). The bundled structures are more evident at this position. Further increase of strain to 0.5 at position 5, it is seen that some of the bundled structures are separated as seen in Figure 4.38(f). Finally, the highest coverage of 1-D nanostructures is found at position 6 (Figure 4.38(g)) where the strain was maximum and calculated to be 0.6.

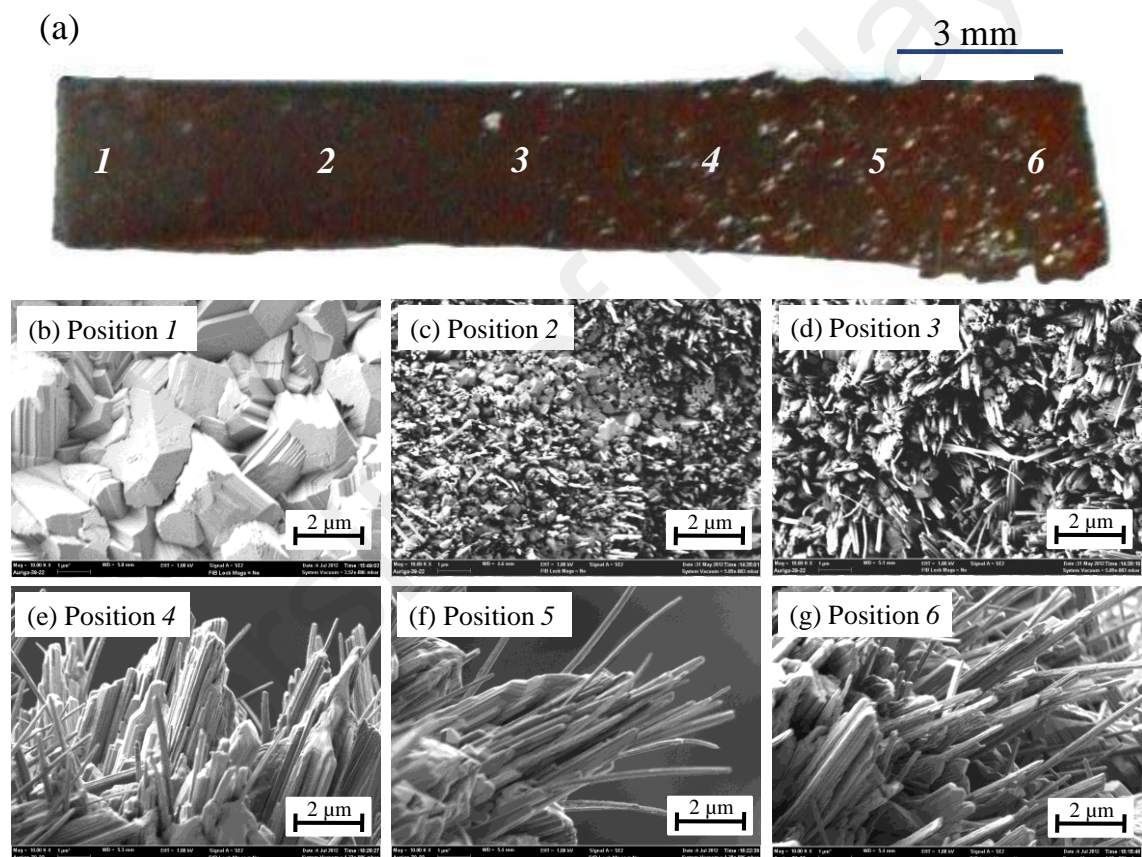


**Figure 4.38: (a) Ti64 sheet (25mm x 3 mm x 1 mm), and FESEM micrograph on the Ti64 sheet after thermal oxidation at 750 °C for 8 hours with 40 ppm oxygen in flowing Ar at (b) position 1, (c) position 2, (d) position 3, (e) position 4, (f) position 5, (g) position 6.**

It is seen from the above observation that incorporation of residual stress by hammering also improves the 1-D coverage on Ti64 sheet. The 1-D coverage is increased with the increase of strain along the length of Ti64 sheet. It is thus, stress clearly plays a significant role in the induced growth of 1-D nanostructures.

(f) ***Role of stress during oxidation***

It is seen that under optimum conditions the as-grown nanostructures are bundled together on low stressed substrates such as Ti64-0h particles (Figure 4.34). However, inducing residual stress by milling separates the 1-D nanostructures and resulted in fine and long 1-D nanostructures as seen on Ti64-20h particles. The exact mechanism of the growth of fine 1-D nanostructures is unknown but it is clear that the presence of residual stress significantly enhances the coverage of 1-D nanostructures on Ti64 substrates. Similar kind of stress induced 1-D growth was seen on copper (Cu) (Kumar et al., 2004; Mema et al., 2011; Yuan & Zhou, 2012) and iron (Fe) (Yuan et al., 2012) substrates during thermal oxidation. This type of stress-induced growth mechanism of whiskers was first proposed by Eshelby (Eshelby, 1953). According to Kumar *et al.* (Kumar et al., 2004), during initial stage of oxidation of Cu, stress build up between the CuO and Cu<sub>2</sub>O layer formed on the surface of the substrate due to the difference in crystallographic structures, molar volumes and densities. The stressed surface released its residual stress by creating new surfaces such as 1-D CuO nanostructures.

In the present case of Ti64 oxidation, this stress induced mechanism is evident because higher coverage of fine and long 1-D nanostructure is found in the samples subjected to higher duration of milling (Figure 4.33 and 4.34) and hammering (Figure 4.38). It is seen that on low stress substrates, the 1-D nanostructures were bundled together (Figure 4.34(a) and 4.38(e-f)). But inducing residual stress by milling or hammering creates new surfaces by separating the bundled structures (Figure 4.34(b) and 4.38(g)). It is assumed that the residual stress in the milled or hammered substrates is released during oxidation by creating more surfaces resulting in high coverage of fine and long 1-D nanostructures.

#### 4.2.2.6 Effects of Oxidation Duration

The effect of oxidation duration on Ti64 substrate is not studied in the literature. Most of the research in the literature were conducted up to 8 hours and the state of oxide nanostructures beyond this time frame was not investigated. No study is also conducted focusing on the oxide nanostructures at the early stage of oxidation. For this reason, in the following sections the effects of oxidation duration on Ti64-0h and Ti64-20h particles is investigated. The oxidation time was varied from 1 min to 24 h. The particles were oxidized under optimum conditions.

##### (a) *Oxidation of as-received Ti64 particles*

The Ti64-0h particles were thermally oxidized under optimum conditions of 750 °C in presence of 15 ppm of O<sub>2</sub> in flowing Ar (500 sccm) for variant duration of time. It should be noted that the Ti64-0h particles possess lamellar microstructures consisting of  $\alpha$ - and  $\beta$ -Ti phase as shown in Figure 4.23(a-b). The Ti64-0h particles were thermally oxidized for up to 24 h and the FESEM images of the oxidized particles are shown in Figure 4.39. It is seen that during initial stage of oxidation up to 15 min, the 1-D nanostructures are seen mainly on  $\beta$  laths of Ti64 particles (Figure 4.39(a-c)). This finding is in agreement with Lee *et al.* (Huyong Lee et al., 2010), who observed the preferential growth of 1-D nanostructures on  $\beta$  laths of Ti-6.85Al-1.6V substrate. Oxidation for 30 min to 4 h resulted in the 1-D nanostructures on both  $\alpha$  grains and  $\beta$  laths as seen in Figure 4.39(d-g). Further increase of oxidation duration for up to 8 h resulted in the decrease of the coverage of 1-D nanostructures (Figure 4.39(h)). Very few 1-D nanostructures are seen for the oxidation duration of 16 h and it is mainly seen on  $\alpha$  grain in Ti64 particles (Figure 4.39(i)). No 1-D nanostructure is seen on  $\beta$  laths of Ti64-0h particles for the oxidation of 16 h. Finally, no 1-D nanostructure is seen on Ti64-0h particles for the oxidation duration of 24 h as shown in Figure 4.39(j).

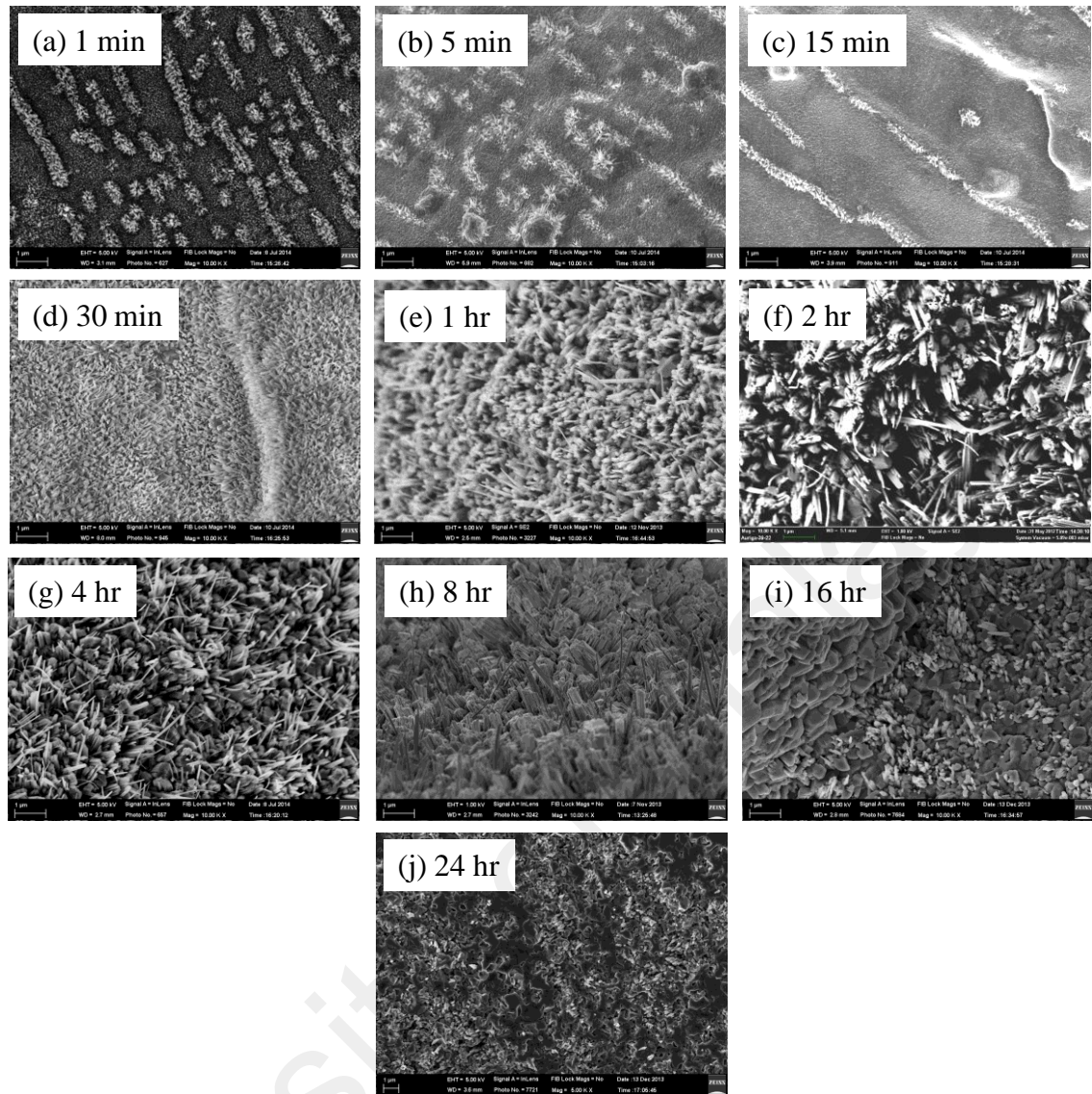


**Figure 4.39: FESEM images of thermally oxidized Ti64-0h particles under optimum conditions of 750 °C in presence of 15 ppm of O<sub>2</sub> in flowing Ar (500 sccm) for variant duration of time (a) 1 min, (b) 5 min, (c) 15 min, (d) 30 min, (e) 1 h, (f) 2 h, (g) 4 h, (h) 8 h, (i) 16 h and (j) 24 h.**

So, from the above observation it is clear that during initial stage of oxidation (0-15 min), 1-D nanostructures are seen mainly on  $\beta$  laths of Ti64 particles. The 1-D nanostructures on  $\alpha$  grains are not fully grown for short oxidation time. Increasing the oxidation time (30 min - 4 h) resulted in fully grown 1-D nanostructures on both  $\alpha$  grains and  $\beta$  laths of Ti64 particles. With further increase of oxidation duration (8-16h), the 1-D nanostructures on  $\beta$  laths are sintered together and 1-D nanostructures are seen only on  $\alpha$  grains. Finally, for 24 h of oxidation the 1-D nanostructures on  $\alpha$  grains are also sintered

and no 1-D nanostructure is seen on the Ti64-0h particles. It should be noted that similar observation was reported for Cu oxidation by Wu *et al.* (F. Wu et al., 2014) where it was shown that the coverage of 1-D nanostructures decreased after reaching an optimum value at 5 h of oxidation duration.

To investigate the reason of preferential growth of 1-D nanostructures on  $\beta$  laths for short oxidation period, the Ti64-0h particles were line scanned after oxidation. Figure 4.40 shows the line scan of the Ti64-0h particles oxidized for 1 min under optimum conditions. The 1-D nanostructures are seen on the  $\beta$  laths of the Ti64 particles. From lateral line scanning it is seen that the counts for oxygen is higher in the  $\beta$  laths compared to the  $\alpha$  grains. So, it is concluded that the oxidation rate is higher on the  $\beta$  laths and for this reason 1-D nanostructures are initiated on  $\beta$  laths during initial stage of oxidation.

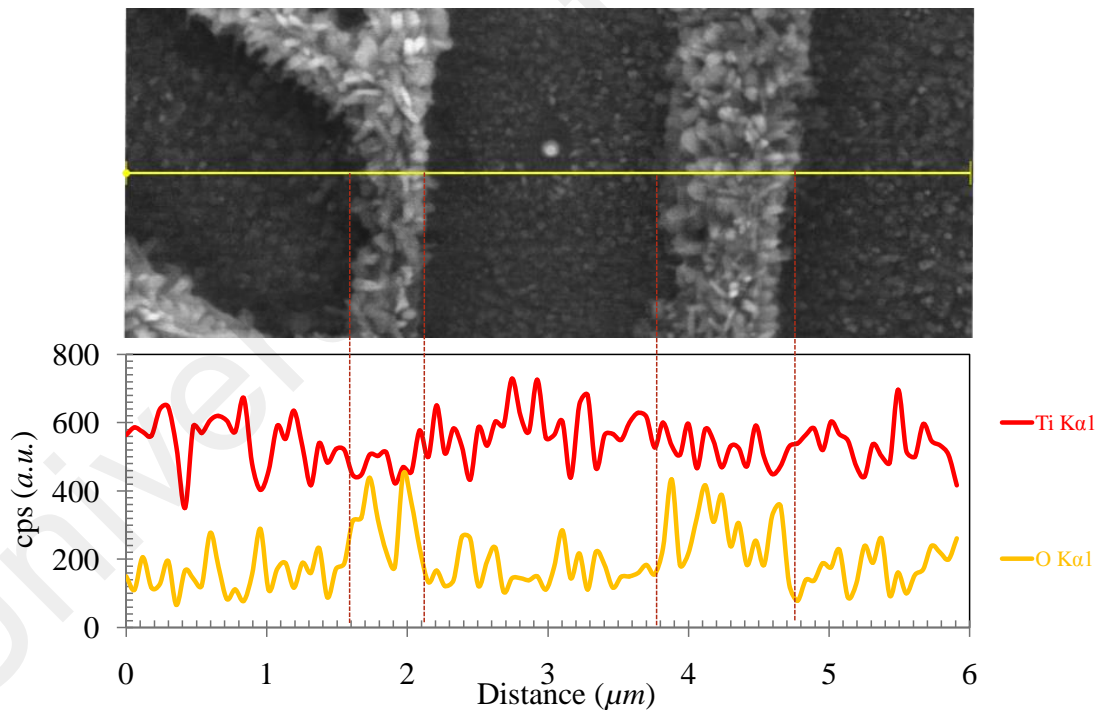


**Figure 4.40: Line scanning of Ti64-0h particles oxidized for 1 min at 750 °C in presence of 15 ppm of O<sub>2</sub> in flowing Ar (500 sccm).**

**(b) Oxidation of milled Ti64 particles**

The Ti64-20h particles were thermally oxidized in a similar condition mentioned previously at temperature of 750 °C in presence of 15 ppm of O<sub>2</sub> in flowing Ar (500

sccm). The oxidation time was varied from 1 min to 24 h and the FESEM image of the oxidized Ti64-20h particles is shown in Figure 4.41. During initial stage of oxidation at 1 min, the whole surface is oxidized homogeneously and 1-D nanostructures nucleated randomly from all over the surface (Figure 4.41(a)). With increasing oxidation time for up to 30 min, the nucleated 1-D nanostructures become thicker as seen in Figure 4.41(b-d). The nucleated 1-D nanostructures are about 200 nm long for the oxidation time of 1 h as seen in Figure 4.41(e). For further increase of oxidation duration to 2 h, the length of 1-D nanostructures is increased (Figure 4.41(f)). It should be noted that for better understanding low magnification images are used for long duration of oxidation. The length and coverage of 1-D nanostructures is highest for 4 h of oxidation as seen in Figure 4.41(g). For further oxidation of 8 and 16 h, the coverage and length of 1-D nanostructures are decreased (Figure 4.41(h-i)). Finally for 24 h of oxidation, very few 1-D nanostructures are seen only at some locations (Figure 4.41(j)).

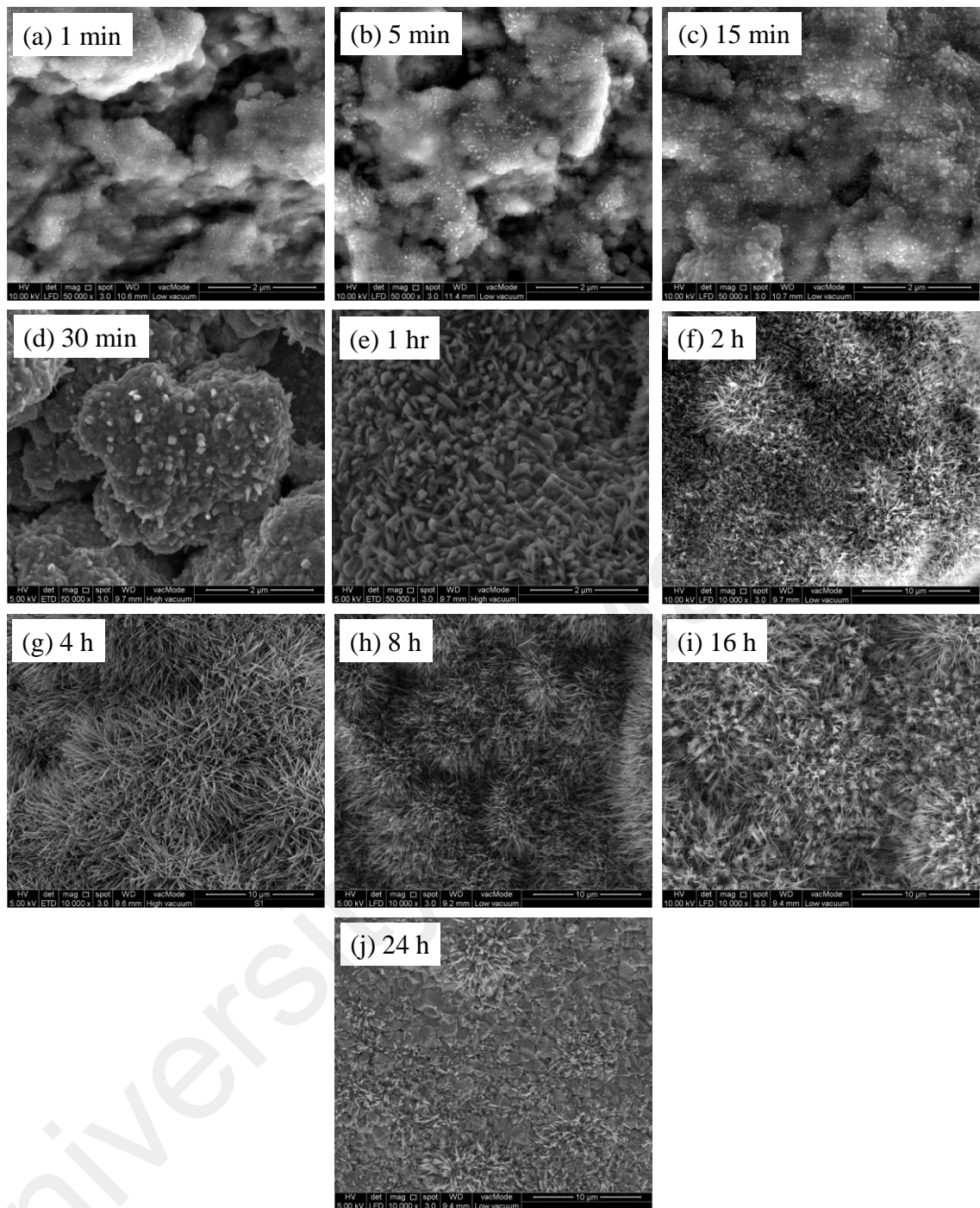


**Figure 4.41: FESEM images of thermally oxidized Ti64-20h particles under optimum conditions of 750 °C in presence of 15 ppm of O<sub>2</sub> in flowing Ar (500 sccm) for different time periods: (a) 1 min, (b) 5 min, (c) 15 min, (d) 30 min, (e) 1 h, (f) 2 h, (g) 4 h, (h) 8 h, (i) 16 h and (j) 24 h.**

It is seen from the above observation that for the as-received Ti64 particles the 1-D nanostructures are initiated from the  $\beta$  laths at the early stage of oxidation due to their higher oxidation rate. At the later stage the 1-D nanostructures are evolved from  $\alpha$  phase of Ti64 particles. It should be noted that due to milling the  $\beta$  laths in Ti64 particles are

distributed all over the surface. For this reason, the nucleation of 1-D nanostructures is distributed all over the surface which resulted in homogeneous distribution of 1-D nanostructures. With increasing the oxidation time up to 4 h, the length and coverage of 1-D nanostructure is increased and after that the coverage is decreased. So, long term of oxidation is not beneficial for obtaining high coverage of 1-D nanostructures on Ti64 substrate.

### 4.2.3 Characterization of Oxidized Ti64 Substrates

The 1-D nanostructures are grown for 4-8 hours at 750 °C on Ti64-20h particles in presence of 15 ppm oxygen in flowing Ar (500 sccm). The as-grown 1-D nanostructures are 2 to 5  $\mu\text{m}$  long with an average diameter of 30-60 nm (Figure 4.34(b)). However, some of the 1-D nanostructures are thicker (diameter > 100 nm) and some of the nanostructures are bundled together. In the following sections the as-grown 1-D nanostructures are characterized by XRD, XPS, EDX, TEM, STEM equipped with EDX spectroscope. The oxide scale beneath the 1-D nanostructures is also characterized by SEM equipped with EDX spectroscope.

#### 4.2.3.1 Surface Characterization of Oxidized Ti64

##### (a) *X-ray diffraction (XRD) of oxidized Ti64 particles*

Figure 4.42 shows the XRD patterns of Ti64-0h and Ti64-20h particles after thermal oxidation for 4 h at 750 °C in the presence of 15 ppm O<sub>2</sub> in flowing Ar (500 sccm). Peaks from  $\beta$ -TiO<sub>2</sub> (rutile) along with  $\alpha$ -Al<sub>2</sub>O<sub>3</sub> (corundum) are observed in both samples. It should be noted that the crystal structure of rutile TiO<sub>2</sub> is tetragonal and corundum Al<sub>2</sub>O<sub>3</sub> is rhombohedral. Since Al is present as an alloying element in Ti64, the peaks of Al<sub>2</sub>O<sub>3</sub> is also observed after thermal oxidation. A very small peak of Ti<sub>5</sub>O<sub>9</sub> is also observed at

the  $2\theta$  angle of  $29.02^\circ$ . The  $\alpha$ - and  $\beta$ -Ti peaks are seen which arise from the un-oxidized core of the particles. No peak can be attributed from the oxides of vanadium.

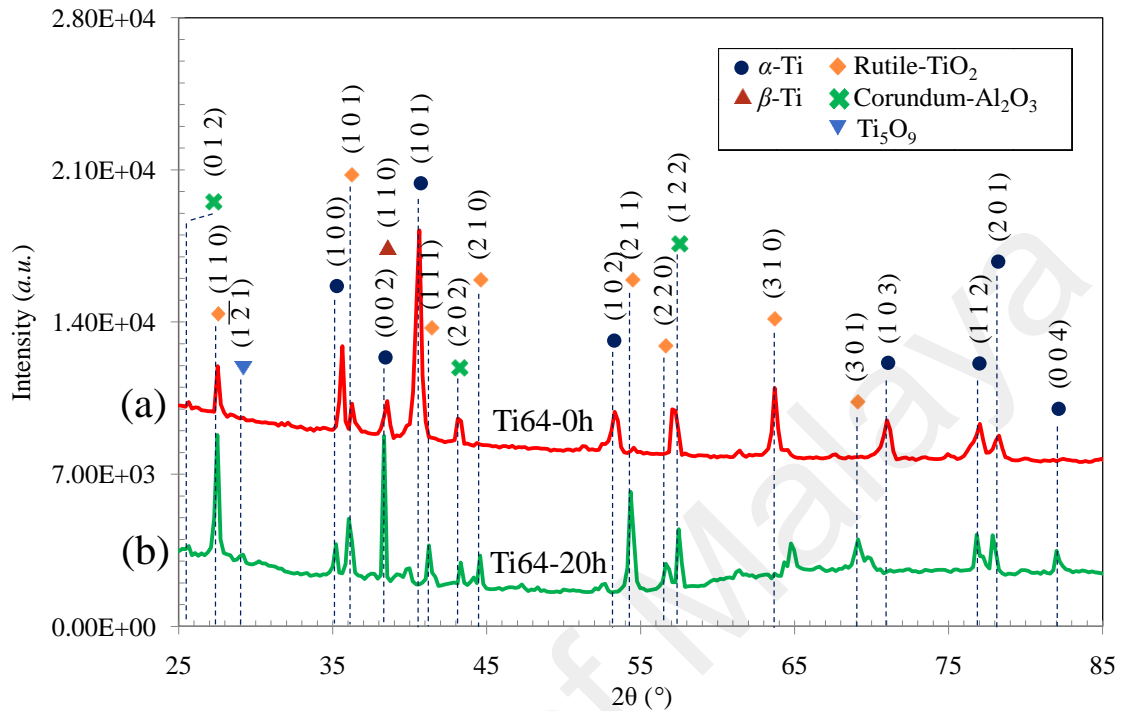


**Figure 4.42: XRD pattern of the Ti64 particles oxidized at  $750^\circ\text{C}$  in presence of 15 ppm oxygen in Ar flowing at 500 sccm (a) oxidized as-received Ti64 (Ti64-0h) and (b) oxidized 20 h milled Ti64 (Ti64-20h).**

Though the presence of rutile  $\text{TiO}_2$  and corundum  $\text{Al}_2\text{O}_3$  is confirmed by XRD, it could not be particularly said which phase is present in the 1-D nanostructure or in the oxide scale beneath the 1-D nanostructure. To resolve this, high resolution characterization such as TEM equipped with EDX are required which is presented in the following sections.

#### (b) X-ray photoelectron spectroscopy (XPS) of oxidized Ti64 sheets

Figure 4.43(a) shows the XPS spectrum of Ti64 sheet after oxidation for 4 h under optimum conditions. In the survey scan Ti2p and O1s peaks are observed. The narrow scan of Ti2p peaks is shown in the Figure 4.43(b). After Gaussian transformation (shown by dotted line) the presence of  $\text{Ti}2p_{1/2}$  and  $\text{Ti}2p_{3/2}$  is observed at 458.5 and 464 eV, respectively which clearly indicates the presence of  $\text{TiO}_2$ . No other peak belonging to lower valence oxides of Ti is seen.

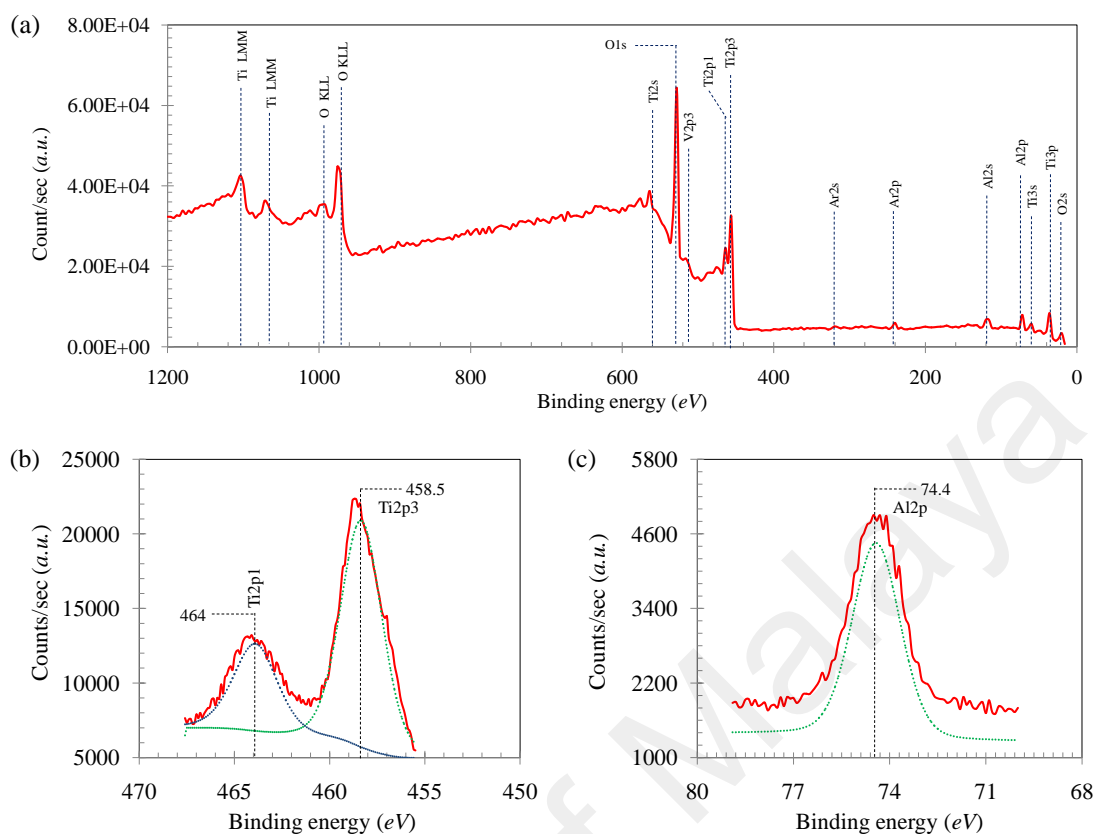


**Figure 4.43: (a) XPS spectra of Ti64 sheet oxidized at 750 °C for 4 h in presence of 15 ppm O<sub>2</sub> in Ar at flow rate of 500 sccm, (b) narrow scan of Ti2p spectra and (c) narrow scan of Al2p spectra.**

The narrow scan of Al2p peak and its Gaussian transformation (dotted line) is shown in Figure 4.43(c). Symmetrical Al2p peak is observed at the binding energy of 74.4 eV which is due to the presence of Al<sub>2</sub>O<sub>3</sub>. So, it is clear from the XPS spectra that during oxidation of Ti64 substrate, both TiO<sub>2</sub> and Al<sub>2</sub>O<sub>3</sub> are formed on the oxidized surface.

### (c) *Energy dispersive X-ray (EDX) spectroscopy of oxidized Ti64*

Energy dispersive X-ray (EDX) analysis was performed on Ti64-20h sample after thermal oxidation for 8 h at 750 °C with 20 ppm of oxygen flowing Ar. Figure 4.44 shows the FESEM image of the oxidized particles and EDX spectra at different locations of X and Y shown in Figure 4.44(a). EDX area analysis at the locations X and Y shows the presence of Ti, Al, V and O (Figure 4.44(b) and (c)). The distribution of these elements

is not clear from the EDX spectra and for this reason high resolution spectroscopy is performed in the next steps.

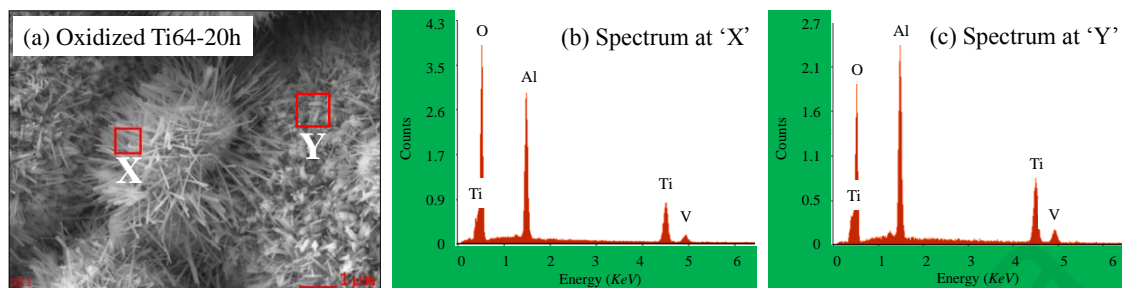
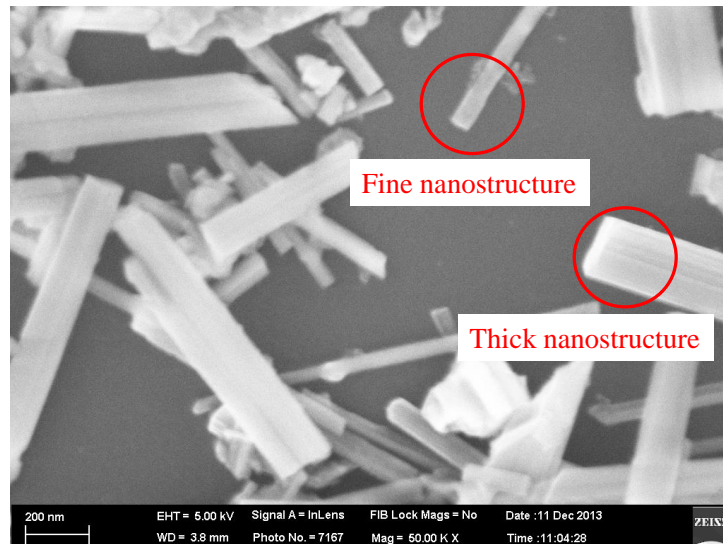


**Figure 4.44: (a) FESEM image of oxidized Ti64-20h particles after thermal oxidation at 750 °C in presence of 20 ppm of O<sub>2</sub> in flowing Ar (500 sccm) for 8 h, (b) EDX spectrum taken at position ‘X’ and (c) EDX spectrum taken at position ‘Y’ shown in figure (a).**

#### 4.2.3.2 Characterization of 1-D Nanostructures on Ti64

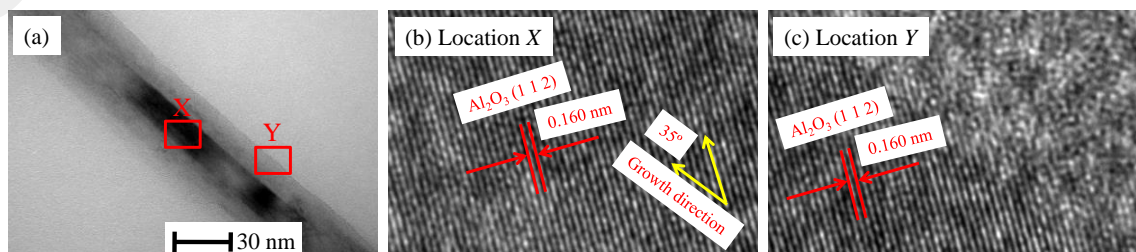
##### (a) *High resolution transmission electron microscopy (HRTEM)*

To characterize the 1-D nanostructures grown on Ti64-20h, the oxidized particles were ultrasonicated in deionized water and transferred to a carbon coated Cu grid through a micropipette. Figure 4.45 shows the FESEM image of the 1-D nanostructures dispersed on a Cu grid. Both fine (diameter: 30-60 nm) and thick (diameter: >100 nm) 1-D nanostructures are seen with no branching or entanglement. The length of the 1-D nanostructures appears to be smaller compared to that attached to the oxidized particles. This is thought to be due to the fracture of 1-D nanostructures during ultrasonication. There are also some irregular shaped tiny particles which are broken pieces of oxide scales caused by ultrasonication. Detailed TEM investigations on a typical fine and thick 1-D nanostructures are described in the followings.



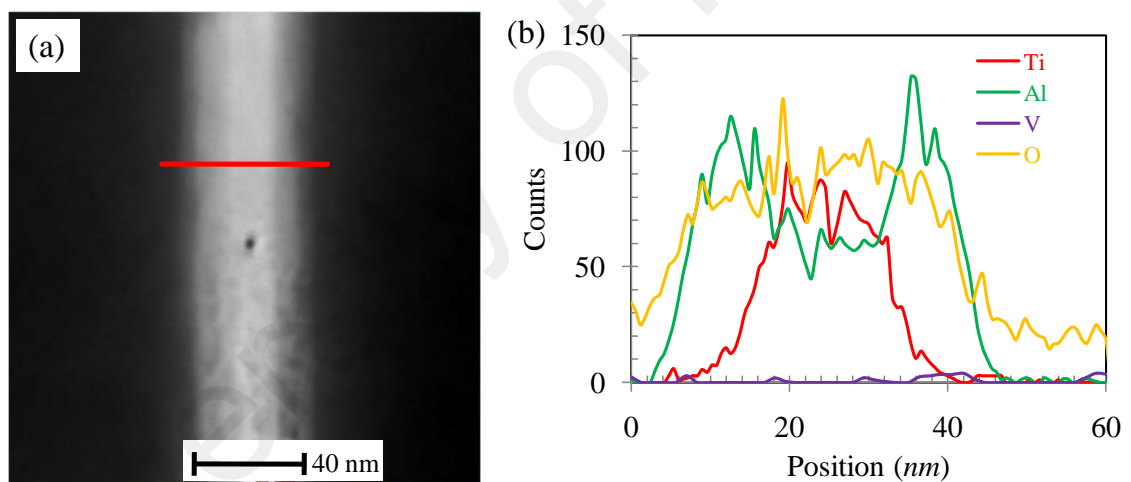
**Figure 4.45: FESEM image of 1-D nanostructures grown on Ti64-20h particles followed by ultrasonication and collection on a Cu grid.**

In Figure 4.46(a), TEM image of a typical fine 1-D nanostructure is shown. A core-shell structure is evident in the nanostructure where the core has a darker contrast compared to the shell. This type of core-shell structure was also reported by Dinan *et al.* (B. J. Dinan et al., 2013) for 1-D nanostructures grown on Ti64 particles by thermal oxidation. Images taken on different 1-D nanostructures reveal that the approximate diameter of the fine nanostructure is 30-60 nm. The thickness of the core varies from 15 to 35 nm, whereas the shell thickness varies from 3 to 15 nm. High resolution TEM (HRTEM) images focused on core (location X) and shell (location Y) reveal the (1 2 2) crystal planes of the shell which belongs to the  $\alpha$ -Al<sub>2</sub>O<sub>3</sub> phase. It is also observed that the fringes of (1 2 2) crystal planes are at about 35° with respect to the growth direction of 1-D nanostructures.



**Figure 4.46: (a) TEM image of a single fine 1-D nanostructure, (b) HRTEM image focused at location X and (c) HRTEM image focused at location Y.**

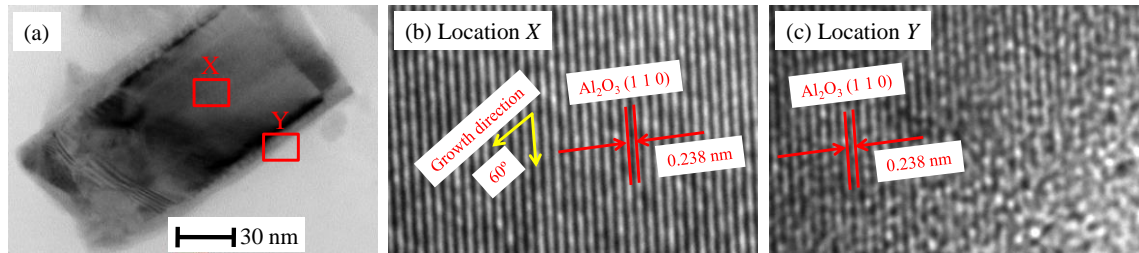
The STEM-EDX line scan of a typical fine 1-D nanostructure is shown in Figure 4.47. Elemental scan across the diameter (Figure 4.47(a)) of the 1-D nanostructure indicates that the counts of oxygen are more or less constant throughout the diameter (Figure 4.47(b)). Counts of Ti are negligible at the outer portion of the 1-D nanostructures, but high at the core. On the other hand, Al counts are high at the outer portion and low at the core. So, these results suggest that the outer portion of the fine 1-D nanostructure is composed of Al and O which is  $\alpha$ -Al<sub>2</sub>O<sub>3</sub>. Though a certain amount of Al is detected in the core (approximately 80 counts), it should be noted that the core of the 1-D nanostructure is surrounded by a shell. So, the counts of Al appearing at the middle of horizontal axis of Figure 4.47(b) come from the shell of the 1-D nanostructures. The core of the 1-D nanostructure is composed of Ti and O which is  $\beta$ -TiO<sub>2</sub>.



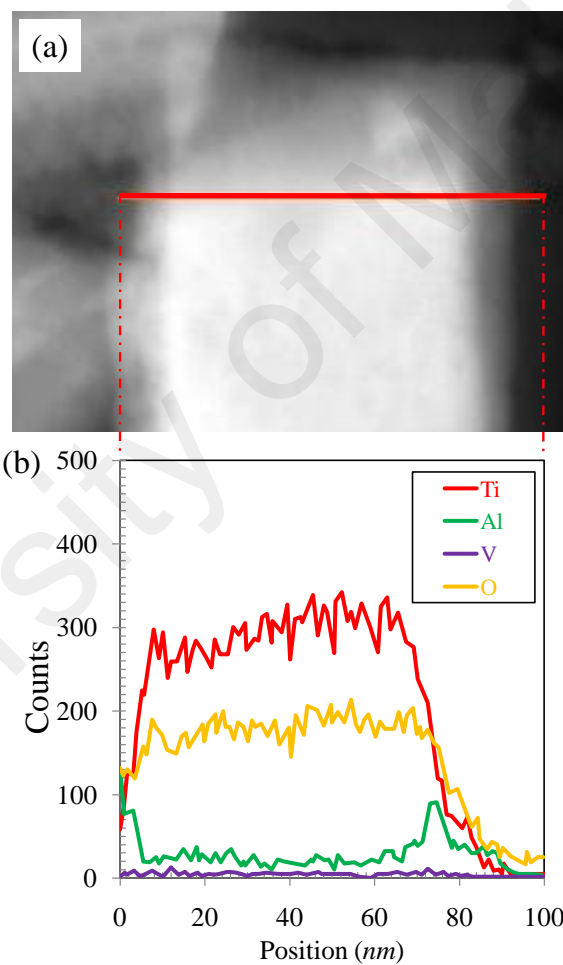
**Figure 4.47: (a) STEM images of a fine 1-D nanostructure and (b) EDX line scanning spectroscopy of fine 1-D nanostructure.**

Figure 4.48(a) shows the TEM images of a thick nanostructure. In this case also, a core-shell structure is evident and the core has darker contrast compared to the shell. The diameter of the thick nanostructures is more than 80 nm. HRTEM image focused on core (location X) and shell (location Y) reveals the crystal plane of (1 1 0) belonging to  $\alpha$ -Al<sub>2</sub>O<sub>3</sub> phase (Figure 4.48(a-b)). No crystal fringe belonging to TiO<sub>2</sub> is detected in HRTEM

image. It is also found that the fringes of (1 1 0) planes of  $\alpha$ - $\text{Al}_2\text{O}_3$  phase are aligned at about  $60^\circ$  with the growth direction of 1-D nanostructure.



**Figure 4.48:** (a) TEM image of a single thick 1-D nanostructure, (b) HRTEM image focused at location X and (c) HRTEM image focused at location Y.



**Figure 4.49:** (a) STEM images of a thick 1-D nanostructure and (b) EDX line scanning spectroscopy of thick 1-D nanostructure.

The STEM image of the thick 1-D nanostructure is shown in Figure 4.49(a) and EDX line scanning spectroscopy is shown in Figure 4.49(b). Similar observation as shown in Figure 4.48 is seen for thick 1-D nanostructures as well. The counts of Ti are found to be

lower at the corner of 1-D nanostructure and higher at the core. On the other hand, the counts of Al are higher at the corner and lower at the core of 1-D nanostructures. Oxygen is found everywhere across the line shown in Figure 4.49(a). This suggests that the core of the thick 1-D nanostructure is composed of  $\beta$ -TiO<sub>2</sub> whereas the shell is composed of  $\alpha$ -Al<sub>2</sub>O<sub>3</sub>.

Figure 4.50(a) shows the TEM image of a bundled nanostructure. In this case, the core-shell feature is not so evident in the nanostructure. The larger thickness and coalition of multiple 1-D nanostructures could be a reason for the reduced transparency of bundled structures. Typically the bundled nanostructures are more than 120 nm in diameter. HRTEM images focused on different locations of bundled nanostructures are shown in Figure 4.50(b-e). In all cases fringes from (0 1 2) planes belonging to  $\alpha$ -Al<sub>2</sub>O<sub>3</sub> phase is seen. It is also seen that (0 1 2) planes from  $\alpha$ -Al<sub>2</sub>O<sub>3</sub> phase are parallel to the growth direction of the 1-D nanostructure.

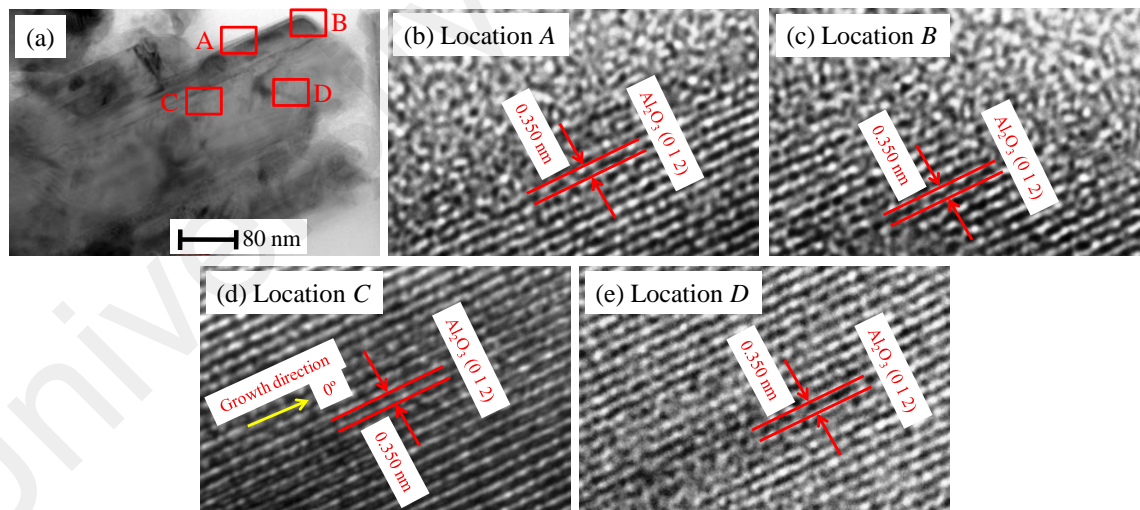


**Figure 4.50: (a) TEM image of a bundled nanostructure, (b) HRTEM image focused at location A, (c) location B, (d) location C and (e) location E.**

To obtain the elemental composition, line scan of a bundled nanostructure was recorded as shown in Figure 4.51(a) and is presented in Figure 4.51(b). The line scanning shows that oxygen is more or less constant everywhere along the diameter. There are

fluctuations in Al and Ti counts across the diameter suggesting that multiple 1-D nanostructures with core-shell features are combined to form a bundled nanostructure. The rise of Al counts at shell as shown in Figure 4.51(b) indicates the presence of  $\alpha$ - $\text{Al}_2\text{O}_3$ , whereas the rise of Ti counts at the intermediate regions indicate the presence of  $\text{TiO}_2$  at the core.

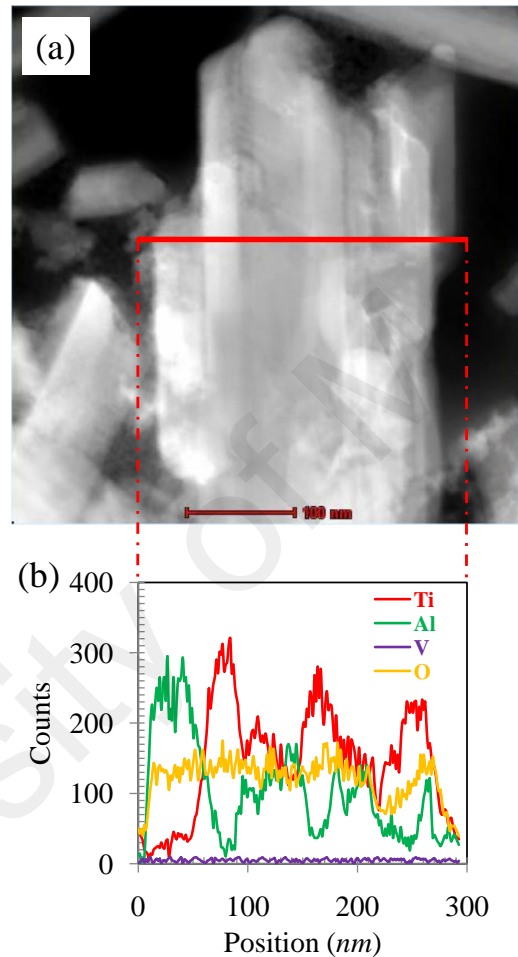


**Figure 4.51: (a) STEM image of a bundled nanostructure and (b) EDX line scanning spectroscopy of the bundled nanostructure.**

(b) *Selected area diffraction analysis*

In Figure 4.52(a-b), bright field and dark field TEM images of the fine 1-D nanostructure grown at 750 °C are shown. In this image the core-shell structure becomes evident. Selected area diffraction (SAD) pattern from this area is shown in Figure 4.52(c). The nanostructure is tilted to a crystallographic orientation whereby the  $\{0\ 0\ 2\}$  planes of the core (i.e. two beam condition) and  $\langle 001 \rangle$  zone axis of the shell become almost parallel

to the TEM transmitted beam. The diffraction spots are indexed in Figure 4.52(c), whereby the encircled strong diffracting spots are relevant to the two beam diffraction of rutile-TiO<sub>2</sub> (labeled R002) and the other weak streaking out spots are relevant to corundum-Al<sub>2</sub>O<sub>3</sub>. A dark field TEM image with illumination of the corundum-Al<sub>2</sub>O<sub>3</sub> phase is shown in Figure 4.52(b). By considering relative rotations between the image and diffraction pattern (~3°) it is confirmed that the growing direction of the 1-D nanostructure is <002> of the rutile-TiO<sub>2</sub> core and this has coincided with the <330> direction of the corundum-Al<sub>2</sub>O<sub>3</sub> shell crystals. The streaks in their diffraction spots (one is marked by a pair of arrows) indicate that the crystal is thin perpendicular to this direction, and this is matching well when compared with the TEM image in Figure 4.52(a) that the corundum-Al<sub>2</sub>O<sub>3</sub> shells are 3-5 nm thick and their growth direction is <110>.

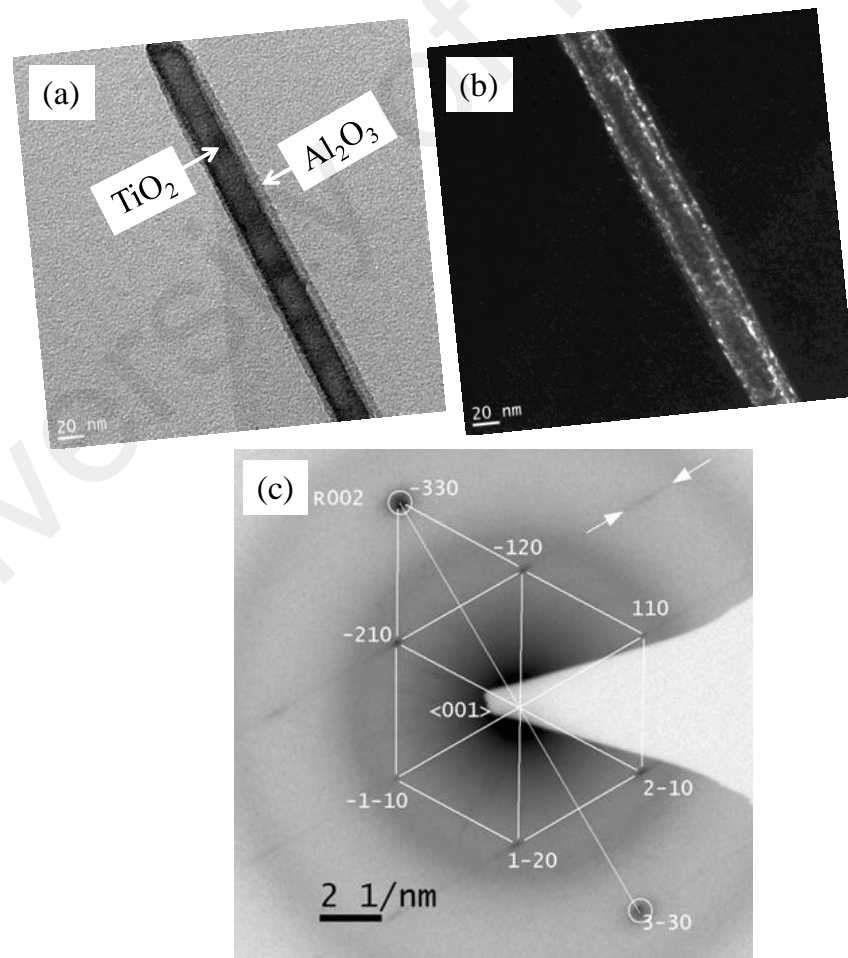


**Figure 4.52: (a) Bright field TEM image, (b) dark field TEM image and (c) SAD pattern of the 1-D nanostructure grown on Ti64 particles at 750 °C for 4 h in the presence of 15 ppm O<sub>2</sub> in flowing Ar (500 sccm).**

#### 4.2.3.3 Cross-sectional Characterization of Oxidized Ti64

During thermal oxidation, oxide scales formed and 1-D nanostructures evolved from the oxide scales. To characterize the oxide scales beneath the 1-D nanostructures, the oxidized particles were mounted in epoxy and polished using standard metallographic techniques. Then the particles were observed under SEM equipped with EDX spectroscopy.

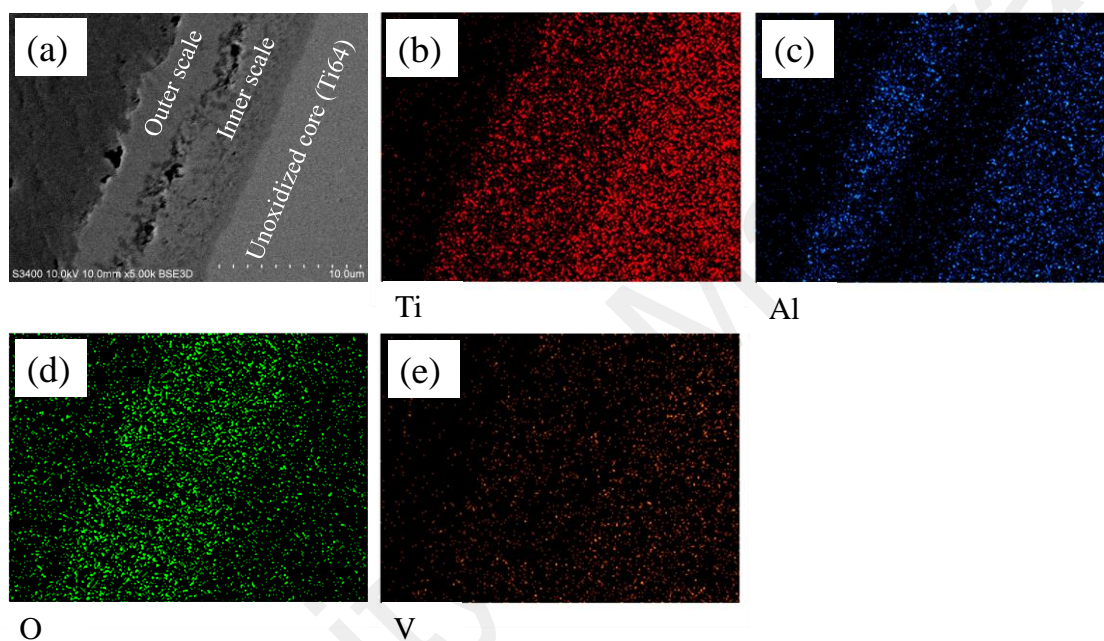


**Figure 4.53: (a) Cross-sectional SEM view of the Ti64-0h particles after thermal oxidation, and corresponding elemental maps of (b) Ti, (c) Al, (d) O and (e) V.**

Figure 4.53 shows the SEM image and corresponding EDX spectroscopy elemental maps of the cross-sectional view of Ti64-0h particles oxidized at 750 °C for 8 h in presence of 15 ppm O<sub>2</sub> in flowing Ar (500 sccm). Double layer of oxide scales are visible on the surface of the particles (Figure 4.53(a)). The thickness of the outer oxide scale is ~5 μm, while the inner oxide scale is a little thicker. A porous interface is seen in between the outer and inner oxide scales. EDX spectroscopy elemental mapping on the cross-section shows the existence of Ti in both oxide scales (Figure 4.53(b)). Al is found only in the outer oxide scale whereas the inner oxide scale is almost Al depleted (Figure

4.53(c)). Oxygen is present in both oxide scales (Figure 4.53(d)). V is detected in small amounts in both oxide scales (Figure 4.53(e)).

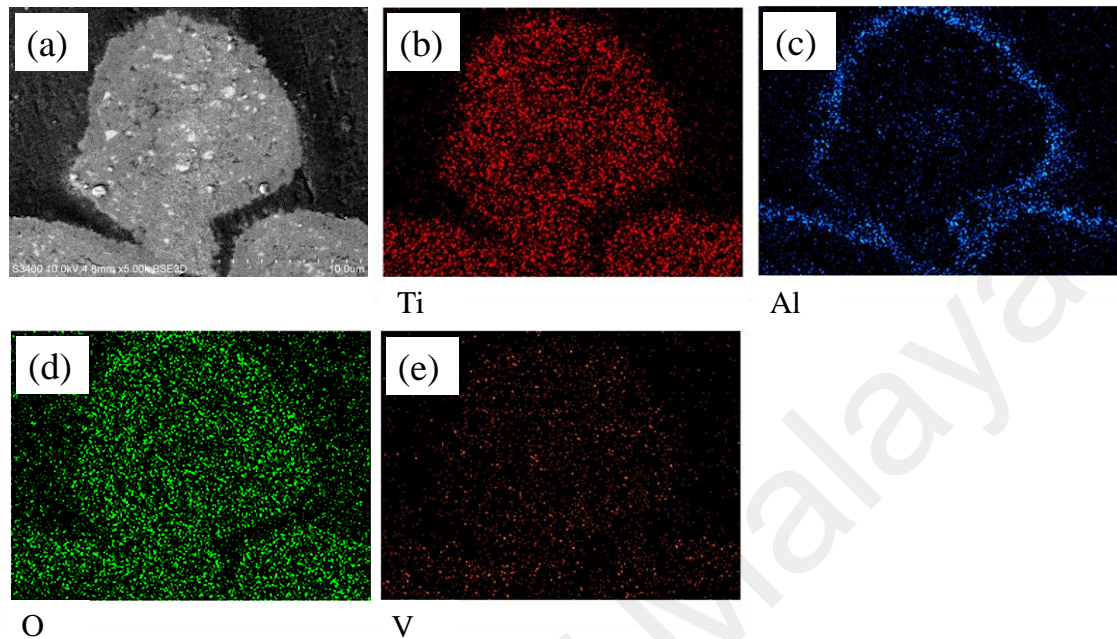


**Figure 4.54: (a) Cross-sectional SEM view of the Ti64-20h particles after thermal oxidation, and corresponding elemental maps of (b) Ti, (c) Al, (d) O and (e) V.**

Figure 4.54 shows the cross-sectional view and corresponding elemental maps of Ti64-20h particles oxidized for 8 h at 750 °C in presence of 15 ppm O<sub>2</sub> in flowing Ar (500 sccm). These milled particles are smaller in size. It was seen that Ti64-20h particles were completely oxidized through the cross-section when the particle size is less than 20 μm. In some bigger particles (>20 μm) an un-oxidized core was seen which is not shown here. For the oxidized Ti64-20h particles, the contrast between two oxide scales is not that obvious as seen in Figure 4.54(a). From the EDX spectroscopy elemental mapping, Ti is detected all over the oxide layer (Figure 4.54(b)). Al atoms are detected at high concentrations only at the surface (Figure 4.54(c)). Oxygen is found to be distributed all over the particles which indicate that the particle is fully oxidized (Figure 4.54(d)). V is detected in trace amount distributed all over the Ti64-20h particles (Figure 4.54(e)). The thickness of the outer oxide scale in oxidized Ti64-20h particles is about 1.3 μm.

EDX spectroscopy spot analysis was carried out at multiple spots on the outer and the inner oxide scales of oxidized Ti64-0h and Ti64-20h particles and the results are tabulated in Table 4.2. The spot analysis was carried out at least eight different points and the average is presented here. The presence of Ti and Al along with oxygen suggests the presence of both TiO<sub>2</sub> and Al<sub>2</sub>O<sub>3</sub> in the outer oxide scale. On the other hand, only Ti and O are spotted at the inner oxide scale suggesting that this layer is TiO<sub>2</sub>. Formation of double layered oxides was also observed during air oxidation of Ti64 (Du, Datta, Lewis, & Burnell-Gray, 1994; H Guleryuz & Cimenoglu, 2005; Hasan Guleryuz & Cimenoglu, 2009). An Al depleted inner oxide scale composed of TiO<sub>2</sub> was reported in the literature for the air oxidation of Ti64 (Du et al., 1994; Hasan Guleryuz & Cimenoglu, 2009). However, the outer oxide scale was reported as Al<sub>2</sub>O<sub>3</sub> during air oxidation of Ti64 alloy (Du et al., 1994; Hasan Guleryuz & Cimenoglu, 2009). This is different from the present observation where both TiO<sub>2</sub> and Al<sub>2</sub>O<sub>3</sub> are present in the outer oxide scale during oxidation of Ti64 in oxygen deprived conditions.

**Table 4.2: Atomic percentage of different elements in the oxide scales of Ti64-0h and Ti64-20h particles.**

Element	Atomic percent (%)	
	Outer oxide scale	Inner oxide scale
Ti	24.91±4.96	35.25±2.39
Al	13.55±5.28	0
O	61.46±1.83	64.75±2.39

According to TiO<sub>2</sub>-Al<sub>2</sub>O<sub>3</sub> phase diagram, TiO<sub>2</sub> and Al<sub>2</sub>O<sub>3</sub> are completely immiscible at the oxidation temperature of 750 °C (Cano, Dosta, Miguel, & Guilemany, 2007). It is also noticed that no solid solution or intermetallic compounds are formed under the present experimental conditions. So, it is believed that the both Al<sub>2</sub>O<sub>3</sub> and TiO<sub>2</sub> grains are present in the outer oxide scale of oxidized Ti64 particles though the exact distribution of the oxides is not clear and further research is required. The EDX spectroscopy spot

analysis on the outer oxide scale indicates that the approximate molecular ratio of  $\text{Al}_2\text{O}_3$  and  $\text{TiO}_2$  is 1:3.

An obvious difference in thickness is observed at the outer oxide scale of Ti64-0h and Ti64-20h particles. The total thickness of the oxide scale is about 10  $\mu\text{m}$  in Ti64-0h particles. On the other hand, Ti64-20h particles are fully oxidized if the diameter of the particle is less than 20  $\mu\text{m}$  (radius <10  $\mu\text{m}$ ). No Al is detected in the inner oxide scale in both types of particles (Figure 4.53 and 4.54). Again, Al is detected in the unoxidized core in bigger particles having radius more than 10  $\mu\text{m}$  (Figure 4.53). So, it is concluded that Al atoms diffuse to the surface from the depth of 10  $\mu\text{m}$ . Due to having much bigger size of Ti64-0h particles, more Al atoms diffuse to the surface from the depth of 10  $\mu\text{m}$  compared with Ti64-20h particles. So, the volume of  $\text{Al}_2\text{O}_3$  is higher in Ti64-0h particles compared with Ti64-20h. As a result, the outer layer thickness is higher in Ti64-0h. Different parameter such as shape of the particles, porosities in the resultant oxides and grain size also could affect the thickness of the outer oxide scale.

#### **4.2.3.4 Structure of Oxidized Ti64 Particles**

Based on the results discussed above, the overall structural characteristics of Ti64 particles after thermal oxidation are schematically shown in Figure 4.55. Though the particles were oxidized under similar conditions, some structural difference is seen between the oxidized Ti64-0h and Ti64-20h particles. In both particles, a double layer of oxide scale is formed during oxidation. The outer oxide scale consists of a mixture of  $\text{Al}_2\text{O}_3$  and  $\text{TiO}_2$  whereas the inner oxide scale is solely  $\text{TiO}_2$ . An un-oxidized core is seen inside if the size of the particle is more than 20  $\mu\text{m}$  such as oxidized Ti64-0h particles (Figure 4.53(a)). Moreover, formation and accumulation of pores are evident between the two oxide scales in Ti64-0h particles. On the other hand, un-oxidized core and

accumulation of pores at the interface between two oxide scales are absent in the particles having size less than  $20\ \mu\text{m}$  such as oxidized Ti64-20h particles (Figure 4.54(a)).

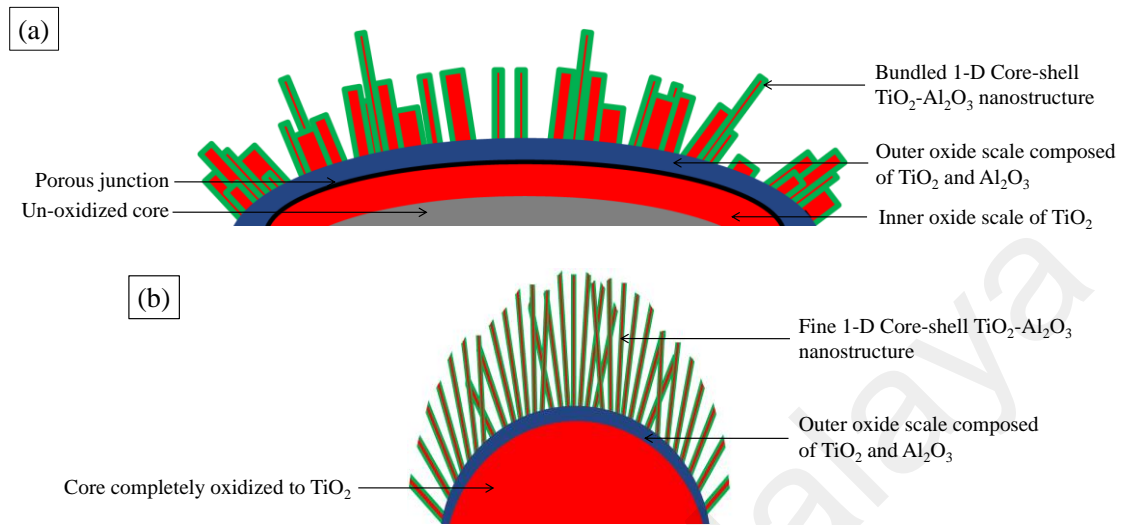


**Figure 4.55: Schematic cross-sectional view after thermal oxidation of spherical Ti64 particles (a) particles having larger diameter ( $>20\ \mu\text{m}$ ) and (b) particles having smaller diameter ( $<20\ \mu\text{m}$ ). The schematics are not proportioned with actual scale.**

The 1-D nanostructures are seen to grow in the outward direction from the oxide scale that formed on the surface. The 1-D nanostructures have a core-shell structure where the core is  $\beta\text{-TiO}_2$  and the shell is  $\alpha\text{-Al}_2\text{O}_3$ . In the oxidized Ti64-0h particles some bundled core-shell structures are also evident as shown in Figure 4.55(a). On the other hand, in oxidized Ti64-20h particles the 1-D core-shell  $\text{TiO}_2\text{-Al}_2\text{O}_3$  nanostructures are fine and long. In general, the structure of the Ti64 particles after thermal oxidation is as follows:  $\text{TiO}_2/\text{Al}_2\text{O}_3$  core-shell 1-D structure  $\rightarrow$  outer oxide scale composed of  $\text{TiO}_2$  and  $\text{Al}_2\text{O}_3$   $\rightarrow$  porous interface (seen only in bigger particles)  $\rightarrow$  inner oxide scale composed of  $\text{TiO}_2$   $\rightarrow$  un-oxidized core (seen in the bigger particles).

#### 4.2.3.5 Epitaxy between 1-D Nanostructures and Ti64 Sheets

In many instances it is seen that the 1-D nanostructures are aligned at certain angles with each other on  $\alpha\text{-Ti}$  grains of Ti64 substrate especially for short duration of oxidation. For long duration of oxidation such relationship it hard to interpret due to growth of

numerous 1-D nanostructures which makes it impossible to find out the root of the growth. It is seen that nuclei of 1-D nanostructures maintain some sort of alignments with the grains in Ti64 substrate. To investigate this issue, a Ti64 sheet was annealed at 1000 °C for 1 h and cooled very slowly inside the furnace to obtain coarse grains of  $\alpha$ -Ti. After that the sheet was polished and etched followed by observation under SEM. Electron backscattered diffraction (EBSD) orientation mapping was performed on the selected area to identify the grain orientations of Ti64 substrates. After that the Ti64 substrates was thermally oxidized for 1 min and the selected grains were observed again under FESEM to identify the relation between crystal orientation of substrate and the alignment of 1-D nanostructures.

(a) **Identification of orientation in inverse pole figure (IPF)**

In EBSD, the crystal orientation in grains is presented by different colors based on inverse pole figure (IPF) triangle. Figure 4.56(a) shows a typical IPF triangle of  $\alpha$ -Ti (hexagonal) crystal. The three corners of the triangle represent  $(0\ 0\ 0\ 1)$ ,  $(2\ \bar{1}\ \bar{1}\ 0)$  and  $(1\ 0\ \bar{1}\ 0)$  planes of  $\alpha$ -Ti which are indicated by red, green and blue colors, respectively.

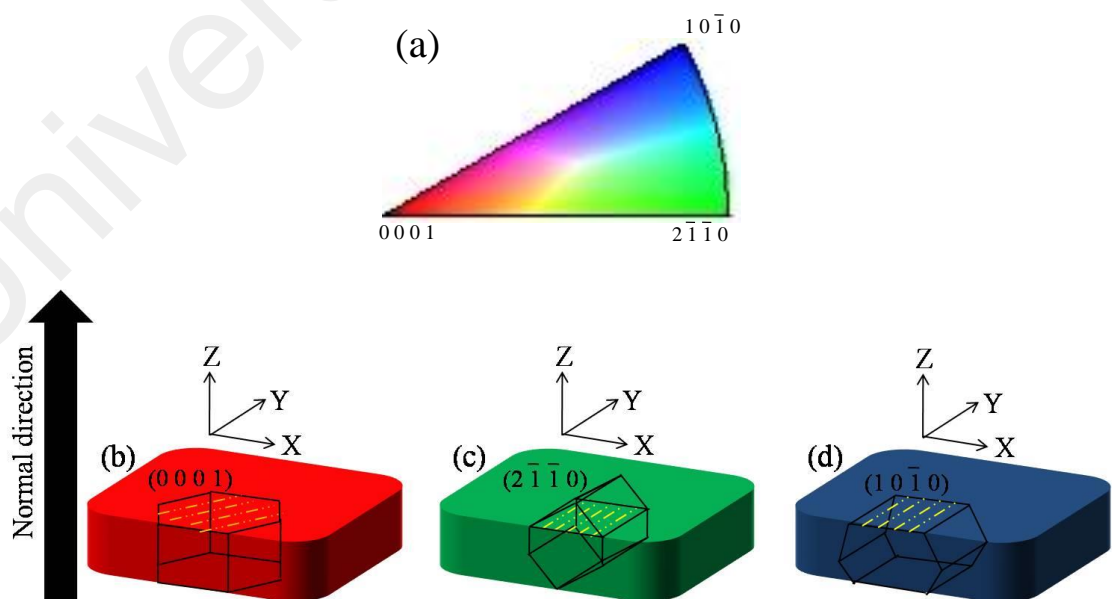


**Figure 4.56: (a) IPF triangle of  $\alpha$ -Ti (hexagonal) crystal, (b-d) Schematic orientations of hexagonal crystals in  $\alpha$ -Ti grains for the corner regions in IPF triangle.**

The schematic illustrations of orientation represented by red, green and blue color in the  $\alpha$ -Ti IPF triangle are presented in Figures 4.56(b-d), respectively. The red color in orientation map indicates that the  $(0\ 0\ 0\ 1)$  plane in  $\alpha$ -Ti crystal is facing the normal to the sheet. The  $(0\ 0\ 0\ 1)$  plane in  $\alpha$ -Ti crystal is shown by the dotted lines in Figure 4.56(b). Similarly, the green and blue color in the orientation map indicates that the  $(2\ \bar{1}\ \bar{1}\ 0)$  and  $(1\ 0\ \bar{1}\ 0)$  crystal planes are facing the normal to the sheet, respectively as shown in Figure 4.56(c-d) by dotted lines.

**(b) Crystal orientation of Ti64 sheet before oxidation**

Figure 4.57(a) shows the SEM image of Ti64 sheet after polishing and etching. The  $\alpha$ -Ti grains are seen to have irregular shapes. The  $\beta$ -Ti phase has been etched away which is situated at the grain boundaries of  $\alpha$ -Ti. In Figure 4.57(b), the corresponding orientation map of Ti64 sheet is shown. In the orientation map, the  $\alpha$ -Ti grains are colored based on their crystal orientation according to the IPF triangle. The grooves in the grain boundary regions appear dark. In the orientation map no perfectly red, green and blue colored grains are observed. This indicates that the  $(0\ 0\ 0\ 1)$ ,  $(2\ \bar{1}\ \bar{1}\ 0)$  and  $(1\ 0\ \bar{1}\ 0)$  crystal planes are not perfectly parallel to the surface but are tilted to some extent. However, some nearly red, green and blue regions are found in the orientation map which is denoted as “R”, “G” and “B” grains, respectively as shown in Figure 4.57(b).

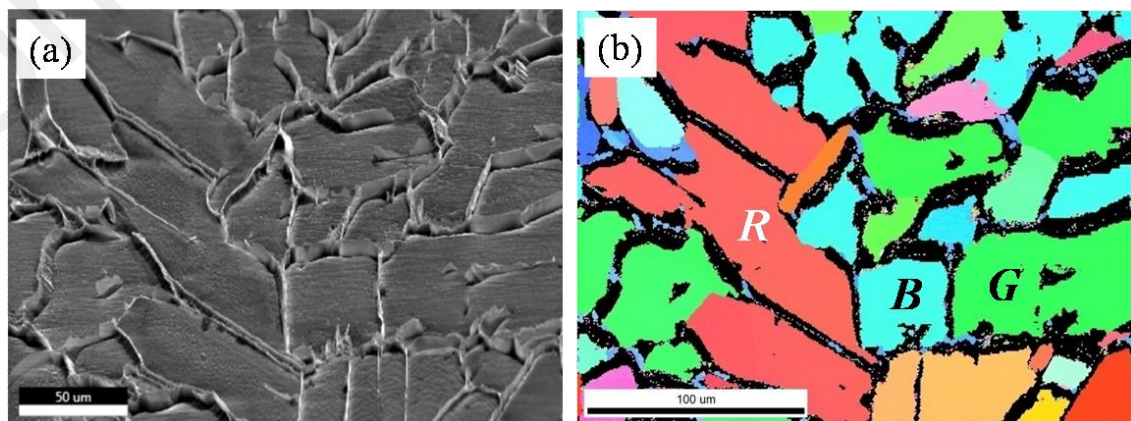


**Figure 4.57: (a) SEM image of the polished Ti64 sheets containing hexagonal crystals in  $\alpha$ -Ti grains and (b) orientation mapping image.**

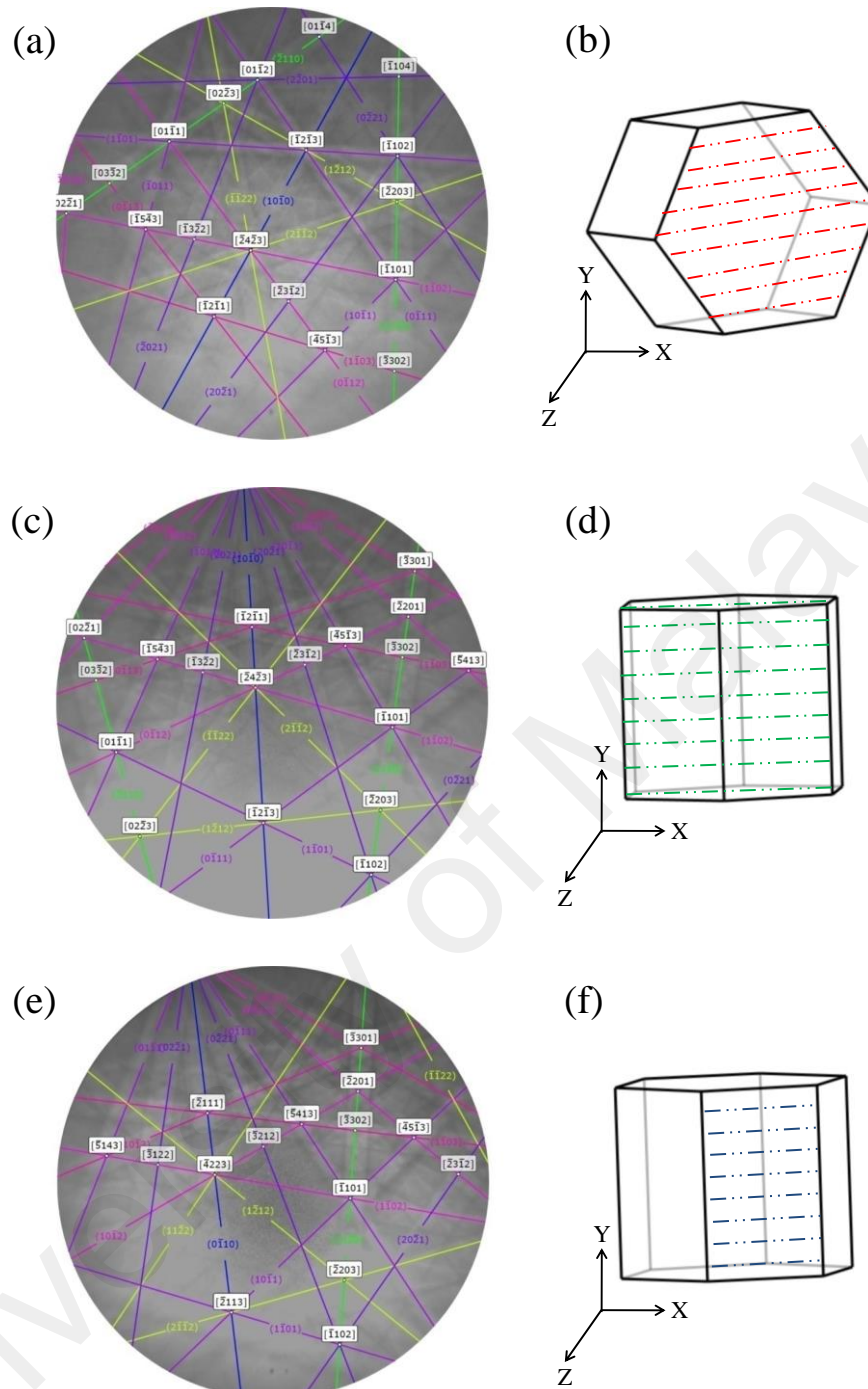


**Figure 4.58: Kikuchi pattern of (a-b) “R” grain and corresponding crystal orientation, (c-d) “G” grain and corresponding crystal orientation and (e-f) “B” grain and corresponding crystal orientation. The  $(0\ 0\ 0\ 1)$ ,  $(2\ \bar{1}\ \bar{1}\ 0)$  and  $(1\ 0\ \bar{1}\ 0)$  planes are shown on the oriented crystal by the dotted lines in Figure (b), (d) and (f), respectively.**

The *Kikuchi* patterns were obtained for the “R”, “G” and “B” grains to investigate the crystal orientations. In Figure 4.58(a-b), the *Kikuchi* pattern and crystal orientation of “R” grain are shown. It is seen that the  $(0\ 0\ 0\ 1)$  plane is not perfectly parallel with the

oxidation surface of the sheet, rather aligned at a certain angle with the surface. It should be noted that the XY axis in the inset of Figure 4.58(b) represents the oxidation surface. Similarly, the *Kikuchi* patterns and crystal orientations of “G” and “B” grains are shown in Figure 4.58(c-f), respectively. In this case also,  $(2 \bar{1} \bar{1} 0)$  and  $(1 0 \bar{1} 0)$  planes are seen to be aligned at certain angles with the surface in “G” and “B” grains, respectively.

(c) *Thermal oxidation of Ti64 sheet*

After orientation mapping, the Ti64 sheet was thermally oxidized for 1 min at 750 °C with 15 ppm of O<sub>2</sub> in flowing Ar (500 sccm). After that the sheet was observed under FESEM at the same location as before (Figure 4.57) and is shown in Figure 4.59. The “R”, “G” and “B” grains are identified in the oxidized sheet and further observed at a higher magnification.

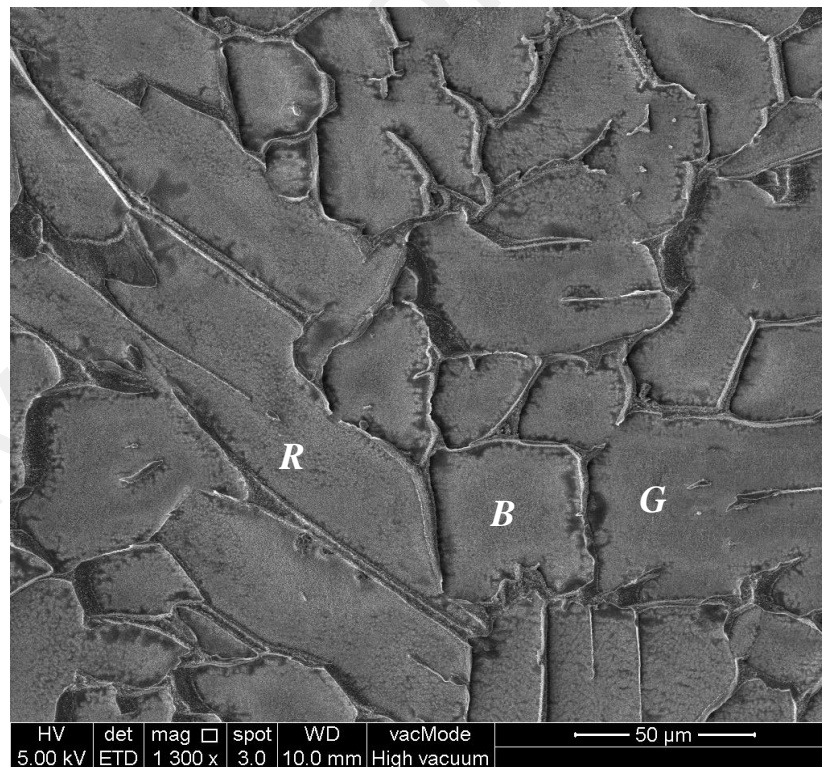


**Figure 4.59: FESEM image of Ti64 sheet oxidized for 1 min identifying similar grains donated by “R”, “G” and “B” shown in the orientation map.**

(d) *Epitaxial growth of 1-D nanostructures on Ti64 sheet*

The high resolution FESEM image of “R” grain is shown in Figure 4.60(a). Oxide scale instead of 1-D nanostructure is seen on the grain. It should be noted that in “R” grain the (0 0 0 1) plane is almost parallel to the oxidation surface. The result suggests that oxidation on (0 0 0 1) plane is not favorable for the growth of 1-D nanostructures.

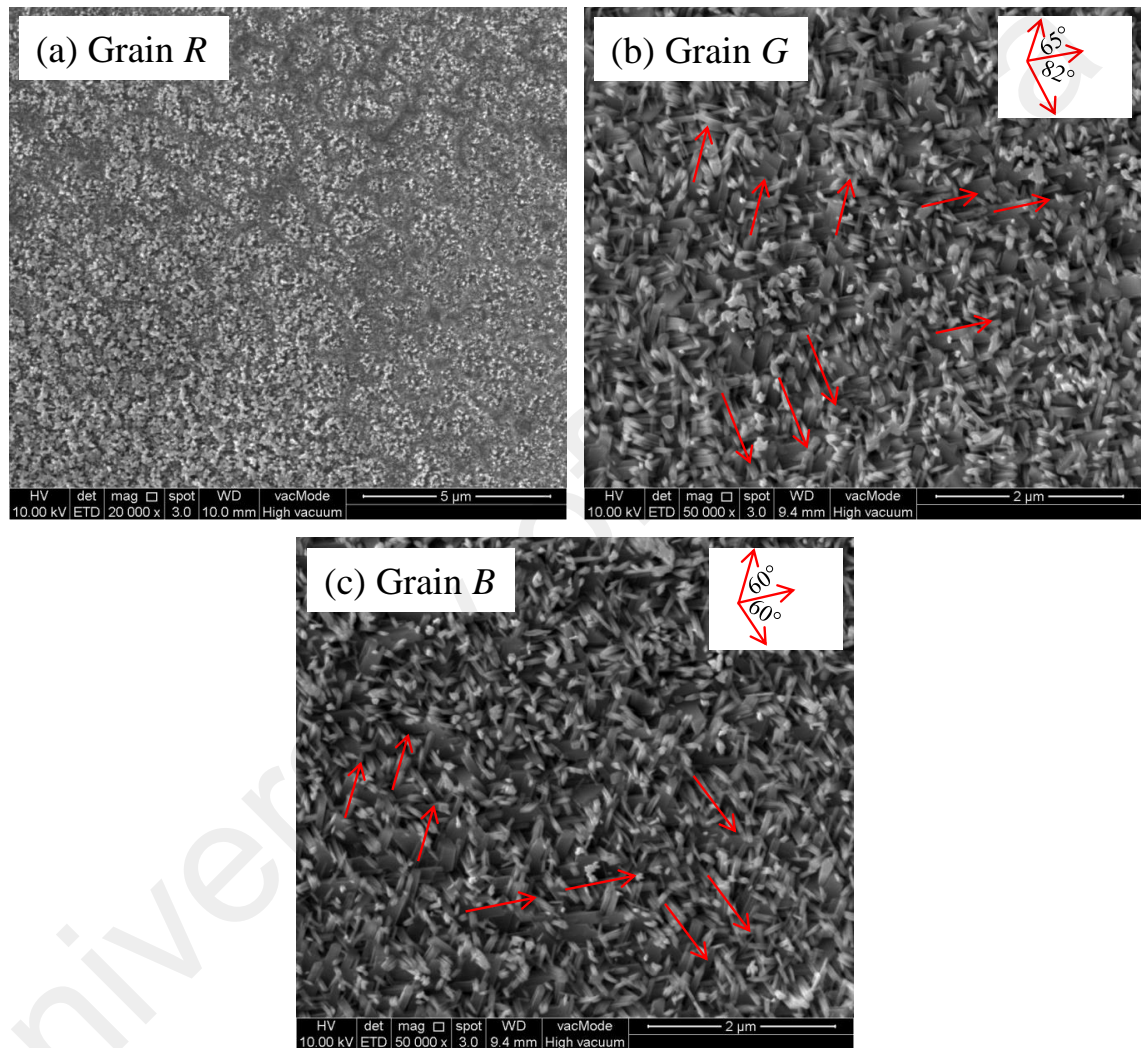


**Figure 4.60: Thermally oxidized Ti64 sheet for 1 min with 15 ppm O<sub>2</sub> in flowing Ar (500 sccm) at 750 °C showing (a) “R” grain where (0 0 0 1) plane is parallel to the oxidation surface, (b) “G” grain where (2  $\bar{1}$   $\bar{1}$  0) plane is parallel to the oxidation surface and (c) “B” grain where (1 0  $\bar{1}$  0) plane is parallel to the oxidation surface.**

Figure 4.60(b) shows the high resolution FESEM image of “G” grain. In this case, the 1-D nanostructures are oriented along three different directions as shown by the red arrows. The angle between the outermost arrows is about 147°. The angles between the

adjacent arrows are 65 and 82°. It should be noted that in “G” grain the  $(2 \bar{1} \bar{1} 0)$  crystallographic plane is parallel to the oxidation surface. In Figure 4.60(c), the 1-D nanostructures on “B” grain are shown. In this case, three 1-D nanostructures are seen to be directed at an angle of 60° with each other. In “B” grain the  $(1 0 \bar{1} 0)$  crystallographic plane is parallel to the oxidation surface.

So, from the above observations it is clear that the 1-D nanostructures grow from the  $(2 \bar{1} \bar{1} 0)$  and  $(1 0 \bar{1} 0)$  crystal planes. To evaluate the epitaxy of 1-D growth with  $\alpha$ -Ti crystals, the angles of different crystal directions observed from the top view are calculated and tabulated in Appendix D. It is seen from the top view projection of  $(2 \bar{1} \bar{1} 0)$  crystallographic plane of  $\alpha$ -Ti that the  $[2 0 \bar{2} 1]$  and  $[2 \bar{2} 0 1]$  directions create angle of 66.9° and 84.8° with the  $[0 \bar{2} 2 1]$  direction as shown in Figure 4.61(a). These values are close to the angles (65° and 82°) of 1-D nanostructures grown in “G” grain as shown in Figure 4.60(b). Similarly, from the top view projection of  $(1 0 \bar{1} 0)$  crystallographic plane, the  $[\bar{2} 0 2 1]$  and  $[2 \bar{2} 0 1]$  directions create an angle of 62.2° with the  $[0 \bar{2} 2 1]$  direction (Figure 4.61(b)) which is close to the angles of 1-D nanostructures on “B” grain (60°) as shown in Figure 4.60(c).

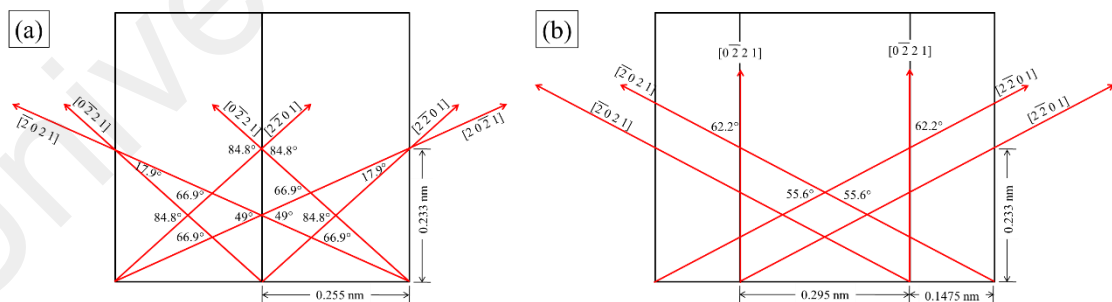


**Figure 4.61: The  $\langle 2 \bar{2} 0 1 \rangle$  directions of hexagonal  $\alpha$ -Ti crystal observed from the top view projections of (a)  $(2 \bar{1} \bar{1} 0)$  crystallographic plane and (b)  $(1 0 \bar{1} 0)$  crystallographic plane.**

So, it is seen from the above observations that the 1-D nanostructure initiates from the  $(2 \bar{1} \bar{1} 0)$  and  $(1 0 \bar{1} 0)$  crystallographic planes of  $\alpha$ -Ti. The 1-D nanostructures grow

in the family of  $\langle 2 \bar{2} 0 1 \rangle$  directions of  $\alpha$ -Ti crystals. However, to reconfirm this epitaxial relationship some critical experiments need to be conducted where perfectly aligned  $\alpha$ -Ti crystal will be used for thermal oxidation.

#### 4.2.3.6 Initial Morphology of 1-D Nanostructures

The 1-D core-shell  $\text{TiO}_2$ - $\text{Al}_2\text{O}_3$  nanostructures originate from the outer oxide scale of oxidized Ti64 substrate. To find out the root from where the 1-D nanostructures originate, a close up view of the interface between the outer oxide scale and 1-D nanostructures was taken as shown in Figure 4.62. For this purpose, Ti64 sheet was intentionally oxidized under non-optimum conditions of 40 ppm  $\text{O}_2$  in flowing Ar (500 sccm) at 750 °C for 8 h to obtain lower coverage of 1-D nanostructures so that clear view of the roots could be obtained. The aim to obtain less coverage is to observe the root regions of 1-D nanostructures.

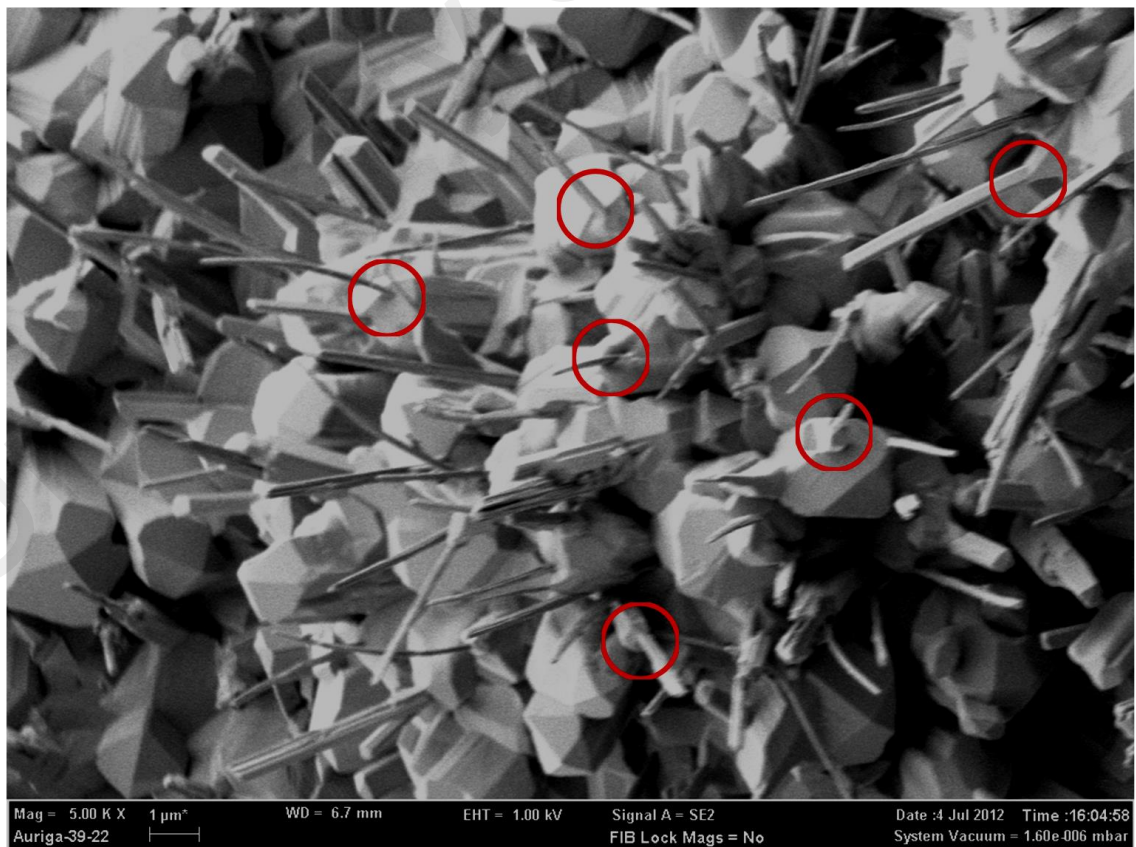


**Figure 4.62: Thermally oxidized Ti64 sheet under non-optimum conditions of 40 ppm  $\text{O}_2$  in flowing Ar (500 sccm) at 750 °C for 8 h.**

It is seen from Figure 4.62 that the 1-D core-shell  $\text{TiO}_2\text{-Al}_2\text{O}_3$  nanostructures originated from the top of the grains of outer oxide scale (mixture of  $\text{TiO}_2$  and  $\text{Al}_2\text{O}_3$ ) as shown by the red circles. It is also seen that the oxide scale beneath the 1-D nanostructures are highly faceted. The 1-D nanostructures are not extruded from the grain boundary regions. Similar observations was made by Yuan *et al.* (Yuan *et al.*, 2012; Yuan *et al.*, 2011) for the growth of 1-D  $\text{Fe}_2\text{O}_3$  and  $\text{CuO}$  nanostructures on Fe and Cu substrates, respectively where the 1-D nanostructures were formed on top of the grains. So, it can be concluded that the growth on top of the grains is the inherent nature for the formation of 1-D nanostructures during thermal oxidation. This is in contrast with the tin whisker growth on tin plated Cu lead frames, where the whiskers are extruded from the grain boundaries and the cross-sectional shape of the whiskers is determined by the geometry of the grain boundary (Barsoum, Hoffman, Doherty, Gupta, & Zavaliangos, 2004).

#### 4.2.4 Mechanism of 1-D Growth on Ti64 Substrates

A few mechanisms have been proposed to explain the growth of 1-D nanostructures on metal substrates during oxidation. These include vapor-liquid-solid (VLS) (Wagner & Ellis, 1964), vapor-solid (VS) (Roy *et al.*, 2003), dislocation driven (Brenner & Sears, 1956; Sears, 1955), self catalytic (Dang, Wang, & Fan, 2003), nanocrystalline seeding (B.-S. Kim *et al.*, 2009) and stress induced process (Eshelby, 1953; Kumar *et al.*, 2004). However, none of these mechanisms is capable of explaining all features of the 1-D growth during thermal oxidation. In the following, the drawbacks of the previously proposed growth mechanisms are discussed and finally one simplified mechanism is proposed for the growth of 1-D core-shell  $\text{TiO}_2\text{-Al}_2\text{O}_3$  nanostructures on Ti64 substrates during oxidation.

In the VLS process, the growth of 1-D nanostructures is initiated by the condensation of the vapor at the tip of the nanostructures in the form of droplets (Wagner & Ellis, 1964).

In the present study, no such foreign droplets were found at the tips of 1-D nanostructures. So, VLS mechanism is not applicable in this present study. On the other hand, in VS mechanism  $\text{TiO}_2$  has to be evaporated and solidified on metal substrates in the form of 1-D nanostructures (Roy et al., 2003). It may be noted that  $\text{TiO}_2$  is stable up to  $1843\text{ }^\circ\text{C}$  at atmospheric pressure. So, under the present experimental conditions ( $650\text{-}900\text{ }^\circ\text{C}$ ), the vapor pressure of  $\text{TiO}_2$  and Ti containing species is significantly low. Even at the reaction temperature of  $1237\text{ }^\circ\text{C}$ , the vapor pressure of Ti is reported to be  $2.05 \times 10^{-9}$  atm (Blocher & Campbell, 1949). If evaporation of Ti or  $\text{TiO}_2$  occurs during oxidation of Ti64 at  $650\text{-}900\text{ }^\circ\text{C}$ , it will also deposit on the wall of quartz tube, substrate and at cold ends of the tube. But no such deposit was observed in the present case. So, VS mechanism is also not applicable for the growth of 1-D nanostructures.

In dislocation driven mechanism, supersaturated vapor deposits at the dislocation steps in the form of 1-D nanostructures (Brenner & Sears, 1956; Sears, 1955). In the present experimental conditions, no super saturated vapor is expected to be present and hence this mechanism is not applicable. In self-catalytic mechanism, the metals need to be heated slightly above their melting point (Dang et al., 2003). In the present case, no such melting can occur at the oxidation temperature ( $650\text{-}900\text{ }^\circ\text{C}$ ) as the melting point of Ti64 is  $1604\text{ }^\circ\text{C}$ . So this mechanism is also not valid in the present case.

Relevant literature survey on air oxidation of Ti64 alloy reported that during oxidation Al diffuses outward and forms  $\text{Al}_2\text{O}_3$  layer (Hasan Guleryuz & Cimenoglu, 2009). A double layer of oxide scales is formed where the outer oxide scale is  $\text{Al}_2\text{O}_3$  and inner oxide scale is  $\text{TiO}_2$  (Du et al., 1994; Hasan Guleryuz & Cimenoglu, 2009). According to Ellingham diagram (Appendix C), the Gibbs free energy for the formation of  $\text{Al}_2\text{O}_3$  is lower than  $\text{TiO}_2$  at the oxidation temperature of  $750\text{ }^\circ\text{C}$  (Ellingham, 1944). So, the formation of  $\text{Al}_2\text{O}_3$  is thermodynamically more favorable than  $\text{TiO}_2$  during oxidation at

750 °C. At the later stage of oxidation, the metal ions diffuse to the surface through interstitial sites to form metal oxides (Stringer, 1960; Taniguchi et al., 2001). On the other hand, oxygen ions diffuse inward via grain boundaries and reacts with Ti to form TiO<sub>2</sub> (Stringer, 1960; Taniguchi et al., 2001).

In the present case, deviations are observed during oxidation of Ti64 in oxygen deprived conditions for the growth of 1-D nanostructures. During oxidation of Ti64 in oxygen deprived conditions resulted in a double layered oxide scale beneath the 1-D nanostructures. The outer oxide scale is composed of TiO<sub>2</sub> and Al<sub>2</sub>O<sub>3</sub> which is different from the air oxidation. None of the previous study provides a complete model for the growth of 1-D nanostructures on Ti64 during oxidation in oxygen deprived conditions. For this reason, a simplified diffusion based model is proposed to explain the growth of 1-D nanostructures on Ti64. This type diffusion based model was proposed in the literature for the growth of 1-D CuO (Yuan et al., 2011) and Fe<sub>2</sub>O<sub>3</sub> (Cai et al., 2012) nanostructures on Cu and Fe substrates, respectively during thermal oxidation.

The schematic of a Ti64 substrate composed of multiple grains are shown in Figure 4.63. During early stage of oxidation, Al diffused outward and reacts with the surface adsorbed oxygen as shown in Figure 4.63(a) (Hasan Guleryuz & Cimenoglu, 2009). For this reason, Al<sub>2</sub>O<sub>3</sub> is nucleated at the surface and an Al depleted layer is formed beneath the surface (Figure 4.63(b)). After the creation of Al depleted layer, Ti atoms start to diffuse to the surface and reacts with the surface adsorbed oxygen to form the nuclei of TiO<sub>2</sub> as shown in Figure 4.63(b-c). As a result, the outer oxide scale composed of TiO<sub>2</sub> and Al<sub>2</sub>O<sub>3</sub> is formed. The TiO<sub>2</sub>-Al<sub>2</sub>O<sub>3</sub> phase diagram shows that TiO<sub>2</sub> and Al<sub>2</sub>O<sub>3</sub> are completely immiscible at the experimental temperatures (Cano et al., 2007). So, the TiO<sub>2</sub> and Al<sub>2</sub>O<sub>3</sub> grains stayed as separate entities in the outer oxide scale.

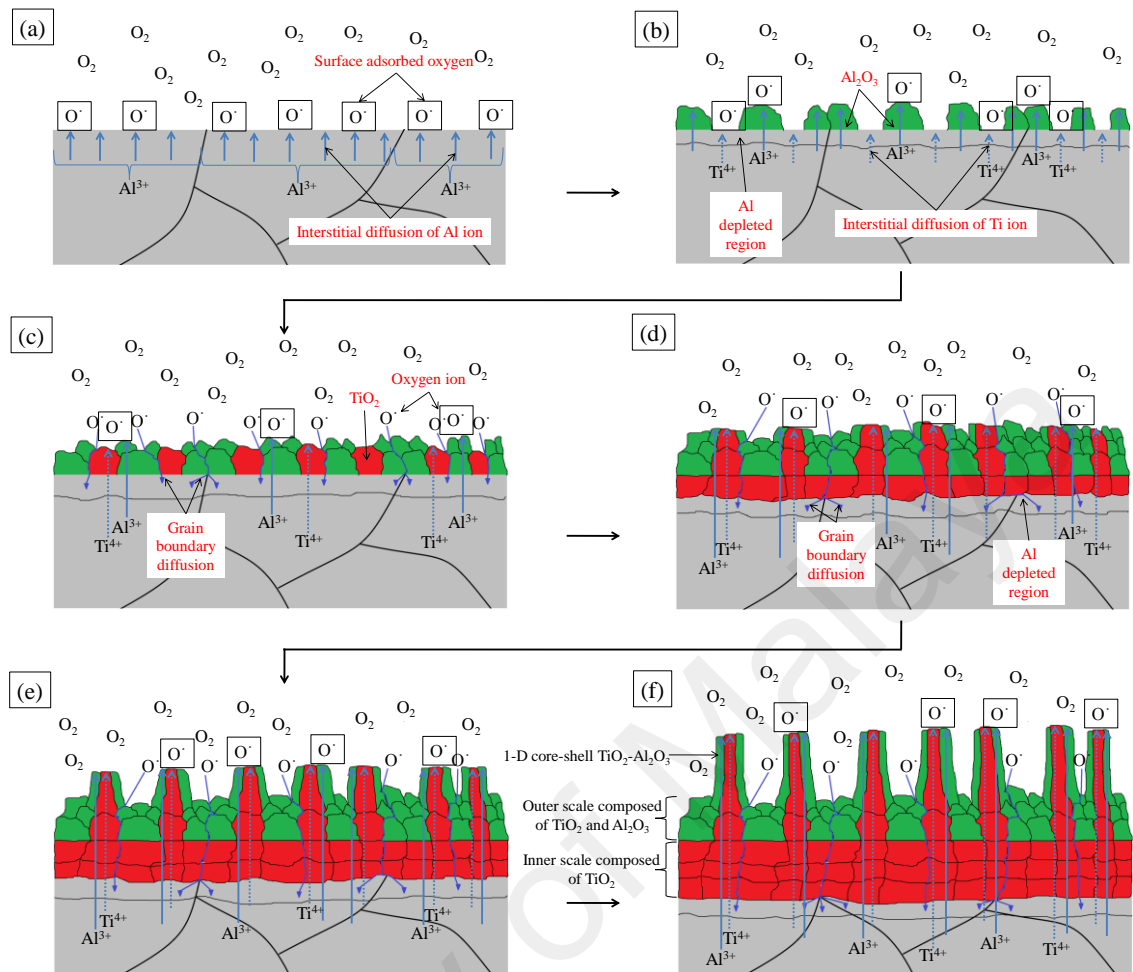


**Figure 4.63: Growth mechanism of 1-D nanostructures on Ti64 substrate during thermal oxidation.**

In the next step, oxygen ions diffuse inward via grain boundaries and reacts with Ti in the Al depleted region to form  $\text{TiO}_2$  as shown in Figure 4.63(d) (Stringer, 1960; Taniguchi et al., 2001). As a result, the inner oxide scale composed of  $\text{TiO}_2$  is formed.

It is believed that stress is induced between the outer and inner oxide layers due to their compositional difference and densities (Kumar et al., 2004). This induced stress is compensated by forming the nuclei of 1-D nanostructures through the diffusion of Ti and Al ions to the outer surface via interstitial sites (Stringer, 1960; Taniguchi et al., 2001) and reacts with surface adsorbed oxygen to form  $\text{TiO}_2$  and  $\text{Al}_2\text{O}_3$  (Figure 4.63(c-d)).

It is reported that during oxidation of Ti64, the growth of 1-D nanostructure occur at the tip of the nuclei (B. Dinan, 2012). So, with the increase of oxidation duration, the Ti

and Al ions keep diffusing to the tip of the 1-D nanostructures via interstitial sites and react on specific crystal plane with adsorbed oxygen to form confined 1-D nanostructure (Figure 4.63(e-f)). Such process of depositing of TiO<sub>2</sub> and Al<sub>2</sub>O<sub>3</sub> onto existing grains is kinetically more favorable than depositing on grain boundaries since it not only has to overcome a nucleation barrier but also blocks the diffusion path of oxygen for the formation of inner oxide scale composed of TiO<sub>2</sub> (Yuan et al., 2011).

It is seen that at high temperatures (>850 °C) or in high oxygen concentrations, oxide scale is formed instead of 1-D nanostructures (Figure 4.21 and 4.26). This general trend seems to indicate that with limited supply of oxygen, the growth of nuclei occurs on certain directions resulting in 1-D nanostructure (Huyong Lee et al., 2010). It is assumed that at higher temperatures (>850 °C) or in higher oxygen partial pressure, the growth of as-grown nuclei occurs in all directions resulting in oxide scale (Huyong Lee et al., 2010).

It is also seen that residual stress on Ti64 particles significantly enhances the coverage of 1-D nanostructures. Fine and long 1-D nanostructures are originated from the particles possessed high residual stress. It is proposed that the residual stress is released during thermal oxidation and new surfaces are created in the form of fine and long nanostructures to compensate the stress.

#### **4.2.5 Summary of Thermal Oxidation of Ti64 Particles**

The as-received Ti64 substrates contains of  $\alpha$  (hexagonal) and  $\beta$  (body-centered cubic) phases of Ti. The synthesis process of 1-D nanostructures on Ti64 is simple and requires only heating the samples in specific oxygen containing environment. This process is unlike the oxidation of pure Ti substrate where the presence of humidity is essential for the growth of 1-D nanostructures. Theoretical calculations revealed that the minimum dynamic oxygen partial pressure for the growth of 1-D nanostructure on Ti64 substrate is

$10^{-11}$  Pa. Oxide scales form instead of 1-D nanostructures when the dynamic oxygen partial pressure exceeds  $3 \times 10^{-9}$  Pa. It is proposed that in the presence of limited supply of oxygen, certain sites of specific crystallographic plane are activated towards oxidation which resulted in 1-D confinement.

The optimum oxidation temperature for the growth of 1-D nanostructure is found to be 750 °C. With increasing the temperatures to 850 °C, the nanostructures become thicker and shorter. Faceted oxide is seen for the oxidation temperature of 900 °C and above.

The alloy microstructures also have impact on the coverage of 1-D growth. It is seen that the presence of lamellar and Widmanstätten structures in Ti64 substrate is beneficial for higher coverage of 1-D growth whereas the 1-D nanostructures are almost depleted in coarse grained  $\alpha/\beta$  structures. It is seen that at the initial stage of oxidation, the 1-D nanostructures originate from the  $\beta$  laths of Ti64 due to their faster rate of oxidation. However, at the later stage, 1-D nanostructures are seen on both  $\alpha$  and  $\beta$  phases. The 1-D nanostructures originate from the  $\{1\ 0\ \bar{1}\ 0\}$  planes of  $\alpha$ -Ti grains in Ti64 substrates. It is seen that an optimum amount of 1-D nanostructures is obtained for 4-8 h of oxidations. Prolonged oxidation reduces the coverage of 1-D nanostructures.

Residual stress plays a significant role to enhance the coverage of 1-D nanostructures on Ti64 substrates. The 1-D nanostructures are longer and finer on stressed substrates compared to the un-stressed substrates. The bundled structures on un-stressed particles are separated on stressed particles. It is proposed that the residual stress is released during oxidation by creating new surfaces in the form of 1-D nanostructures.

Result show that the 1-D nanostructures are 2-5  $\mu\text{m}$  long and 30-60 nm in diameter. However, some thick nanostructures having diameter more than 100 nm are also seen on oxidized surface. Core-shell structures are evident in the 1-D nanostructures where the

core is rutile  $\text{TiO}_2$  and shell is corundum  $\text{Al}_2\text{O}_3$ . The growth directions of rutile  $\text{TiO}_2$  and corundum  $\text{Al}_2\text{O}_3$  are  $\langle 0\ 0\ 2 \rangle$  and  $\langle 1\ 1\ 0 \rangle$ , respectively.

During oxidation, double layer of oxides are formed on Ti64 substrates. The outer oxide scale is composed of a mixture of  $\text{TiO}_2$  and  $\text{Al}_2\text{O}_3$  whereas the inner oxide scale is only  $\text{TiO}_2$ . The 1-D nanostructures originate in outward directions from the outer oxide scales. Close observation revealed that the 1-D nanostructures originate from the top of the grains in outer oxide scale. Based on these findings a diffusion based growth model is proposed to explain the growth mechanism of 1-D nanostructures on Ti64 substrates.

#### 4.2.6 Comparison of 1-D Growth on Ti and Ti64 Substrates

Compared with other methods such as hydrothermal (Han et al., 2007; Rout et al., 2007), electrospinning (Landau et al., 2008; B. Wang et al., 2010), anodization (A. Hu et al., 2011; H. Li, Cao, Liu, Su, & Dong, 2012; H. F. Lu et al., 2008; Paulose et al., 2005), nanocarving (Carney et al., 2005; Yoo et al., 2004b), UV lithography and dry plasma etching (Francioso et al., 2008), the process of thermal oxidation is much faster and convenient for synthesizing 1-D nanostructures on Ti and Ti64 substrates. However, the process of oxidation is somewhat different for Ti and Ti64 substrates. The resultant 1-D nanostructures after oxidation also differ from each other to some extent. In Table 4.3, the comparison between the 1-D nanostructures on Ti and Ti64 substrates are tabulated in terms of processing, physical and chemical characteristics. It is seen that the oxidation of Ti and Ti64 for the growth of 1-D nanostructures requires minute amount of oxygen in humid and dry environment, respectively. Residual stress has significant effect to enhance the coverage of 1-D nanostructures on Ti and Ti64 particles. The resultant 1-D nanostructure on Ti is  $\text{TiO}_2$  whereas on Ti64 it is core-shell  $\text{TiO}_2\text{-Al}_2\text{O}_3$ .

**Table 4.3: Comparison of 1-D nanostructures grown on Ti and Ti64 substrates.**

Processing, physical and chemical characteristics	Characteristics	Ti	Ti64
Substrate conditions	Crystal structure	$\alpha$ (hexagonal) Ti	Mixture of $\alpha$ (hexagonal) and $\beta$ (body-centered cubic) of Ti
	Alloy microstructure	Coarse grain of $\alpha$ -Ti	Mixture of $\alpha$ - and $\beta$ -Ti in the form of lamellar, Widmanstätten and coarse grain
Growth conditions	Optimum oxidation temperature	750 °C	750 °C
	Oxidation environment	Humid environment	Dry environment
	Optimum dynamic oxygen partial pressure	$10^{-11}$ - $3 \times 10^{-10}$ Pa	$10^{-11}$ - $3 \times 10^{-9}$ Pa
	Optimum oxidation duration	Not studied	4-8 h
	Residual stress	Compressive residual stress significantly improved the coverage of 1-D nanostructures	Compressive residual stress significantly improved the coverage of 1-D nanostructures
Resultant 1-D nanostructures	Length	5-10 $\mu\text{m}$	2-5 $\mu\text{m}$
	Diameter	50-200 nm	Generally 30-60 nm. But some thick structures having diameter more than 100 nm is seen
	Morphology	Entangled nanostructures. Four types of 1-D nanostructures exists: (1) stacked, (2) ribbon, (3) plateau and (4) lamppost shaped	Straight nanostructures. Three types of nanostructures exists: (1) fine, (2) thick and (3) bundled shaped
	Structural composition	1-D $\text{TiO}_2$	1-D core-shell $\text{TiO}_2$ - $\text{Al}_2\text{O}_3$
	Crystallography	$\text{TiO}_2$ : Rutile (tetragonal)	$\text{TiO}_2$ : Rutile (tetragonal) $\text{Al}_2\text{O}_3$ : Corundum (rhombohedral)
	Growth Direction	Not studied	$\text{TiO}_2$ : $\langle 0\ 0\ 2 \rangle$ $\text{Al}_2\text{O}_3$ : $\langle 1\ 1\ 0 \rangle$
	Epitaxial relation	Not studied	1-D nanostructures originated from the $\{1\ 0\ -1\ 0\}$ plane of $\alpha$ -Ti
Coverage	Low to medium	High	

**Table 4.3, Continued.**

Processing, physical and chemical characteristics	Characteristics	Ti	Ti64
	Number of oxide scale	Multilayered	Double layered
	Composition of oxide scale	TiO <sub>2</sub> is formed at the gas-oxide interface. Ti <sub>3</sub> O <sub>5</sub> , Ti <sub>2</sub> O <sub>3</sub> , and TiO formed at the oxide-metal interface	The outer oxide scale composed of TiO <sub>2</sub> and Al <sub>2</sub> O <sub>3</sub> . Inner oxide scale composed of TiO <sub>2</sub> only
Oxide scale beneath 1-D nanostructure	Origin of 1-D nanostructure	Originated from the outer oxide scale of TiO <sub>2</sub> . 1-D nanostructures are formed on top of the existing grains of outer oxide scale	Originated from the outer oxide scale composed of TiO <sub>2</sub> and Al <sub>2</sub> O <sub>3</sub> . 1-D nanostructures are formed on top of the existing grains of outer oxide scale
	Role of oxide scales	Due to presence of multilayer, stress is induced among the layers. The stress might be compensated by forming nucleation seeds of 1-D nanostructures	Due to presence of multilayer, stress is induced among the layers. The stress might be compensated by forming nucleation seeds of 1-D nanostructures
Growth Mechanism	-	Diffusion based model	Diffusion based model

### 4.3 Gas Sensing

In the previous sections the growth of 1-D nanostructures and characterization of oxidized Ti and Ti64 substrates were described. For the preparation of sensors, some selected growth conditions are utilized with some optimization for the preparation of sensors. In the following sections the details of sensor preparation and gas sensing is presented.

#### 4.3.1 Gas Sensing Nanostructures

During the growth of 1-D nanostructures on Ti and Ti64 substrates, different types of nanostructures are obtained. On Ti particles oxide scale, stacked, ribbon, plateau, and lamp post shaped nanostructures are obtained at different oxidation conditions. On the other hand, on Ti64 particles thick, bundled and fine nanostructures are obtained. For gas sensing applications only 1-D nanostructures on Ti and Ti64 particles are investigated due to their high surface areas. For this reason, three types of structures are chosen for gas sensing applications as follows:

01. 1-D nanostructures grown on Ti-20h particles during oxidation at 750 °C for 4 h with 5 ppm O<sub>2</sub> in Ar flown at 150 sccm as shown in Figure 4.64(a). This sensor contains curved 1-D nanostructures (mostly stacked 1-D nanostructures with small amount of ribbon, plateau and lamp post shape nanostructures) on oxidized Ti-20h particles. This sensor is designated as “S-1” in the following sections of this chapter.
02. 1-D nanostructures grown on Ti64-20h particles during oxidation at 750 °C for 4 h with 15 ppm O<sub>2</sub> in Ar flown at 500 sccm as shown in Figure 4.64(b). This sensor contains fine 1-D core-shell TiO<sub>2</sub>-Al<sub>2</sub>O<sub>3</sub> nanostructures on oxidized Ti64-20h particles. This sensor is designated as “S-2” in the following sections of this chapter.

03. 1-D nanostructures grown on Ti64-20h particles during oxidation at 800 °C for 4 h with 15 ppm O<sub>2</sub> in Ar flown at 500 sccm as shown in Figure 4.64(c). This sensor contains thick and short 1-D core-shell TiO<sub>2</sub>-Al<sub>2</sub>O<sub>3</sub> nanostructures on oxidized Ti64-20h particles though some fine 1-D nanostructures are seen. This sensor is designated as “S-3” in the following sections of this chapter.

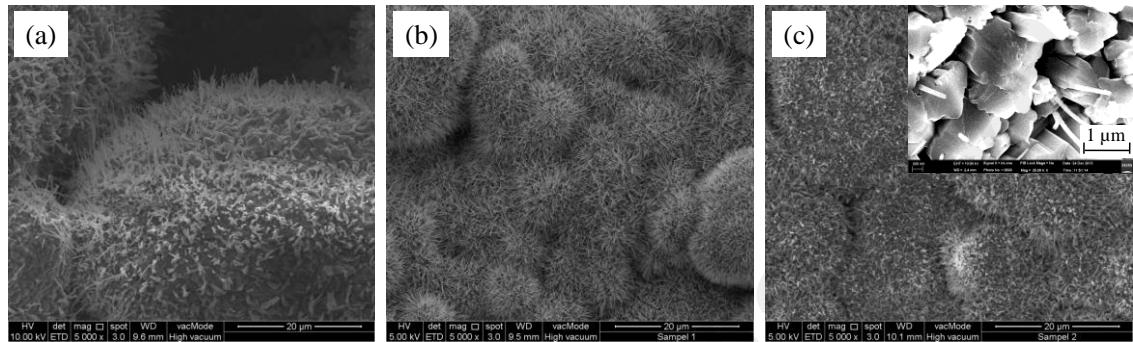


**Figure 4.64: 1-D nanostructures for gas sensing (a) S-1 sensor contains TiO<sub>2</sub> nanostructures on Ti-20h particles grown at 750 °C, (b) S-2 sensor contains fine core-shell TiO<sub>2</sub>-Al<sub>2</sub>O<sub>3</sub> nanostructures on Ti64-20h particles grown at 750 °C and (c) S-3 sensor contains thick core-shell TiO<sub>2</sub>-Al<sub>2</sub>O<sub>3</sub> nanostructures on Ti64-20h particles grown at 800 °C.**

From Figure 4.64, it is seen that the composition, structural morphology and density of 1-D nanostructures is varied in the sensors. In Table 4.4, the variations in compositions, structural morphology and density of 1-D nanostructures in the sensors are summarized.

**Table 4.4: The structural morphology, density of 1-D nanostructures and surface area of the sensors.**

Sensor identifications	S-1 sensor	S-2 sensor	S-3 sensor
Morphology	1-D TiO <sub>2</sub> on oxidized Ti-20h particles	1-D fine core-shell TiO <sub>2</sub> -Al <sub>2</sub> O <sub>3</sub> nanostructures on oxidized Ti64-20h particles	1-D thick core-shell TiO <sub>2</sub> -Al <sub>2</sub> O <sub>3</sub> nanostructures on oxidized Ti64-20h particles
Density of 1-D nanostructures (1-D nanostructure/m <sup>2</sup> )	1.27x10 <sup>11</sup>	6.7x10 <sup>12</sup>	1.9x10 <sup>12</sup>

### **4.3.2 Optimization of Sensor Fabrication**

In the previous section the growth conditions and characterization of oxidized Ti64 particles are described. For the preparation of the sensors, similar growth conditions were utilized. However, further optimization was required for the preparation of functional sensors which is discussed in the following sections.

#### **4.3.2.1 Sensors with Different wt% of Particle Loading**

Prior to oxidation, during the preparation of sensor, the Ti-20h and Ti64-20h particles were dispersed in an ink with different wt% of particle loading. The as-prepared ink was semitransparent. After loading Ti64-20h particles, the ink became blackish color.

#### **4.3.2.2 Determination of Resistance of As-prepared Sensors**

Prior to oxidation, the Ti64-20h particles were dispersed in the ink with particle loading up to 20 wt% as described in the previous section. Then 3  $\mu\text{L}$  of the composite ink was dropped on Au interdigitated alumina substrates followed by thermal oxidation. For being a functional sensor, the resistance of the sensor should be in the semiconducting range at the operating temperature. For this reason, the resistance of the as-prepared sensors containing varying amount of particle loading was measured at room temperature (RT), 450  $^{\circ}\text{C}$  and 650  $^{\circ}\text{C}$ . One such example is shown in Figure 4.65 where the resistance of the S-2 sensors containing varying amount of particle loading is presented. It is seen that for 0 wt% and 1 wt% of particle loading in the ink, the resistance of the sensors are measured overloaded (OVL) at all temperatures. For the loading of 2 to 5 wt% particles in the ink, the resistance is seen OVL at RT but in the order of  $\sim 10^4$  and  $\sim 10^7$   $\Omega$  at 450  $^{\circ}\text{C}$  and 650  $^{\circ}\text{C}$ , respectively. On the other hand, for 10 to 20 wt% of particle loading in the ink, the sensor shows low resistance at 450  $^{\circ}\text{C}$  and 650  $^{\circ}\text{C}$ . So, it is concluded that 2

to 5 wt% of particle loading in the ink is the optimum for the preparation of functional sensors.

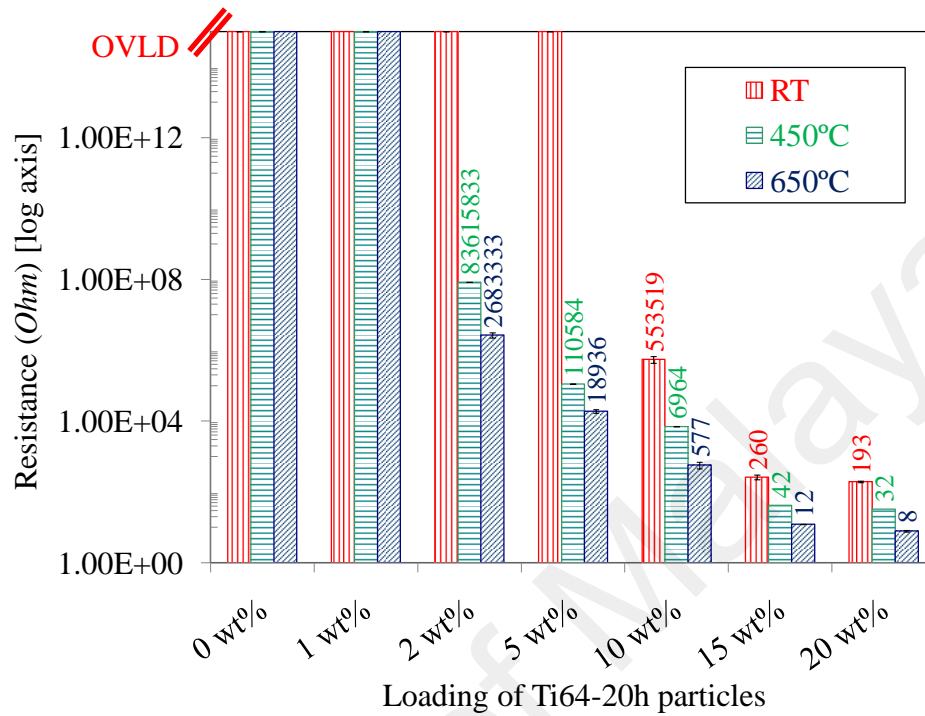


**Figure 4.65: Resistance of the S-2 sensors containing varying amount of particle loading at room temperature, 450 °C and 650 °C.**

#### 4.3.2.3 Relation between Sensor Resistance and Particle Loading

To understand the relation between the loading of particles in the ink and resistance, the S-2 sensors with varying amount of particles loading were observed under stereoscope in top view at different magnifications as shown in Figure 4.66. It is seen that for 1 wt% of loading, the particles are clustered during oxidation and maintained some distance between Au electrodes as shown in Figure 4.66(a-b). For 2-5 wt% of loading in the ink, the clusters of oxidized particles are linked between the electrodes. One such example is shown in Figure 4.66(c-d) for 5 wt% of Ti64 loading. Finally, for 10-20 wt% of loading, a dense film of oxidized particles is formed. One such example of 20 wt% of particle loading is shown in Figure 4.66(e-f).

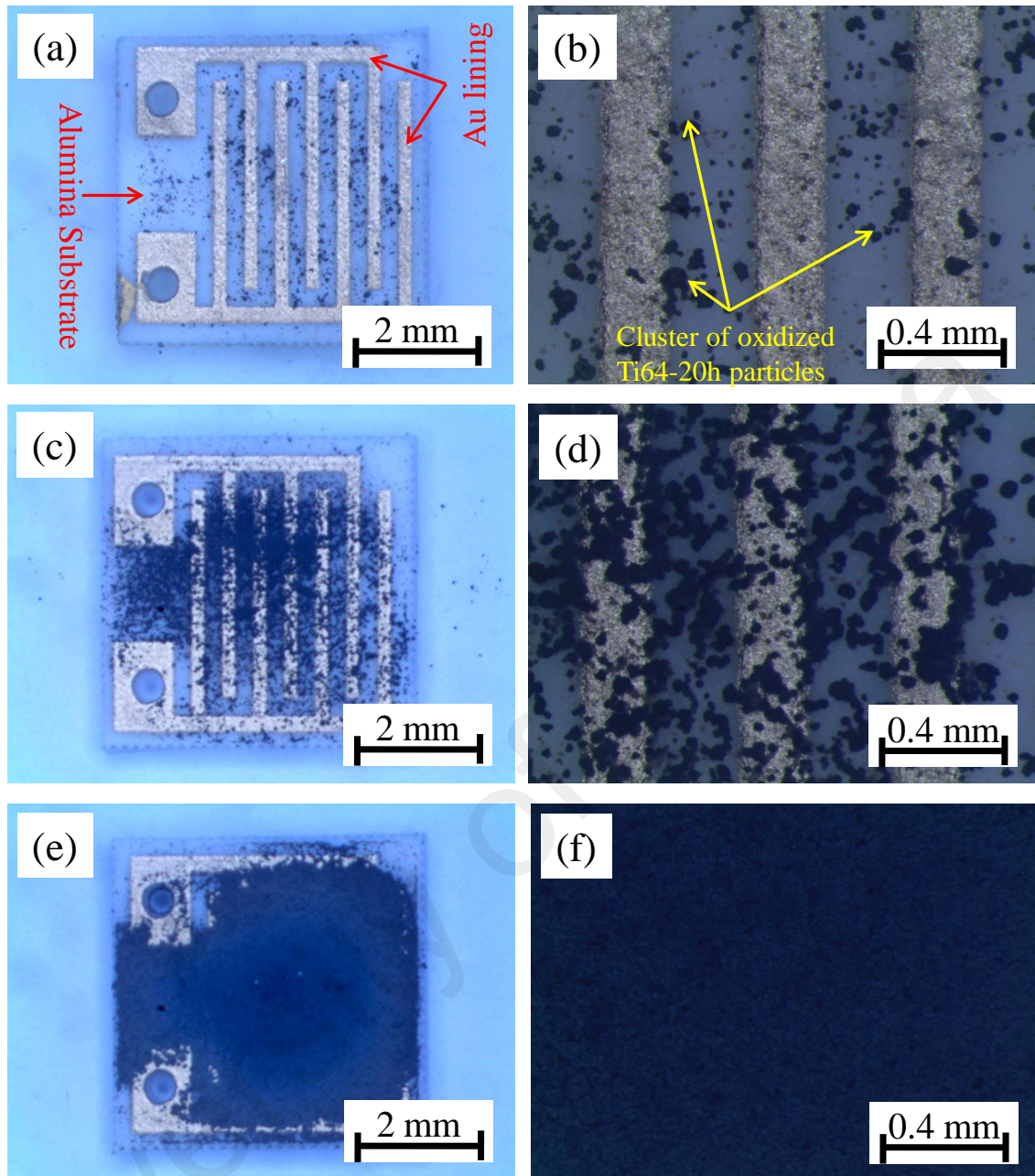


**Figure 4.66: Top view of the as-prepared S-2 sensors at different magnifications prepared from ink containing different wt% of particles (a-b) 1 wt% of Ti64 particles in the ink, (c-d) 5 wt% of Ti64 particles in the ink and (e-f) 20 wt% of Ti64 particles in the ink.**

To further elucidate the effect of particle loading in the ink, part of the oxidized layer in S-2 sensor containing 10 wt% of particle loading was carefully removed by a blade. The oxidized particles were detached as a flake as seen in Figure 4.67(a). Then one top side and one flip side of the flake were placed on FESEM sample holder. The stereoscopic view of the top and flip side particles are shown in Figure 4.67(b). Then the top side and

flip side particles were observed under FESEM as shown in Figure 4.67(c-d). It is seen that the top side particles have long and fine 1-D core-shell  $\text{TiO}_2\text{-Al}_2\text{O}_3$  nanostructures (Figure 4.67(c)). On the other hand, the flip side particles are almost depleted of 1-D nanostructures (Figure 4.67(d)). It is assumed that during the preparation of sensors from the ink containing particle loading more than 5 wt%, only top side particles oxidized properly resulting in 1-D nanostructures, whereas flip side particles oxidized partially.

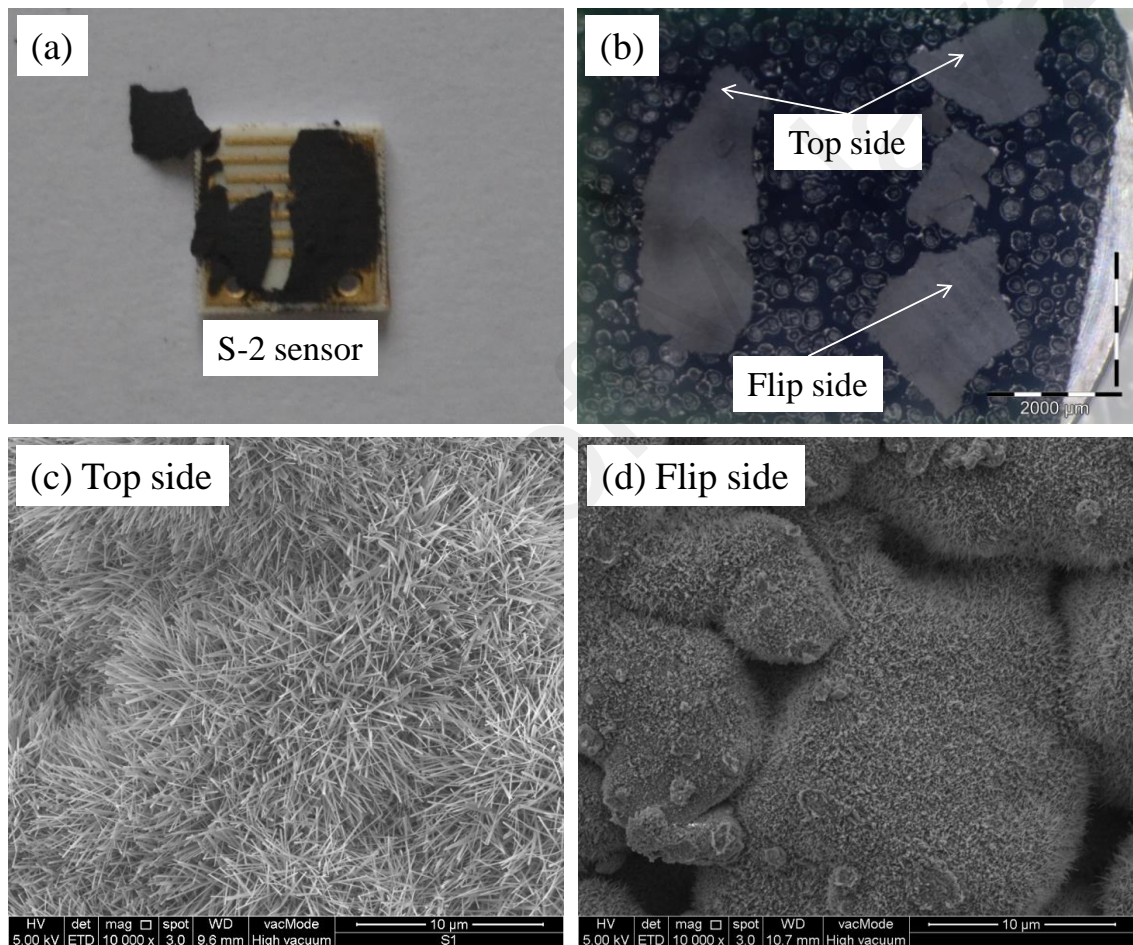


**Figure 4.67: (a) The particles of S-2 sensor containing 10 wt% of loading is detached as flakes, (b) stereoscopic view of the top side and flip side facing particles, (c) FESEM image of the top side facing particles and (d) FESEM image of the flip side facing particles.**

To confirm the elemental compositions in the top side and flip side facing particles, EDX spectroscopy analysis was performed at different spots and tabulated in Table 4.5. The Ti and oxygen content in the top side particles are  $25.3 \pm 6.3$  at% and  $63.7 \pm 4.9$  at%, respectively. On the other hand, the Ti and oxygen content in the flip side particles are

77±11.8 at% and 15.5±3.8 at%, respectively. So, it is seen that the Ti content is increased and oxygen content is decreased from the top side to flip side particles, respectively. So, it is concluded that, the flip side particles in the sensors are not fully oxidized at high loading and are still partially conductive which might be the reason of low resistance in these sensors.

**Table 4.5: Elemental composition of top side and flip side particles in S-2 sensors prepared from ink containing 10 wt% of particle loading.**

Particle identification	Ti (at%)	Al (at%)	V (at%)	O (at%)
Top side facing particles	25.3±6.3	8.6±2.5	2.3±0.9	63.7±4.9
Flip side facing particles	77±11.8	4.4±0.42	3.1±0.2	15.5±3.8

From the above observations, three different scenarios are depicted in the sensors for different wt% of particle loading and the schematics are presented in Figure 4.68. It should be noted that, in all cases 1-D nanostructures are formed on the top side particles of the sensors.

01. For 0-1 wt% of loading, there is not enough particles to create conducting path after oxidation as shown in Figure 4.68(a). For this reason the resistance of the sensors were seen OVLD at all temperatures.
02. For 2-5 wt% of loading only one or few layers of oxidized particles are formed. In this case all particles are fully oxidized. The oxidized particles are connected by the 1-D nanostructures (Figure 4.68(b)). For this reason sensors prepared from the inks containing 2-5 wt% of particles showed resistance in the semiconducting range at elevated temperatures.
03. Sensors prepared from the inks containing more than 5 wt% of Ti64-20h particles are observed to have multiple layers of oxidized particles. But in this case, only the top layers are thermally oxidized having 1-D nanostructures whereas the underneath is partially oxidized or un-oxidized (Figure 4.68(c)) depending on the

layer thickness. Due to presence of metallic particles underneath, electrons can easily pass from one electrode to another. For this reason, the resistance of these sensors is in conducting range even at room temperatures.

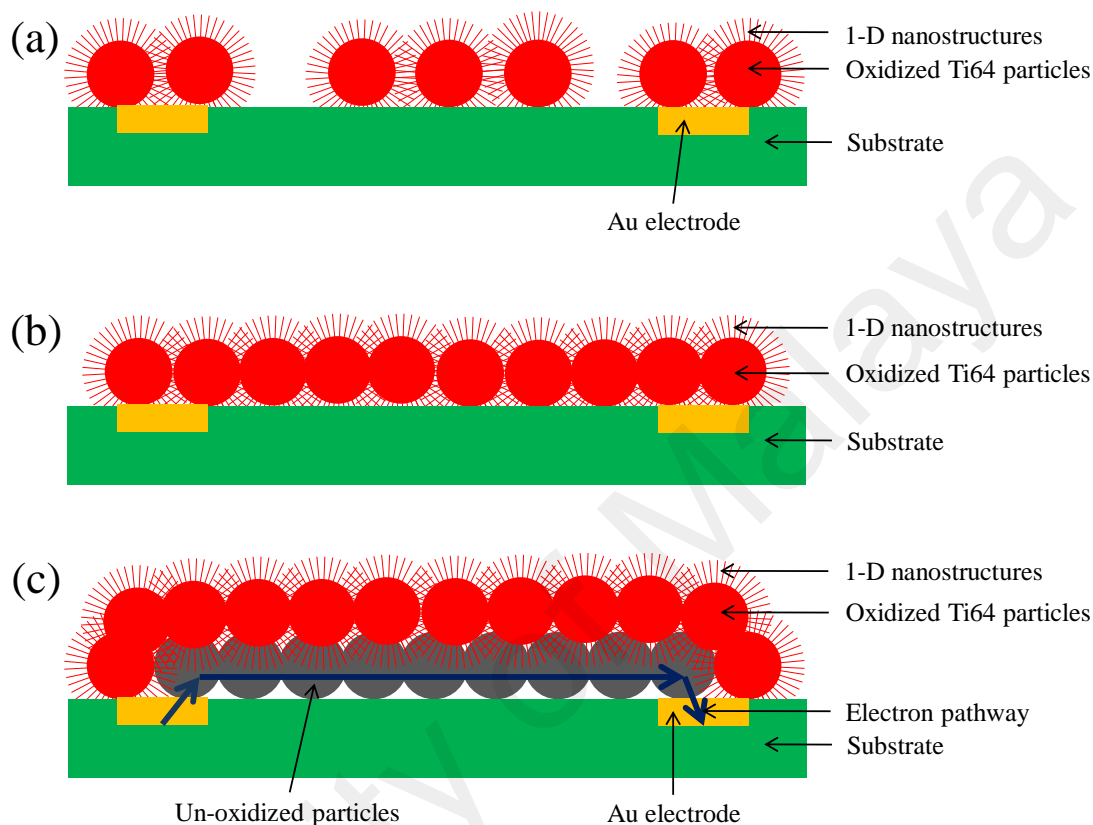


**Figure 4.68: Schematics of the sensors prepared from ink containing different wt% of particles (a) loading of <2 wt%, (b) loading of 2-5 wt% and (c) loading of >5 wt%.**

From the above observation it is clear that loading of particles in the ink during the preparation of sensors has significant effect on the resistance. Loading of less amount of particles (<2 wt%) leads to overload resistance whereas loading of high amount of particles (>5 wt%) leads to very low resistance. The optimum amount of particles in the ink for gas sensing application is 2-5 wt%. For this reason, in the following sections 5 wt% of particle loading in the ink is used for gas sensing applications.

### 4.3.3 Gas Sensing Performance

The gas sensing performance of thermally oxidized Ti-20h (S-1 sensor) and Ti64-20h (S-2 and S-3 sensors) particles were tested towards different reducing and oxidizing gases including hydrogen ( $H_2$ ), hydrogen sulfide ( $H_2S$ ), carbon monoxide (CO), methane ( $CH_4$ ), methanol ( $CH_3OH$ ), ethanol ( $C_2H_5OH$ ), ethylene ( $C_2H_4$ ), nitrogen dioxide ( $NO_2$ ) and oxygen ( $O_2$ ). For the preparation of sensors 5 wt% of particles were loaded in the ink. After that 3  $\mu$ L ink was dropped on the gold (Au) interdigitated alumina substrate through a micro pipette. After that the substrate along with the particles was thermally oxidized under the conditions mentioned in section 4.3.1. Then the response of the as-prepared sensors was measured towards different gases as presented below.

#### 4.3.3.1 Effects of Composition, Morphology and Selectivity

To determine the effect of composition and oxide morphology towards sensing performance, sensors S-1, S-2 and S-3 were exposed to 1000 ppm of target gases at 650  $^{\circ}$ C. In all cases,  $N_2$  was used as background gas except for sensing  $NO_2$ , for which air was used as the background gas. The optimum composition and oxide morphology is selected by comparing the responses towards different gases. The selectivity of the sensors towards certain gases is also determined.

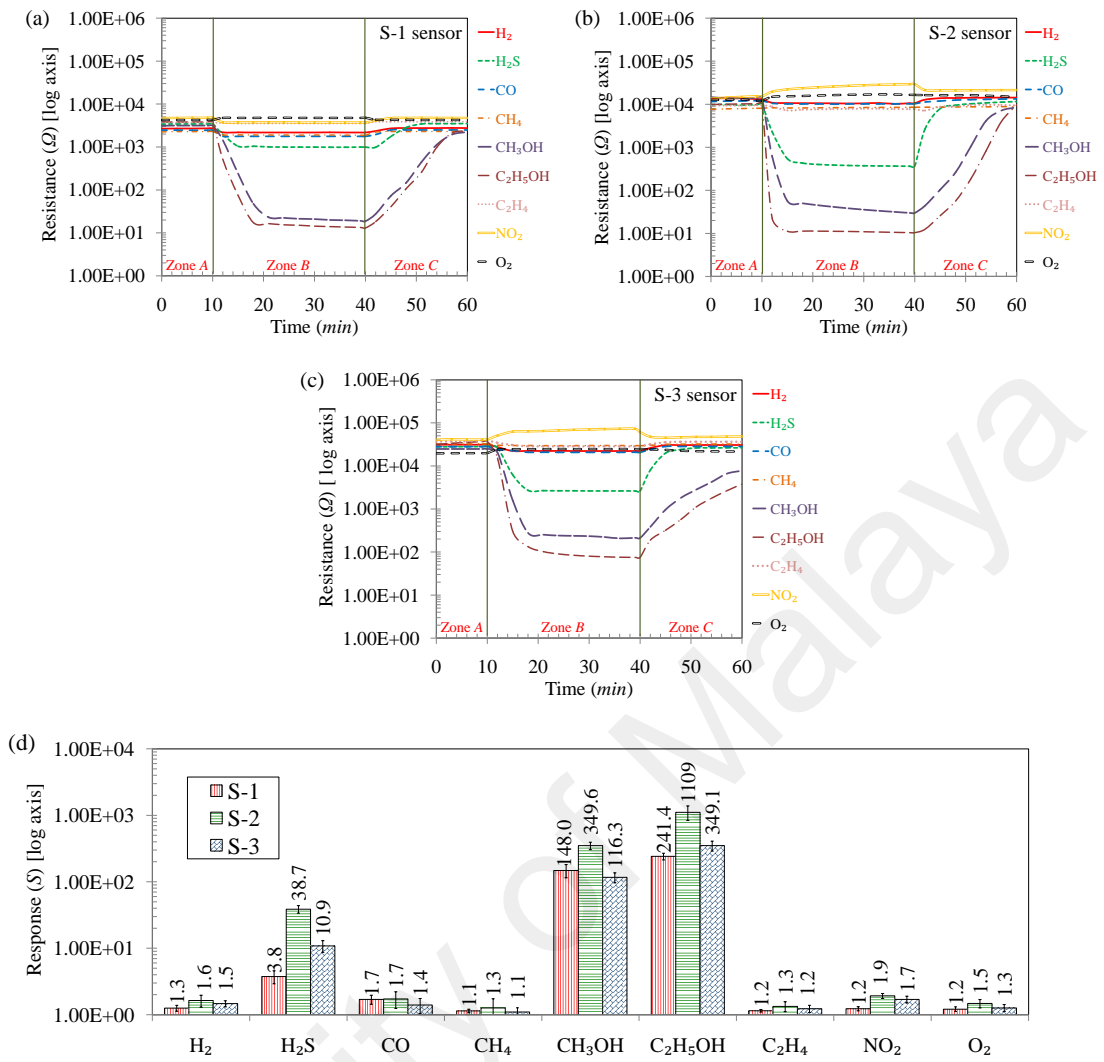


**Figure 4.69: Resistance response towards 1000 ppm of H<sub>2</sub>, H<sub>2</sub>S, CO, CH<sub>4</sub>, CH<sub>3</sub>OH, C<sub>2</sub>H<sub>5</sub>OH, C<sub>2</sub>H<sub>4</sub>, NO<sub>2</sub> and O<sub>2</sub> at 650 °C of (a) S-1 sensor, (b) S-2 sensor, (c) S-3 sensor and (d) comparison of the sensing response among the S-1, S-2 and S-2 sensors.**

Figure 4.69(a-c) shows the resistance responses of S-1, S-2 and S-3 sensors at 650 °C. In the response curves, three distinct zones can be seen. Zone A is the region where the background gas (N<sub>2</sub> or air) was flown into the quartz tube for 10 min at a rate of 500 sccm. The average value of the resistance in zone A is denoted as  $R_o$ . It is noticed that the average value of  $R_o$  in S-1 is about  $2 \times 10^3$ – $4 \times 10^3$  Ω which is lowest compared with the sensor S-2 ( $1 \times 10^4$ – $2 \times 10^4$  Ω) and S-3 ( $3 \times 10^4$ – $4 \times 10^4$  Ω). It should be noted that sensor S-1 is composed of 1-D TiO<sub>2</sub> nanostructures on oxidized Ti-20h particles. On the other hand, sensor S-2 and S-3 is composed of 1-D core-shell TiO<sub>2</sub>-Al<sub>2</sub>O<sub>3</sub> nanostructures where the

semiconducting  $\text{TiO}_2$  is surrounded by insulating  $\text{Al}_2\text{O}_3$  layer. Due to presence of insulating layer on semiconducting  $\text{TiO}_2$ , the value of  $R_o$  in S-2 and S-3 sensor is higher than S-1 sensor. The value of  $R_o$  in S-3 sensor is higher than that of S-2 due to less coverage of 1-D nanostructures in S-3 sensors which creates fewer connections for current flow.

In the zone *B* of the response curves, 1000 ppm of target gas in the presence of the background gas ( $\text{N}_2$  was used as background gas for all target gases except for  $\text{NO}_2$  where air was used as background gas) was introduced into the quartz tube for 30 min at the same flow rate. It is seen that the resistance of the sensors is decreased due to the presence of reducing gases ( $\text{H}_2$ ,  $\text{H}_2\text{S}$ ,  $\text{CO}$ ,  $\text{CH}_4$ ,  $\text{CH}_3\text{OH}$ ,  $\text{C}_2\text{H}_5\text{OH}$  and  $\text{C}_2\text{H}_4$ ). On the other hand, the resistance of all sensors is increased in the presence of  $\text{O}_2$  as target gas. However, different phenomenon is observed for the oxidizing  $\text{NO}_2$ . It is seen that the resistance of S-1 sensor decreases in the presence of  $\text{NO}_2$  whereas it is increased in S-2 and S-3 sensors. This phenomenon is explained in details in section 4.3.6.2. After stabilizing the resistance in Zone *B*, the average value of resistance is taken which is denoted as  $R_g$ . Finally, in zone *C*, background gas was flown into the quartz tube for the recovery of sensors to their initial resistances.

The response ( $R_o/R_g$  or  $R_g/R_o$ ) of the S-1, S-2 and S-3 sensors was calculated from Figure 4.69(a-c) and presented in Figure 4.69(d). It is seen that the response of S-2 sensor is higher for all gases compared with S-1 and S-3 sensors. This is due to having higher density of 1-D nanostructures in S-2 sensors which provides more sites for gas adsorption and desorption resulting higher response. So, it is concluded that sensor prepared by thermal oxidation of Ti64-20h particles at  $750\text{ }^\circ\text{C}$  possessed optimum structure for gas sensing.

From the resistance curves (Figure 4.69(a-c)), it is also seen that the sensors have insignificant responses towards H<sub>2</sub>, CO, CH<sub>4</sub>, C<sub>2</sub>H<sub>4</sub>, NO<sub>2</sub> and O<sub>2</sub>; significant amount of response is seen only for H<sub>2</sub>S, CH<sub>3</sub>OH and C<sub>2</sub>H<sub>5</sub>OH gases. For 1000 ppm H<sub>2</sub>S, CH<sub>3</sub>OH and C<sub>2</sub>H<sub>5</sub>OH the responses of S-2 sensor are 38.7, 349.6, and 1109, respectively. So, it is concluded that 1-D core-shell TiO<sub>2</sub>-Al<sub>2</sub>O<sub>3</sub> nanostructures grown at 750 °C (sensor S-2) shows selectivity towards H<sub>2</sub>S, CH<sub>3</sub>OH and C<sub>2</sub>H<sub>5</sub>OH. Thus, further investigations of the sensors were carried out on S-2 sensors towards H<sub>2</sub>S, CH<sub>3</sub>OH and C<sub>2</sub>H<sub>5</sub>OH gases only.

#### 4.3.3.2 Performance towards H<sub>2</sub>S, CH<sub>3</sub>OH and C<sub>2</sub>H<sub>5</sub>OH

It is seen from Table 4.4 that the sensing structures grown at 750 °C on Ti64-20h particles (sensor S-2) possessed higher density of 1-D nanostructures compared with structures grown at 750 °C on Ti-20h particles (sensor S-1) and structures grown at 800 °C on Ti64-20h particles (sensor S-3). The S-2 sensor showed better sensing performance compared with sensor S-1 and S-3. The sensors showed selectivity only for H<sub>2</sub>S, CH<sub>3</sub>OH and C<sub>2</sub>H<sub>5</sub>OH gases. So, further evaluation of the performance is carried out only for S-2 sensors towards H<sub>2</sub>S, CH<sub>3</sub>OH and C<sub>2</sub>H<sub>5</sub>OH gases.

##### (a) *Optimum temperature for gas sensing*

To find out the optimum operating temperature, S-2 sensors was exposed to 1000 ppm H<sub>2</sub>S, CH<sub>3</sub>OH and C<sub>2</sub>H<sub>5</sub>OH at temperatures ranging from 100 to 650 °C. The change in resistance of the sensors towards H<sub>2</sub>S, CH<sub>3</sub>OH and C<sub>2</sub>H<sub>5</sub>OH at different temperatures is shown in Figure 4.70(a-c). It is seen that the change in the resistance of the sensors is negligible towards all gases until 300 °C. Upon increasing the temperatures from 400 to 650 °C the sensors show a significant drop in the resistance during the exposure to the target gases (zone B). However, highest drop in the resistance is seen at 650 °C for all gases. Re-exposure of the sensor to the background gas shows different phenomenon for

different gases (zone C). For the case of  $\text{H}_2\text{S}$ , the resistance of the sensor is fully recovered at all temperatures (Figure 4.70(a)). But for  $\text{CH}_3\text{OH}$  and  $\text{C}_2\text{H}_5\text{OH}$  the resistance of the sensors is not recovered until 20 min in the temperatures ranging from 400 to 600 °C (Figure 4.70(b-c)). Longer exposure of the sensors might lead to full recovery in resistance for the exposure to  $\text{CH}_3\text{OH}$  and  $\text{C}_2\text{H}_5\text{OH}$ , but in that case the recovery time of the sensors would be significantly long. Further increase of the operating temperature to 650 °C leads to full recovery for the  $\text{CH}_3\text{OH}$  and  $\text{C}_2\text{H}_5\text{OH}$  gases as well (Figure 4.70(b-c)). So, 650 °C is considered the optimum operating temperature of the sensors. It should be noted that the 1-D nanostructures were grown at 750 °C by thermal oxidation. For this reason, the effect of operating temperature higher than 650 °C was not investigated as it may cause possible alteration of the 1-D nanostructures.

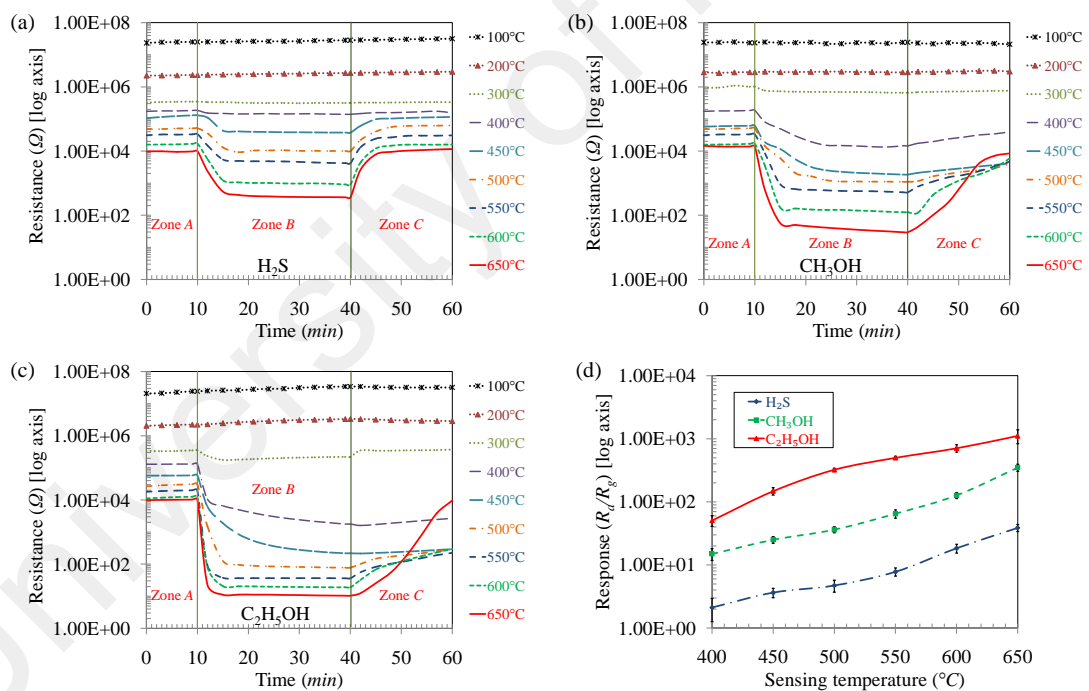


**Figure 4.70: Effects of operating temperatures on S-2 sensor during the exposure of 1000 ppm of (a)  $\text{H}_2\text{S}$ , (b)  $\text{CH}_3\text{OH}$ , (c)  $\text{C}_2\text{H}_5\text{OH}$  and (d) relation between sensor response and operating temperatures for 1000 ppm  $\text{H}_2\text{S}$ ,  $\text{CH}_3\text{OH}$  and  $\text{C}_2\text{H}_5\text{OH}$ .**

The responses of the sensors towards 1000 ppm of  $\text{H}_2\text{S}$ ,  $\text{CH}_3\text{OH}$  and  $\text{C}_2\text{H}_5\text{OH}$  are calculated at different temperatures from the resistance curves and are presented in Figure 4.70(d). It is seen that the response of the sensors increases with increasing temperatures.

In all temperatures,  $C_2H_5OH$  possessed highest sensitivity compared with  $CH_3OH$  followed by  $H_2S$ . For  $H_2S$ ,  $CH_3OH$  and  $C_2H_5OH$  the sensitivity is increased from 2.1, 14.9 and 50.6 to 38.7, 349.6 and 1109 as the temperature is increased from 400 to 650 °C, respectively.

(b) *Effects of gas concentration*

The response of S-2 sensor was measured in the presence of varying concentration of target gases ( $H_2S$ ,  $CH_3OH$  and  $C_2H_5OH$ ) at the optimum operating temperature of 650 °C as presented in Figure 4.71(a). It is seen that at all concentrations of the target gases (20-1000 ppm) the resistance of the sensors is dropped. However, the drop in the resistance is higher at the higher concentration of the target gases.

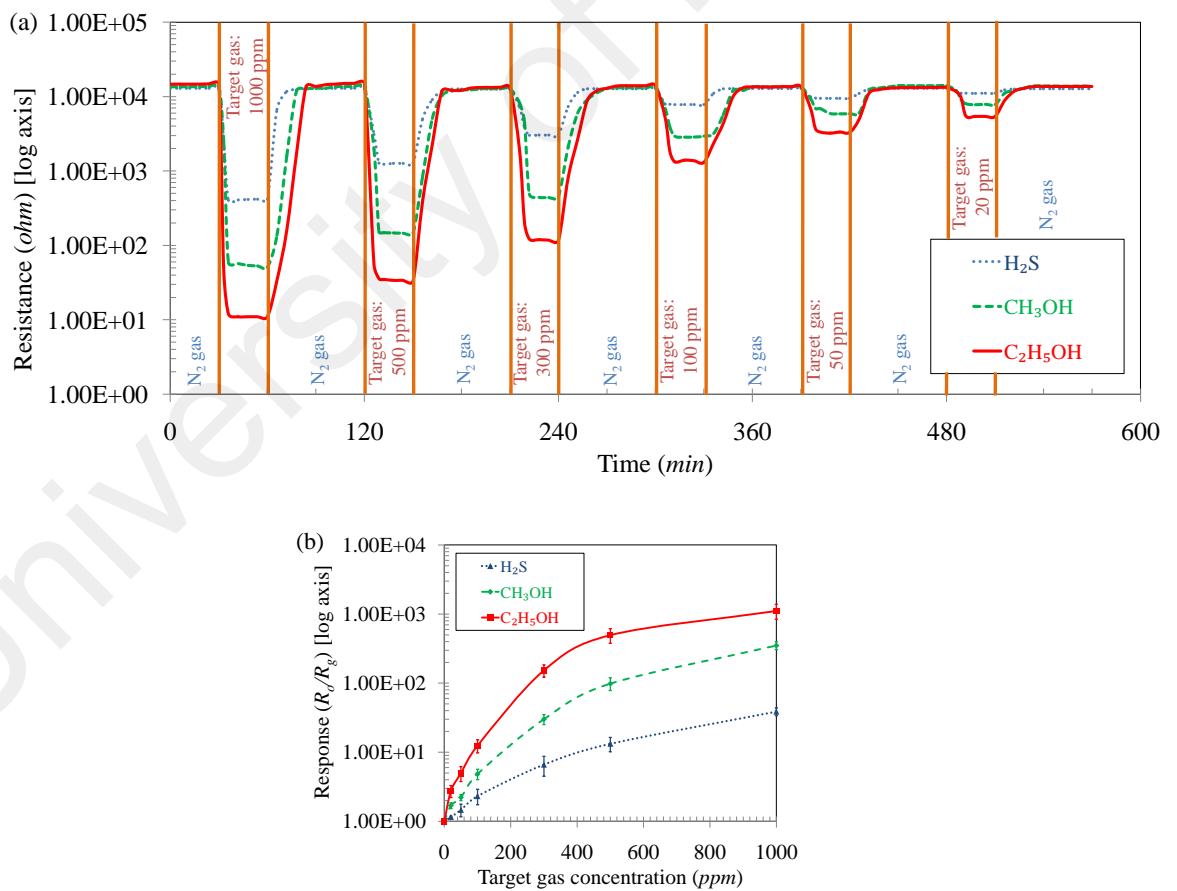


**Figure 4.71: Effects of target gas concentration on the performance of S-2 sensor at 650 °C for exposure to  $H_2S$ ,  $CH_3OH$  and  $C_2H_5OH$  (a) resistance as a function of gas concentration and (b) effects of target gas concentrations on response.**

The response of the S-2 sensor was calculated for different concentrations of target gases and is presented in Figure 4.71(b). It is seen that with increasing concentration of the target gas the sensitivity of the sensor is increased. For increasing the concentration of H<sub>2</sub>S, CH<sub>3</sub>OH and C<sub>2</sub>H<sub>5</sub>OH from 20 ppm to 1000 ppm the sensitivity of the S-2 is increased from 1.16, 1.69 and 2.25 to 38.7, 349.6 and 1109, respectively. At all concentrations of the target gases, the sensitivity are higher for C<sub>2</sub>H<sub>5</sub>OH compared to CH<sub>3</sub>OH and H<sub>2</sub>S gases.

(c) ***Response and recovery time***

The response and recovery times of S-2 sensors were measured from Figure 4.71(a) and are presented in Figure 4.72. It is seen that the response and recovery times are dependent on the concentration of the target gases. The response time decreases with increasing concentrations of target gases as shown in Figure 4.72(a). This could be due to the fact that at high concentration of target gas the 1-D nanostructures are quickly saturated with adsorbed gas molecules. For this reason, less time is required for stable response. In all cases, the response time is longer for H<sub>2</sub>S compared with CH<sub>3</sub>OH followed by C<sub>2</sub>H<sub>5</sub>OH. The response time for 20 ppm of H<sub>2</sub>S, CH<sub>3</sub>OH and C<sub>2</sub>H<sub>5</sub>OH is 13.7, 13.6 and 11.7 min which reduced to 6.5, 5.2 and 3.5 min for 1000 ppm of the target gas, respectively.

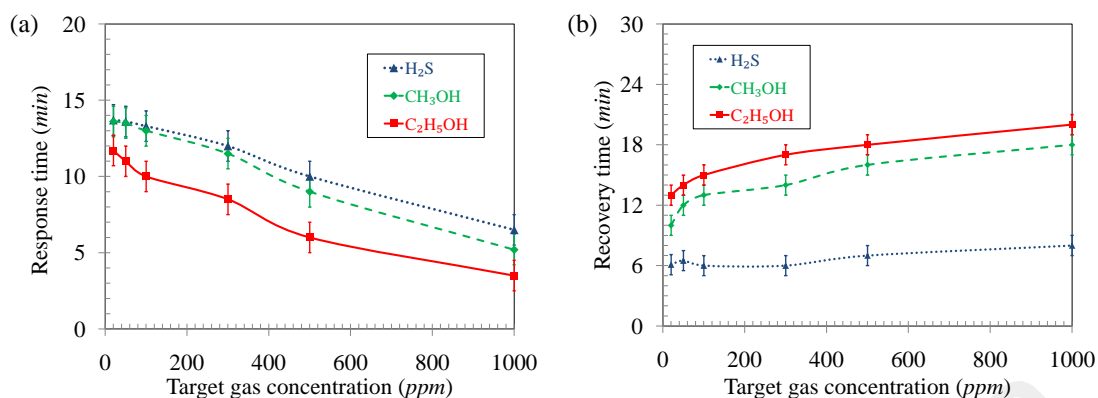


**Figure 4.72: (a) Response and (b) recovery times of S-2 sensor during the exposure of different concentrations of target gases (H<sub>2</sub>S, CH<sub>3</sub>OH and C<sub>2</sub>H<sub>5</sub>OH) at optimum operating temperature of 650 °C.**

A different behavior is observed for the recovery time of S-2 sensor as shown in Figure 4.72(b). With increasing the concentration of target gases, the recovery time of the sensors is increased. At higher concentrations of target gas more molecules are adsorbed at the surface of 1-D nanostructures. So, it takes longer time for the molecules to desorb leading to longer recovery time. For all concentrations, the longest recovery time is seen for C<sub>2</sub>H<sub>5</sub>OH followed by CH<sub>3</sub>OH and H<sub>2</sub>S. The recovery time for 20 ppm H<sub>2</sub>S, CH<sub>3</sub>OH and C<sub>2</sub>H<sub>5</sub>OH is 6.1, 10 and 13 min which increase to 8, 18 and 20 min, respectively for 1000 ppm of target gases. Similar, concentration dependent response and recovery time were reported in the literature for C<sub>2</sub>H<sub>5</sub>OH and NO<sub>2</sub> detection using TiO<sub>2</sub> nanotubes (Hazra & Bhattacharyya, 2014; Saruhan, Yüce, Gönüllü, & Kelm, 2013).

#### 4.3.4 Characterization of Nanostructures before Recovery

To investigate the morphology of the oxide nanostructures before recovery, the S-2 sensors were exposed to 1000 ppm H<sub>2</sub>S, CH<sub>3</sub>OH and C<sub>2</sub>H<sub>5</sub>OH for 30 min at 650 °C. After that the sensors were normalized in the similar target gas environment (not recovered) and did not expose to the background gas. The sensors were observed under FESEM and characterized by EDX, TEM and Raman spectroscopy. In the following sections the

details of the morphology and characterization of 1-D core-shell  $\text{TiO}_2\text{-Al}_2\text{O}_3$  nanostructures during sensing is presented.

#### 4.3.4.1 Appearance of Sensors

The as-prepared S-2 sensors possessed 1-D core-shell  $\text{TiO}_2\text{-Al}_2\text{O}_3$  nanostructures which appeared as dark brown color. During the exposure to  $\text{H}_2\text{S}$ , the sensor turned into black color. Exposure to  $\text{CH}_3\text{OH}$  and  $\text{C}_2\text{H}_5\text{OH}$ , the sensors appear as bluish dark color. The change in color of the sensors during the exposure to different gases is tabulated in Table 4.6.

**Table 4.6: Change in color of the sensors during exposure to different gases.**

Sensors Identification	Color of the sensors
As-prepared	Dark brown
Exposed to $\text{H}_2\text{S}$	Black
Exposed to $\text{CH}_3\text{OH}$	Bluish dark
Exposed to $\text{C}_2\text{H}_5\text{OH}$	Bluish dark

From the above observations it is anticipated that some morphological and chemical alteration might have happened in the sensors during the exposure of  $\text{H}_2\text{S}$ ,  $\text{CH}_3\text{OH}$  and  $\text{C}_2\text{H}_5\text{OH}$ . To investigate this issue further, sensing nanostructures were examined by FESEM, EDX, TEM and Raman spectroscopy.

#### 4.3.4.2 Morphological Observations and Characterization

Figure 4.73 shows the FESEM images of the 1-D core-shell  $\text{TiO}_2\text{-Al}_2\text{O}_3$  nanostructures after exposing to  $\text{H}_2\text{S}$ ,  $\text{CH}_3\text{OH}$  and  $\text{C}_2\text{H}_5\text{OH}$ . The as-prepared sensor nanostructures are shown as a reference in Figure 4.73(a). It is seen that during the exposure of  $\text{H}_2\text{S}$ ,  $\text{CH}_3\text{OH}$  and  $\text{C}_2\text{H}_5\text{OH}$  the coverage of 1-D nanostructures is reduced and the nanostructures appears to be shorter (Figure 4.73(b-d)).

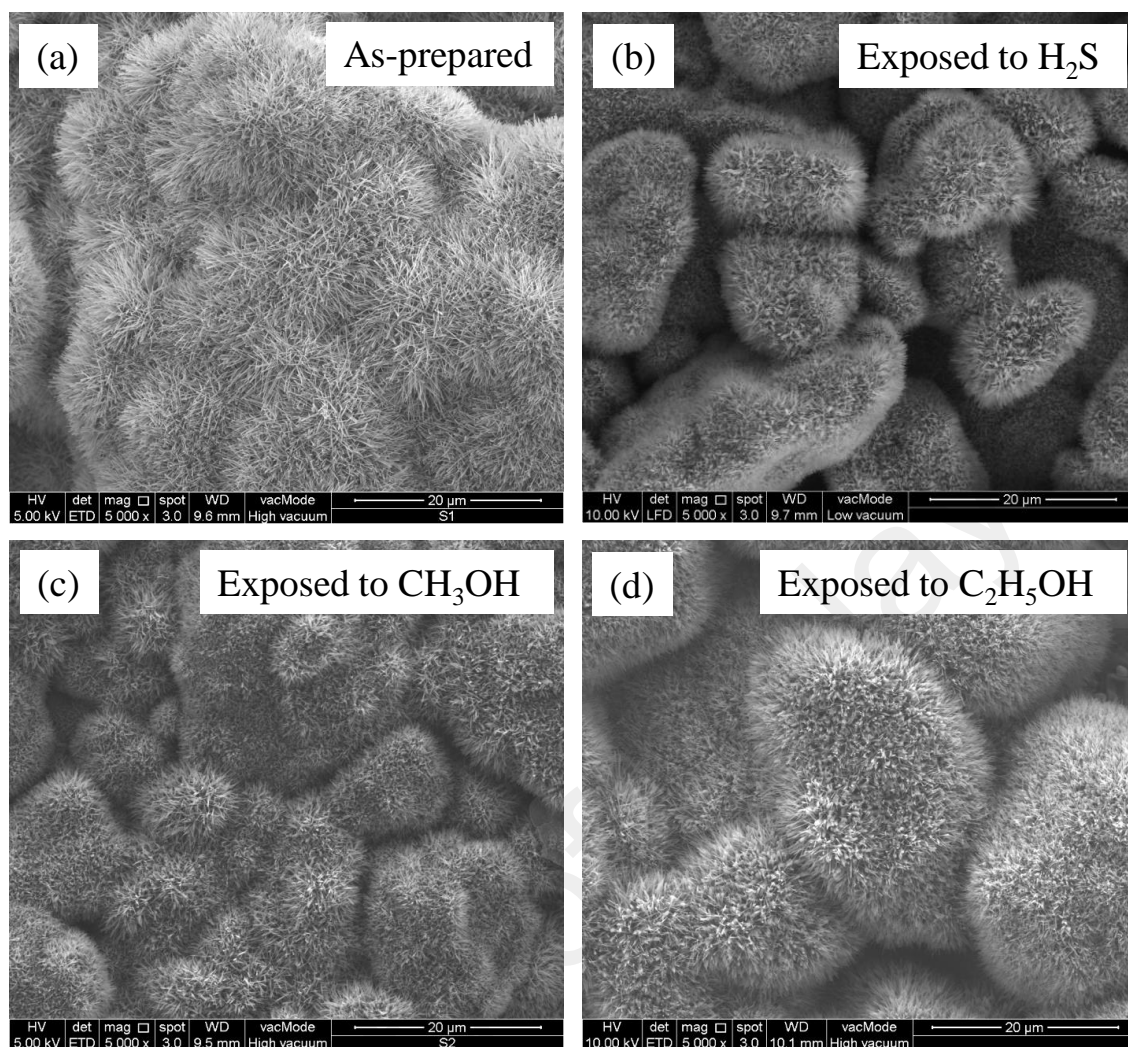


**Figure 4.73: FESEM image of the sensors containing 1-D nanostructures grown on Ti64-20h particles at 750 °C for 4 h with 15 ppm O<sub>2</sub> flow in flowing Ar (a) as-prepared sensor, (b-d) sensor exposed to 1000 ppm H<sub>2</sub>S, CH<sub>3</sub>OH and C<sub>2</sub>H<sub>5</sub>OH respectively in N<sub>2</sub> at 650 °C for 30 min.**

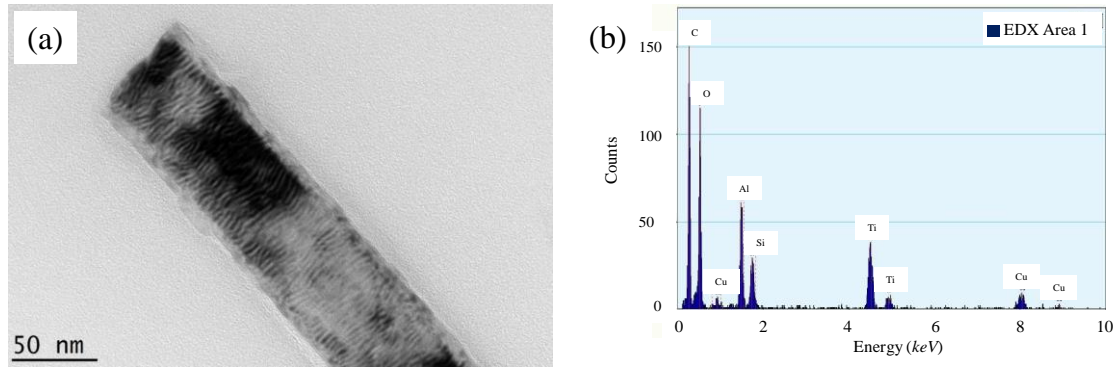
The EDX spectroscopy analysis of the sensors on different spots after exposure to 1000 ppm H<sub>2</sub>S, CH<sub>3</sub>OH and C<sub>2</sub>H<sub>5</sub>OH gas is tabulated in Table 4.7. The EDX analysis on as-prepared sensor is also presented as a reference. It is seen that the 1-D core-shell TiO<sub>2</sub>-Al<sub>2</sub>O<sub>3</sub> nanostructures in as-prepared S-2 sensor contains 22.5±5.8 at% of Ti which is increased to 33.5±2.3 at% during the exposure of H<sub>2</sub>S. On the other hand, the oxygen content is decreased from 61.5±4.5 at% to 56.5±2.4 at% during the exposure of H<sub>2</sub>S. So, it is believed that the presence of H<sub>2</sub>S partially reduces the TiO<sub>2</sub> to metallic Ti.

Exposure to CH<sub>3</sub>OH and C<sub>2</sub>H<sub>5</sub>OH increases the Ti content to some extent as seen in Table 4.7. However, it is seen that the carbon content is slightly increases in the S-2 sensors during exposure of CH<sub>3</sub>OH and C<sub>2</sub>H<sub>5</sub>OH. So, it is assumed that during sensing CH<sub>3</sub>OH and C<sub>2</sub>H<sub>5</sub>OH is dissociated and a carbon layer is deposited on the 1-D nanostructures. It should be noted that the EDX spectroscopy analysis is not too accurate and for this reason at least 5 spots were analyzed for each case. To further confirm the EDX spectroscopy results, TEM and Raman spectroscopy was performed on the sensors after exposing to the target gases.

**Table 4.7: Elemental composition of the sensors in as-prepared conditions and after exposing to different target gases.**

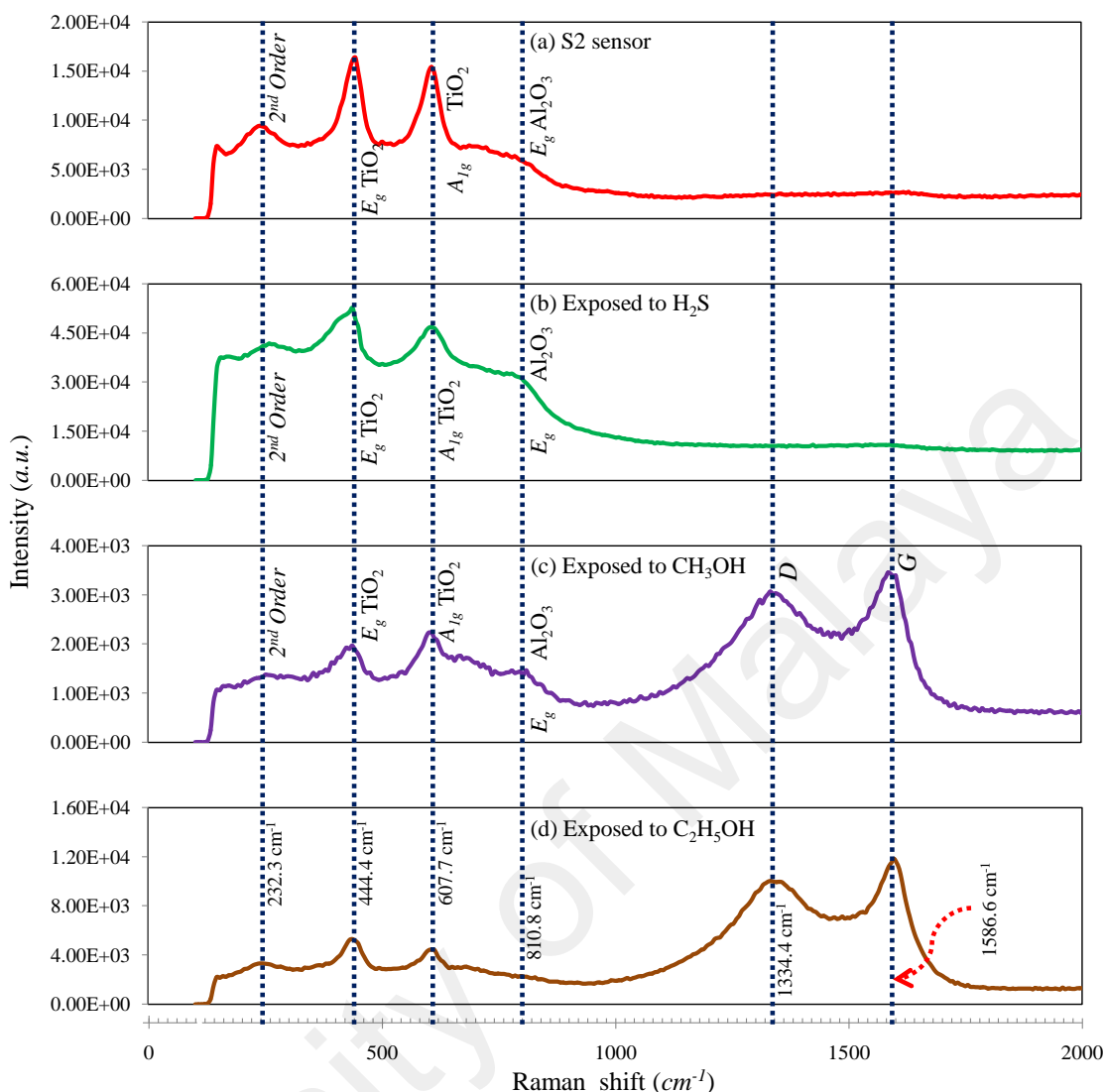
Sensor identification	Ti (at%)	Al (at%)	V (at%)	O (at%)	C (at%)
As- prepared S-2 sensor	22.5±5.8	11.4±2	1.43±0.06	61.5±4.5	3.2±0.7
Exposed to H <sub>2</sub> S	33.5±2.3	5.7±1.1	0.9±0.2	56.5±2.4	3.4±0.2
Exposed to CH <sub>3</sub> OH	27.6±6.8	6.5±3.2	1.7±0.7	60.2±6.5	4.0±1.9
Exposed to C <sub>2</sub> H <sub>5</sub> OH	23.2±3.8	9.7±1.8	1.6±0.1	59.5±2.0	6.0±0.5

Figure 4.74(a) shows the TEM images of the 1-D nanostructures after exposure to 1000 ppm C<sub>2</sub>H<sub>5</sub>OH gas for 30 min at 650 °C. The EDX spectroscopy area analysis on the 1-D nanostructures shows high content of carbon (C) together with Ti, Al, O and little amount of Cu (Figure 4.74(b)). The peaks of Cu are attributed from the Cu grid for holding the samples. So, it is reasonable to assume that a layer of C is deposited on the 1-D nanostructures during the exposure of C<sub>2</sub>H<sub>5</sub>OH. Similar phenomenon is observed for CH<sub>3</sub>OH exposure to the sensors. However, this fact is further confirmed by Raman spectroscopy.



**Figure 4.74: TEM image of 1-D core-shell TiO<sub>2</sub>-Al<sub>2</sub>O<sub>3</sub> nanostructures after exposing to 1000 ppm C<sub>2</sub>H<sub>5</sub>OH for 30 min at 650 °C and (b) EDX spectroscopy area analysis of 1-D nanostructure.**

Figure 4.75 shows the peaks from Raman spectroscopy of S-2 sensor after exposure to 1000 ppm of H<sub>2</sub>S, CH<sub>3</sub>OH and C<sub>2</sub>H<sub>5</sub>OH at 650 °C for 30 min. The Raman peaks from the as-prepared S-2 sensor is also shown as a reference in Figure 4.75(a). Four characteristic bands are observed at 232.3, 444.4, 607.7 and 810.8 cm<sup>-1</sup> in the as-prepared S-2 sensor. The bands at 444.4 and 607.7 cm<sup>-1</sup> are indexed to the Raman active modes  $E_g$  and  $A_{1g}$  of rutile TiO<sub>2</sub>, respectively (Parker & Siegel, 1990). The broad band at 232.3 cm<sup>-1</sup> results from the second-order scattering or disorder effects of rutile TiO<sub>2</sub> (Parker & Siegel, 1990). The peak at 810.8 cm<sup>-1</sup> is attributed to the Raman active modes  $E_g$  of corundum Al<sub>2</sub>O<sub>3</sub> (Xu, Huang, & Xu, 1995).



**Figure 4.75: Raman spectroscopy analysis of (a) as-prepared S-2 sensor and (b-d) after exposing to 1000 ppm of H<sub>2</sub>S, CH<sub>3</sub>OH and C<sub>2</sub>H<sub>5</sub>OH, respectively at 650 °C for 30 min.**

Figure 4.75(b) shows the Raman spectra of S-2 sensor after exposure to 1000 ppm H<sub>2</sub>S at 650 °C for 30 min. It is seen that the positions of the rutile-TiO<sub>2</sub> and corundum Al<sub>2</sub>O<sub>3</sub> peaks remained the same. So, it is concluded that no additional elements were deposited on the 1-D nanostructures during the exposure of H<sub>2</sub>S.

Exposing the sensors to 1000 ppm CH<sub>3</sub>OH and C<sub>2</sub>H<sub>5</sub>OH at 650 °C for 30 min resulted in two additional peaks located at 1334.4 and 1586.6 cm<sup>-1</sup> as shown in Figure 4.75(c-d). These peaks correspond to the D (diamond) and G (graphite) bands of C, respectively (Ferrari & Robertson, 2000). However, presence of G peak in the range of 1580-1596

$\text{cm}^{-1}$  is an indication of amorphous carbon (Ferrari & Robertson, 2000; Yeh, Chen, Hwang, Gan, & Kou, 2006). Since no shift is evident in the *G* peak ( $1586.6 \text{ cm}^{-1}$ ), it is clearly demonstrated that an amorphous layer of carbon is deposited on the 1-D core-shell  $\text{TiO}_2\text{-Al}_2\text{O}_3$  nanostructures during the exposure of  $\text{CH}_3\text{OH}$  and  $\text{C}_2\text{H}_5\text{OH}$ .

#### 4.3.5 Characterization of Nanostructures after Recovery

After exposing to 1000 ppm  $\text{H}_2\text{S}$ ,  $\text{CH}_3\text{OH}$  and  $\text{C}_2\text{H}_5\text{OH}$  at  $650 \text{ }^\circ\text{C}$  for 30 min, the 1-D nanostructures in S-2 sensors are recovered in  $\text{N}_2$  for 20 min. The sensors were then observed under FESEM and characterized by Raman spectroscopy as presented in the following sections.

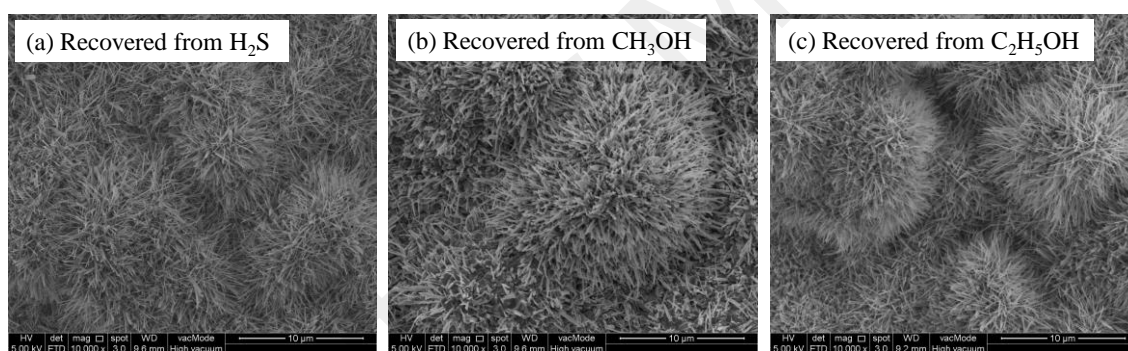


**Figure 4.76: FESEM images of 1-D nanostructures in S-2 sensors after recovery from the exposure of (a)  $\text{H}_2\text{S}$ , (b)  $\text{CH}_3\text{OH}$  and (c)  $\text{C}_2\text{H}_5\text{OH}$ .**

Figure 4.76 shows the FESEM images of the S-2 sensors after exposing to 1000 ppm  $\text{H}_2\text{S}$ ,  $\text{CH}_3\text{OH}$  and  $\text{C}_2\text{H}_5\text{OH}$  followed by recovery in  $\text{N}_2$  at  $650 \text{ }^\circ\text{C}$  for 20 min. It is seen that the 1-D nanostructures are fully recovered from the exposure of  $\text{H}_2\text{S}$ ,  $\text{CH}_3\text{OH}$  and  $\text{C}_2\text{H}_5\text{OH}$ . High coverage of 1-D nanostructures are seen after the recovery from  $\text{H}_2\text{S}$ ,  $\text{CH}_3\text{OH}$  and  $\text{C}_2\text{H}_5\text{OH}$ .

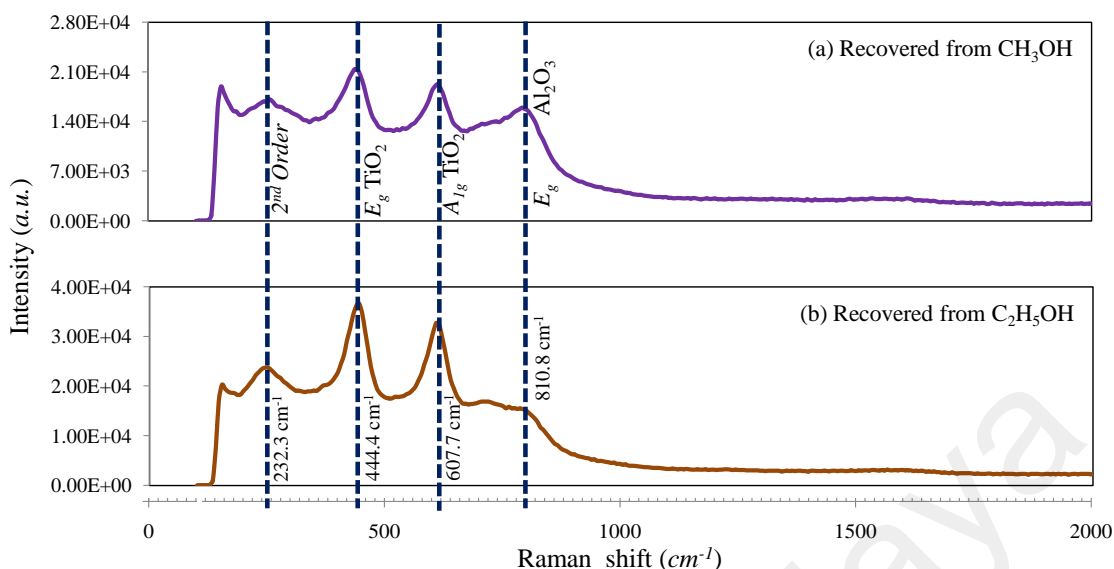


**Figure 4.77: Raman spectroscopy analysis of S-2 sensor after recovery in  $N_2$  for 20 min at  $650\text{ }^\circ\text{C}$  from (a)  $CH_3OH$  and (b)  $C_2H_5OH$ .**

Figure 4.77 shows the peaks of Raman spectra of S-2 sensors after recovery from  $CH_3OH$  and  $C_2H_5OH$ . Four characteristic peaks are observed at 232.3, 444.4, 607.7 and  $810.8\text{ cm}^{-1}$  in the recovered sensors which are identical to the as-prepared S-2 sensor shown in Figure 4.75(a). No peak is observed at  $1334.4$  and  $1586.6\text{ cm}^{-1}$  regions corresponding to the *D* (diamond) and *G* (graphite) bands of amorphous carbon, respectively. It should be noted that during the exposure of  $CH_3OH$  and  $C_2H_5OH$ , the *D* and *G* bands of amorphous carbon were observed as shown in Figure 4.75(c-d). So, the deposited amorphous carbon on 1-D nanostructures is fully removed during recovery as  $CO_2$  by reacting with  $O_2$  present in  $N_2$  background.

#### 4.3.6 Stability and Reproducibility of Sensors

The 1-D nanostructures are fully recovered after recovery from  $H_2S$ ,  $CH_3OH$  and  $C_2H_5OH$  gases as shown in Figure 4.76. So, it is concluded that the 1-D nanostructures did not react with the target gases at the operating temperatures and the interactions of the target gases with the 1-D nanostructures are reversible.

**Table 4.8: Response of the as-prepared and stored S-2 sensors towards 1000 ppm of H<sub>2</sub>S, CH<sub>3</sub>OH and C<sub>2</sub>H<sub>5</sub>OH gases in N<sub>2</sub> background at 650 °C.**

Target gas	Response of as-prepared sensors	Stored sensors			
		Re-exposed immediately	Re-exposed after 1 day	Re-exposed after 1 month	Re-exposed after 6 months
H <sub>2</sub> S	38.7	36.6	44.02	43.9	33.2
CH <sub>3</sub> OH	349.6	360.6	377.4	301.5	370.6
C <sub>2</sub> H <sub>5</sub> OH	1109	987.1	1264.9	1004.4	1346.4

The S-2 sensors were re-examined towards 1000 ppm H<sub>2</sub>S, CH<sub>3</sub>OH and C<sub>2</sub>H<sub>5</sub>OH gases immediately after sensing and the results were reproduced with  $\pm 15\%$  deviations as shown in Table 4.8. The sensors were stored in the laboratory and re-examined towards 1000 ppm H<sub>2</sub>S, CH<sub>3</sub>OH and C<sub>2</sub>H<sub>5</sub>OH gases after one day, one month and six months. The response results of the sensors were reproduced with a variation of  $\pm 15\%$  as shown in Table 4.8.

#### 4.3.7 Mechanism of Gas Sensing

The 1-D nanostructures grown at 750 °C on Ti64-20 particles possessing core-shell TiO<sub>2</sub>-Al<sub>2</sub>O<sub>3</sub> nanostructures showed highest sensitivity compared with other sensors. The sensors showed selective sensitivity towards H<sub>2</sub>S, CH<sub>3</sub>OH and C<sub>2</sub>H<sub>5</sub>OH. The presence of Al<sub>2</sub>O<sub>3</sub> layer on semiconducting TiO<sub>2</sub> has significant effect on the sensing performance. In the following sections the role of Al<sub>2</sub>O<sub>3</sub> layer on TiO<sub>2</sub>, and semiconducting behavior of TiO<sub>2</sub> are discussed. Based on the discussion a model is proposed for the mechanism of gas sensing. The performance determining factors for gas sensing is highlighted and the results are compared with the reported results in the following sections.

##### 4.3.7.1 Role of Al<sub>2</sub>O<sub>3</sub> on Sensing Structure

To understand the role of Al<sub>2</sub>O<sub>3</sub> shell layer on the core of TiO<sub>2</sub> in 1-D nanostructures, sensors were prepared using only Al<sub>2</sub>O<sub>3</sub> nanoparticles (Sigma Aldrich, 50 nm). For this,

5 wt% of Al<sub>2</sub>O<sub>3</sub> nanoparticles were dispersed in the ink in a similar process mentioned in section 3.2.5 and 3 μL of the composite ink was deposited on the Au interdigitated substrate using micropipette. Then the Au interdigitated substrate along with Al<sub>2</sub>O<sub>3</sub> nanoparticles was heat treated at 750 °C for 4 h in an Ar environment. The sensitivity of the as-prepared Al<sub>2</sub>O<sub>3</sub>-sensor was measured towards 1000 ppm of H<sub>2</sub>, H<sub>2</sub>S, CO, CH<sub>4</sub>, CH<sub>3</sub>OH, C<sub>2</sub>H<sub>5</sub>OH, C<sub>2</sub>H<sub>4</sub>, NO<sub>2</sub> and O<sub>2</sub> at 650 °C in similar process mentioned for S-2 sensors. The resistance of the Al<sub>2</sub>O<sub>3</sub>-sensor was found to be overloaded in N<sub>2</sub> and synthetic air (order of 10<sup>9</sup> Ω) and no noticeable change in resistance was seen during the exposure of target gases. So, Al<sub>2</sub>O<sub>3</sub> layer on TiO<sub>2</sub> is not susceptible to any gases during sensing. In addition, relevant literature survey showed that corundum-Al<sub>2</sub>O<sub>3</sub> possesses high band gap of ~8.8 eV (French, 1990). So, it is clear that Al<sub>2</sub>O<sub>3</sub> layer in the shell of 1-D nanostructure act as an insulation layer on TiO<sub>2</sub>. The change in resistance during gas sensing is attributed to semiconducting rutile-TiO<sub>2</sub> which has a band gap of 3.3±0.5 eV (Tezuka et al., 1994).

#### 4.3.7.2 Semiconducting Behavior of Rutile TiO<sub>2</sub>

Rutile phase of TiO<sub>2</sub> possesses *p*-type semiconducting behavior where the sensor resistance is increased in reducing environment (HY Lee & Akbar, 2008) and decreased in oxidizing environment (Saruhan et al., 2013). On the other hand, anatase phase of TiO<sub>2</sub> possess *n*-type semiconducting behavior where the resistance of the sensor is decreased during exposure to reducing gases (Paulose et al., 2005) and increased in oxidizing gases (Landau et al., 2008). In this present case, the S-1, S-2 and S-3 sensors possess 1-D nanostructures consisting rutile phase of TiO<sub>2</sub>. In the XRD analysis, no peak of the anatase phase of TiO<sub>2</sub> is observed in the oxidized Ti and Ti64 particles (Figure 4.13 and 4.42). So, the sensors in these present investigations should exhibit *p*-type sensing behavior. However, from response curve shown in Figure 4.69(b-c) depicts that the

resistance of the S-2 and S-3 sensors decreased in reducing environment and increased in oxidizing environment which is typical for *n*-type sensing behavior.

Knauth and Tuller (Knauth & Tuller, 1999) and Li *et al.* (Xiangoan Li, Ramasamy, & Dutta, 2009) reported that oxygen partial pressure has a significant role on the semiconducting behavior of rutile TiO<sub>2</sub>. Under high partial pressure of oxygen (2-21%), rutile exhibit *p*-type semiconducting behavior at temperatures below 1000 °C due to hole conductivity. In the present experiments, N<sub>2</sub> was used as a background gas for all gases except for testing NO<sub>2</sub>. The N<sub>2</sub> cylinder contained trace amount of O<sub>2</sub> (5-10 ppm) as impurity. So, the partial pressure of oxygen is substantially low on the sensors during sensing experiments. For this reason, all sensors (S-1, S-2 and S-3) showed *n*-type sensing behavior when N<sub>2</sub> was used as background gas. However, a different scenario is observed during testing NO<sub>2</sub>. Synthetic air containing 21% of O<sub>2</sub> was also used as a background gas during NO<sub>2</sub> detection. In this case the resistance of the S-1 sensor is decreased in the presence of NO<sub>2</sub> which is typical *p*-type sensing behavior. On the other hand, the resistance of S-2 and S-3 sensors was increased during the exposure of oxidizing NO<sub>2</sub> in synthetic air which is typical for *n*-type sensors. So, in the present case, the *n*-type behavior of S-2 and S-3 sensors is not dependent on the oxygen partial pressure but the inherent properties of the sensors. It should be noted that S-2 and S-3 sensor possessed an insulating Al<sub>2</sub>O<sub>3</sub> layer on semiconducting TiO<sub>2</sub> which is absent in S-1 sensor. So, the presence of Al<sub>2</sub>O<sub>3</sub> layer on TiO<sub>2</sub> has significant effects on the *n*-type behavior of S-2 and S-3 sensors.

It was reported that strong oxygen adsorption on surface sites of rutile leads to the formation of an inverted layer which is responsible for *p*-type conductivity (Xiangoan Li *et al.*, 2009). In the case of S-2 and S-3 sensors, the interaction between surface adsorbed oxygen and TiO<sub>2</sub> is weak due to the presence of the insulating Al<sub>2</sub>O<sub>3</sub> layer on TiO<sub>2</sub>. As a

result, no inverted layer is created resulting in *n*-type semiconducting behavior of the S-2 and S-3 sensors.

#### 4.3.7.3 Proposed Mechanism of Gas Sensing

The gas sensing mechanism of single metal oxide is explained by surface depletion model (Akbar & Younkman, 1997). According to this model, an electron depleted layer is created on the surface of *n*-type metal oxides due to oxygen adsorption in the form of  $O^-$ ,  $O_2^-$  or even  $O^{2-}$  ion and as a result the resistance of the metal oxide is increased. In presence of reducing gases, the resistance of the *n*-type metal oxides is decreased due to electron donation by the reducing gases. On the other hand, in presence of oxidizing gases the resistance of *n*-type metal oxides is increased. An opposite phenomenon is observed for *p*-type metal oxides towards reducing and oxidizing gases. However, to explain the gas sensing mechanism of 1-D and 3-D core-shell nanostructures, modified surface depletion models are proposed and reviewed by different researchers (Miller et al., 2014; S. Sen et al., 2010; Y. Wang et al., 2015). The schematic of band bending of core-shell heterostructures is presented in Figure 2.13. It was proposed that the presence of *n-n* junction in 1-D core-shell nanostructures transfers electrons to the lower energy conduction band to form an “electron accumulation” layer (Figure 2.13(a-b)) (Miller et al., 2014; Zeng et al., 2010). The electron accumulation layer is depleted by subsequent oxygen adsorptions. As a result, the resistance of the 1-D nanostructure is increased and better performance is seen towards electron donating reducing gases. On the other hand, for the case of *p-p* junction, electrons are transferred to lower energy Fermi levels and “hole depletion” and “hole accumulation” layers are formed at the interface (Figure 2.13(c-d)) (Y. Wang et al., 2015). Adsorption of oxygen at the surface transfers holes to the “hole depleted” layer and thus the resistance of *p-p* interface is decreased. In presence of reducing gases the resistance of the *p-p* interface is increased due to electron-hole

recombination process. Similarly,  $p$ - $n$  junction increases the resistance of the 1-D nanostructures by electron-hole recombination process and depletion layer is created at the interface (Figure 2.13(e-f)). Presence of reducing gas reduces the resistance of the  $p$ - $n$  interface by donating electrons (Miller et al., 2014).

In the present case, no  $n$ - $n$ ,  $p$ - $p$  or  $n$ - $p$  junctions are created at the interface of 1-D core-shell  $\text{TiO}_2$ - $\text{Al}_2\text{O}_3$  nanostructures. None of the literature proposed a mechanism of gas sensing for an insulating layer on semiconducting oxide. It is seen that during exposure to  $\text{H}_2\text{S}$ , the S-2 sensors shows higher content of metallic Ti and lower content of oxygen as presented in Table 4.7. It shows that the 1-D nanostructures are partially reduced in presence of  $\text{H}_2\text{S}$ . On the other hand, in presence of  $\text{CH}_3\text{OH}$  and  $\text{C}_2\text{H}_5\text{OH}$ , an amorphous carbon layer is deposited on 1-D nanostructures. So, two different mechanisms are responsible for sensing  $\text{H}_2\text{S}$  and alcohols ( $\text{CH}_3\text{OH}$  and  $\text{C}_2\text{H}_5\text{OH}$ ) as presented below.

(a) ***Interaction with  $\text{H}_2\text{S}$***

During sensing of  $\text{H}_2\text{S}$ , the 1-D core-shell  $\text{TiO}_2$ - $\text{Al}_2\text{O}_3$  nanostructures were partially reduced as seen in Table 4.7. Previously it was reported that insulating layer of  $\text{Al}_2\text{O}_3$  on conducting substrates such as Ni (Weimer et al., 2008) and NiAl (Iwasaki & Sudoh, 2002) is capable of possessing electron tunneling properties. It was reported that varistors having  $\text{Al}_2\text{O}_3$  tunnel junction thicknesses of 44 nm on Ni particles switches from insulating to conducting state and this behavior was explained by Fowler-Nordheim mechanism (Weimer et al., 2008). In the present case, the thickness of  $\text{Al}_2\text{O}_3$  layer on 1-D  $\text{TiO}_2$  is 8-15 nm. So, it is reasonable to assume that similar electron tunneling phenomenon is applicable for the insulating  $\text{Al}_2\text{O}_3$  layer on  $\text{TiO}_2$ . So, the gas sensing mechanism of 1-D core-shell  $\text{TiO}_2$ - $\text{Al}_2\text{O}_3$  is explained by the electron tunneling assisted surface depletion model.

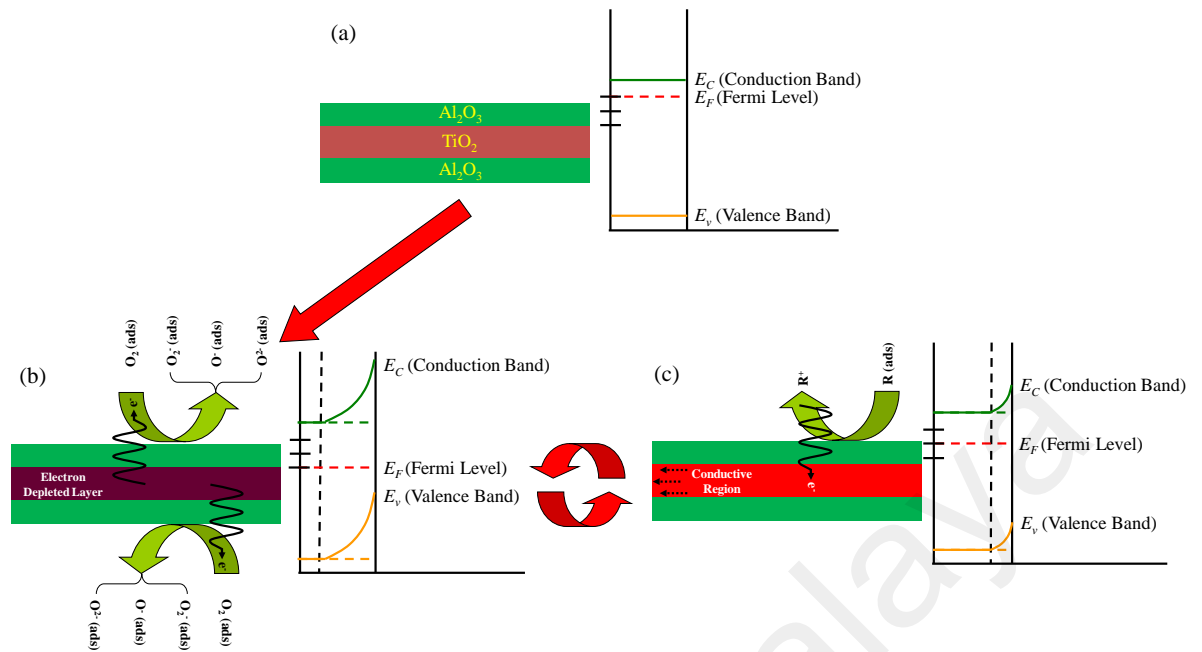
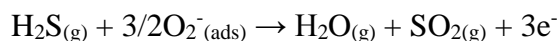


**Figure 4.78: Proposed electron tunneling assisted surface depletion model for sensing reducing gas using 1-D core-shell  $\text{TiO}_2\text{-Al}_2\text{O}_3$  nanostructure: (a) before adsorption of oxygen; (b) during adsorption of oxygen and (c) in reducing environment where  $R$  represents reducing gas.**

The intrinsic property of  $n$ -type 1-D  $\text{TiO}_2$  is shown in Figure 4.78(a) possessing of valence band ( $E_V$ ), conduction band ( $E_C$ ) and Fermi level ( $E_F$ ) in between. The 1-D rutile- $\text{TiO}_2$  is surrounded by shell layer of  $\text{Al}_2\text{O}_3$ . In the ambient environment, oxygen is adsorbed on the surface of the shell layer in the form of  $\text{O}^-$ ,  $\text{O}_2^-$  or  $\text{O}^{2-}$  and electrons are captured from the conduction band ( $E_C$ ) of  $\text{TiO}_2$  through electron tunneling as shown in Figure 4.78(b). Due to capturing of electron from the conduction band ( $E_C$ ) of  $\text{TiO}_2$  an electron depleted layer is created (Figure 4.78(b)). As a result, the resistance of the sensor is increased. In reducing environment, electrons are donated by the target gas and the resistance of the 1-D core-shell  $\text{TiO}_2\text{-Al}_2\text{O}_3$  is decreased as shown in Figure 4.78(c). The electrons are capable to move to the adjacent 1-D nanostructures by electron tunneling through  $\text{Al}_2\text{O}_3$  shell layer and the resistance of the sensor is decreased in reducing environment as seen in Figure 4.78(a-b). In oxidizing environment ( $\text{NO}_2$  and  $\text{O}_2$ ) opposite phenomenon is observed and as a result the resistance of the sensors is increased (Figure 4.78(b-c)).

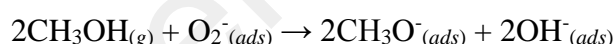
Relevant literature survey on the catalytic action of TiO<sub>2</sub> shows that H<sub>2</sub>S strongly interacts and adsorbs on the surface of TiO<sub>2</sub> at temperatures above 300 °C to form H<sub>2</sub>O and SO<sub>2</sub> by the following reactions (Y. Wang et al., 2015; Yanxin et al., 1999):



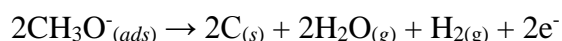
Due to this catalytic reactions oxygen vacancy is created on TiO<sub>2</sub> which is responsible for decreased resistance in the sensors (Beck & Siegel, 1992; Yanxin et al., 1999). It is also reported that, rutile phase of TiO<sub>2</sub> interacts strongly with H<sub>2</sub>S compared with anatase (Beck & Siegel, 1992).

(b) ***Interaction with CH<sub>3</sub>OH and C<sub>2</sub>H<sub>5</sub>OH***

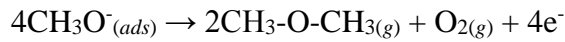
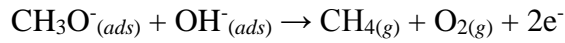
The as-prepared S-2 sensors are composed of 1-D core-shell TiO<sub>2</sub>-Al<sub>2</sub>O<sub>3</sub> nanostructures as presented in the schematics of Figure 4.79(a). Due to possessing insulating layer of Al<sub>2</sub>O<sub>3</sub> on semiconducting TiO<sub>2</sub> the S-2 sensors showed high resistance (1x10<sup>4</sup>-2x10<sup>4</sup> Ω) at the operating temperatures of 650 °C. During sensing, CH<sub>3</sub>OH is dissociated to methoxides and adsorbs on the surface of TiO<sub>2</sub> by catalytic reactions as follows (K. Kim & Barteau, 1989):



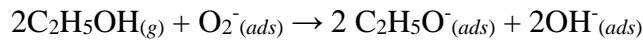
The adsorbed methoxide dissociates to amorphous carbon and deposit on the 1-D nanostructures during exposure to CH<sub>3</sub>OH by the following reaction (K. Kim & Barteau, 1989):



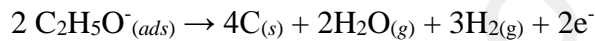
The remaining adsorbed methoxide reacts with the hydroxyl groups to form methane (CH<sub>4</sub>) and dissociates to dimethyl ether (CH<sub>3</sub>-O-CH<sub>3</sub>), formaldehyde (HCHO) and carbon monoxide (CO) under different conditions at high temperatures by the following reactions (K. Kim & Barteau, 1989):



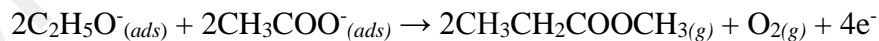
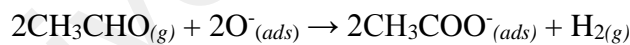
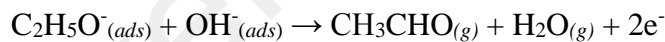
Similarly, adsorption of  $\text{C}_2\text{H}_5\text{OH}$  on the surface of  $\text{TiO}_2$  is largely dissociative and yields ethoxide as follows (Idriss & Seebauer, 2000):



The adsorbed ethoxide dissociates to amorphous carbon and deposit on the 1-D nanostructures during the exposure to  $\text{C}_2\text{H}_5\text{OH}$  by the following reaction (Idriss & Seebauer, 2000; K. Kim & Barteau, 1989):



The remaining adsorbed ethoxide desorbs as acetaldehyde ( $\text{CH}_3\text{CHO}$ ) with other minor products such as acetone ( $\text{CH}_3\text{-C(O)-CH}_3$ ) and ethyl acetate ( $\text{CH}_3\text{CH}_2\text{COOCH}_3$ ) by the following reactions (Idriss & Seebauer, 2000):



It is seen from the above reactions that electrons are donated to the 1-D nanostructures during the exposure of  $\text{CH}_3\text{OH}$  and  $\text{C}_2\text{H}_5\text{OH}$ . However, a drastic drop in resistance (from the order of  $\sim 10^4 \Omega$  to  $\sim 10\Omega$ ) is observed in S-2 sensors during the exposure of  $\text{CH}_3\text{OH}$  and  $\text{C}_2\text{H}_5\text{OH}$  which cannot be obtained only by electron donations. It is seen from the above reactions that amorphous carbon is created as a byproduct and assumed to be

deposited as a continuous layer on the surface of 1-D nanostructures as shown in the schematic of Figure 4.79(b). It is reported that the resistance of amorphous carbon at high temperatures is quite low (Mominuzzaman, Krishna, Soga, Jimbo, & Umeno, 1999) and as a result the resistance of the sensor is decreased at the gas sensing temperatures during the exposure of  $\text{CH}_3\text{OH}$  and  $\text{C}_2\text{H}_5\text{OH}$ . During the recovery process the amorphous carbon is converted to  $\text{CO}_2$  by reacting with oxygen in  $\text{N}_2$  background and as a result the resistance of the sensor is increased again.

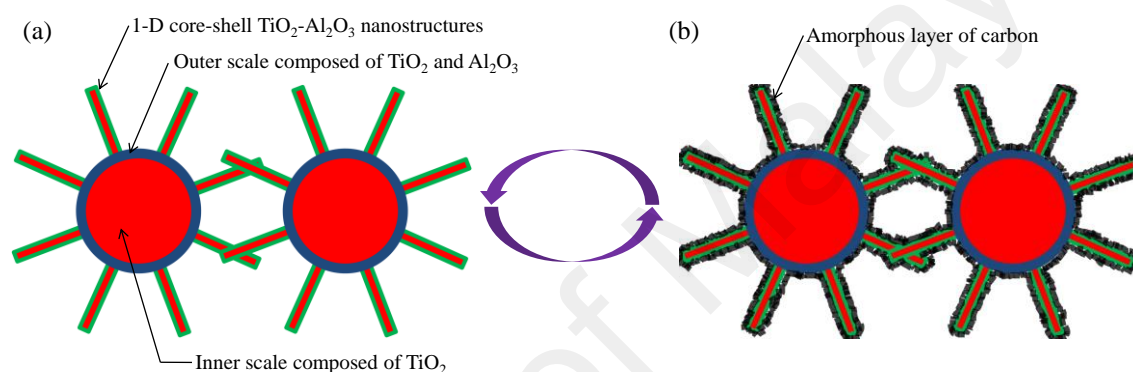


**Figure 4.79: Schematics of  $\text{CH}_3\text{OH}$  and  $\text{C}_2\text{H}_5\text{OH}$  sensing using 1-D core-shell  $\text{TiO}_2\text{-Al}_2\text{O}_3$  nanostructures: (a) sensor in ambient environment and (b) sensors in  $\text{CH}_3\text{OH}$  and  $\text{C}_2\text{H}_5\text{OH}$  gas containing environment.**

#### 4.3.7.4 Performance Determining Factors for Sensing

Two types of sensing mechanisms are proposed during testing of different gases. The electron tunneling assisted surface depletion model is capable of explaining the general behavior of the 1-D core-shell  $\text{TiO}_2\text{-Al}_2\text{O}_3$  nanostructures towards different gases. It is seen that the sensors (S-1, S-2 and S-3) exhibited negligible change in resistance during the exposure of  $\text{H}_2$ ,  $\text{CO}$ ,  $\text{CH}_4$ ,  $\text{C}_2\text{H}_4$ ,  $\text{NO}_2$  and  $\text{O}_2$ . However, the change in resistance is consistent with the electron tunneling assisted surface depletion model; i.e., the resistance of the sensors is decreased in reducing environment and increased in oxidizing environment. Significant drop in the resistance was seen only for  $\text{H}_2\text{S}$ ,  $\text{CH}_3\text{OH}$  and  $\text{C}_2\text{H}_5\text{OH}$  gases. However, the decrease of resistance in presence of  $\text{CH}_3\text{OH}$  and  $\text{C}_2\text{H}_5\text{OH}$  is too high and cannot be explained only by electron tunneling assisted surface depletion

model. It was seen from the Raman spectra (Figure 4.75) that during sensing of CH<sub>3</sub>OH and C<sub>2</sub>H<sub>5</sub>OH, amorphous layer of C is deposited on the 1-D nanostructures which is responsible for drastic drop in resistance of the sensors.

Beside the sensing mechanisms, there are some other factors which also influence the performance of the sensors. The performance towards specific gas depends on the combination of two factors (Miller et al., 2014):

1. *Structure*: decreased grain size or increased surface area improves the performance of the sensor.
2. *Surface*: catalytic reactions of the surface improve the performance towards specific gases.

The effect of the *structure* is prominent in the present case as it is seen that with increasing the density of 1-D nanostructures resulted in higher sensitivity (Table 4.4). The sensor S-2 possessed about three fold higher responses compared with S-1 and S-3 sensors due to having higher number of 1-D nanostructure (Figure 4.64 and Table 4.4). However, the most significant factor for sensing H<sub>2</sub>S, CH<sub>3</sub>OH and C<sub>2</sub>H<sub>5</sub>OH is attributed to *surface* effect by the catalytic activity of TiO<sub>2</sub> towards H<sub>2</sub>S, CH<sub>3</sub>OH and C<sub>2</sub>H<sub>5</sub>OH as shown by the chemical reactions in section 4.3.6.3.

#### 4.3.7.5 Comparison of Gas Sensing

Table 4.9 summarizes the results on response towards different target gases obtained in the present work and compared with the published result shown in Table 2.4. It is seen in the published literature that the response values of different TiO<sub>2</sub> based sensors are highly scattered and hard to make any direct comparison with the present work (Table 2.4).

In the literature, the response towards  $H_2$  is reported as high as  $10^3$  (O. K. Varghese et al., 2003) and  $10^9$  (Paulose et al., 2005) using  $TiO_2$  nanotubes prepared by anodization method (Table 2.4). On the other hand, in the present case, the maximum response towards  $H_2$  was 1.6 (Table 4.9). Similarly, the response towards CO reported in the literature is as high as 12.6 (Mohammadi, 2014), 21 (B. Wang et al., 2010) and  $\sim 100$  (Birkefeld et al., 1992) where the sensors were fabricated by sol-gel, electrospinning and cold pressing process, respectively. It was seen that doping of Cu in  $TiO_2$  (B. Wang et al., 2010) or usage of binary mixture of  $TiO_2-Al_2O_3$  (Birkefeld et al., 1992; Mohammadi, 2014) is beneficial towards CO sensing. However, in the present case, the sensors are insensitive towards CO and the highest response towards CO is only 1.7 as seen in Table 4.9.

The reported highest sensitivity towards  $C_2H_5OH$  is  $2.5 \times 10^5$  obtained by using commercial  $TiO_2$  nanoparticles (Arafat et al., 2014) as presented in Table 2.4. It was seen that the initial resistance ( $R_o$ ) of the sensor using  $TiO_2$  nanoparticles is significantly high (order of  $10^7 \Omega$ ) which drops to  $\sim 10^2 \Omega$  during the exposure of  $C_2H_5OH$ . In another case, the response towards  $C_2H_5OH$  is seen to be 13801 using  $TiO_2$  nanotubes prepared by anodization process (Kwon et al., 2012). In the present case, the highest response towards  $C_2H_5OH$  is 1109 as seen in Table 4.9. However, response as low as 41.4 was also obtained towards  $C_2H_5OH$  as reported in the literature (Phanichphant et al., 2011).

Comparing Table 2.4 and 4.9, sensors with better responses compared with the present work is reported in the literature. A common trend is observed in Table 2.4 that sensors prepared by anodization process normally possess higher response compared with others (Kwon et al., 2012; O. K. Varghese et al., 2003). The higher response of the anodized sensors might be attributed to their defect states which make the sensors more prone towards the catalytic reactions with the target gases. On the other hand, the sensors

prepared by thermal oxidation in the present case is highly crystalline and therefore possess less defects which might reduce the response towards different gases. It is also seen in Table 2.4 that commercial TiO<sub>2</sub> nanoparticles and cold pressed samples possess good response. It should be noted that the initial resistance of these sensors is very high which dropped in presence of target gases resulted in better response.

University of Malaya

**Table 4.9: Response towards different gases obtained in the present work.**

Gas tested	Sensor Identification	Morphology	Fabrication route	Sensitivity		Response time	Recovery time	
				Response	Concentration			Temperature
H <sub>2</sub>	S-1	1-D TiO <sub>2</sub> on Ti particles	Thermal oxidation	1.3	1000 ppm	650 °C	2 min	4 min
	S-2	Fine 1-D core-shell TiO <sub>2</sub> -Al <sub>2</sub> O <sub>3</sub> on Ti64 particles		1.6			3 min	3 min
	S-3	Thick and fine 1-D core-shell TiO <sub>2</sub> -Al <sub>2</sub> O <sub>3</sub> on Ti64 particles		1.5			4 min	4 min
H <sub>2</sub> S	S-1	1-D TiO <sub>2</sub> on Ti particles	Thermal oxidation	3.8	1000 ppm	650 °C	8 min	10 min
	S-2	Fine 1-D core-shell TiO <sub>2</sub> -Al <sub>2</sub> O <sub>3</sub> on Ti64 particles		38.7			6.5 min	8 min
	S-3	Thick and fine 1-D core-shell TiO <sub>2</sub> -Al <sub>2</sub> O <sub>3</sub> on Ti64 particles		10.9			8 min	7 min
CO	S-1	1-D TiO <sub>2</sub> on Ti particles	Thermal oxidation	1.7	1000 ppm	650 °C	2 min	4 min
	S-2	Fine 1-D core-shell TiO <sub>2</sub> -Al <sub>2</sub> O <sub>3</sub> on Ti64 particles		1.7			3 min	3 min
	S-3	Thick and fine 1-D core-shell TiO <sub>2</sub> -Al <sub>2</sub> O <sub>3</sub> on Ti64 particles		1.4			3 min	4 min
CH <sub>4</sub>	S-1	1-D TiO <sub>2</sub> on Ti particles	Thermal oxidation	1.1	1000 ppm	650 °C	2 min	4 min
	S-2	Fine 1-D core-shell TiO <sub>2</sub> -Al <sub>2</sub> O <sub>3</sub> on Ti64 particles		1.3			3 min	3 min
	S-3	Thick and fine 1-D core-shell TiO <sub>2</sub> -Al <sub>2</sub> O <sub>3</sub> on Ti64 particles		1.1			3 min	4 min
CH <sub>3</sub> OH	S-1	1-D TiO <sub>2</sub> on Ti particles	Thermal oxidation	148	1000 ppm	650 °C	7 min	18 min
	S-2	Fine 1-D core-shell TiO <sub>2</sub> -Al <sub>2</sub> O <sub>3</sub> on Ti64 particles		349.6			5.2 min	18 min
	S-3	Thick and fine 1-D core-shell TiO <sub>2</sub> -Al <sub>2</sub> O <sub>3</sub> on Ti64 particles		116.3			7 min	20 min

**Table 4.9, Continued.**

Gas tested	Sensor Identification	Morphology	Fabrication route	Sensitivity		Response time	Recovery time	
				Response	Concentration			
C <sub>2</sub> H <sub>5</sub> OH	S-1	1-D TiO <sub>2</sub> on Ti particles	Thermal oxidation	241.4	1000 ppm	650 °C	6.5 min	18 min
	S-2	Fine 1-D core-shell TiO <sub>2</sub> -Al <sub>2</sub> O <sub>3</sub> on Ti64 particles		1109			3.5 min	20 min
	S-3	Thick and fine 1-D core-shell TiO <sub>2</sub> -Al <sub>2</sub> O <sub>3</sub> on Ti64 particles		349.1			7 min	20 min
C <sub>2</sub> H <sub>4</sub>	S-1	1-D TiO <sub>2</sub> on Ti particles	Thermal oxidation	1.2	1000 ppm	650 °C	2 min	3 min
	S-2	Fine 1-D core-shell TiO <sub>2</sub> -Al <sub>2</sub> O <sub>3</sub> on Ti64 particles		1.3			6 min	3 min
	S-3	Thick and fine 1-D core-shell TiO <sub>2</sub> -Al <sub>2</sub> O <sub>3</sub> on Ti64 particles		1.2			2 min	3 min
NO <sub>2</sub>	S-1	1-D TiO <sub>2</sub> on Ti particles	Thermal oxidation	1.2	1000 ppm	650 °C	2 min	3 min
	S-2	Fine 1-D core-shell TiO <sub>2</sub> -Al <sub>2</sub> O <sub>3</sub> on Ti64 particles		1.9			3 min	3 min
	S-3	Thick and fine 1-D core-shell TiO <sub>2</sub> -Al <sub>2</sub> O <sub>3</sub> on Ti64 particles		1.7			2 min	3 min
O <sub>2</sub>	S-1	1-D TiO <sub>2</sub> on Ti particles	Thermal oxidation	1.2	1000 ppm	650 °C	4 min	3 min
	S-2	Fine 1-D core-shell TiO <sub>2</sub> -Al <sub>2</sub> O <sub>3</sub> on Ti64 particles		1.5			3 min	3 min
	S-3	Thick and fine 1-D core-shell TiO <sub>2</sub> -Al <sub>2</sub> O <sub>3</sub> on Ti64 particles		1.3			2 min	4 min

#### 4.3.8 Summary of Gas Sensing

The sensors are prepared on the substrate by an in-situ thermal oxidation process. Three types of nanostructures are produced and investigated towards gas sensing applications. The sensors possessing of fine 1-D core-shell TiO<sub>2</sub>-Al<sub>2</sub>O<sub>3</sub> nanostructures on Ti64 particles show the highest response compared with sensors possessing thick nanostructures on Ti64 particles and 1-D TiO<sub>2</sub> nanostructures on Ti particles. The optimum sensing temperature is found to be 650 °C. Selective sensing is observed only for H<sub>2</sub>S, CH<sub>3</sub>OH and C<sub>2</sub>H<sub>5</sub>OH gases though in all cases highest response is seen towards C<sub>2</sub>H<sub>5</sub>OH. The response towards 1000 ppm H<sub>2</sub>S, CH<sub>3</sub>OH and C<sub>2</sub>H<sub>5</sub>OH at 650 °C is found to be 38.7, 349.6 and 1109, respectively.

The 1-D core-shell TiO<sub>2</sub>-Al<sub>2</sub>O<sub>3</sub> sensors show *n*-type sensing behavior. A modified electron tunneling assisted surface depletion model is proposed to explain the interactions with core-shell TiO<sub>2</sub>-Al<sub>2</sub>O<sub>3</sub> nanostructures and target gases. It is proposed that due to enhanced catalytic activity towards H<sub>2</sub>S, CH<sub>3</sub>OH and C<sub>2</sub>H<sub>5</sub>OH resulted in selective responses of the sensors. During CH<sub>3</sub>OH and C<sub>2</sub>H<sub>5</sub>OH sensing an amorphous layer of carbon is deposited on the 1-D core-shell TiO<sub>2</sub>-Al<sub>2</sub>O<sub>3</sub> nanostructures and as a result the resistance of the sensor is dropped significantly.

#### 4.4 Summary of Thesis

This thesis contains three major parts: (1) growth of 1-D nanostructures on Ti particle, (2) growth of 1-D nanostructures on Ti64 substrates and (3) gas sensing using 1-D nanostructures. In the first part the 1-D TiO<sub>2</sub> nanostructures are successfully grown on Ti particles by thermal oxidation process. The growth of 1-D nanostructures on Ti substrate requires heating at 750 °C in presence of minute amount of oxygen (5 ppm) in humid Ar flow. High concentration of oxygen resulted in the formation of oxide scale instead of 1-D nanostructure. It is seen that residual stress significantly enhances the coverage of 1-D

nanostructures on Ti substrates. The resulted 1-D nanostructures are approximately 5-10  $\mu\text{m}$  long possessing of rutile phase with different shapes.

The growth of 1-D nanostructures on Ti64 substrates also requires heating at 700-800  $^{\circ}\text{C}$  in the presence of minute amount of oxygen ( $<100$  ppm) in dry Ar flow. With increasing the oxidation temperatures, the resultant nanostructures become thicker. Similar to Ti substrates, residual stress in the substrate significantly enhances the coverage of 1-D nanostructures. The resultant 1-D nanostructures possessed rutile- $\text{TiO}_2$  in the core and corundum- $\text{Al}_2\text{O}_3$  in the shell.

The 1-D nanostructures obtained by thermal oxidation are used for gas sensing. It is seen that the fine 1-D core-shell  $\text{TiO}_2$ - $\text{Al}_2\text{O}_3$  nanostructures on Ti64 particles show highest sensitivity towards all gases. However, selective sensitivity is observed only for  $\text{H}_2\text{S}$ ,  $\text{CH}_3\text{OH}$  and  $\text{C}_2\text{H}_5\text{OH}$ . The enhanced catalytic activity of  $\text{H}_2\text{S}$ ,  $\text{CH}_3\text{OH}$  and  $\text{C}_2\text{H}_5\text{OH}$  with  $\text{TiO}_2$  resulted in selective response. Deposition of amorphous layer of carbon on the sensing nanostructures during the exposure of  $\text{CH}_3\text{OH}$  and  $\text{C}_2\text{H}_5\text{OH}$  significantly reduces the resistance of the sensors and as a result higher response is observed.

## CHAPTER 5: CONCLUSIONS AND RECOMMENDATIONS

### 5.1 Conclusions

In this work, one dimensional (1-D)  $\text{TiO}_2$  and core-shell  $\text{TiO}_2\text{-Al}_2\text{O}_3$  nanostructures were grown on Ti and Ti-6Al-4V (Ti64) substrates, respectively by thermal oxidation. The thermal oxidation process is optimized for the growth of 1-D nanostructures on Ti and Ti64 substrates. The as-grown 1-D nanostructures on Ti and Ti64 substrates are utilized for gas sensing applications. The conclusions from this work is listed in the following sections.

#### 5.1.1 Growth of Nanostructures on Ti Particles

- The optimum temperature for the growth of 1-D nanostructures on Ti particles is 750 °C in the presence of minute amount of  $\text{O}_2$  in humid Ar environments. Theoretical calculations show that the dynamic oxygen partial pressure should be between  $1 \times 10^{-11}$ - $3 \times 10^{-10}$  Pa for the 1-D growth on Ti particles. Oxide scale is seen instead of 1-D nanostructures at higher concentration of  $\text{O}_2$ .
- The residual stress has significant effect to enhance the coverage of 1-D nanostructures on Ti particles.
- The 1-D nanostructures formed on Ti particles is composed of rutile  $\text{TiO}_2$ . Oxide scale composed of  $\text{TiO}_2$ ,  $\text{Ti}_3\text{O}_5$ ,  $\text{Ti}_2\text{O}_3$  and  $\text{TiO}$  are formed beneath the 1-D nanostructures during oxidation.

#### 5.1.2 Growth of Nanostructures on Ti64 Substrates

- The optimum temperature for 1-D growth on Ti64 substrates is 750 °C in the presence of minute amount of  $\text{O}_2$  in dry Ar environment. Theoretical calculations

show that the dynamic oxygen partial pressure required for 1-D growth on Ti64 substrate is between  $1 \times 10^{-11}$ - $3 \times 10^{-9}$  Pa. Oxide scale is seen instead on 1-D nanostructures at high dynamic oxygen partial pressure.

- The microstructures of the as-received Ti64 substrate have effect on the 1-D growth. The lamellar and Widmanstätten structure of Ti64 is beneficial for 1-D growth whereas no 1-D nanostructure is seen in coarse grained samples.
- Residual stress significantly enhances the coverage of 1-D nanostructures on Ti64 substrates.
- At the initial stage of oxidation (1-15 min), the 1-D nanostructures are initiated from the  $\beta$  laths due to their faster rate of oxidation. At the later stage of oxidation, the 1-D nanostructures grow on  $\alpha$  grains of Ti. The optimum oxidation duration is 4-8 h. Prolonged oxidation resulted in oxide scale.
- The as-grown nanostructures possess core-shell structure. The core of the nanostructure is rutile-TiO<sub>2</sub> whereas the shell is corundum Al<sub>2</sub>O<sub>3</sub>. The growth direction of TiO<sub>2</sub> and Al<sub>2</sub>O<sub>3</sub> are  $\langle 0\ 0\ 2 \rangle$  and  $\langle 1\ 1\ 0 \rangle$ , respectively.
- Double layer of oxide scale is formed during oxidation of Ti64 substrates. The 1-D nanostructures are originated in outward direction from the outer oxide scale. The outer oxide scale is composed of a mixture of TiO<sub>2</sub> and Al<sub>2</sub>O<sub>3</sub> whereas the inner oxide scale is composed of TiO<sub>2</sub>.
- 1-D nanostructure initiates from the  $(2\ \bar{1}\ \bar{1}\ 0)$  and  $(1\ 0\ \bar{1}\ 0)$  crystallographic planes of  $\alpha$ -Ti. The 1-D nanostructures grow in the family of  $\langle 2\ \bar{2}\ 0\ 1 \rangle$  directions of  $\alpha$ -Ti crystals.

### 5.1.3 Gas Sensing

- The fine 1-D core-shell  $\text{TiO}_2\text{-Al}_2\text{O}_3$  nanostructures on Ti64 particles have better sensing response compared with thick core-shell  $\text{TiO}_2\text{-Al}_2\text{O}_3$  nanostructures on Ti64 particles and 1-D  $\text{TiO}_2$  nanostructures on Ti particles.
- The particle loading on the substrate has significant effect on sensing performance. Higher loading of particles during the preparation of sensor resulted in insufficient oxidation leading to high conductivity in the as-prepared sensors. The optimum amount of particle loading in the ink during the preparation of sensor is 2-5 wt%.
- The optimum sensing temperature of the sensor is 650 °C. The sensors show selective response towards  $\text{H}_2\text{S}$ ,  $\text{CH}_3\text{OH}$  and  $\text{C}_2\text{H}_5\text{OH}$ . In all cases the sensitivity towards  $\text{C}_2\text{H}_5\text{OH}$  is higher compared with  $\text{CH}_3\text{OH}$  followed by  $\text{H}_2\text{S}$ . The response of the fine 1-D core-shell  $\text{TiO}_2\text{-Al}_2\text{O}_3$  sensor at 650 °C towards 1000 ppm  $\text{H}_2\text{S}$ ,  $\text{CH}_3\text{OH}$  and  $\text{C}_2\text{H}_5\text{OH}$  are 38.7, 349.6 and 1109, respectively.
- The response time of the sensor decreases with increasing the target gas whereas the recovery time increases.
- An electron tunneling assisted surface depletion model is proposed to explain the general sensing mechanism of 1-D core-shell  $\text{TiO}_2\text{-Al}_2\text{O}_3$  sensors. However, enhance catalytic activity of  $\text{TiO}_2$  towards  $\text{H}_2\text{S}$ ,  $\text{CH}_3\text{OH}$  and  $\text{C}_2\text{H}_5\text{OH}$  is reason for selectivity.
- Amorphous layer of carbon is deposited on the 1-D nanostructure during the exposure of  $\text{CH}_3\text{OH}$  and  $\text{C}_2\text{H}_5\text{OH}$  gases. For this reason the resistance of the sensor dropped and as a result higher response is seen for these gases.

## 5.2 Recommendations

The results obtained from this work point out numerous interesting directions which can be investigated in future. Some of the future research directions are mentioned below.

- From this study it is seen that the growth of 1-D nanostructures on Ti and Ti64 substrates depends on dynamic oxygen partial pressure. Below a certain dynamic oxygen partial pressure, no oxidation occurs and above a certain pressure oxide scales are seen. Theoretical calculations show that the dynamic oxygen partial pressure is a function of flow rate, oxygen concentration and tube diameter. So, in future, oxidation process can be carried out with different tube diameters to validate the theory. Moreover, this theory can be generalized for 1-D growth on other metals such as copper (Cu), iron (Fe), tungsten (W) etc.
- Oxidation of Ti64 alloy substrates resulted in binary 1-D core-shell  $\text{TiO}_2\text{-Al}_2\text{O}_3$  nanostructures. It is observed that the 1-D nanostructures initiate from the  $\beta$  laths of Ti64 substrates. In future, oxidation can be carried out on other  $\beta$  or near  $\beta$  alloys of Ti such as Ti-10V-2Fe-3Al, Ti-13V-11Cr-3Al, Ti-8Mo-8V-2Fe-3Al etc. It is expected that 1-D nanostructures with different morphologies and compositions would evolve during oxidation of these alloys.
- The gas sensitivity of the 1-D core-shell  $\text{TiO}_2\text{-Al}_2\text{O}_3$  nanostructures can be improved by loading different types of catalyst nanoparticles such as Pd, Pt, Ag and Au on the nanostructures. It is expected that the activation energy for the adsorption of gas molecules will be reduced by increasing catalytic surface area and catalytic activation of gas molecules. As a result, the sensor could be operated at low temperatures. It is also expected that the lower limit of detection, response time and recovery time of the sensor will improved.
- It is known that human breath contains trace amount of “breath marker” due to different diseases. Reported results show that “breath marker” for diabetics,

kidney diseases, lungs inflammations, liver diseases, schizophrenia, bacterial infection and asthma are acetone, ammonia, carbon monoxides, dimethyl sulfide, ethane, hydrogen cyanide and nitric oxide, respectively. In future, attempts can be taken to detect different diseases from human breath using gas sensors.

University of Malaya

## REFERENCES

- Akbar, S. A., & Younkman, L. B. (1997). Sensing mechanism of a carbon monoxide sensor based on anatase titania. *Journal of The Electrochemical Society*, 144(5), 1750-1753.
- Al-Hardan, N., Abdullah, M., Aziz, A. A., & Ahmad, H. (2010). Low operating temperature of oxygen gas sensor based on undoped and Cr-doped ZnO films. *Applied Surface Science*, 256(11), 3468-3471.
- Arafat, M., Haseeb, A., & Akbar, S. A. (2014). A selective ultrahigh responding high temperature ethanol sensor using TiO<sub>2</sub> nanoparticles. *Sensors*, 14(8), 13613-13627.
- Baik, J. M., Kim, M. H., Larson, C., Chen, X., Guo, S., Wodtke, A. M., & Moskovits, M. (2008). High-yield TiO<sub>2</sub> nanowire synthesis and single nanowire field-effect transistor fabrication. *Applied Physics Letters*, 92(24), 242111.
- Baratto, C., Sberveglieri, G., Onischuk, A., Caruso, B., & Di Stasio, S. (2004). Low temperature selective NO<sub>2</sub> sensors by nanostructured fibres of ZnO. *Sensors and Actuators B: Chemical*, 100(1), 261-265.
- Barsoum, M. W., Hoffman, E. N., Doherty, R. D., Gupta, S., & Zavaliangos, A. (2004). Driving force and mechanism for spontaneous metal whisker formation. *Physical Review Letters*, 93(20), 206104.
- Beck, D. D., & Siegel, R. W. (1992). The dissociative adsorption of hydrogen sulfide over nanophase titanium dioxide. *Journal of materials research*, 7(10), 2840-2845.
- Biesinger, M. C., Lau, L. W., Gerson, A. R., & Smart, R. S. C. (2010). Resolving surface chemical states in XPS analysis of first row transition metals, oxides and hydroxides: Sc, Ti, V, Cu and Zn. *Applied Surface Science*, 257(3), 887-898.
- Birkefeld, L. D., Azad, A. M., & Akbar, S. A. (1992). Carbon monoxide and hydrogen detection by anatase modification of titanium dioxide. *Journal of the American Ceramic Society*, 75(11), 2964-2968.
- Blocher, J. M., & Campbell, I. (1949). Vapor pressure of titanium. *Journal of the American Chemical Society*, 71(12), 4040-4042.
- Brenner, S., & Sears, G. (1956). Mechanism of whisker growth—III nature of growth sites. *Acta Metallurgica*, 4(3), 268-270.
- Bruno, L., Pijolat, C., & Lalauze, R. (1994). Tin dioxide thin-film gas sensor prepared by chemical vapour deposition: Influence of grain size and thickness on the electrical properties. *Sensors and Actuators B: Chemical*, 18(1-3), 195-199.
- Cabot, A., Arbiol, J., Morante, J. R., Weimar, U., Bârsan, N., & Göpel, W. (2000). Analysis of the noble metal catalytic additives introduced by impregnation of as

obtained SnO<sub>2</sub> sol-gel nanocrystals for gas sensors. *Sensors and Actuators B: Chemical*, 70(1), 87-100.

Cai, R., Li, T., Wang, Y., Wang, C., Yuan, L., & Zhou, G. (2012). Formation of modulated structures in single-crystalline hexagonal  $\alpha$ -Fe<sub>2</sub>O<sub>3</sub> nanowires. *Journal of Nanoparticle Research*, 14(8), 1-11.

Cano, I. G., Dosta, S., Miguel, J. R., & Guilemany, J. M. (2007). Production and characterization of metastable Al<sub>2</sub>O<sub>3</sub>-TiO<sub>2</sub> ceramic materials. *Journal of materials science*, 42(22), 9331-9335.

Cao, Y., Hu, P., Pan, W., Huang, Y., & Jia, D. (2008). Methanal and xylene sensors based on ZnO nanoparticles and nanorods prepared by room-temperature solid-state chemical reaction. *Sensors and Actuators B: Chemical*, 134(2), 462-466.

Carley, A., Roberts, J., & Roberts, M. (1990). Dissociative chemisorption and localized oxidation states at titanium surfaces. *Surface Science*, 225(3), L39-L41.

Carney, C. M., Yoo, S., & Akbar, S. A. (2005). TiO<sub>2</sub>-SnO<sub>2</sub> nanostructures and their H<sub>2</sub> sensing behavior. *Sensors and Actuators B: Chemical*, 108(1), 29-33.

Chai, G., Lupan, O., Chow, L., & Heinrich, H. (2009). Crossed zinc oxide nanorods for ultraviolet radiation detection. *Sensors and Actuators A: Physical*, 150(2), 184-187.

Chang, J., Kuo, H., Leu, I., & Hon, M. (2002). The effects of thickness and operation temperature on ZnO: Al thin film CO gas sensor. *Sensors and Actuators B: Chemical*, 84(2), 258-264.

Chaudhari, G., Bambole, D., Bodade, A., & Padole, P. (2006). Characterization of nanosized TiO<sub>2</sub> based H<sub>2</sub>S gas sensor. *Journal of materials science*, 41(15), 4860-4864.

Chen, G., Stolojan, V., Cox, D., Giusca, C., & Silva, S. (2006). *Growth of tungsten oxide nanowires using simple thermal heating*. Paper presented at the 2006 IEEE Conference on Emerging Technologies-Nanoelectronics.

Chen, X., & Mao, S. S. (2007). Titanium dioxide nanomaterials: synthesis, properties, modifications, and applications. *Chem. Rev*, 107(7), 2891-2959.

Chen, Y., Nie, L., Xue, X., Wang, Y., & Wang, T. (2006). Linear ethanol sensing of SnO<sub>2</sub> nanorods with extremely high sensitivity. *Applied Physics Letters*, 88(8), 83105-83105.

Cheng, X., Xu, Y., Gao, S., Zhao, H., & Huo, L. (2011). Ag nanoparticles modified TiO<sub>2</sub> spherical heterostructures with enhanced gas-sensing performance. *Sensors and Actuators B: Chemical*, 155(2), 716-721.

Choi, Y.-J., Hwang, I.-S., Park, J.-G., Choi, K. J., Park, J.-H., & Lee, J.-H. (2008). Novel fabrication of an SnO<sub>2</sub> nanowire gas sensor with high sensitivity. *Nanotechnology*, 19(9), 095508.

- Choi, Y. J., Seeley, Z., Bandyopadhyay, A., Bose, S., & Akbar, S. A. (2007). Aluminum-doped TiO<sub>2</sub> nano-powders for gas sensors. *Sensors and Actuators B: Chemical*, 124(1), 111-117.
- Choopun, S., Wongrat, E., & Hongsith, N. (2010). *Metal-oxide nanowires by thermal oxidation reaction technique*: INTECH Open Access Publisher.
- Chueh, Y. L., Hsieh, C. H., Chang, M. T., Chou, L. J., Lao, C. S., Song, J. H., . . . Wang, Z. L. (2007). RuO<sub>2</sub> nanowires and RuO<sub>2</sub>/TiO<sub>2</sub> core/shell nanowires: from synthesis to mechanical, optical, electrical, and photoconductive properties. *Advanced materials*, 19(1), 143-149.
- Comini, E., Faglia, G., Sberveglieri, G., Pan, Z., & Wang, Z. L. (2002). Stable and highly sensitive gas sensors based on semiconducting oxide nanobelts. *Applied Physics Letters*, 81, 1869-1871.
- Cullity, B. D., & Stock, S. R. (2001). Elements of X-ray diffraction. *Prentice Hall, Upper Saddle River, NJ., 3rd Edition*, 435.
- Cvelbar, U., Chen, Z., Sunkara, M. K., & Mozetič, M. (2008). Spontaneous growth of superstructure  $\alpha$ -Fe<sub>2</sub>O<sub>3</sub> nanowire and nanobelt arrays in reactive oxygen plasma. *small*, 4(10), 1610-1614.
- Dang, H., Wang, J., & Fan, S. (2003). The synthesis of metal oxide nanowires by directly heating metal samples in appropriate oxygen atmospheres. *Nanotechnology*, 14(7), 738.
- Daotong, S., Songmee, N., Thongtem, S., & Singjai, P. (2007). Size-controlled growth of TiO<sub>2</sub> nanowires by oxidation of titanium substrates in the presence of ethanol vapor. *Scripta materialia*, 57(7), 567-570.
- Diebold, U. (2003). The surface science of titanium dioxide. *Surface science reports*, 48(5), 53-229.
- Dinan, B. (2012). Growth of titania nanowires by thermal oxidation. *The Ohio State University, USA, PhD thesis*.
- Dinan, B., Gallego-Perez, D., Lee, H., Hansford, D., & Akbar, S. (2013). Thermally grown TiO<sub>2</sub> nanowires to improve cell growth and proliferation on titanium based materials. *Ceramics International*, 39(5), 5949-5954.
- Dinan, B. J., Dregia, S. A., & Akbar, S. A. (2013). Growth of coaxial nanowires by thermal oxidation of Ti64 alloy. *Materials Technology*, 28(5), 280-285.
- Dong, K.-Y., Choi, J.-K., Hwang, I.-S., Lee, J.-W., Kang, B. H., Ham, D.-J., . . . Ju, B.-K. (2011). Enhanced H<sub>2</sub>S sensing characteristics of Pt doped SnO<sub>2</sub> nanofibers sensors with micro heater. *Sensors and Actuators B: Chemical*, 157(1), 154-161.
- Du, H. L., Datta, P. K., Lewis, D. B., & Burnell-Gray, J. S. (1994). Air oxidation behaviour of Ti- 6Al- 4V alloy between 650 and 850°. *Corrosion science*, 36(4), 631-642.

- Dutta, P. K., Frank, M., Hunter, G. W., & George, M. (2005). Reactively sputtered titania films as high temperature carbon monoxide sensors. *Sensors and Actuators B: Chemical*, 106(2), 810-815.
- Ellingham, H. J. T. (1944). Reducibility of oxides and sulfides in metallurgical processes. *J Soc Chem Ind*, 63, 125-133.
- Erdem, B., Hunsicker, R. A., Simmons, G. W., Sudol, E. D., Dimonie, V. L., & El-Aasser, M. S. (2001). XPS and FTIR surface characterization of TiO<sub>2</sub> particles used in polymer encapsulation. *Langmuir*, 17(9), 2664-2669.
- Eshelby, J. (1953). A tentative theory of metallic whisker growth. *Physical Review*, 91(3), 755.
- Feng, P., Wan, Q., & Wang, T. (2005). Contact-controlled sensing properties of flowerlike ZnO nanostructures. *Applied Physics Letters*, 87(21), 213111.
- Ferrari, A. C., & Robertson, J. (2000). Interpretation of Raman spectra of disordered and amorphous carbon. *Physical review B*, 61(20), 14095.
- Fields, L., Zheng, J., Cheng, Y., & Xiong, P. (2006). Room-temperature low-power hydrogen sensor based on a single tin dioxide nanobelt. *Applied Physics Letters*, 88(26), 3102.
- Fitzpatrick, M., Fry, A., Holdway, P., Kandil, F., Shackleton, J., & Suominen, L. (2005). Determination of residual stresses by X-ray diffraction. *DTI, Measurement Good Practice Guide No. 52, Issue 2*.
- Francioso, L., Taurino, A., Forleo, A., & Siciliano, P. (2008). TiO<sub>2</sub> nanowires array fabrication and gas sensing properties. *Sensors and Actuators B: Chemical*, 130(1), 70-76.
- French, R. H. (1990). Electronic band structure of Al<sub>2</sub>O<sub>3</sub>, with comparison to AlON and AlN. *Journal of the American Ceramic Society*, 73(3), 477-489.
- Galatsis, K., Li, Y., Wlodarski, W., Comini, E., Sberveglieri, G., Cantalini, C., . . . Passacantando, M. (2002). Comparison of single and binary oxide MoO<sub>3</sub>, TiO<sub>2</sub> and WO<sub>3</sub> sol-gel gas sensors. *Sensors and Actuators B: Chemical*, 83(1), 276-280.
- Galerie, A., Wouters, Y., & Petit, J. P. (1997). *Interfacial reactions and diffusion during the thermal oxidation of titanium in water vapour*. Paper presented at the Materials science forum.
- Garzella, C., Comini, E., Tempesti, E., Frigeri, C., & Sberveglieri, G. (2000). TiO<sub>2</sub> thin films by a novel sol-gel processing for gas sensor applications. *Sensors and Actuators B: Chemical*, 68(1), 189-196.
- Göbel, M., Sunderkötter, J., Mircea, D., Jenett, H., & Stroosnijder, M. (2000). Study of the high-temperature oxidation behaviour of Ti and Ti<sub>4</sub>Nb with SNMS using tracers. *Surface and Interface Analysis*, 29(5), 321-324.

- Gou, X., Wang, G., Yang, J., Park, J., & Wexler, D. (2008). Chemical synthesis, characterisation and gas sensing performance of copper oxide nanoribbons. *Journal of Materials Chemistry*, 18(9), 965-969.
- Guleryuz, H., & Cimenoglu, H. (2005). Surface modification of a Ti-6Al-4V alloy by thermal oxidation. *Surface and Coatings Technology*, 192(2), 164-170.
- Guleryuz, H., & Cimenoglu, H. (2009). Oxidation of Ti-6Al-4V alloy. *Journal of Alloys and Compounds*, 472(1), 241-246.
- Guo, Z., Li, M., & Liu, J. (2008). Highly porous CdO nanowires: preparation based on hydroxy- and carbonate-containing cadmium compound precursor nanowires, gas sensing and optical properties. *Nanotechnology*, 19(24), 245611.
- Han, C.-H., Hong, D.-W., Kim, I.-J., Gwak, J., Han, S.-D., & Singh, K. C. (2007). Synthesis of Pd or Pt/titanate nanotube and its application to catalytic type hydrogen gas sensor. *Sensors and Actuators B: Chemical*, 128(1), 320-325.
- Hansen, B. J., Lu, G., & Chen, J. (2008). Direct oxidation growth of CuO nanowires from copper-containing substrates. *Journal of Nanomaterials*, 2008, 48.
- Hao, Q., Li, L., Yin, X., Liu, S., Li, Q., & Wang, T. (2011). Anomalous conductivity-type transition sensing behaviors of n-type porous  $\alpha$ -Fe<sub>2</sub>O<sub>3</sub> nanostructures toward H<sub>2</sub>S. *Materials Science and Engineering: B*, 176(7), 600-605.
- Hauk, V. M. (1982). in: E. Kula, V. Weiss (Eds.), Residual stress and stress relaxation. *Plenum Press*, 117.
- Hazra, A., & Bhattacharyya, P. (2014). Tailoring of the gas sensing performance of TiO<sub>2</sub> nanotubes by 1-D vertical electron transport technique. *IEEE Transactions on Electron Devices*, 61(10), 3483-3489.
- Hsueh, T.-J., Hsu, C.-L., Chang, S.-J., & Chen, I.-C. (2007). Laterally grown ZnO nanowire ethanol gas sensors. *Sensors and Actuators B: Chemical*, 126(2), 473-477.
- Hu, A., Cheng, C., Li, X., Jiang, J., Ding, R., Zhu, J., . . . Huang, X. (2011). Two novel hierarchical homogeneous nanoarchitectures of TiO<sub>2</sub> nanorods branched and P25-coated TiO<sub>2</sub> nanotube arrays and their photocurrent performances. *Nanoscale research letters*, 6(1), 1-6.
- Hu, P., Du, G., Zhou, W., Cui, J., Lin, J., Liu, H., . . . Chen, S. (2010). Enhancement of ethanol vapor sensing of TiO<sub>2</sub> nanobelts by surface engineering. *ACS applied materials & interfaces*, 2(11), 3263-3269.
- Huang, M. H., Wu, Y., Feick, H., Tran, N., Weber, E., & Yang, P. (2001). Catalytic growth of zinc oxide nanowires by vapor transport. *Advanced materials*, 13(2), 113-116.
- Huo, K., Zhang, X., Fu, J., Qian, G., Xin, Y., Zhu, B., . . . Chu, P. K. (2009). Synthesis and field emission properties of rutile TiO<sub>2</sub> nanowires arrays grown directly on a

Ti metal self-source substrate. *Journal of nanoscience and nanotechnology*, 9(5), 3341-3346.

Huo, K., Zhang, X., Hu, L., Sun, X., Fu, J., & Chu, P. K. (2008). One-step growth and field emission properties of quiasligned TiO<sub>2</sub> nanowire/carbon nanocone core-shell nanostructure arrays on Ti substrates. *Applied Physics Letters*, 93(1), 3105.

Hwang, I.-S., Kim, S.-J., Choi, J.-K., Choi, J., Ji, H., Kim, G.-T., . . . Lee, J.-H. (2010). Synthesis and gas sensing characteristics of highly crystalline ZnO–SnO<sub>2</sub> core-shell nanowires. *Sensors and Actuators B: Chemical*, 148(2), 595-600.

Hwang, Y. J., Boukai, A., & Yang, P. (2008). High density n-Si/n-TiO<sub>2</sub> core/shell nanowire arrays with enhanced photoactivity. *Nano letters*, 9(1), 410-415.

Hyodo, T., Sasahara, K., Shimizu, Y., & Egashira, M. (2005). Preparation of macroporous SnO<sub>2</sub> films using PMMA microspheres and their sensing properties to NO<sub>x</sub> and H<sub>2</sub>. *Sensors and Actuators B: Chemical*, 106(2), 580-590.

Idriss, H., & Seebauer, E. (2000). Reactions of ethanol over metal oxides. *Journal of Molecular Catalysis A: Chemical*, 152(1), 201-212.

Imawan, C., Solzbacher, F., Steffes, H., & Obermeier, E. (2000). Gas-sensing characteristics of modified-MoO<sub>3</sub> thin films using Ti-overlayers for NH<sub>3</sub> gas sensors. *Sensors and Actuators B: Chemical*, 64(1), 193-197.

Iwasaki, H., & Sudoh, K. (2002). Electron tunneling through an Al<sub>2</sub>O<sub>3</sub> thin film on NiAl (110) in scanning tunneling microscopy. *Japanese journal of applied physics*, 41(12R), 7496.

Jin, Y. Z., Zhu, Y. Q., Whitby, R. L., Yao, N., Ma, R., Watts, P. C., . . . Walton, D. R. (2004). Simple approaches to quality large-scale tungsten oxide nanoneedles. *The Journal of Physical Chemistry B*, 108(40), 15572-15577.

Kaewsai, D., Jaruwongjinda, W., Daothong, S., Singjai, P., Watcharapasorn, A., & Jiansirisomboon, S. (2010). Phase and microstructure of TiO<sub>2</sub> nanowires synthesized by thermal oxidation. *Journal of the Microscopy Society of Thailand*, 24(2), 145-148.

Kang, W., & Kim, C. (1994). Performance analysis of a new metal-insulator-semiconductor capacitor incorporated with Pt-SnO<sub>x</sub> catalytic layers for the detection of O<sub>2</sub> and CO gases. *Journal of Applied Physics*, 75(8), 4237-4242.

Kim, B.-S., Koo, T.-W., Lee, J.-H., Kim, D. S., Jung, Y. C., Hwang, S. W., . . . Whang, D. (2009). Catalyst-free growth of single-crystal silicon and germanium nanowires. *Nano letters*, 9(2), 864-869.

Kim, K., & Barteau, M. (1989). Reactions of methanol on TiO<sub>2</sub> (001) single crystal surfaces. *Surface Science*, 223(1-2), 13-32.

Kim, S. S., Park, J. Y., Choi, S.-W., Kim, H. S., Na, H. G., Yang, J. C., & Kim, H. W. (2010). Significant enhancement of the sensing characteristics of In<sub>2</sub>O<sub>3</sub> nanowires by functionalization with Pt nanoparticles. *Nanotechnology*, 21(41), 415502.

- Kim, W.-S., Kim, H.-C., & Hong, S.-H. (2010). Gas sensing properties of MoO<sub>3</sub> nanoparticles synthesized by solvothermal method. *Journal of Nanoparticle Research*, 12(5), 1889-1896.
- Klöber, J., Ludwig, M., & Schneider, H. (1991). Effects of thickness and additives on thin-film SnO<sub>2</sub> gas sensors. *Sensors and Actuators B: Chemical*, 3(1), 69-74.
- Knauth, P., & Tuller, H. (1999). Electrical and defect thermodynamic properties of nanocrystalline titanium dioxide. *Journal of Applied Physics*, 85, 897-902.
- Kong, X., & Li, Y. (2005). High sensitivity of CuO modified SnO<sub>2</sub> nanoribbons to H<sub>2</sub>S at room temperature. *Sensors and Actuators B: Chemical*, 105(2), 449-453.
- Korotcenkov, G., Brinzari, V., Schwank, J., DiBattista, M., & Vasiliev, A. (2001). Peculiarities of SnO<sub>2</sub> thin film deposition by spray pyrolysis for gas sensor application. *Sensors and Actuators B: Chemical*, 77(1), 244-252.
- Korotcenkov, G., & Cho, B. (2009). Thin film SnO<sub>2</sub>-based gas sensors: film thickness influence. *Sensors and Actuators B: Chemical*, 142(1), 321-330.
- Kremer, R., & Auer, W. (1997). Influence of Moisture on the oxidation of  $\gamma$ -TiAl. *Materials and Corrosion*, 48(1), 35-39.
- Kumar, A., Srivastava, A., Tiwari, P., & Nandedkar, R. (2004). The effect of growth parameters on the aspect ratio and number density of CuO nanorods. *Journal of Physics: Condensed Matter*, 16(47), 8531.
- Kurajica, S., Tkalčec, E., Matijašić, G., Čurković, L., Schauerperl, Z., Šipušić, J., & Mandić, V. (2011). Influence of agglomeration and contamination in the course of amorphous powder grinding on structure and microstructure of sintered mullite. *Croatica Chemica Acta*, 84(1), 63-71.
- Kwon, Y., Kim, H., Lee, S., Chin, I.-J., Seong, T.-Y., Lee, W. I., & Lee, C. (2012). Enhanced ethanol sensing properties of TiO<sub>2</sub> nanotube sensors. *Sensors and Actuators B: Chemical*, 173, 441-446.
- Landau, O., Rothschild, A., & Zussman, E. (2008). Processing-microstructure-properties correlation of ultrasensitive gas sensors produced by electrospinning. *Chemistry of Materials*, 21(1), 9-11.
- Lee, H., & Akbar, S. (2008). Sensing behavior of TiO<sub>2</sub> thin film prepared by r.f. reactive sputtering. *Sensor Letters*, 6(6), 1049-1053.
- Lee, H., Dregia, S., Akbar, S., & Alhoshan, M. (2010). Growth of 1-D TiO<sub>2</sub> nanowires on Ti and Ti alloys by oxidation. *Journal of Nanomaterials*, 2010, 64.
- Leng, M., Chen, Y., & Xue, J. (2014). Synthesis of TiO<sub>2</sub> nanosheets via an exfoliation route assisted by a surfactant. *Nanoscale*, 6(15), 8531-8534.
- Li, H., Cao, L., Liu, W., Su, G., & Dong, B. (2012). Synthesis and investigation of TiO<sub>2</sub> nanotube arrays prepared by anodization and their photocatalytic activity. *Ceramics International*, 38(7), 5791-5797.

- Li, X., Ramasamy, R., & Dutta, P. K. (2009). Study of the resistance behavior of anatase and rutile thick films towards carbon monoxide and oxygen at high temperatures and possibilities for sensing applications. *Sensors and Actuators B: Chemical*, 143(1), 308-315.
- Li, X., Sugui, T., Xianyu, B., & Liqing, C. (2013). Influence of heat treatment on microstructure and creep properties of hot continuous rolled Ti-6Al-4V alloy. *Materials Science and Engineering: A*, 559, 401-406.
- Liao, L., Lu, H., Li, J., He, H., Wang, D., Fu, D., . . . Zhang, W. (2007). Size dependence of gas sensitivity of ZnO nanorods. *The Journal of Physical Chemistry C*, 111(5), 1900-1903.
- Liu, B., & Aydil, E. S. (2009). Growth of oriented single-crystalline rutile TiO<sub>2</sub> nanorods on transparent conducting substrates for dye-sensitized solar cells. *Journal of the American Chemical Society*, 131(11), 3985-3990.
- Liu, Y., Liao, L., Pan, C., Li, J., Dai, Y., & Chen, W. (2008). Modulated structure assisted growth and properties of Fe<sub>3</sub>O<sub>4</sub> nanoneedle films using a thermal oxidation process in the air. *The Journal of Physical Chemistry C*, 112(4), 902-910.
- Liu, Z., Yamazaki, T., Shen, Y., Kikuta, T., Nakatani, N., & Kawabata, T. (2007). Room temperature gas sensing of p-type TeO<sub>2</sub> nanowires. *Applied Physics Letters*, 90(17), 173119.
- Lu, G., Bernasek, S. L., & Schwartz, J. (2000). Oxidation of a polycrystalline titanium surface by oxygen and water. *Surface Science*, 458(1), 80-90.
- Lu, H. F., Li, F., Liu, G., Chen, Z.-G., Wang, D.-W., Fang, H.-T., . . . Cheng, H.-M. (2008). Amorphous TiO<sub>2</sub> nanotube arrays for low-temperature oxygen sensors. *Nanotechnology*, 19(40), 405504.
- Lü, R., Zhou, W., Shi, K., Yang, Y., Wang, L., Pan, K., . . . Fu, H. (2013). Alumina decorated TiO<sub>2</sub> nanotubes with ordered mesoporous walls as high sensitivity NO<sub>x</sub> gas sensors at room temperature. *Nanoscale*, 5(18), 8569-8576.
- Lu, X., & Yin, L. (2011). Porous Indium oxide nanorods: synthesis, characterization and gas sensing properties. *Journal of Materials Science & Technology*, 27(8), 680-684.
- Luo, Q., & Jones, A. (2010). High-precision determination of residual stress of polycrystalline coatings using optimised XRD-sin<sup>2</sup>ψ technique. *Surface and Coatings Technology*, 205(5), 1403-1408.
- Lupan, O., Chai, G., & Chow, L. (2007). Fabrication of ZnO nanorod-based hydrogen gas nanosensor. *Microelectronics Journal*, 38(12), 1211-1216.
- Lupan, O., Chai, G., & Chow, L. (2008). Novel hydrogen gas sensor based on single ZnO nanorod. *Microelectronic Engineering*, 85(11), 2220-2225.

- Lupan, O., Emelchenko, G., Ursaki, V., Chai, G., Redkin, A., Gruzintsev, A., . . . Cuenya, B. R. (2010). Synthesis and characterization of ZnO nanowires for nanosensor applications. *Materials Research Bulletin*, 45(8), 1026-1032.
- Ma, Y., Wang, W., Liao, K., & Kong, C. (2002). Study on sensitivity of nano-grain ZnO gas sensors. *Journal of Wide Bandgap Materials*, 10(2), 113-120.
- Mai, L., Hu, B., Hu, T., Chen, W., & Gu, E. (2006). Electrical Property of Mo-doped VO<sub>2</sub> nanowire array film by melting-quenching sol-gel Method. *The Journal of Physical Chemistry B*, 110(39), 19083-19086.
- Mai, L., Xu, L., Gao, Q., Han, C., Hu, B., & Pi, Y. (2010). Single  $\beta$ -AgVO<sub>3</sub> nanowire H<sub>2</sub>S sensor. *Nano letters*, 10(7), 2604-2608.
- Mema, R., Yuan, L., Du, Q., Wang, Y., & Zhou, G. (2011). Effect of surface stresses on CuO nanowire growth in the thermal oxidation of copper. *Chemical Physics Letters*, 512(1), 87-91.
- Meng, L., Chen, H., Li, C., & Dos Santos, M. P. (2014). Growth of the [110] oriented TiO<sub>2</sub> nanorods on ITO substrates by sputtering technique for dye-sensitized solar cells. *Frontiers in Materials*, 1, 14.
- Miller, D. R., Akbar, S. A., & Morris, P. A. (2014). Nanoscale metal oxide-based heterojunctions for gas sensing: a review. *Sensors and Actuators B: Chemical*, 204, 250-272.
- Min, Y., Tuller, H. L., Palzer, S., Wöllenstein, J., & Böttner, H. (2003). Gas response of reactively sputtered ZnO films on Si-based micro-array. *Sensors and Actuators B: Chemical*, 93(1), 435-441.
- Mochida, T., Kikuchi, K., Kondo, T., Ueno, H., & Matsuura, Y. (1995). Highly sensitive and selective H<sub>2</sub>S gas sensor from rf sputtered SnO<sub>2</sub> thin film. *Sensors and Actuators B: Chemical*, 25(1), 433-437.
- Mohammadi, M. (2014). Semiconductor TiO<sub>2</sub>-Al<sub>2</sub>O<sub>3</sub> thin film gas sensors derived from aqueous particulate sol-gel process. *Materials Science in Semiconductor Processing*, 27, 711-718.
- Mominuzzaman, S. M., Krishna, K. M., Soga, T., Jimbo, T., & Umeno, M. (1999). Optical absorption and electrical conductivity of amorphous carbon thin films from camphor: a natural source. *Japanese journal of applied physics*, 38(2R), 658.
- Montméat, P., Lalauze, R., Viricelle, J.-P., Tournier, G., & Pijolat, C. (2004). Model of the thickness effect of SnO<sub>2</sub> thick film on the detection properties. *Sensors and Actuators B: Chemical*, 103(1), 84-90.
- Montoro, L. A., Corio, P., & Rosolen, J. M. (2007). A comparative study of alcohols and ketones as carbon precursor for multi-walled carbon nanotube growth. *Carbon*, 45(6), 1234-1241.

- Na, C. W., Woo, H.-S., Kim, I.-D., & Lee, J.-H. (2011). Selective detection of NO<sub>2</sub> and C<sub>2</sub>H<sub>5</sub>OH using a Co<sub>3</sub>O<sub>4</sub>-decorated ZnO nanowire network sensor. *Chemical Communications*, 47(18), 5148-5150.
- Nadeem, A., Waterhouse, G., & Idriss, H. (2012). The reactions of ethanol on TiO<sub>2</sub> and Au/TiO<sub>2</sub> anatase catalysts. *Catalysis Today*, 182(1), 16-24.
- Nasibulin, A. G., Rackauskas, S., Jiang, H., Tian, Y., Mudimela, P. R., Shandakov, S. D., . . . Kauppinen, E. I. (2009). Simple and rapid synthesis of  $\alpha$ -Fe<sub>2</sub>O<sub>3</sub> nanowires under ambient conditions. *Nano Research*, 2(5), 373-379.
- Oh, E., Choi, H.-Y., Jung, S.-H., Cho, S., Kim, J. C., Lee, K.-H., . . . Jeong, S.-H. (2009). High-performance NO<sub>2</sub> gas sensor based on ZnO nanorod grown by ultrasonic irradiation. *Sensors and Actuators B: Chemical*, 141(1), 239-243.
- Park, J.-A., Moon, J., Lee, S.-J., Kim, S. H., Chu, H. Y., & Zyung, T. (2010). SnO<sub>2</sub>-ZnO hybrid nanofibers-based highly sensitive nitrogen dioxides sensor. *Sensors and Actuators B: Chemical*, 145(1), 592-595.
- Parker, J., & Siegel, R. (1990). Calibration of the Raman spectrum to the oxygen stoichiometry of nanophase TiO<sub>2</sub>. *Applied Physics Letters*, 57(9), 943-945.
- Patra, A. K., Das, S. K., & Bhaumik, A. (2011). Self-assembled mesoporous TiO<sub>2</sub> spherical nanoparticles by a new templating pathway and its enhanced photoconductivity in the presence of an organic dye. *Journal of Materials Chemistry*, 21(11), 3925-3930.
- Paulose, M., Varghese, O. K., Mor, G. K., Grimes, C. A., & Ong, K. G. (2005). Unprecedented ultra-high hydrogen gas sensitivity in undoped titania nanotubes. *Nanotechnology*, 17(2), 398.
- Peng, H., & Li, J. (2008). Quantum confinement and electronic properties of rutile TiO<sub>2</sub> nanowires. *The Journal of Physical Chemistry C*, 112(51), 20241-20245.
- Peng, X., & Chen, A. (2004). Aligned TiO<sub>2</sub> nanorod arrays synthesized by oxidizing titanium with acetone. *Journal of Materials Chemistry*, 14(16), 2542-2548.
- Peng, X., & Chen, A. (2005). Dense and high-hydrophobic rutile TiO<sub>2</sub> nanorod arrays. *Applied Physics A*, 80(3), 473-476.
- Peng, X., Wang, J., Thomas, D. F., & Chen, A. (2005). Tunable growth of TiO<sub>2</sub> nanostructures on Ti substrates. *Nanotechnology*, 16(10), 2389.
- Pérez, P. (2007). On the influence of water vapour on the oxidation behaviour of pure Ti. *Corrosion science*, 49(3), 1172-1185.
- Phanichphant, S., Liewhiran, C., Wetchakun, K., Wisitsoraat, A., & Tuantranont, A. (2011). Flame-made Nb-doped TiO<sub>2</sub> ethanol and acetone sensors. *Sensors*, 11(1), 472-484.
- Prevéy, P. S. (1986). X-ray diffraction residual stress techniques. *ASM International, ASM Handbook*, 10, 380-392.

- Prevéy, P. S. (1996). Current applications of X-ray diffraction residual stress measurement. *Development in Materials Characterization Technologies*, ASM International, Materials Park, OH, 103-110.
- Qi, Q., Zhang, T., Liu, L., & Zheng, X. (2009). Synthesis and toluene sensing properties of SnO<sub>2</sub> nanofibers. *Sensors and Actuators B: Chemical*, 137(2), 471-475.
- Qurashi, A., El-Maghraby, E., Yamazaki, T., & Kikuta, T. (2010). Catalyst supported growth of In<sub>2</sub>O<sub>3</sub> nanostructures and their hydrogen gas sensing properties. *Sensors and Actuators B: Chemical*, 147(1), 48-54.
- Qurashi, A., Yamazaki, T., El-Maghraby, E., & Kikuta, T. (2009). Fabrication and gas sensing properties of In<sub>2</sub>O<sub>3</sub> nanopushpins. *Appl. Phys. Lett*, 95(153109), 1-153109.
- Rao, G. T., & Rao, D. T. (1999). Gas sensitivity of ZnO based thick film sensor to NH<sub>3</sub> at room temperature. *Sensors and Actuators B: Chemical*, 55(2), 166-169.
- Rella, R., Spadavecchia, J., Manera, M., Capone, S., Taurino, A., Martino, M., . . . Tunno, T. (2007). Acetone and ethanol solid-state gas sensors based on TiO<sub>2</sub> nanoparticles thin film deposited by matrix assisted pulsed laser evaporation. *Sensors and Actuators B: Chemical*, 127(2), 426-431.
- Ren, S., Bai, Y., Chen, J., Deng, S., Xu, N., Wu, Q., & Yang, S. (2007). Catalyst-free synthesis of ZnO nanowire arrays on zinc substrate by low temperature thermal oxidation. *Materials Letters*, 61(3), 666-670.
- Rout, C. S., Kulkarni, G., & Rao, C. (2007). Room temperature hydrogen and hydrocarbon sensors based on single nanowires of metal oxides. *Journal of Physics D: Applied Physics*, 40(9), 2777.
- Roy, V., Djurišić, A., Chan, W., Gao, J., Lui, H., & Surya, C. (2003). Luminescent and structural properties of ZnO nanorods prepared under different conditions. *Applied Physics Letters*, 83(1), 141-143.
- Sadek, A. Z., Choopun, S., Wlodarski, W., Ippolito, S. J., & Kalantar-zadeh, K. (2007). Characterization of ZnO nanobelt-based gas sensor for H<sub>2</sub>, NO<sub>2</sub>, and hydrocarbon sensing. *IEEE Sensors Journal*, 7(6), 919-924.
- Saruhan, B., Yüce, A., Gönüllü, Y., & Kelm, K. (2013). Effect of Al doping on NO<sub>2</sub> gas sensing of TiO<sub>2</sub> at elevated temperatures. *Sensors and Actuators B: Chemical*, 187, 586-597.
- Savage, N. O., Akbar, S. A., & Dutta, P. K. (2001). Titanium dioxide based high temperature carbon monoxide selective sensor. *Sensors and Actuators B: Chemical*, 72(3), 239-248.
- Sears, G. (1955). A mechanism of whisker growth. *Acta Metallurgica*, 3(4), 367-369.
- Sen, I., Tamirisakandala, S., Miracle, D., & Ramamurty, U. (2007). Microstructural effects on the mechanical behavior of B-modified Ti-6Al-4V alloys. *Acta Materialia*, 55(15), 4983-4993.

- Sen, S., Kanitkar, P., Sharma, A., Muthe, K., Rath, A., Deshpande, S., . . . Yakhmi, J. (2010). Growth of SnO<sub>2</sub>/W<sub>18</sub>O<sub>49</sub> nanowire hierarchical heterostructure and their application as chemical sensor. *Sensors and Actuators B: Chemical*, 147(2), 453-460.
- Seo, M.-H., Yuasa, M., Kida, T., Huh, J.-S., Shimanoe, K., & Yamazoe, N. (2009). Gas sensing characteristics and porosity control of nanostructured films composed of TiO<sub>2</sub> nanotubes. *Sensors and Actuators B: Chemical*, 137(2), 513-520.
- Shi, J., & Wang, X. (2011). Growth of rutile titanium dioxide nanowires by pulsed chemical vapor deposition. *Crystal Growth & Design*, 11(4), 949-954.
- Shi, S., Liu, Y., Chen, Y., Zhang, J., Wang, Y., & Wang, T. (2009). Ultrahigh ethanol response of SnO<sub>2</sub> nanorods at low working temperature arising from La<sub>2</sub>O<sub>3</sub> loading. *Sensors and Actuators B: Chemical*, 140(2), 426-431.
- Singh, N., Gupta, R. K., & Lee, P. S. (2011). Gold-nanoparticle-functionalized In<sub>2</sub>O<sub>3</sub> nanowires as CO gas sensors with a significant enhancement in response. *ACS applied materials & interfaces*, 3(7), 2246-2252.
- Song, H.-J., Han, M.-K., Jeong, H.-G., Lee, Y.-T., & Park, Y.-J. (2014). Microstructure analysis of Ti-xPt alloys and the effect of Pt content on the mechanical properties and corrosion behavior of Ti alloys. *Materials*, 7(5), 3990-4000.
- Srivastava, H., Tiwari, P., Srivastava, A., & Nandedkar, R. (2007). Growth and characterization of  $\alpha$ -Fe<sub>2</sub>O<sub>3</sub> nanowires. *Journal of Applied Physics*, 102(5), 054303.
- Stringer, J. (1960). The oxidation of titanium in oxygen at high temperatures. *Acta Metallurgica*, 8(11), 758-766.
- Sun, Y., Fuge, G. M., & Ashfold, M. N. (2004). Growth of aligned ZnO nanorod arrays by catalyst-free pulsed laser deposition methods. *Chemical Physics Letters*, 396(1), 21-26.
- Sysoev, V., Schneider, T., Goschnick, J., Kiselev, I., Habicht, W., Hahn, H., . . . Kolmakov, A. (2009). Percolating SnO<sub>2</sub> nanowire network as a stable gas sensor: direct comparison of long-term performance versus SnO<sub>2</sub> nanoparticle films. *Sensors and Actuators B: Chemical*, 139(2), 699-703.
- Tan, A., Ismail, R., Chua, K., Ahmad, R., Akbar, S., & Pinguan-Murphy, B. (2014). Osteogenic potential of in situ TiO<sub>2</sub> nanowire surfaces formed by thermal oxidation of titanium alloy substrate. *Applied Surface Science*, 320, 161-170.
- Tan, B., & Wu, Y. (2006). Dye-sensitized solar cells based on anatase TiO<sub>2</sub> nanoparticle/nanowire composites. *The Journal of Physical Chemistry B*, 110(32), 15932-15938.
- Tan, Y., Li, C., Wang, Y., Tang, J., & Ouyang, X. (2008). Fast-response and high sensitivity gas sensors based on SnO<sub>2</sub> hollow spheres. *Thin Solid Films*, 516(21), 7840-7843.

- Taniguchi, S., Hongawara, N., & Shibata, T. (2001). Influence of water vapour on the isothermal oxidation behaviour of TiAl at high temperatures. *Materials Science and Engineering: A*, 307(1), 107-112.
- Tezuka, Y., Shin, S., Ishii, T., Ejima, T., Suzuki, S., & Sato, S. (1994). Photoemission and Bremsstrahlung isochromat spectroscopy studies of TiO<sub>2</sub> (rutile) and SrTiO<sub>3</sub>. *Journal of the Physical Society of Japan*, 63(1), 347-357.
- Tian, Y., Lu, H., Wang, D., Li, J., Shuai, M., & Fu, Q. (2008). Synthesis of zinc oxide hollow spherical structure via precursor-template and formation mechanism. *Journal of the Physical Society of Japan*, 77(7), 074603.
- Varghese, B., Haur, S. C., & Lim, C.-T. (2008). Nb<sub>2</sub>O<sub>5</sub> nanowires as efficient electron field emitters. *The Journal of Physical Chemistry C*, 112(27), 10008-10012.
- Varghese, O. K., Gong, D., Paulose, M., Ong, K. G., & Grimes, C. A. (2003). Hydrogen sensing using titania nanotubes. *Sensors and Actuators B: Chemical*, 93(1), 338-344.
- Wagner, R., & Ellis, W. (1964). Vapor-liquid-solid mechanism of single crystal growth. *Applied Physics Letters*, 4(5), 89-90.
- Wan, Q., Li, Q., Chen, Y., Wang, T.-H., He, X., Li, J., & Lin, C. (2004). Fabrication and ethanol sensing characteristics of ZnO nanowire gas sensors. *Applied Physics Letters*, 84(18), 3654-3656.
- Wan, Q., Lin, C., Yu, X., & Wang, T. (2004). Room-temperature hydrogen storage characteristics of ZnO nanowires. *Applied Physics Letters*, 84(1), 124-126.
- Wang, B., Zhao, Y., Hu, L., Cao, J., Gao, F., Liu, Y., & Wang, L. (2010). Improved and excellent CO sensing properties of Cu-doped TiO<sub>2</sub> nanofibers. *Chinese Science Bulletin*, 55(3), 228-232.
- Wang, C., Chu, X., & Wu, M. (2006). Detection of H<sub>2</sub>S down to ppb levels at room temperature using sensors based on ZnO nanorods. *Sensors and Actuators B: Chemical*, 113(1), 320-323.
- Wang, C., Yin, L., Zhang, L., Xiang, D., & Gao, R. (2010). Metal oxide gas sensors: sensitivity and influencing factors. *Sensors*, 10(3), 2088-2106.
- Wang, D., Chu, X., & Gong, M. (2006). Gas-sensing properties of sensors based on single-crystalline SnO<sub>2</sub> nanorods prepared by a simple molten-salt method. *Sensors and Actuators B: Chemical*, 117(1), 183-187.
- Wang, H.-T., Kang, B., Ren, F., Tien, L., Sadik, P., Norton, D., . . . Lin, J. (2005). Hydrogen-selective sensing at room temperature with ZnO nanorods. *Applied Physics Letters*, 86(24), 243503.
- Wang, Y., Cao, Y., Li, Y., Jia, D., & Xie, J. (2014). Directed synthesis of TiO<sub>2</sub> nanorods and their photocatalytic activity. *Ceramics International*, 40(8), 11735-11742.

- Wang, Y., Qu, F., Liu, J., Wang, Y., Zhou, J., & Ruan, S. (2015). Enhanced H<sub>2</sub>S sensing characteristics of CuO-NiO core-shell microspheres sensors. *Sensors and Actuators B: Chemical*, 209, 515-523.
- Weimer, M. A., Hakim, L. F., King, D. M., Liang, X., Weimer, A. W., George, S. M., . . . Groner, M. D. (2008). Ultrafast metal-insulator varistors based on tunable Al<sub>2</sub>O<sub>3</sub> tunnel junctions. *Applied Physics Letters*, 92(16), 164101.
- Wooldridge, M., Torek, P., Donovan, M., Hall, D., Miller, T., Palmer, T., & Schrock, C. (2002). An experimental investigation of gas-phase combustion synthesis of SiO<sub>2</sub> nanoparticles using a multi-element diffusion flame burner. *Combustion and flame*, 131(1), 98-109.
- Wu, F., Myung, Y., & Banerjee, P. (2014). Unravelling transient phases during thermal oxidation of copper for dense CuO nanowire growth. *CrystEngComm*, 16(16), 3264-3267.
- Wu, J.-M., Shih, H. C., & Wu, W.-T. (2005). Growth of TiO<sub>2</sub> nanorods by two-step thermal evaporation. *Journal of Vacuum Science & Technology B*, 23(5), 2122-2126.
- Wu, J.-M., Wu, W.-T., & Shih, H. C. (2005). Characterization of single-crystalline TiO<sub>2</sub> nanowires grown by thermal evaporation. *Journal of The Electrochemical Society*, 152(8), G613-G616.
- Wu, W.-Y., Chang, Y.-M., & Ting, J.-M. (2010). Room-temperature synthesis of single-crystalline anatase TiO<sub>2</sub> nanowires. *Crystal Growth & Design*, 10(4), 1646-1651.
- Xia, Y., Yang, P., Sun, Y., Wu, Y., Mayers, B., Gates, B., . . . Yan, H. (2003). One-dimensional nanostructures: synthesis, characterization, and applications. *Advanced materials*, 15(5), 353-389.
- Xie, R.-C., & Shang, J. K. (2007). Morphological control in solvothermal synthesis of titanium oxide. *Journal of materials science*, 42(16), 6583-6589.
- Xu, J.-a., Huang, E., & Xu, L. Y. (1995). Raman study at high pressure and the thermodynamic properties of corundum: Application of Kieffer's model. *American Mineralogist*, 80(11-12), 1157-1165.
- Yamazoe, N. (1991). New approaches for improving semiconductor gas sensors. *Sensors and Actuators B: Chemical*, 5(1-4), 7-19.
- Yang, X., Wang, C., Yang, Y., Zhang, Y., Jia, X., Chen, J., & Ji, X. (2015). Anatase TiO<sub>2</sub> nanocubes for fast and durable sodium ion battery anodes. *Journal of Materials Chemistry A*, 3(16), 8800-8807.
- Yang, Z., Li, L.-M., Wan, Q., Liu, Q.-H., & Wang, T.-H. (2008). High-performance ethanol sensing based on an aligned assembly of ZnO nanorods. *Sensors and Actuators B: Chemical*, 135(1), 57-60.
- Yanxin, C., Yi, J., Wenzhao, L., Rongchao, J., Shaozhen, T., & Wenbin, H. (1999). Adsorption and interaction of H<sub>2</sub>S/SO<sub>2</sub> on TiO<sub>2</sub>. *Catalysis Today*, 50(1), 39-47.

- Yeh, C., Chen, M., Hwang, J., Gan, J., & Kou, C. (2006). Field emission from a composite structure consisting of vertically aligned single-walled carbon nanotubes and carbon nanocones. *Nanotechnology*, *17*(24), 5930.
- Ying, Z., Wan, Q., Song, Z., & Feng, S. (2004). SnO<sub>2</sub> nanowhiskers and their ethanol sensing characteristics. *Nanotechnology*, *15*(11), 1682.
- Yoo, S., Akbar, S. A., & Sandhage, K. H. (2004a). Nanocarving of bulk titania crystals into oriented arrays of single-crystal nanofibers via reaction with hydrogen-bearing gas. *Advanced materials*, *16*(3), 260-264.
- Yoo, S., Akbar, S. A., & Sandhage, K. H. (2004b). Nanocarving of titania (TiO<sub>2</sub>): a novel approach for fabricating chemical sensing platform. *Ceramics International*, *30*(7), 1121-1126.
- Yu, J., Chen, Y., & Glushenkov, A. M. (2009). Titanium oxide nanorods extracted from ilmenite sands. *Crystal Growth and Design*, *9*(2), 1240-1244.
- Yu, T., Zhu, Y., Xu, X., Yeong, K. S., Shen, Z., Chen, P., . . . Sow, C. H. (2006). Substrate-friendly synthesis of metal oxide nanostructures using a hotplate. *small*, *2*(1), 80-84.
- Yuan, L., Wang, Y., Cai, R., Jiang, Q., Wang, J., Li, B., . . . Zhou, G. (2012). The origin of hematite nanowire growth during the thermal oxidation of iron. *Materials Science and Engineering: B*, *177*(3), 327-336.
- Yuan, L., Wang, Y., Mema, R., & Zhou, G. (2011). Driving force and growth mechanism for spontaneous oxide nanowire formation during the thermal oxidation of metals. *Acta Materialia*, *59*(6), 2491-2500.
- Yuan, L., & Zhou, G. (2012). Enhanced CuO nanowire formation by thermal oxidation of roughened copper. *Journal of The Electrochemical Society*, *159*(4), C205-C209.
- Yunarti, R. T., Lee, M., Hwang, Y. J., Choi, J.-W., Suh, D. J., Lee, J., . . . Ha, J.-M. (2014). Transition metal-doped TiO<sub>2</sub> nanowire catalysts for the oxidative coupling of methane. *Catalysis Communications*, *50*, 54-58.
- Zeng, W., Liu, T., & Wang, Z. (2010). Sensitivity improvement of TiO<sub>2</sub>-doped SnO<sub>2</sub> to volatile organic compounds. *Physica E: Low-dimensional Systems and Nanostructures*, *43*(2), 633-638.
- Zhang, J., Wang, S., Wang, Y., Xu, M., Xia, H., Zhang, S., . . . Wu, S. (2009). Facile synthesis of highly ethanol-sensitive SnO<sub>2</sub> nanoparticles. *Sensors and Actuators B: Chemical*, *139*(2), 369-374.
- Zhang, N., Yu, K., Li, Q., Zhu, Z., & Wan, Q. (2008). Room-temperature high-sensitivity H<sub>2</sub>S gas sensor based on dendritic ZnO nanostructures with macroscale in appearance. *Journal of Applied Physics*, *103*(10), 4305.

- Zheng, W., Lu, X., Wang, W., Li, Z., Zhang, H., Wang, Z., . . . Wang, C. (2009). Assembly of Pt nanoparticles on electrospun  $\text{In}_2\text{O}_3$  nanofibers for  $\text{H}_2\text{S}$  detection. *Journal of colloid and interface science*, 338(2), 366-370.
- Zheng, X., Li, J., & Zhou, Y. (2004). X-ray diffraction measurement of residual stress in PZT thin films prepared by pulsed laser deposition. *Acta Materialia*, 52(11), 3313-3322.
- Zhou, X., Li, J., Ma, M., & Xue, Q. (2011). Effect of ethanol gas on the electrical properties of ZnO nanorods. *Physica E: Low-dimensional Systems and Nanostructures*, 43(5), 1056-1060.

University of Malaya

## LIST OF PUBLICATIONS AND PAPERS PRESENTED

### ISI Indexed Journal Papers

1. Arafat, M. M., Haseeb, A. S. M. A., Akbar, S. A., & Quadir, M. Z. (2017). In-situ fabricated gas sensors based on one dimensional core-shell TiO<sub>2</sub>-Al<sub>2</sub>O<sub>3</sub> nanostructures. *Sensors and Actuators B: Chemical*, 238, 972-984.
2. Arafat, M. M., Haseeb, A. S. M. A., & Akbar, S. A. (2014). Growth and characterization of the oxide scales and core/shell nanowires on Ti-6Al-4V particles during thermal oxidation. *Ceramics International*, 41(3), 4401-4409.
3. Arafat, M. M., Haseeb, A. S. M. A., & Akbar, S. A. (2014). A selective ultrahigh responding high temperature ethanol sensor using TiO<sub>2</sub> nanoparticles. *Sensors*, 14, 13613-13627.
4. Arafat, M. M., Haseeb, A. S. M. A., Dinan, B., & Akbar, S. A. (2013). Stress enhanced TiO<sub>2</sub> nanowire growth on Ti-6Al-4V particles by thermal oxidation. *Ceramics International*, 39(6), 6517-6526.

### Conference Paper

1. Arafat, M. M., Haseeb, A. S. M. A., & Akbar, S. A. (2014). Selective sensing of ethanol gas by using core/shell TiO<sub>2</sub>/Al<sub>2</sub>O<sub>3</sub> nanowires grown on Ti-6Al-4V particles. *AUN/SEED-Net Regional Conference on Materials Engineering 2014 in Conjunction with the 3<sup>rd</sup> UM-JWRI International Seminar*, 11-12 November, 2014, Kuala Lumpur, Malaysia, Abstract ID: RCME064.

### Book Chapters

1. Arafat, M. M., Haseeb, A. S. M. A. & Akbar, S. A. (2016). Synthesis of one dimensional nanostructures of TiO<sub>2</sub> by thermal oxidation. In: *Saleem Hashmi (editor-in-chief), Reference Module in Materials Science and Materials Engineering (Mochida et al.), Oxford: Elsevier*, 1-13.
2. Arafat, M. M., Haseeb, A. S. M. A., & Akbar, S. A. (2014). Developments in semiconducting oxide-based gas-sensing materials. *Comprehensive Materials Processing, Vol. 13, First Edition*, 205-219.